



HAL
open science

Rate coefficients and branching ratio measurements for reactions of astrochemical relevance involving CN radicals

Divita Gupta

► **To cite this version:**

Divita Gupta. Rate coefficients and branching ratio measurements for reactions of astrochemical relevance involving CN radicals. Chemical Physics [physics.chem-ph]. Université de Rennes, 2021. English. NNT : 2021REN1S129 . tel-03934779

HAL Id: tel-03934779

<https://theses.hal.science/tel-03934779>

Submitted on 11 Jan 2023

HAL is a multi-disciplinary open access archive for the deposit and dissemination of scientific research documents, whether they are published or not. The documents may come from teaching and research institutions in France or abroad, or from public or private research centers.

L'archive ouverte pluridisciplinaire **HAL**, est destinée au dépôt et à la diffusion de documents scientifiques de niveau recherche, publiés ou non, émanant des établissements d'enseignement et de recherche français ou étrangers, des laboratoires publics ou privés.

THÈSE / UNIVERSITÉ DE RENNES 1

pour le grade de

DOCTEUR DE L'UNIVERSITÉ DE RENNES 1

Mention principale: Physique

Mention secondaire: Chimie

Ecole doctorale "Matière, Molécules et Matériaux"

présentée par

Divita GUPTA

préparée à l'unité de recherche UMR CNRS 6251 IPR

Institut de Physique de Rennes

UFR Sciences et Propriétés de la Matière

**Rate Coefficients and
Branching Ratio
Measurements for Reactions
of Astrochemical Relevance
Involving CN Radicals**

Thèse soutenue à Rennes

le 06 Octobre 2021

devant le jury composé de :

Dwayne HEARD

Professeur, University of Leeds/rapporteur

Christa FITTSCHEN

Directeur de recherche, Université de Lille/rapporteur

Marie-Aline MARTIN-DRUMEL

Chargée de recherche, Université de Paris-Saclay/
examineur

Ludovic BIENNIER

Chargé de recherche, CNRS, Université de Rennes 1/
examineur

Ilsa COOKE

Ingénieur de recherche, Université de Rennes 1/
co-encadrante de thèse

Ian SIMS

Professeur, Université de Rennes 1/directeur de thèse

*You can't cross the
sea merely by
standing and
staring at the water.*

RABINDRANATH

TAGORE

Acknowledgements

First and foremost, I would like to thank my supervisor Ian Sims for welcoming into the group, and giving me the unique and such a fulfilling opportunity to work on the CRESUCHIRP project. I am grateful for all his guidance and support through these three years. I am immensely fortunate to have had Ilsa Cooke as my co-supervisor. These three years seemed to fly by when working with her— her constant encouragement and belief in my scientific skills has helped me become the researcher I am today.

The best part of this journey was the joy of working with the CRESUCHIRP Team— Ilsa, Théo, Brian, Omar, Myriam, and Tom. I am hugely grateful to have shared the scientific space with all of them, as they made science and developing the new lab that has its challenges a whole lot more fun. I have thoroughly enjoyed all our “out-of-work” drinking gatherings, both in-person and over Zoom.

The whole Astrolab team at IPR has been very supportive and has provided great company. I appreciate their scientific inputs on projects during our meetings and all the wonderful fun conversations I’ve had with them. I am especially thankful to Jonathan Courbe and Jonathan Thièven for their technical help.

I am also grateful to Prof. Dwayne Heard for having me as a visiting researcher to learn the MESMER program. Although my time was cut short due to COVID situation, I thoroughly enjoyed meeting and discussing with Mark, Desmond, and Nic, and overall loved visiting Leeds. I am happy that I got the chance to work with Joey for the aromatics research and look forward to seeing you in person again.

I will always cherish our friendship, Asma and Adel. Thank you for all the wonderful meals. I will miss not being able to have our random weekend breakfasts together.

I am extremely thankful to my parents for all their love, support and encouragement during this journey. I also want to thank my brother, Archit for supporting my journey to scientific research.

Mayank, I am incredibly thankful for your love and support. This journey, both personally and scientifically, would not have been this enjoyable without you.

Abstract

Low-temperature laboratory studies to explore CN radical reactions relevant to interstellar environments were performed using the CRESU technique coupled with pulsed laser photolysis–laser induced fluorescence and chirped–pulse Fourier transform microwave spectroscopy.

Rate coefficients for the reaction of CN radical with methanol, benzene, and toluene were measured from 296 K down to 16 K using the pulsed–laser photolysis–laser induced fluorescence technique by monitoring the CN radical concentration over time. A negative temperature dependence was observed for the reaction of methanol with the CN radical, presented in Chapter 4, typical of what has been seen previously for other radical–neutral reactions that do not possess potential energy barriers. The measurements significantly deviate from the values currently in the Kinetics Database for Astrochemistry (KIDA) that are used in various astrochemical models and recommendations for updated values are provided. Chapter 5 covers the kinetics measurements for the reaction of two aromatic molecules, benzene and toluene, with CN radical which shows that these reactions remain fast down to 16 K. The potential interstellar implications of these measurements in the light of the recent detection of cyano–substituted benzene in the interstellar medium are discussed.

The second part of this thesis was focused on investigating the product channel–specific branching ratios for the reaction of CN radical with propene at 35 K. These experiments were performed using the recently developed E–band chirped pulse FT-microwave spectrometer integrated with the CRESU technique allowing detection of one product channel, which is the first measurement of its kind for this reaction below room temperature. The results for this reaction are presented in Chapter 6 along with the future direction for this study.

Keywords – Chemical Kinetics, Astrochemistry, Gas-phase reactions, CRESU (Reaction Kinetics in Uniform Flow), PLP–LIF, Chirped pulse microwave spectroscopy, Branching ratio

Resumé

Des études en laboratoire à basse température pour explorer des réactions impliquant le radical CN, d'intérêt astrochimique ont été réalisées en utilisant la technique CRESU couplée aux techniques de photolyse par laser pulsée - fluorescence induite par laser et spectroscopie micro-ondes à transformée de Fourier à impulsions chirpées.

Les coefficients de vitesse pour la réaction du radical CN avec le méthanol, le benzène, et le toluène ont été mesurés de 296 K à 16 K en utilisant la technique de photolyse par laser pulsée - fluorescence induite par laser en mesurant la concentration du radical CN en fonction du temps. Une dépendance thermique négative a été observée pour la réaction du méthanol avec le CN, présentée dans le chapitre 4, typique de ce qui a été vu précédemment pour d'autres réactions radicalaires neutres qui ne possèdent pas de barrières énergétiques potentielles. Les mesures diffèrent considérablement des valeurs présentées dans la base de données cinétique pour l'astrochimie (KIDA) utilisées dans divers modèles astrochimiques. Le chapitre 5 couvre les mesures de cinétique pour la réaction entre deux molécules aromatiques, le benzène et le toluène et le radical CN, démontrant que ces réactions restent rapides jusqu'à 16 K. Les implications interstellaires potentielles de ces mesures à la lumière de la détection récente de cyano-substitution du benzène dans le milieu interstellaire sont discutées.

La deuxième partie de cette thèse s'est concentrée sur l'étude du rapport de branchement spécifique pour la réaction du radical CN avec le propène à 35 K. Ces expériences ont été réalisées à l'aide du spectromètre micro-ondes par transformée de Fourier à impulsions chirpées en bande E récemment développé intégré avec la technique CRESU. Permettant la détection d'un produit de réaction, qui est une première pour cette réaction en dessous de la température ambiante. Les résultats de cette réaction sont présentés au chapitre 6 ainsi que les perspectives de cette étude.

Mots clés – Cinétique chimique, Astrochimie, Réactions en phase gazeuse, CRESU (Cinétique de Réaction en Ecoulement Supersonique Uniforme), PLP-LIF, Spectroscopie micro-onde à impulsions chirpées, Rapport de branchement

Publications

List of Publications (thesis work)

- **Divita Gupta**, Sidaty Cheikh Sid Ely, Ilsa R. Cooke, Théo Guillaume, Omar Abdelkader Khedaoui, Thomas S. Hearne, Brian M Hays, Ian R. Sims; Low Temperature Kinetics of the Reaction Between Methanol and the CN Radical, *The Journal of Physical Chemistry A*, 123(46), 9995-10003 doi: 10.1021/acs.jpca.9b08472
- Ilsa R. Cooke, **Divita Gupta**, Joseph P. Messinger, Ian R. Sims; Benzonitrile as a Proxy for Benzene in the Cold ISM: Low-Temperature Rate Coefficients for CN + C₆H₆; *The Astrophysical Journal Letters* 2020, 891(2), L41, doi: 10.3847/2041-8213/ab7a9c (<https://arxiv.org/pdf/2003.02101.pdf>)
- Joseph P. Messinger, **Divita Gupta**, Ilsa R. Cooke, Mitchio Okumura, Ian R. Sims; Rate Constants of the CN + Toluene Reaction from 15 – 294 K and Interstellar Implications; *The Journal of Physical Chemistry A*. 2020, doi: 10.1021/acs.jpca.0c06900

Publications from contributory projects

- Brian M Hays, Théo Guillaume, Thomas S. Hearne, Ilsa R. Cooke, **Divita Gupta**, Omar Abdelkader Khedaoui, Sébastien Le Picard, Ian R. Sims; Design and performance of an E-band chirped pulse spectrometer for kinetics applications: OCS – He pressure broadening; *Journal of Quantitative Spectroscopy and Radiative Transfer* 2020, 250, 107001, doi: 10.1016/j.jqsrt.2020.107001
- Brian M Hays, **Divita Gupta**, Théo Guillaume, Omar Abdelkader Khedaoui, Ilsa R. Cooke, Frank Thibault, Francois Lique, Frank Demouchel, Ian R. Sims; Measuring the Difference in Collisional Interaction of HCN and HNC with He at Low Temperatures (*Submitted*)
- Théo Guillaume, **Divita Gupta**, Brian M Hays, Ilsa R. Cooke, Omar Abdelkader Khedaoui, Thomas S. Hearne, Myriam Drissi, Ian R. Sims; Quantitative Detection of Bimolecular Reaction Products in Continuous Low-Temperature Uniform Supersonic Flows by Chirped Pulse Millimeter-Wave Spectroscopy (*Under preparation*)

Contents

Abstract	i
List of Figures	vii
List of Tables	xv
1 Introduction	1
1.1 Astrochemical Background	1
1.1.1 Interstellar medium	3
1.1.2 Planets, moons and planetoids	5
1.2 Interplay: Observations, Theory & Experiments	6
1.2.1 Observations	7
1.2.2 Theoretical calculations and astrochemical modeling	8
1.2.3 Experiments	8
1.3 Gas-phase Reactions	10
1.3.1 Reaction kinetics	11
1.3.1.1 Temperature dependence of rate coefficients	12
1.3.1.2 Pressure dependence of rate coefficients	14
1.3.2 Product-specific kinetics/branching ratios	15
1.4 Reaction Kinetics Theories	16
1.4.1 Simple collision theory	16
1.4.2 Transition state theory	17
1.4.3 Capture theory	18
1.4.3.1 Semi-Empirical model	19
1.5 Outline of this thesis	20
2 Experimental methodology	21
2.1 Introduction	21
2.2 The CRESU technique	21
2.2.1 Comparison with other cooling techniques	23
2.2.2 Laval nozzle characterisation	24
2.2.3 CRESU chambers at Rennes	27
2.2.3.1 CRESU-B	28
2.2.3.2 CRESU-Chirp	29
2.3 Liquid flow controller	30
2.4 Radical Generation	31
2.4.1 UV-Visible spectrometer setup	33
2.5 Laser Induced Fluorescence Spectroscopy	36
2.5.1 PLP-LIF setup available at Rennes	38
2.5.2 Data acquisition and analysis	39

2.6	Chirped–pulse microwave spectroscopy	41
2.6.1	Setup developed at Rennes	43
2.6.2	Data acquisition	46
2.6.3	Data analysis	48
3	Theoretical calculations	51
3.1	Introduction	51
3.2	Quantum Mechanics	51
3.2.1	Levels of theories used	52
3.2.2	Basis sets used	52
3.3	Parameters/Quantities computed in this work	53
3.3.1	Geometry optimisation	53
3.3.2	Potential Energy Surface Calculations	53
3.3.3	Thermochemistry	54
4	Low temperature reaction kinetics of CN radical with methanol	55
4.1	Introduction	55
4.2	Experimental Methodology and Results	57
4.2.1	Experimental Measurements	57
4.2.2	Experimental Results	59
4.3	Theoretical Methodology and Results	62
4.3.1	Theoretical Calculations	62
4.3.2	Theoretical Results	64
4.4	Discussion	64
4.5	Conclusion	66
5	Low temperature reaction kinetics of CN radical with aromatic molecules: benzene and toluene	69
5.1	Introduction	69
5.2	Experimental Methodology and Results	72
5.2.1	Experimental Measurements	72
5.2.2	Experimental Results	73
5.2.2.1	CN + Benzene	73
5.2.2.2	CN + Toluene	77
5.3	Theoretical Methodology and Results	79
5.3.1	Theoretical Calculations	80
5.3.2	Theoretical Results	81
5.4	Discussion	82
5.4.1	Chemical Kinetics	82
5.4.2	Reaction products	85
5.4.3	Astrophysical Implications	87
5.5	Conclusion	90
6	Low temperature product branching ratios for the reaction of CN radical with propene	93
6.1	Introduction	93
6.2	Experimental methodology and results	97
6.2.1	Experimental measurements	97
6.2.2	Experimental results	98
6.3	Theoretical methodology and results	103

6.3.1	Theoretical calculations	103
6.3.2	Theoretical results	103
6.4	Discussion	104
6.5	Conclusion and future outlook	107
7	Summary and future perspective	109
	References	113
	Appendix	128
A.1	Appendix	129
A1	Pitot profiles of the nozzles used	129
A2	UV-Vis spectrometer analysis	143
A3	Second order plots	147
	A3.1 CN + Methanol	147
	A3.2 CN + Benzene	149
	A3.3 CN + Toluene	153
A4	ICN spectrum and comparison	162
A5	VAR and INT files for the cyanopropene isomers	163
A6	Skimmer chamber details and comparison with CRESU Classic	166
A7	Optimised geometries	168
	A7.1 CN + Methanol	168
	A7.2 CN + Toluene	170
	A7.3 CN + Propene	172
	Annex	197
	Résumé détaillé	198

List of Figures

1.1.1	Stages of star- and planet formation, as the gas/dust are recycled during the cycle. Image reproduced from van Dishoeck [2014] with credit to NASA/ESA/ESO/NRAO.	2
1.1.2	Optical image of the Carina nebula from the Hubble Telescope Credit: NASA/ESA/M. Livio.	3
1.1.3	True color photograph of layers of clouds in Titan's atmosphere with an overlay of molecules detected in Titan's atmosphere. Titan image credit: NASA.	5
1.2.1	Violin plot showing the masses of molecules detected over different wavelength ranges. Reproduced from McGuire [2018].	7
1.2.2	Modeled gas-phase column densities of benzonitrile, various cyanopolynes, and CN in TMC-1 as a function of time in solid colored lines. The dots with dashed horizontal lines show the abundances derived from observations. Reproduced from [McGuire et al., 2018].	9
1.3.1	General cases for exothermic reactions. The top panels show an approximate potential energy surface, while the bottom panels show the log of the rate coefficient against inverse of temperature. a, A reaction with a substantial barrier, which adheres approximately to the Arrhenius equation. b, A reaction with no barrier, showing strongly non-Arrhenius behaviour. c, A reaction passing through an initial weakly bound complex and then over a barrier (which may or may not be above the reagent energy): the reaction adheres to the Arrhenius equation only at higher temperatures. Reproduced from Sims [2013].	13
1.3.2	Rate coefficients, k (left), and the ratio, $k(T)/k(300\text{ K})$ (right), as a function of temperature for the reaction of OH with several organic molecules. Reproduced from Heard [2018].	14
1.3.3	Pressure dependence of the rate coefficient for an association process, described by the Lindemann-Hinshelwood mechanism.	15
1.4.1	Hard sphere collision model depicting the impact parameter (b) used to estimate reaction cross-section.	16
2.2.1	Laval nozzle with a convergent-divergent design used for generating low temperature supersonic flows. Simulation image credit: Omar Abdelkader Khedaoui.	22
2.2.2	Isentropic flow and the boundary layer which arises due to a real nozzle profile, instead of an ideal profile. The boundary layer thickness, which varies for different nozzle designs and flow temperatures, is typically the same order of magnitude as the isentropic core. Image from Fournier et al. [2017]	23
2.2.3	2-dimensional Pitot tube setup used for nozzle characterisation, installed in CRESU-B chamber. Image credit: Martin Fournier.	25
2.2.4	Pitot impact pressure characterization of a Laval nozzle with He as buffer gas to achieve an average temperature of 14.8 K and ~ 6 mm isentropic core.	26

2.2.5	Picture of both the chambers used in this work. The main pumping system is used to pump both chambers, and another turbo pump is used for the pumping of a secondary chamber, explained in section 2.2.3.2	27
2.2.6	CRESUChirp chamber schematic showing the different regions: (A) Chamber region where the reaction takes place and from where the excimer laser enters, (B) Reservoir which is fitted with a nozzle, (C) Skimmer chamber which is pumped by a turbo pump, (D) 4-way cross which is connected to the pumps and the CRESU-B chamber. Image adapted from Théo Guillaume.	29
2.3.1	The liquid flow system, including a flow meter, gas flow controller, and a CEM, used for introducing the liquid reactants in this work.	30
2.3.2	Liquid flow meter calibration: Measured mass of propanol against the expected mass, which was measured by the area under the curve for the flow rate against time. . . .	32
2.4.1	Precursor/ICN vessel, fitted with a glass frit, used to flow in the precursor with a buffer gas flowing in from the top.	32
2.4.2	Schematic for the UV-Vis spectrometer setup integrated with the precursor (ICN) vessel to measure the precursor concentration going into the main CRESU flow. . .	33
2.4.3	Output from the Igor Pro code showing the absorbance measured for ICN on the left-axis and a comparison of literature absorption cross-section with the absorption-cross section calculated using the measured absorbance.	34
2.4.4	The heating pad apparatus used with the ICN vessel along with the controller. . . .	35
2.4.5	ICN concentration stability over time with (black filled circles) and without (orange filled squares) the heating pad.	36
2.5.1	The CN $B^2\Sigma^+(v'=0) \leftarrow X^2\Sigma^+(v''=0)$ laser induced fluorescence scheme utilised for the laboratory detection of CN radicals in this work. The red upward arrow represents the laser excitation wavelength utilised to excite CN to its first electronically excited state. The green downward arrow represents the off-resonant fluorescent emission. Figure credit: Ilsa R. Cooke	36
2.5.2	Schematic of a CRESU apparatus configured for the study of neutral-neutral reactions using laser-induced fluorescence, based on the setup at the Université de Rennes. The reactant, buffer gas, and radical reactant precursor are delivered to the reservoir via a series of flow controllers. The gas mixture enters the chamber through the Laval nozzle, through which expansion produces a uniform supersonic flow. Radicals are produced in the supersonic beam by photolysis of a precursor using radiation from a fixed frequency pulsed excimer laser and are detected by LIF that is excited using tunable radiation from a dye laser. Image from Cooke and Sims [2019]	37
2.5.3	Optics setup utilised to focus the fluorescence onto the photomultiplier tube (not to scale). The blue dotted lines indicate the focusing action of the optics.	38
2.5.4	CN spectrum recorded under CRESU conditions at 83 K, shown in blue, in comparison with the simulation at 83 K using PGOPHER Western [2017]	39
2.5.5	Picture of the electronics rack used for the PLP-LIF experiments.	40
2.5.6	PMT and LIF signals, as collected during an LIF experiment (using simulated data).	41
2.6.1	Visual representation of the principle of chirped-pulse microwave spectroscopy or the effect of chirped microwave radiation on molecular species. Figure credit: Ilsa R. Cooke	42
2.6.2	Schematic of the E-band spectrometer used in this work with the digitizer in as the acquisition device. Image from Hays et al. [2020].	44
2.6.3	CRESUCHIRP E-band setup developed at Université de Rennes.	46

2.6.4	Schematic of the data acquisition scheme for measuring laser-produced products in the skimmer chamber formed via reaction or photolysis. The insets show the time-domain data when the pre-laser frames are averaged and subtracted from the remaining frames.	47
2.6.5	Schematic of the multicolour pulses which allow us to monitor the various species at the same time as the FID collected has a combination of the FIDs from the different species. Figure credit: Ilsa R. Cooke	48
3.3.1	An illustration of a potential energy surface.	54
4.2.1	LIF signal, in red, recorded for the reaction between methanol and CN radical in the left panel for a temperature of 168 K, fit to a single exponential decay function (black solid line). The right panel shows the second-order kinetics plot where the pseudo-first order rate coefficients are plotted against the methanol concentrations. The black line shows the fit yielding the second-order bimolecular rate coefficient. The red point corresponds to the k_{1st} obtained from the decay shown in the left panel at a methanol density of $2.22 \times 10^{14} \text{ cm}^{-3}$	58
4.2.2	Measurement of pseudo-first order rate coefficient as a function of methanol as a test for clustering of methanol at 83 K in black, with a buffer gas density of $4.9 \times 10^{16} \text{ cm}^{-3}$ and 296 K in red, with a buffer gas density of $9 \times 10^{16} \text{ cm}^{-3}$. The solid black line for the data at 83 K is used to stress on the deviation from linear behaviour.	60
4.2.3	Rate coefficients for the reaction of CN radicals with methanol displayed on log-log scale as a function of temperature. The filled black circles are the experiments performed with the CRESU setup using EM I and the filled green circles are the experiments using EM II. The blue diamond represents the work of Sayah et al. [1988] and the magenta diamond represents the work of Janssen and Hershberger [2015]. The modified Arrhenius fit: $\alpha(T/300)^\beta e^{-\gamma/T}$ with the fitting parameters: $\alpha = (1.39 \pm 0.06) \times 10^{11}$, $\beta = -0.40 \pm 0.08$ and $\gamma = -13.6 \pm 3.6$, where the errors are 1σ	61
4.2.4	The CRESU experimental data (black filled circles) fit with a modified Arrhenius equation (black solid line) and the prediction based on the room temperature value from this work using capture theory from Faure et al. [2009] (green dashed line). The current KIDA recommendation for this reaction is shown in pink	62
4.3.1	Relative reaction energy (in kJ mol^{-1}) calculated at CCSD(T)/aug-cc-pVTZ//CCSD/aug-cc-pVTZ for the product channels considered in this work.	63
5.2.1	Kinetics data obtained using PLP-LIF in continuous CRESU flows for a temperature of 72 K. The left panel shows CN radical LIF signal decay of $\text{CN}(B^2\Sigma^+ \rightarrow X^2\Sigma^+)$ at a benzene density of $1.6 \times 10^{13} \text{ cm}^{-3}$ fit with a single exponential decay function (black line). The right panel shows the second-order kinetics plot where the pseudo-first order rate coefficients are plotted against the benzene concentration. The black line shows the fit yielding the second-order bimolecular rate coefficient. The red point corresponds to the k_{1st} obtained from the decay shown in the left panel.	73
5.2.2	Measurement of pseudo-first order rate coefficient as a function of benzene density as a test for clustering of benzene at 16 K. The black hollow boxes show the measurements show a linear behaviour and could be used for the linear fit (black line) to provide the second-order rate coefficient at this temperature. (These test measurements were not used in the final analysis; a different nozzle with a lower density was used for the low temperature (15 K) measurements.)	75

5.2.3	The pseudo- k_{1st} for the reaction between CN and benzene at 23 K with [benzene] at $2 \times 10^{13} \text{ cm}^{-3}$ shown as a function of varying excimer laser (248 nm) fluence. . . .	75
5.2.4	Rate coefficients for the reaction of the CN radical with benzene as a function of temperature displayed on a log-log scale. The circles are the data taken here using the continuous CRESU in Rennes, with helium buffer gas in red, nitrogen in blue and argon in green. The black diamonds are the data taken by Trevitt et al. [2010] using a pulsed CRESU. The cyan triangle shows the estimated rate coefficient used by McGuire et al. [2018] to model the abundance of benzonitrile in TMC-1 at 7 K. The black horizontal line shows the mean value over the temperature range.	76
5.2.5	Kinetics data for the CN + toluene obtained using PLP-LIF in continuous CRESU flows for a temperature of 83 K. The left panel shows LIF signal decay of $\text{CN}(B^2\Sigma^+ \rightarrow X^2\Sigma^+)$ at a toluene density of $4.8 \times 10^{13} \text{ cm}^{-3}$ fit with a single exponential decay function (black line). The right panel shows the second-order kinetics plot where the pseudo-first order rate coefficients are plotted against the toluene concentration. The black line shows the fit yielding the second-order bimolecular rate coefficient. The red point corresponds to the k_{1st} obtained from the decay shown in the left panel.	77
5.2.6	Rate coefficients for the reaction of the CN radical with toluene as a function of temperature displayed on a log-log scale. The circles are the data taken here using the continuous CRESU in Rennes, with helium buffer gas in red, nitrogen in blue and argon in pink. The black triangle is the datum taken by Trevitt et al. [2010] using a pulsed CRESU. The black horizontal line shows the mean value over the temperature range.	78
5.2.7	The pseudo- k_{1st} for the reaction between CN and toluene at 110 K with [toluene] at $9 \times 10^{12} \text{ cm}^{-3}$ shown as a function of varying excimer laser (248 nm) fluence. . . .	78
5.3.1	The reaction pathways of the CN + toluene reaction and possible products of the abstraction (R1-R4) and CN-addition (R5-R8) channels that are considered in the theoretical calculations.	80
5.3.2	The stationary points for PES for the CN + toluene reaction, performed at (U)M06-2X/aug-cc-pVTZ and include zero-point energy corrections, showing the abstraction (abs-) pathways (blue) and addition-elimination (add- and elim-) pathways (red), the latter of which can undergo an internal hydrogen shift (-bridge). Note that a barrier leading to the formation of $\text{C}_6\text{H}_5\text{CH}_2 + \text{HCN}$ could not be located despite several attempts.	81
5.4.1	Experimental kinetics of the CN radical + toluene measured using PLP-LIF, at room temperature (294 K). The left panel shows LIF signal decay of $\text{CN}(B^2\Sigma^+ \rightarrow X^2\Sigma^+)$ at a toluene density of $7.1 \times 10^{13} \text{ cm}^{-3}$ fit with a single exponential decay function (black line). The right panel shows the second-order kinetics plot where the pseudo-first order rate coefficients are plotted against the toluene concentration. The black line shows the fit yielding the second-order bimolecular rate coefficient. The red filled circle corresponds to the k_{1st} obtained from the decay shown in the left panel showing decay of the CN signal and resulting second-order plot at 294 K.	84
5.4.2	Modeled gas-phase column densities of benzonitrile in TMC-1 as a function of time in solid coloured lines. The dots with dashed horizontal lines show the abundances derived from observations. Reproduced from McGuire et al. [2018]. The black dot shows the measured abundance in TMC-1 and the solid line shows the modeled abundance using a rate coefficient of $3 \times 10^{-10} \text{ cm}^3 \text{ s}^{-1}$	88

6.1.1	The reaction pathways of the CN + propene reaction and possible products of the addition-elimination (R1–R4) and abstraction (R5–R8) channels that are considered in the theoretical calculations.	95
6.2.1	Propene spectrum, in black, recorded at ~ 5 K using a chirp 69–71 GHz shown along with the catalog lines from CDMS, in red. The A and E components arise due to the internal rotation of the methyl group in propene. The blue asterisk represent an electronic spur.	98
6.2.2	Rotation diagram using the line intensities of the propene spectrum in the range 69–71 GHz. The rotational temperature is calculated as the negative inverse of the slope and $T_{\text{rot}} = (4.9 \pm 0.5)$ K was measured.	99
6.2.3	Spectrum obtained at ~ 5 K for a mixture of cis and trans 1-cyano propene shown along with the simulated catalog lines using SPCAT at slightly higher temperature of 9 K.	100
6.2.4	Measurement of propene rotational transition intensity at as a function of number density of propene in the flow as a test for clustering of propene at 35 K.	101
6.2.5	ICN number density in the CRESU flow during the reactions of CN with ethene and propene	101
6.2.6	Spectrum recorded 350 μs after the excimer laser pulse compared with the simulated spectra (9 K) of the products using SPCAT.	102
6.2.7	The rise in intensity of the rotational feature from vinyl cyanide over time from the reaction of CN + propene. The time stamps indicate the delay from the excimer laser pulse/start of reaction. The top inset shows the time dependence of the line intensity.	103
6.3.1	Potential Energy Surface the reaction of CN + propene. All energies are zero-point corrected and are given at (U)M06-2X/cc-pvTZ in kcal/mol.	104
6.4.1	Vinyl cyanide rotational line intensity from the reactions of CN with ethene and propene as a function of time.	105
7.0.1	Simulated spectrum of methoxy (CH_3O) at 20 K and room temperature. The inset shows the spectral lines over the frequency range accessible at Rennes. Adapted Image credit: Ilsa Cooke.	110
A1.1	Pitot profile for 17 K nozzle with He buffer gas	129
A1.2	Pitot profile for 15 K nozzle with He buffer gas	130
A1.3	Pitot profile for 24 K nozzle with He buffer gas	131
A1.4	Pitot profile for 25 K nozzle with He buffer gas	132
A1.5	Pitot profile for 35 K nozzle with Ar buffer gas	133
A1.6	Pitot profile for 36 K nozzle with He buffer gas	134
A1.7	Pitot profile for 53 K nozzle with Ar buffer gas	135
A1.8	Pitot profile for 72 K nozzle with He buffer gas	136
A1.9	Pitot profile for 83 K nozzle with N_2 buffer gas	137
A1.10	Pitot profile for 97 K nozzle with Ar buffer gas	138
A1.11	Pitot profile for 112 K nozzle with Ar buffer gas	139
A1.12	Pitot profile for 141 K nozzle with Ar buffer gas	140
A1.13	Pitot profile for 168 K nozzle with Ar buffer gas	141
A1.14	Pitot profile for 200 K nozzle with N_2 buffer gas	142
A4.1	ICN microwave spectrum	162
A4.2	Comparison of the relative intensities measured over time for ICN in the CRESU flow measured with chirped pulse microwave spectroscopy and calculated using UV-Vis spectrometer	162

A6.1	Computational simulations performed to calculate the temperature profile inside the secondary chamber, after the flow at 35 K expands. Credit: Omar Abdelkader Khedaoui.	167
A6.2	Comparison of time-domain and frequency-domain data collected with and without the secondary expansion. Credit: Omar Abdelkader Khedaoui.	167

List of Tables

2.2.1	Mean temperature, gas density, Mach number, length of the uniform/stable flow, total flows used and chamber pressure obtained for the nozzles utilised in this work for kinetic studies, characterised via impact pressure measurements.	26
2.4.1	Parameters of the laser and CN radicals generated at 248 nm (100 Hz for the chirped-pulse experiments).	35
4.2.1	Rate Coefficients for the Reaction of the CN Radical with Methanol Measured at Different Temperatures, with the Associated Experimental Parameters ^a	59
4.3.1	Reaction Enthalpies $\Delta H_r^\circ(298.15 \text{ K})$, in kJ mol^{-1} , Calculated for Each Channel Using CBS-QB3 Compared with the Enthalpy Values Calculated from the Values Provided in the Active Thermochemical Table Ver. 1.22 e74a	63
5.2.1	Rate coefficients for the reaction of the CN radical with benzene measured at different temperatures, with the associated experimental parameters ^a	74
5.2.2	Rate coefficients for the reaction of the CN radical with toluene measured at different temperatures, with the associated experimental parameters ^a	79
5.3.1	Zero-point corrected reaction energies and Gibbs energies of the reaction products calculated in this work. Note that some reaction pathways result in the same products.	82
6.2.1	Details of the multicolor pulse used for monitoring the products from the reaction CN + propene.	102
6.4.1	Conditions and the calculated parameters for the two reaction scans, CN + C ₂ H ₄ and CN + C ₃ H ₆ , used in this work and for calibration. Nozzle total density and 100,000 acquisitions each	105

Chapter 1

Introduction

1.1 Astrochemical Background

Astrochemistry has been defined as ‘the study of the formation, destruction and excitation of molecules in astronomical environments and their influence on the structure, dynamics and evolution of astronomical objects’ by Alexander Dalgarno, a pioneer of this field. Astrochemistry is a relatively young interdisciplinary field lying at the nexus of astronomy, chemistry, and physics.

An astronomer’s periodic table is fairly restricted as the Universe consists primarily of hydrogen and helium, 90% and 8% by number, respectively. In fact, all other elements are referred to as ‘metals’ by astronomers which significantly deviates from a chemist’s definition. Oxygen, carbon, and nitrogen are the next most abundant elements which are still orders of magnitude less abundant than hydrogen. For a long time, the exotic conditions of space or “vacuum” were deemed too extreme for any interesting chemistry to happen.

However, over the past ca. 50 years, more than 200 different chemical species [McGuire, 2018] have been detected in the interstellar space, driven by the construction of increasing powerful radio-astronomical facilities and experimental advancements. We now know that chemical complexity varies over the various stages of stellar evolution, shown in Figure 1.1.1, as the material in space is recycled.

The first stage is a pre-stellar core which begins with diffuse “cold” clouds, densities ranging from $10\text{--}10^2\text{ cm}^{-3}$, and over time can slowly accumulate towards the centre. This leads to an increase in the density at the centre, up to 10^6 cm^{-3} and a decrease in temperature, one of the reasons being the inability of UV photons from the surroundings to penetrate deep enough towards the centre. During

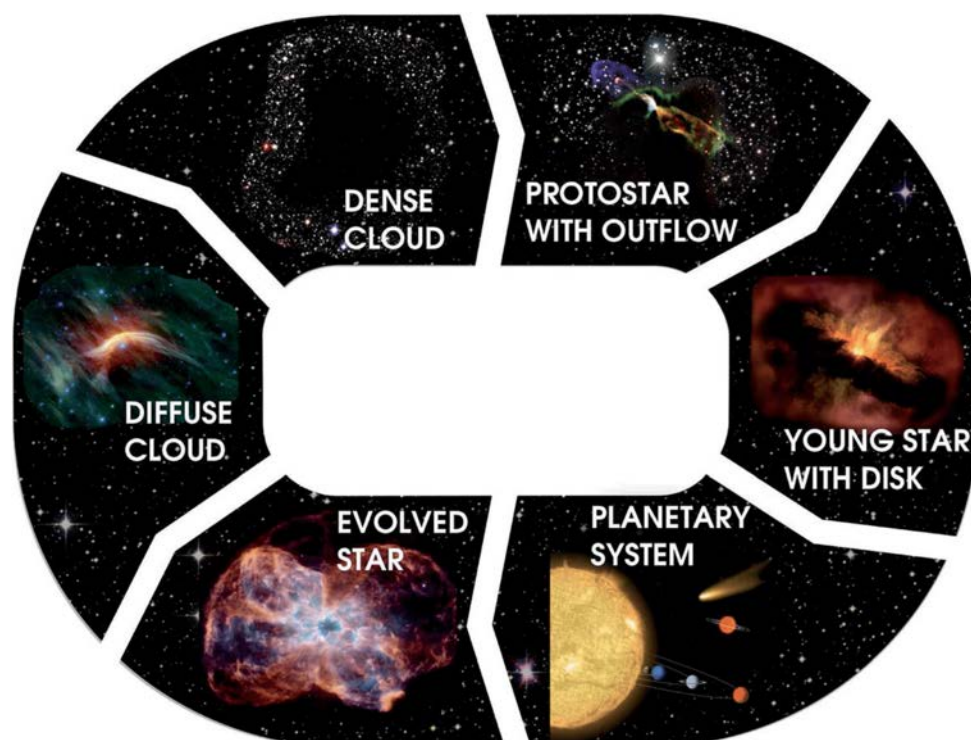


Figure 1.1.1: Stages of star- and planet formation, as the gas/dust are recycled during the cycle. Image reproduced from van Dishoeck [2014] with credit to NASA/ESA/ESO/NRAO.

this stage, the small molecules present in gas phase like carbon monoxide (CO), water (H₂O), among others begin to freeze-out onto the cold dust grain surfaces. Figure 1.1.2 shows an optical image of Carina nebula, where the dust in a cloud can be seen. As this collapse progresses, the gravitational energy gets converted into radiation and an outflow of matter is generated. The region warms up and the molecules previously frozen in grain mantles gain mobility and/or can sublime into the gas phase to form new larger/more complex species. Complex species by astronomical standards are defined quite differently compared to a general organic chemist's definition. Any molecule containing more than or equal to 6 atoms [Herbst and van Dishoeck, 2009] is referred to as a complex organic molecule (COM) by an astronomer.

Eventually, the envelope depletes and only a disk remains, referred to as a protoplanetary disk. A temperature gradient persists in these disks as the hot regions towards the centre see a wide variety of chemistry, while in the cold regions, molecules begin to freeze-out again, this time along with newly formed species during the prestellar stage. Over time, grain/dust particles begin to aggregate to form meteoritic material and planetsimals. The last stage is the formation of a planetary system as gradual coagulation continues. At the end of a stellar life cycle, the star/sun loses its nuclear fuel and explodes or collapses- releasing all the material into interstellar space.

The chemical species, thus, can prove to be as excellent diagnostic of the stage of the stellar cycle as they shed light on the physical conditions and processes, including number densities, temperatures, and gas dynamics, in the regions they are detected. The molecules also play an important active role by assisting the cooling mechanisms which are very important for facilitating the collapse of molecular clouds, the formation of stars, and radiative equilibrium in the ISM. Much of the chemistry in space takes place at temperatures and pressures very different to those on Earth and over much longer timescales, millions of years, compared to the time scales than those experienced on our Earth. However, from a chemist's perspective, interstellar space provides a unique environment to study molecular behaviour under extreme conditions. This combination makes astrochemistry a fascinating and vibrant research field for chemists, astronomers, and physicists alike.

1.1.1 Interstellar medium

The interstellar medium, the space between stars, is host to an astonishingly rich chemical inventory. Most molecules in these environments are not large by the standards of terrestrial chemistry, with most molecules ranging from 2 to 12 atoms [McGuire, 2018] along with a couple of fullerenes (60 and 70 atoms) [Berne et al., 2013, Cami et al., 2010]. A few recent discoveries comprise slightly bigger species



Figure 1.1.2: Optical image of the Carina nebula from the Hubble Telescope Credit: NASA/ESA/M. Livio.

like cyano-cyclopentadiene (12 atoms) [McCarthy et al., 2021], benzonitrile (13 atoms) [Burkhardt et al., 2021b, McGuire et al., 2018], indene (17 atoms) [Burkhardt et al., 2021a, Cernicharo et al., 2021] and cyano-naphthalenes (19 atoms) [McGuire et al., 2021].

This rich chemical inventory contains many species which would be quite exotic by terrestrial standards. Taurus molecular cloud (TMC-1) is a particularly well studied star-forming region and is notable for a wide variety of cyano-polyynes (HC_nN family of linear molecules, $n=3, 5, 7, 9, 11$) [Freeman and Millar, 1983, Loomis et al., 2021]. These detections further inspire new chemical physics research to understand their spectroscopy and formation/destruction pathways. A handful of aromatic species have also been detected very recently in TMC-1 [McCarthy et al., 2021, McGuire et al., 2018]. The number of detected aromatics in the ISM, however is very small (only about 2% of the total detections), which is strange when compared to Chemical Abstracts Service (CAS) where $\sim 80\%$ of the 135 million organic compounds, used in the terrestrial laboratories, registered contain at least one such ring.

Other exotic molecules in interstellar environments include molecular ions, like C_4H^- , HCO^+ , and a large range of radicals. Another feature among the molecules found in the ISM are isotopologue species, where one or more atoms in a molecule are isotopes such as deuterium, ^{13}C , ^{15}N , ^{17}O , ^{18}O , and ^{34}S , etc. Many interstellar regions have reported high deuterium-to-hydrogen abundance, referred to as deuterium fractionation, in the various isotopologues detected, which has puzzled astronomers for a long time. The deuterium fractionation in some regions has been found to be as high as 10^4 [Bacmann et al., 2003, Pagani et al., 2009] compared to the cosmic abundances indicating fascinating chemistry.

For a long time, ion chemistry was thought of to be the main driver of chemistry in the ISM with about 15% of the >200 molecules detected being ionic. This was based on the knowledge that long-range interactions induced by the (charged) ionic species can allow molecular species to interact in the extremely low density molecular clouds, and most ion-molecule reactions are also barrierless and exothermic allowing them to proceed in the cold interstellar environments. Over the past couple of decades, however, the role of neutral–neutral reactions has been established [Heard, 2018, Morales et al., 2010, Ocaña et al., 2019, Sims et al., 1993] as many of these reactions have fast rate coefficients at low temperatures due to either a submerged barriers or by proceeding via stable complexes.

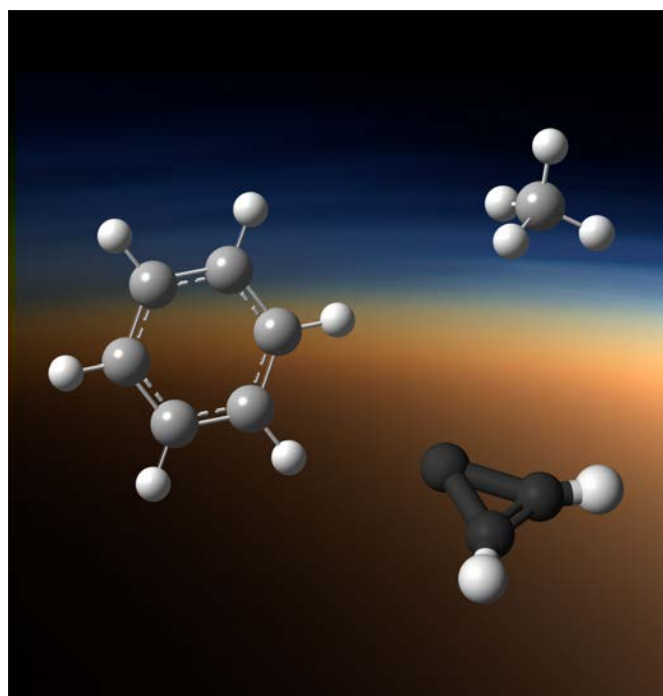


Figure 1.1.3: True color photograph of layers of clouds in Titan's atmosphere with an overlay of molecules detected in Titan's atmosphere. Titan image credit: NASA.

1.1.2 Planets, moons and planetoids

Earth's atmosphere is host to a wide range of chemistry within its various layers, and this chemistry can vary as the temperature, molecular density, and UV photon flux changes. Many molecules have also been detected on other planets of our solar system like CO [Encrenaz et al., 2004], H₂O [De Graauw et al., 1997], PH₃ [Ridgway et al., 1976], NO [Krasnopolsky, 2006], HCN [Tokunaga et al., 1981], H₂S [Irwin et al., 2018], C₃H₄ [De Graauw et al., 1997], among others.

A few molecules have also been detected on Earth's moon, despite its lack of atmosphere, with the latest detection being that of water which was detected by SOFIA [Honniball et al., 2021]. Jupiter and Saturn have 79 and 82 moons each, many of which have an atmosphere and show signs of exciting chemistry. CO₂ has been detected on Callisto [Carlson, 1999] (Jupiter's moon), and Dione and Rhea [Teolis and Waite, 2016] (Saturn's moons), while O₂ has been detected on three of Jupiter's moons [Hall et al., 1998, 1995, Liang et al., 2005] and two of Saturn's [Teolis and Waite, 2016].

By far, one of the most explored atmospheres following Earth's has been that of Titan, shown in Figure 1.1.3. Titan is the largest moon of Saturn and has a dense atmosphere mainly made up of nitrogen (N₂) and methane (CH₄) [Kuiper, 1944]. A rich chemistry is induced by UV/solar radiation and electrically charged heavy particles coming from Saturn's magnetosphere. The N₂ bond is predominantly broken

via dissociative ionisation at higher altitude layers which leads to the formation of various nitriles like HCN. The CH_4 in Titan's atmosphere, on the other hand, is photodissociated by Lyman α radiation which forms smaller hydrocarbon species. These small hydrocarbons can further react with each other to form larger hydrocarbons like C_2H_2 , C_2H_4 , C_3H_6 , etc. The carbon and nitrogen chemistry, both in the gas and aerosol phases, in Titan is thus of a significant interest for astrochemists. Nitriles have gathered special attention in the astrobiology community as they are thought to be precursors for prebiotic chemistry given their ability to form amino acids.

Both N_2 and CH_4 have also been detected on Triton, a moon of Neptune, [Broadfoot et al., 1989, Cruikshank and Silvaggio, 1979] and Pluto [Cruikshank et al., 1976, Owen et al., 1993]. This points towards possible interesting nitrile chemistry on these planetoids as well, and highlights the importance of studying and modeling nitrile chemistry at low temperatures.

We are now also entering a new era in exoplanetary science, as illustrated by the recent award of the 2019 Nobel Prize to James Peebles, Didier Queloz, and Michel Mayor for their pioneering advancements in this field [Gibney and Castelvaggi, 2019]. State-of-the-art observations are now able to provide the high sensitivity required to place detailed constraints on the physio-chemical properties of exoplanetary atmospheres. Detections include CH_4 [Ge et al., 2006], HCN [Giacobbe et al., 2021], and OH [Nugroho et al., 2021] highlight interesting chemistry undergoing in these far-away regions. While the temperatures in the atmospheres of Titan range from 80–200 K, most observed exoplanets to date have high temperatures (~ 80 –3000 K) as they are hot gas giants. So while this remains outside the scope of this work, it shows the rich chemistry in planetary atmospheres, both in our Solar system and outside.

1.2 Interplay: Observations, Theory & Experiments

While astrochemistry began as a subdiscipline of astronomy, it is now an independent thriving interdisciplinary field with a strong synergistic interplay between observations, computations/modeling, and experiments. Three main kinds of scientific activities are undertaken in the field: (i) identification of the species, (ii) construction and application of chemical models, and (iii) experimental and theoretical efforts.

Astronomers need data on molecular spectroscopy, including spectra of exotic and unstable species that are difficult to isolate in the laboratory igniting new chemical physics research. Astrochemical

modeling requires information of various chemical processes to predict the abundances of a variety of chemical species. The astronomical detections can be used to derive the abundances of molecules in a wide range of regions with varying physical conditions which further helps refine the astrochemical models, and may even hint towards other possible species in these extra-terrestrial environments.

1.2.1 Observations

The energy levels of molecular species are quantized into electronic, vibrational and rotational states, and transitions between these have been used to discover molecules in a host of different sources. The electronic transitions generally lie in the optical and ultraviolet range, shown in Figure 1.2.1, while the vibrational transitions within an electronic level and rotational transitions within a given electronic and vibrational level lie in infrared (IR), and (sub)millimeter and far-infrared wavelengths respectively. Figure 1.2.1 shows a range of molecules found in the interstellar and circumstellar regions which can be observed using their transitions over the different wavelength ranges. Figure 1.2.1 also illustrates the use of varied detection techniques for molecules of different masses.

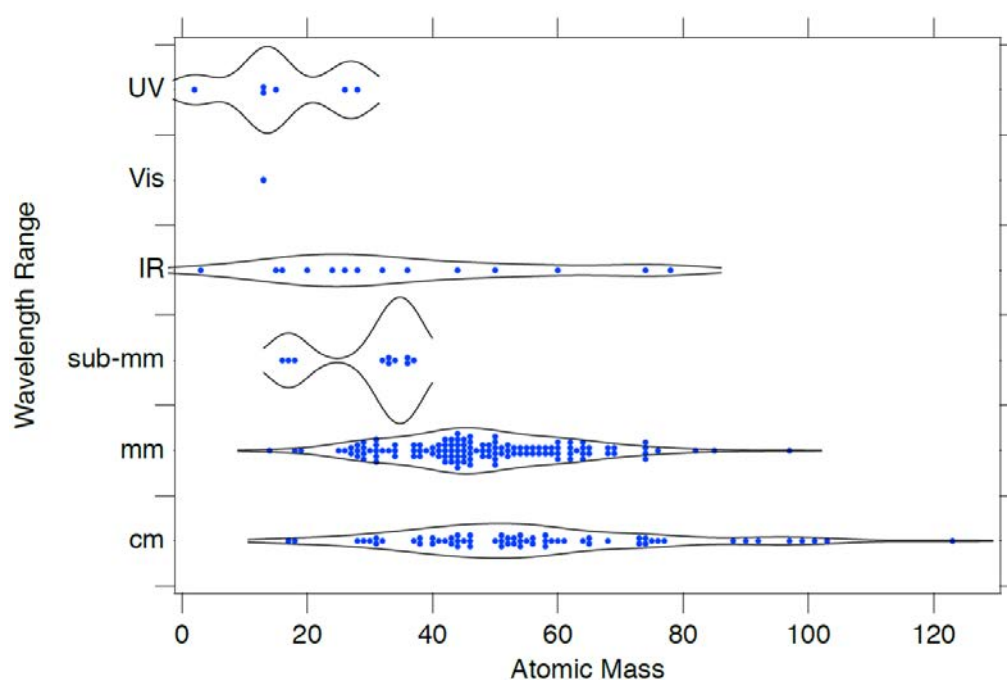


Figure 1.2.1: Violin plot showing the masses of molecules detected over different wavelength ranges. Reproduced from McGuire [2018].

The first detection of a molecule in the interstellar medium was the methyldyne (CH) radical which was discovered using its distinct emission features in the ultraviolet (UV) region by McKellar [1940], Swings and Rosenfeld [1937]. Since that detection, the number of new discoveries grew steadily, albeit

slowly. However, the advent of radio astronomy in 1960s has led to a sharp rise in the number of detections, with almost 3.7 per year [McGuire, 2018] since the 1960s.

One major limitation of radio astronomy, however, is that it can only detect molecules with a dipole moment. Symmetric molecules like benzene, which has been proposed as the building block of bigger polycyclic-aromatic hydrocarbons (PAHs), cannot be detected using this technique. Instead, the use of proxies to determine the abundance of molecules without dipole moments has been suggested, but this requires rigorous tests via experiments and/or theoretical calculations to verify their applicability.

1.2.2 Theoretical calculations and astrochemical modeling

Since the kinetic and spectroscopic data for many of the chemical systems is either required for exotic systems or under extreme conditions, researchers often take advantage of computational quantum tools available. This includes, but is not limited to, rotational transition frequencies for species and reaction rate coefficients.

Astrochemical kinetic models are used to simulate the time-dependent chemical evolution of species in astrophysical environments, performed by integrating a system of coupled, nonlinear differential rate law equations. Most of these models use the network of chemical reactions available on chemical databases like KIDA (<http://kida.astrophy.u-bordeaux.fr/networks.html>), UdfA (<http://udfa.ajmarkwick.net/>), NIST (<https://kinetics.nist.gov/kinetics/>), among a few others.

An example of an output from an astrochemical model is shown in Figure 1.2.2, which uses either experimentally measured, theoretically derived rates, or in many cases intuitive guesses, for the different formation and destruction routes possible for a species. While in some cases, the models can predict the abundances found in certain astrophysical environments quite well, others may not be able to do so, for example for the cyano-naphthalenes detected in TMC-1 [McGuire et al., 2021]. This points towards a lack of accurate measurements on the reaction kinetics used in astrochemical models.

1.2.3 Experiments

Given the chemical and physical diversity within the astrophysical environments, accurate measurements for various processes in ice/gas phase, and gas–grain surfaces are required to understand

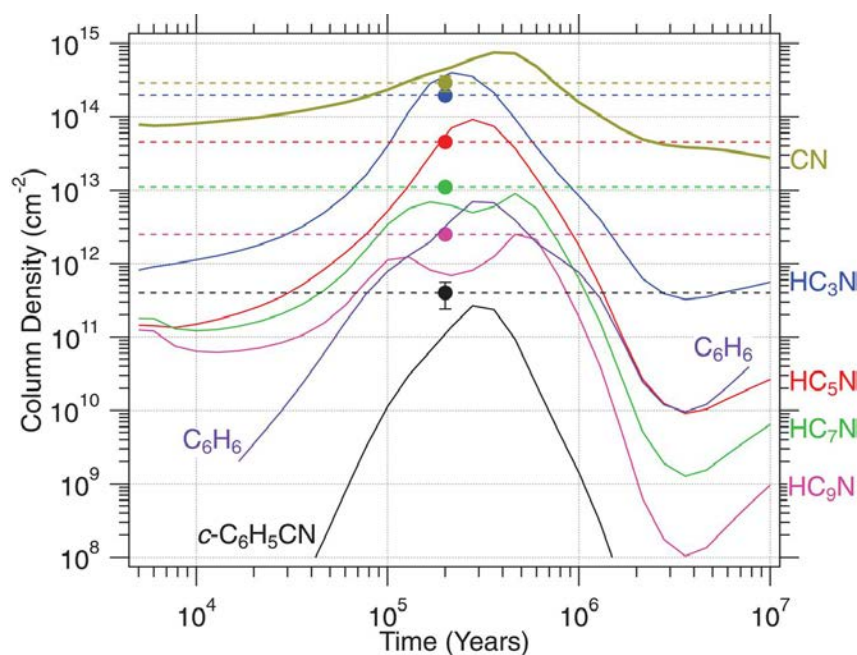


Figure 1.2.2: Modeled gas-phase column densities of benzonitrile, various cyanopolyynes, and CN in TMC-1 as a function of time in solid colored lines. The dots with dashed horizontal lines show the abundances derived from observations. Reproduced from [McGuire et al., 2018].

the complete chemical complexity of the ISM.

Most of the detected gaseous interstellar and circumstellar molecules have been observed via their rotational spectral lines, which are recorded and characterised in laboratories. Multiple spectral databases like CDMS (<http://www.astro.uni-koeln.de/site/vorhersagen/>), Splatalogue (<http://www.splatalogue.net/>), the JPL Catalog (<http://spec.jpl.nasa.gov/home.html>), contain the details on these experimental studies to ease the process of assigning the interstellar molecular lines.

Reaction rate coefficients, for each detected molecule, as mentioned in the section above, are required for astrochemical modeling. The experimental measurements can also help predict the possibility of other molecules that may be present in the ISM. Because the fundamental quantum chemical theories, on which theoretical estimates are based, may get tested at the low temperatures relevant to the ISM, experimental measurements act as a gold standard.

The focus of this thesis is to understand the gas-phase neutral-neutral chemistry of complex molecules in the ISM, and a number of detailed reviews have been published on this topic [Cooke and Sims, 2019, Heard, 2018, Sims, 2013, Sims and Smith, 1995, Trevitt and Goulay, 2016]. A few of the experimental techniques relevant to measuring their kinetic parameters are discussed here.

The Pulsed-Laser Photolysis-Laser Induced Fluorescence (PLP-LIF) technique has revolutionised

the study of reaction rate coefficients as it allows one to follow the change in concentration of very low concentration of radical species (reactant) over time. These measurements can be used to measure the overall rate coefficient. However, many reactions proceed via multiple channels, which will be discussed in detail in section 1.3.2, knowledge of the different products in such multichannel reactions is crucial to accurately reproduce complex astrophysical environments.

Branching ratio measurements are very challenging as multiple product channels need to be detected at high sensitivity at the same time. The LIF measurement technique can be applied to measure the presence and growth kinetics of particular products [Bergeat and Loison, 2001, Douglas et al., 2018, Gannon et al., 2007]. The LIF technique, however, cannot be used directly for these measurements as the fluorescence signals cannot provide concentration values. So, these measurements are coupled with a calibration reaction to determine absolute concentrations of product channels.

Another technique used to measure branching ratios is mass spectrometry coupled with tunable vacuum ultraviolet synchrotron photoionisation [Bouwman et al., 2013, Lockyear et al., 2015, Soorkia et al., 2011, Trevitt et al., 2009]. Mass spectrometry is an extremely sensitive technique, and the tunable photoionisation energies from synchrotron sources, like the Advanced Light Source (ALS) and SOLEIL, can be used to distinguish between the different products and reaction intermediates.

Crossed-beam experiments is another useful technique for these measurements and has contributed greatly to our understanding of elementary reaction dynamics. Reactants confined into molecular beams cross each other at a specific collision energy, determined by the angle of collision and the speed of the beams. The products can then be analysed by velocity map imaging, or by using a movable mass spectrometer [Balucani et al., 2000b, Lee et al., 1969, Lin et al., 2003].

Broadband chirped-pulse Fourier transform microwave (CP-FTMW) spectroscopy, developed by Brooks Pate and colleagues [Brown et al., 2008], is an exciting technique as it allows for detection of multiple species with high molecular specificity. CP-FTMW has recently been used to study the branching ratio of reactions at low temperatures by Abeysekera et al. [2014a] and Oldham et al. [2014].

1.3 Gas-phase Reactions

As mentioned earlier in section 1.2.2, networks of reactions must be built including their individual reaction rate coefficients to solve for the time-dependent molecular abundances and to reproduce

astronomical observations. The majority of bimolecular gas-phase reactions in astrophysical environments can be placed in the one of following classes: (i) ion-neutral reactions, (ii) neutral-neutral reactions, (iii) radiative association reactions, and (iv) dissociative recombination reactions. Here, I will cover different aspects of reaction kinetics and branching ratios essential to understand the reaction parameters needed for astrochemical modeling.

1.3.1 Reaction kinetics

The rate law for a reaction is defined as the time rate of change in concentration of one of the reactants or products. If we consider a general reaction



, its rate can be related to the concentrations and the stoichiometry as

$$\text{rate} = \frac{1}{c} \frac{d[C]}{dt} = \frac{1}{d} \frac{d[D]}{dt} = -\frac{1}{a} \frac{d[A]}{dt} = -\frac{1}{b} \frac{d[B]}{dt} \quad (1.3.1)$$

$$\text{rate} = k[A]^m[B]^n \quad (1.3.2)$$

The overall order of the reaction is defined as the sum of the individual powers, order = $m + n$. A key point to note is that m and n are equal to the stoichiometric factors only in case of elementary reactions. Elementary reactions are defined as single step reactions, and comprise of unimolecular or bimolecular reactions. Given the extremely low densities in the ISM, three-body are extremely rare and hence only the elementary reactions are relevant.

For a first-order reaction, $A \longrightarrow$ products, for which the differential form of the rate law is

$$-\frac{d[A]}{dt} = k[A] \quad (1.3.3)$$

Integration of this equation yields

$$A(t) = A_0 \exp(-kt) \quad (1.3.4)$$

where A_0 is the initial concentration of A and $A(t)$ is the concentration of A at time t . This relationship means that decay of the reactant is exponential and the term $\ln([A(t)]/A_0)$ against time is a linear curve with a negative slope which gives the rate coefficient for the reaction (slope = $-k$).

For second-order reactions of the type, $A + B \longrightarrow$ products, the differential rate law can be represented as

$$-\frac{d[A]}{dt} = k[A][B] \quad (1.3.5)$$

So, to calculate the reaction rate, the concentration of both the reactants is needed. This is the case for the reactions considered in this work, as the reactions of the CN radical are considered with a series of other reactants. However, it can be difficult to measure accurate concentrations of unstable species, and in many cases, the species/radicals can react with themselves leading to errors in concentration measurements.

The experimental conditions to study second-order reactions are often adjusted to make the reaction rate law to appear as first order in one of the reactants and zero order in the other— a condition that holds true when $B_0 \gg A_0$. So, the differential rate law becomes

$$-\frac{d[A]}{dt} = k[A]B_0 \quad (1.3.6)$$

This, termed as pseudo-first order, allows one to solve the differential rate law similar to as shown above for a first-order reaction to give

$$A(t) = A_0 \exp(-kB_0t) \quad (1.3.7)$$

This allows one to calculate/measure the pseudo-first order rate coefficient (k_{1st}), defined as kB_0 , which can be used to calculate the overall rate coefficient by collecting a series of measurements with varying $[B]$ and the linear relationship between the pseudo- k_{1st} and $[B]_0$.

1.3.1.1 Temperature dependence of rate coefficients

The temperature dependence of the reaction rate provides a crucial basis for understanding reactions on a molecular level. The temperature dependence of rate coefficients for most reactions can be expressed by the Arrhenius equation:

$$k(T) = A \exp(-E_A/RT)$$

where A is a pre-exponential factor, E_A the activation energy, and T the gas kinetic temperature. A general case for an exothermic reaction, described by the Arrhenius equation, is shown in panel a of

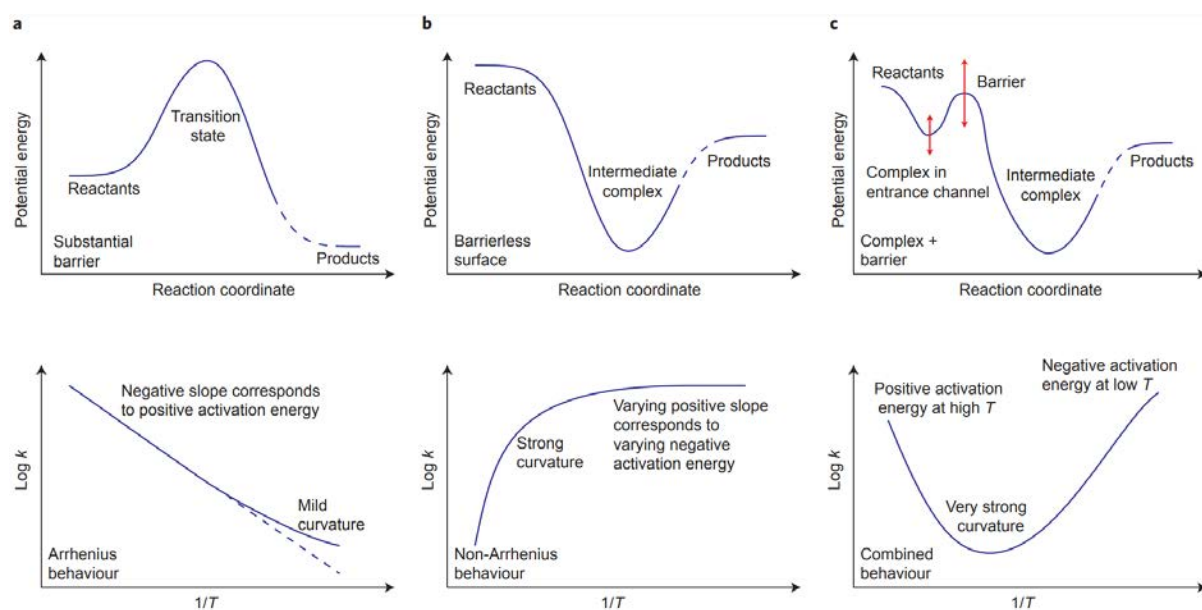


Figure 1.3.1: General cases for exothermic reactions. The top panels show an approximate potential energy surface, while the bottom panels show the log of the rate coefficient against inverse of temperature. a, A reaction with a substantial barrier, which adheres approximately to the Arrhenius equation. b, A reaction with no barrier, showing strongly non-Arrhenius behaviour. c, A reaction passing through an initial weakly bound complex and then over a barrier (which may or may not be above the reagent energy): the reaction adheres to the Arrhenius equation only at higher temperatures. Reproduced from Sims [2013].

Figure 1.3.1.

While, most chemical reactions adhere to the kinetics described by the Arrhenius equation to a good approximation, this equation can no longer explain the reactions with no barrier, or a reaction which passes through an initial weakly bound complex before it goes over a barrier. These examples are shown in panels b and c, respectively, of Figure 1.3.1. In such cases, a modified Arrhenius equation can often be used in order to express the temperature dependence of the rate coefficient:

$$k(T) = \alpha(T/(300 \text{ K}))^\beta \exp(-E_A/RT) \quad (1.3.8)$$

This equation is used to represent the temperature dependence of reaction rate coefficients over a range of temperatures, and the three parameters α , β , and γ , can be used to extrapolate $k(T)$ over various temperatures. Many reactions of astrochemical interest involving ions or radicals (species with one or more unpaired electrons) show non-Arrhenius behaviour; a few examples of which are shown in Figure 1.3.2.

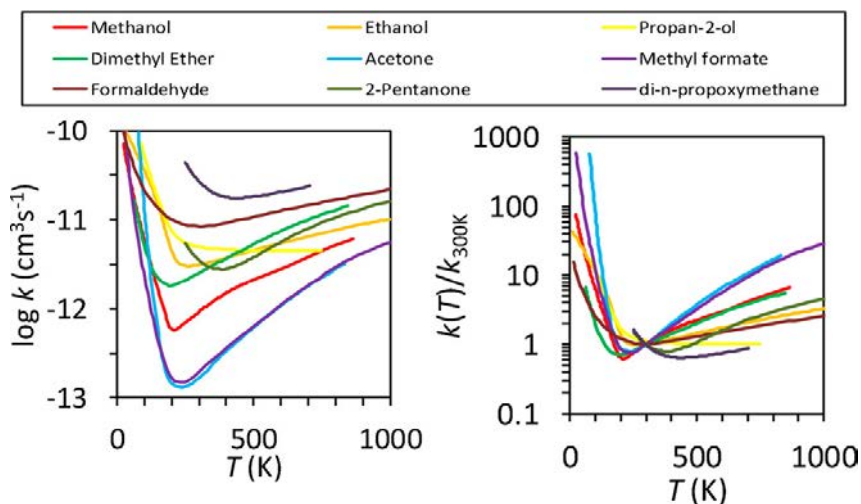
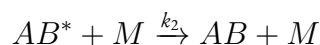
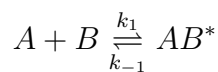


Figure 1.3.2: Rate coefficients, k (left), and the ratio, $k(T)/k(300\text{ K})$ (right), as a function of temperature for the reaction of OH with several organic molecules. Reproduced from Heard [2018].

1.3.1.2 Pressure dependence of rate coefficients

Some reactions also show a pressure dependence of the reaction rates. The mechanism proposed by Lindemann and Hinshelwood is used to understand such cases.



In the above scheme, the reactants A and B can associate to form an activated complex, AB^* . The complex can then either redissociate to form reactants or stabilise via collisions with the bath gas, M, to yield the stabilised adduct (AB).

The differential rate law, assuming a steady-state approximation, for such a scenario gives

$$\frac{d[AB]}{dt} = k_2[AB^*][M] = \frac{k_2k_1[A][B][M]}{k_2[M] + k_{-1}} \quad (1.3.9)$$

Two limiting cases can then be considered:

- Low-pressure limit: At low pressures, the rate of stabilisation will be much less than the rate of dissociation, $k_2[M] \ll k_{-1}$. In such a case, the overall rate coefficient becomes

$$\frac{d[AB]}{dt} = \frac{k_2k_1[A][B][M]}{k_{-1}} \quad (1.3.10)$$

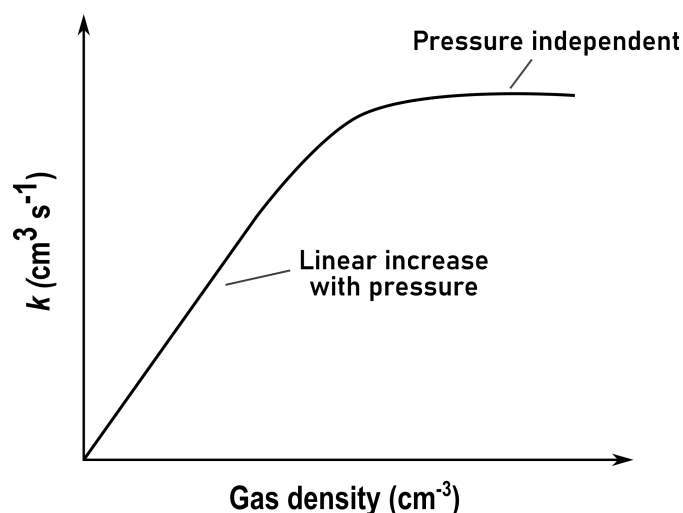


Figure 1.3.3: Pressure dependence of the rate coefficient for an association process, described by the Lindemann-Hinshelwood mechanism.

making it a third order process as the rate is now directly proportional to the concentration of the third-body (M) and hence the pressure.

- High-pressure limit: At high pressures, [M] is so large such that $k_2[M] \gg k_{-1}$. So, the overall rate coefficient becomes

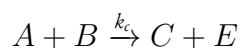
$$\frac{d[AB]}{dt} = \frac{k_2 k_1 [A][B][M]}{k_2 [M]} \quad (1.3.11)$$

and the dependence on [M] gets cancelled out such that it is only a second-order process.

An example is shown in Figure 1.3.3, where at low pressures, the rate coefficient increases linearly, and at high pressure it is pressure-independent.

1.3.2 Product-specific kinetics/branching ratios

The reaction between A and B may also lead to several product channels:



In such multichannel reactions, rate coefficients are defined for each channel, and related to overall reaction rate coefficient by their branching ratios. For the above example, the overall rate coefficient, k will be the sum of product specific rate coefficients, $k_c + k_d$. The product branching ratios can then

be defined as

$$\alpha_c = k_c/k \quad \text{and} \quad \alpha_d = k_d/k \quad (1.3.12)$$

Progress in the measurements of such product branching ratios has been much slower than the overall reaction kinetics measurements, especially as a function of temperature and in particular at low temperatures. This difficulty arises from the limitation on the experimental detection techniques which would need to be universal (detect all reaction channel products), highly sensitive, and multiplexed (detect multiple species at the same time).

1.4 Reaction Kinetics Theories

Kinetics theories are used to provide a theoretical basis for understanding, and predicting reaction rate coefficients. A few of them are presented here to have a better microscopic/macroscopic understanding of the reaction rate coefficients obtained in this work.

1.4.1 Simple collision theory

This is the simplest theory, based on the hard-sphere model of collisions, and is based on the barrier height of a reaction, as shown in top image of panel a in Figure 1.3.1. It proposes that a reaction takes place only when:

- reactant species collide with one another
- the colliding partners have sufficient energy to overcome the barrier height

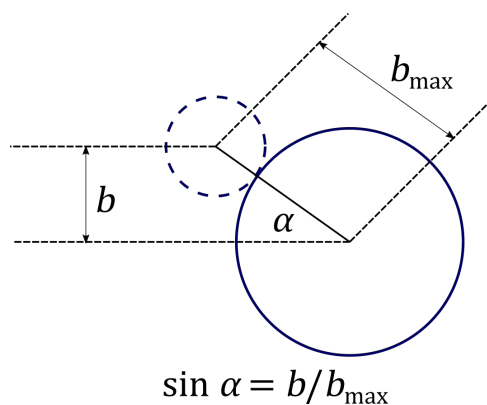


Figure 1.4.1: Hard sphere collision model depicting the impact parameter (b) used to estimate reaction cross-section.

It then assumes that the reactants are hard spheres and that no inter-molecular forces are present. As an example, let's take a collision between two reactants: A and B, with radii r_a and r_b , shown in Figure 1.4.1, and a number density of n_a and n_b , respectively. The relative speed between the two species is v_r . The collision is only considered when the two species are in contact, or the distance between the two species (b) $< b_{\max} = r_a + r_b$, also defined as the impact parameter. Based on the Maxwell-Boltzmann distribution of speed, the collision frequency can be calculated as

$$Z = \pi b_{\max}^2 n_a n_b \sqrt{\frac{8k_b T}{\pi \mu}} \quad (1.4.1)$$

Recalling the second assumption of this theory, only the molecules with enough energy to overcome the barrier to the reaction will lead to a reactive collision and using the Boltzmann energy distribution which depends on the temperature, the rate of the reaction can be calculated as

$$k(T) = \pi b_{\max}^2 n_a n_b \sqrt{\frac{8k_b T}{\pi \mu}} \exp\left(-\frac{E_A}{kT}\right) \quad (1.4.2)$$

where E_A is the barrier energy.

Some modified versions have been developed as the assumption that every collision will have enough energy to react is an overestimation, given that in most cases the reactants also need to be in a favorable orientation for the reaction to take place. This introduces a so-called steric factor, p , with $p < 1$ to give a modified version where

$$k(T) = p \pi b_{\max}^2 n_a n_b \sqrt{\frac{8k_b T}{\pi \mu}} \exp\left(-\frac{E_A}{kT}\right) \quad (1.4.3)$$

1.4.2 Transition state theory

While the collision theory addresses the barrier height of a reaction, a key parameter missing from that treatment is the “width” of the barrier. The transition state theory attempts to address that gap by incorporating the width or the structure of the reaction channel leading over the activation barrier.

The reaction between the reactants, A and B, proceeds via a formation of an activated complex AB^*



The steady state assumption is considered which means once the reactants cross the activated complex, they cannot revert back on the potential surface to form reactants. This means

$$\frac{d[\text{products}]}{dt} = k_2[\text{AB}^*] \quad (1.4.5)$$

This theory also assumes that the reactants are equilibrated either in a canonical (fixed temperature) or a microcanonical (fixed exact energy) ensemble such that either the $k(T)$ or the $k(E)$ values can be obtained. Thus, the rate coefficient can be calculated using the one-way local flux over the dividing surface which is determined by the Boltzmann distribution. This gives a reaction rate of

$$k = \frac{k_B T}{h} \frac{Q^\ddagger}{Q} \exp\left(\frac{-E_o}{k_B T}\right) \quad (1.4.6)$$

where E_o is the critical minimum energy of the transition state, Q and Q^\ddagger are the partition functions for the reactants and transition state, respectively, h is the Planck's constant, k_B is the Boltzmann constant and T is the temperature.

Given the assumption that all the trajectories crossing into products cannot revert is taken into consideration, this rate coefficient places an upper limit on the real reaction rate coefficient.

1.4.3 Capture theory

Both the above described theories are relevant for reactions involving a barrier, however, many reactions relevant at low temperatures are barrierless. This is particularly true for ion-molecule reactions due to the long-range interaction induced by the ion's electrostatic potential. As highlighted in section 1.3, it is well established now that many radical-radical reactions and even some radical-molecule reactions can be barrierless.

Capture theory was first developed by Langevin [1905] for ions and polarisable atoms. In that case, the interaction is proportional to r^{-4} and the long range coefficient is given by

$$c_4 = \frac{1}{2} \alpha q^2 \quad (1.4.7)$$

where q is the charge of the ion, and α is the polarisability of the ion/atom.

To calculate the rate coefficient for an ion-molecule reaction, an assumption is made that the molecule

is spherical and the ion is a charged point. The effective potential can then be represented as

$$V_{\text{eff}}(r) = -\frac{1}{2} \frac{\alpha q^4}{r^4} + \frac{L^2}{2\mu r^2} \quad (1.4.8)$$

where L is the orbital angular momentum, r is the distance between the two species, and μ is the system's reduced mass. The critical impact parameter (b^*) for this case is derived as the distance where the potential is the maximum which gives

$$b^* = \left(\frac{2\alpha q^2}{E_r} \right)^{1/4} \quad (1.4.9)$$

If the impact parameter $b = 0$, there is no centrifugal component and the ion is attracted directly and reacts. However, if the ion cannot cross the centrifugal barrier in cases when the relative energy is lower than the effective potential (V_{eff}), the ion is ejected. If the ion has enough energy, the ion crosses the barrier and the forces attracts it further until a collision takes place. By assuming every collision as reactive, Langevin rate coefficient can be derived as

$$k_L = 2\pi \sqrt{\frac{\alpha q^2}{\mu}} \quad (1.4.10)$$

1.4.3.1 Semi-Empirical model

The Langevin theory, however, fails to estimate the rate coefficients for the radical-neutral reactions as the attractive forces are much smaller than those for an ion, and the long range attraction may not be valid anymore, with short range forces becoming more relevant. While certain theories include improvements like considering an equivalent evaluation of the rate coefficient using quantum mechanics, there is also some interest in semi-empirical methods. One such model described by Faure et al. [2009] is explained here which allows one to compare experimentally measured values to make a theoretical estimation of the rate coefficient.

The theoretical method of Faure et al. [2009] uses the capture theory expression given by Stoecklin et al. [1991]

$$k(\text{T}) = 2\sqrt{\frac{2\pi}{\mu}} \Gamma\left(\frac{2}{3}\right) (2C_6)^{1/3} (k_B T_n)^{1/6} \quad (1.4.11)$$

where μ is the reduced mass, k_B is the Boltzmann constant, $\Gamma(x)$ the gamma function, and C_6 is the

dispersion coefficient determined by the London formula

$$C_6^{\text{London}} = \frac{3}{2} \frac{I_1 I_2}{I_1 + I_2} \alpha_1 \alpha_2 \quad (1.4.12)$$

where I_1 and I_2 are ionisation potentials and α_1 and α_2 the polarizabilities of the two reactants. This expression however underestimates the dispersion and hence the C_6 coefficient is taken as twice the C_6^{London} .

Theoretical rate coefficients are then calculated at two low temperature values in the range [5, 130] K using the above equations. These can then be combined with an experimentally available/measured rate coefficient to obtain an analytically interpolated modified Arrhenius Equation fit parameters, $k(T) = \alpha (T/(300 \text{ K}))^\beta \exp(-\gamma/T)$.

1.5 Outline of this thesis

The aim of this thesis is to provide measurements of overall and product-specific rate coefficients for reactions relevant to low-temperature interstellar environments. Given the ubiquity of CN radical across various astrophysical sources [Gautier et al., 2011, Henkel et al., 1988, Hily-Blant et al., 2008, Jefferts et al., 1970, Vuitton et al., 2007], it was the radical of choice for this work.

Chapter 2 provides a summary of the CRESU technique, used to reach the low temperatures, followed by details of the two spectroscopic tools used in this work. Chapter 3 briefly summarizes the computational quantum chemistry package used for electronic structure calculations to aid the understanding of reactions studied.

Chapters 4 and 5 present the overall rate coefficient measurements performed down to 16 K for the reactions of CN radical with methanol, and benzene and toluene, respectively. Chapter 6 provides the branching ratio measurements for the reaction of the CN radical with propene. These measurements aim to improve the kinetics databases needed for more accurate astrochemical models at low temperatures.

Chapter 2

Experimental methodology

2.1 Introduction

Measuring the kinetics of reactions at low temperatures has two major components: reaching the low-temperatures and then following the concentration (or relative concentration) of either the reactants or the products over time. In this chapter, I will cover the details of the technique used to obtain low temperatures and the two spectroscopic techniques, laser-induced fluorescence spectroscopy and chirped-pulse microwave spectroscopy, used in this thesis.

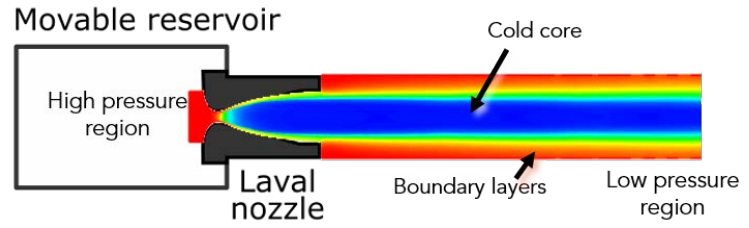
2.2 The CRESU technique

CRESU is a French acronym that stands for Cinétique de Réaction en Ecoulement Supersonique Uniforme, or defined as “Reaction Kinetics in Uniform Supersonic Flow”. The CRESU technique was first developed in an aerodynamics laboratory and applied to study ion–molecule reaction kinetics by Rowe et al. [1984], which marked a revolution in the study of low-temperature kinetics.

The technique is based on isentropic expansion of a gas through an axisymmetric Laval nozzle to reach temperatures as low as 6 K. The Laval nozzle has a convergent-divergent design, shown schematically in Figure 2.2.1a, and the expansion of a gas through it takes place in two stages. The gas enters the nozzle from a high-pressure (order of tens–hundreds of mbar) reservoir, shown in Figure 2.2.1b, whose volume is large enough that the gas can be considered at rest before entering the nozzle. In the convergent part of the nozzle, the gas is accelerated from zero velocity till it reaches a Mach number



(a) Picture of a 3-D printed Laval nozzle which provides a temperature of 10 K with He as buffer gas.



(b) Schematic of a Laval convergent-divergent nozzle with a simulated temperature map.

Figure 2.2.1: Laval nozzle with a convergent-divergent design used for generating low temperature supersonic flows. Simulation image credit: Omar Abdelkader Khedaoui.

(M), defined as the ratio of the velocity of flow to the speed of sound, of unity at the throat. The flow then expands adiabatically and isentropically through the divergent part of the nozzle to reach supersonic speeds with Mach numbers as high as 7. If the conditions of an ideal gas are met, a collimated flow well defined in temperature and density can be achieved.

The flow in the Laval nozzle is compressible and a variation of Bernoulli's equation, Equation 2.2.1, can be applied

$$C_p T_{\text{flow}} + \frac{v_{\text{flow}}^2}{2} = C_p T_0 \quad (2.2.1)$$

where C_p is the specific heat at constant pressure, v_{flow} is the fluid velocity in the flow, and T is the temperature of the fluid. As the expansion is isentropic, the equation 2.2.2

$$PV^\gamma = \text{constant} \quad (2.2.2)$$

where V is the occupied volume and γ is the ratio of specific heat capacities ($\gamma = \frac{C_p}{C_v}$; C_p and C_v are the specific heat capacities at constant pressure and volume respectively) is applicable in the nozzle.

For an ideal gas, $C_p - C_v = R$ can be used and the flow speed can be calculated as

$$v_{\text{flow}} = \sqrt{\frac{\gamma RT}{M_m}} \quad (2.2.3)$$

where M_m is the molar mass of the gas. By replacing these conditions into equation 2.2.1, the

temperature of the flow can be calculated as

$$T_{\text{flow}} = T_0 \left(1 + \frac{\gamma - 1}{2} M^2 \right)^{-1} \quad (2.2.4)$$

The unique geometry of Laval nozzle provides a uniform flow, with a well-defined temperature and density, which can last for several decimetres, with a time scale of hundreds of microseconds. The density in the flow remains relatively high (typically 10^{15} – 10^{18} cm^{-3}) which ensures thermal equilibrium via sufficient collisions.

There are however several assumptions which are not met under working conditions. For a collimated flow, the pressure in the flow must be equal to the pressure outside the flow (in the chamber for a CRESU experiment). But since the fluid viscosity is never zero, it imposes the condition that the velocity at wall/chamber contact must be maintained at zero. Also, a small heat exchange with outer layers can occur which implies that the process is not strictly adiabatic. This creates a secondary non-isentropic boundary layer/flow of thickness δ , shown in Figure 2.2.2, which allows a zero fluid velocity at wall contact and a gradient of speed increasing orthogonal to the flow direction. Thus, while an isentropic core is achieved with the CRESU technique, an additional outer boundary layer, shown in Figure 2.2.1b, also exists where isentropicity is not achieved.

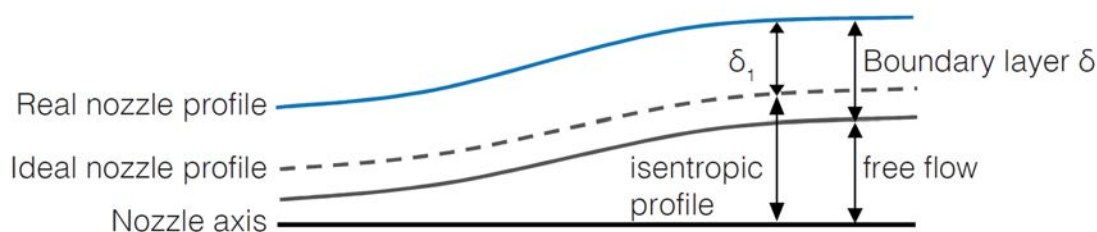


Figure 2.2.2: Isentropic flow and the boundary layer which arises due to a real nozzle profile, instead of an ideal profile. The boundary layer thickness, which varies for different nozzle designs and flow temperatures, is typically the same order of magnitude as the isentropic core. Image from Fournier et al. [2017]

2.2.1 Comparison with other cooling techniques

Other cooling techniques have been used to reach low temperatures for both spectroscopic and kinetic studies. Two of the most common techniques are cryogenic cooling and supersonic jets. Cryogenic cooling involves the use of low-temperature fluids to cool the reagents, normally via collisions with buffer gas that is in turn cooled by contact with the cold walls of the reaction cell. This technique,

however, requires that the gases must be present at partial pressures that are well below their vapour pressures at the wall temperature so that condensation and adsorption on the wall does not interfere with the experimental studies. For studying the kinetics of reactions involving radicals, mixtures of the radical precursor, reagent gas, and inert diluent (usually He) can be flowed through a cylindrical reaction cell at a speed that is sufficiently rapid to prevent the precursor from freezing out but sufficiently slow to allow the gases to cool close to the temperature of the cell wall. The range of temperatures that can be used for kinetic studies with this technique is limited by the cryogenic temperature and the vapour pressure of the reactants.

In a free jet expansion, gas is expanded from a high-pressure reservoir through a small orifice/pinhole creating a free jet which is typically followed by an insertion of a skimmer into its supersonic zone to generate a molecular beam. While temperatures as low as 1 K can be achieved using this technique, the free jet expansion has strong gradients of density and temperature along the axis of the jet which makes it difficult to perform quantifiable kinetic experiments. These free jets have been used to study collisional dynamics as conditions of low collision energy can be achieved, but the low-collision environment also means that the gas mixture does not reach thermally equilibrated conditions and hence cannot be used for finding the rate constants for bimolecular reactions.

2.2.2 Laval nozzle characterisation

All the Laval nozzles are designed based on desired flow conditions, temperature, pressure, and flows, and the geometry profile is tested using computational fluid dynamics (CFD). The precision of nozzle geometry, especially the throat, is a very critical part. Nozzles used in this work were either machined with metal or 3D printed with light activated resin. Any significant imperfections in the geometry can perturb the subsequent supersonic flows. Given the importance of uniform flow conditions, impact pressure measurements were performed using a Pitot probe, shown in Figure 2.2.3, to have a reliable flow characterisation with the operating conditions.

A Pitot probe is a hollow tube placed parallel to the flow propagation to measure fluid flow velocity. The Pitot tube employed to characterise the nozzles used in this thesis is shown in Figure 2.2.3, is a 10 cm long, 1/8 inch diameter stainless steel tube. It is mounted on a motorised translational platform to achieve spatial characterisation—7 cm lateral and 60 cm along the main axis. In the vertical axis, a HeNe laser was used to align the tube along the flow axis. The supersonic flow generated by the Laval nozzle on contact with the tip of the probe comes to a stagnation point and this strong

impact creates a shockwave lasting for a few millimetres before the entrance of the tube. Due to this shockwave, the flow properties change drastically and irreversibly as the pressure, temperature and density increase instantaneously. The impact pressure (P_i) at the stagnation point is measured by a pressure sensor (MKS 626C 1 or 10 torr) at the other end of the tube which can then be related to the flow/reservoir pressure (P_o) by equation 2.2.5 to determine Mach number (M) and other thermodynamic parameters

$$P_i = P_o \left(\frac{\gamma + 1}{2} \right)^{\frac{\gamma+1}{\gamma-1}} M^{\frac{2\gamma}{\gamma-1}} \left(\gamma M^2 - \frac{\gamma-1}{2} \right)^{\frac{1}{1-\gamma}} \quad (2.2.5)$$

For the isentropic core, relationships between M and temperature (T), and number density (n) and pressure (P) of the flow can be calculated using the reservoir pressure (P_o), temperature (T_o) and number density (n_o) by

$$\frac{T_o}{T} = 1 + \frac{\gamma-1}{2} M^2 \quad (2.2.6)$$

$$\frac{n_o}{n} = \left(\frac{T_o}{T} \right)^{\frac{1}{\gamma-1}} \quad (2.2.7)$$

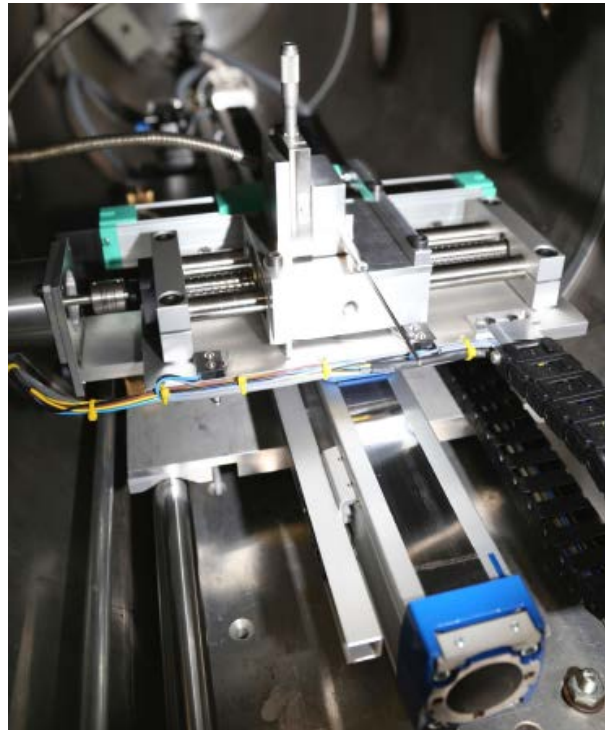
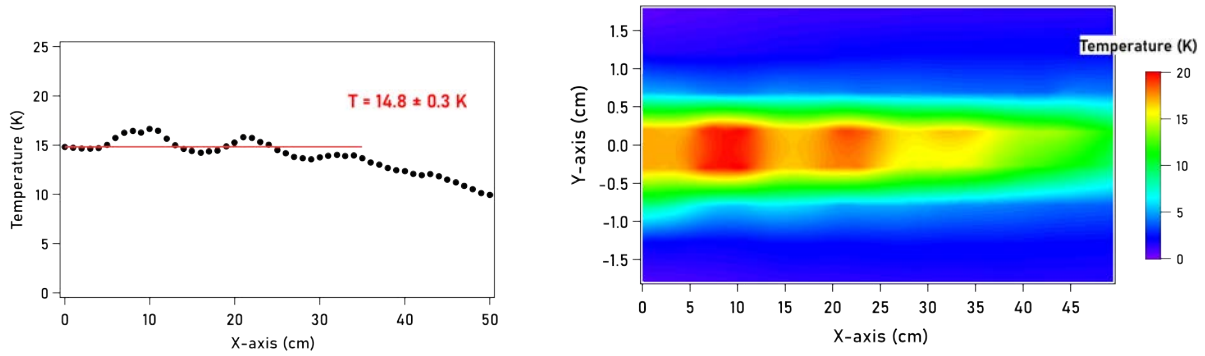


Figure 2.2.3: 2-dimensional Pitot tube setup used for nozzle characterisation, installed in CRESU-B chamber. Image credit: Martin Fournier.



(a) 1D Pitot probe measurement along axis of the flow (b) 2D Pitot probe measurement along and lateral to the flow axis.

Figure 2.2.4: Pitot impact pressure characterization of a Laval nozzle with He as buffer gas to achieve an average temperature of 14.8 K and ~ 6 mm isentropic core.

$$\frac{P_o}{P} = \left(\frac{T_o}{T} \right)^{\frac{\gamma}{\gamma-1}} \quad (2.2.8)$$

An example of the 1D and 2D mapping of a nozzle which provides an average temperature of 14.8 K with He as buffer gas is shown in Figure 2.2.4. As can be seen in Figure 2.2.4a, the temperature measured along the flow axis remains uniform for around 35 cm. The 2D map, shown in Figure 2.2.4b, was obtained by measuring the impact pressure using the Pitot tube with a step size of 0.5 cm

Table 2.2.1: Mean temperature, gas density, Mach number, length of the uniform/stable flow, total flows used and chamber pressure obtained for the nozzles utilised in this work for kinetic studies, characterised via impact pressure measurements.

T (K)	Buffer gas	Total density (10^{16} cm^{-3})	Mach number	Length of flow (cm)	Flow (SLM)	Chamber pressure (mbar)
15	He	5.05	7.5	25	52.5	0.114
17	He	5.05	7.0	30	51.7	0.137
24	He	18.3	5.8	33	93.4	0.630
25	He	6.99	5.6	16	52.8	0.266
35	Ar	5.26	4.7	55	20.5	0.280
36	He	5.28	4.6	32	84.7	0.293
53	Ar	20.2	3.7	28	64.5	1.508
72	He	6.01	3.1	25	97.7	0.640
83	N ₂	4.88	3.6	77.1	52	0.550
97	Ar	15.45	2.5	24	61.4	2.160
112	Ar	2.78	2.2	49	44.1	0.440
141	Ar	6.95	1.8	23	19.5	1.450
168	Ar	9.01	1.5	18	19.5	2.170
200	N ₂	5.32	1.5	25	50	1.529

along the flow axis and lateral to it after which it was interpolated. Being an axisymmetric flow, the temperature map for all the planes parallel to the axis of flow will be similar. A key point to be noted is that the temperature is calculated using the equations 2.2.6–2.2.8 under the assumption that the flow is isentropic, and since, as discussed in section 2.2, that assumption no longer holds for the boundary layer, the temperature values for that region as displayed in Figure 2.2.4b are not correct.

The flow parameters of the nozzles used for the experiments in this thesis obtained via Pitot probe measurements are summarized in Table 2.2.1. The 1D and 2D profiles for these nozzles are provided in the Appendix. To perform experiments at room temperature, it is essential that no expansion takes place through the nozzle used. For this, any nozzle with a wide throat (3–5 cm) was used (with a reduced pumping capacity) such that the reservoir and chamber were maintained at the same pressure.

2.2.3 CRESU chambers at Rennes

Two different CRESU chambers, shown in Figure 2.2.5, were used in this work— one of which is coupled with a photo-multiplier tube for PLP–LIF measurements and the other with a home-built microwave spectrometer. These techniques and their implementation at Rennes will be discussed in sections 2.5 and 2.6.

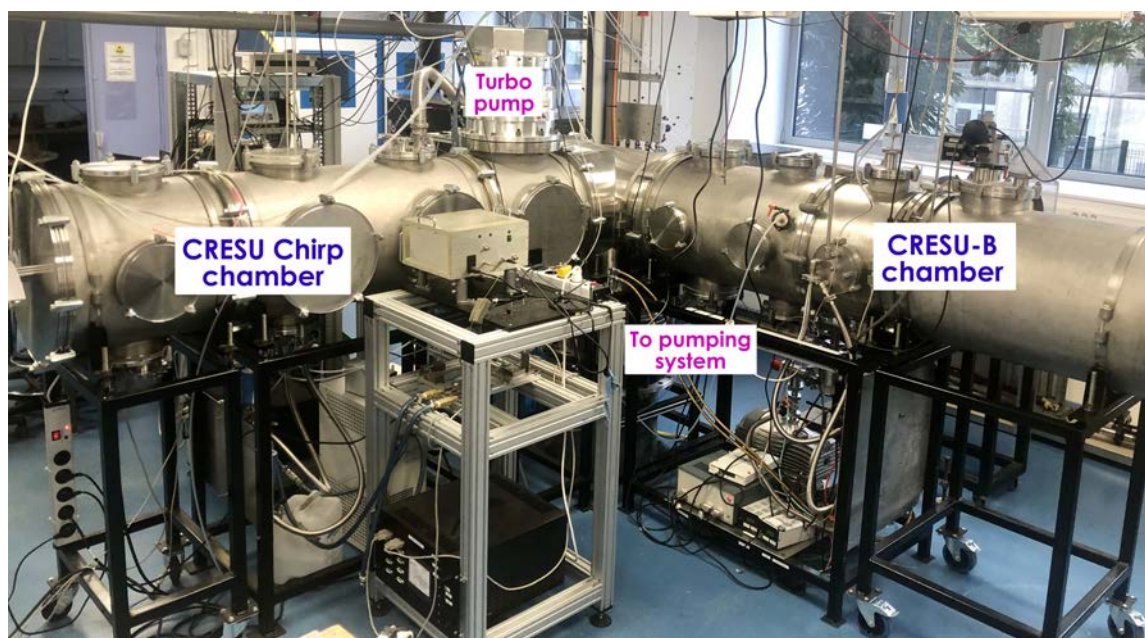


Figure 2.2.5: Picture of both the chambers used in this work. The main pumping system is used to pump both chambers, and another turbo pump is used for the pumping of a secondary chamber, explained in section 2.2.3.2

The CRESU chamber used for the PLP–LIF work has been named CRESU–B as it was initially built and located in Birmingham [James et al., 1998], and later moved to Rennes in 2003. The CRESU–B chamber used during the work presented here was in a different room, from where it was later shifted in 2020, as shown in Figure 2.2.5. The other chamber has been developed under the ERC funded CRESUCHIRP project and will be described in detail in a fellow doctoral student’s (Théo Guillaume) thesis. Both the CRESU chambers produce continuous flows and are pumped by a series of pumps including a primary and 4 roots blower pumps with a total effective pumping capacity of ca. $30,000 \text{ m}^3 \text{ hr}^{-1}$. The pumping capacity can be adjusted using a butterfly valve. While the CRESU technique used in this work involve continuous flows, several pulsed variations are also used in various research groups like the Heard group at Leeds and the Jiménez group at Ciudad Real. The pulsed variations can reach the required uniform thermally equilibrated conditions with limited pumping capacity and have a reduced gas consumption though they might have some technical limitations.

2.2.3.1 CRESU–B

The CRESU–B chamber is a stainless steel cylinder chamber, ca. 4 m long, 0.5 m diameter. Inside the chamber, a 0.4 m long movable reservoir with capacity of around 12 L is mounted on rails and has a porous plate fixed inside to ensure a non–turbulent flow of a well-mixed gas mixture of reactants, precursor, and buffer gas. The nozzle can be mounted onto this reservoir and can be easily changed to reach different temperatures. Multiple flanges are available across the chamber to feedthrough gas/electrical connections, and optical/Brewster windows. Inside the chamber, the reservoir’s position can adjusted such that the uniform flow is maintained between the photomultiplier tube optics, detailed in section 2.5.

The system is equipped with numerous pressure sensors in the range 1–1000 Torr (all MKS Baratron Absolute capacitance manometers) interfaced through MKS PR4000 and 4000B readouts. Multiple mass flow controllers, via a MKS 647C controller to an RS232 interface, are used to flow gases: MKS Massflo 1179A models (1,2,5 SLM, 100 SCCM, 20 SCCM) and 1559A models (100 SLM), and Bronkhorst F201CV model (100 SCCM). The liquid flow setup used for liquid reactants will be detailed in section 2.3.

Two National Instruments NI PCI 6229 and NI USB 6229 multipurpose I/O cards are used to interface various components, such as motor commands (reservoir, Pitot), readout of analogue pressure signals, and synchronisation of signals. A Stanford Research Delay Generator model 535

(DG 535) coupled to a custom pulse generator are used to generate trigger commands for the lasers and acquisition. A Labview program is used to gather all the readout pressures, adjust flows, follow nozzle parameters, and to make the fit/decay computations.

2.2.3.2 CRESU–Chirp

A new CRESU chamber has recently been designed and built, schematic shown in Figure 2.2.6. The chamber is a 3 m long, 0.5 m diameter stainless steel tube. The design uses similar aspects of CRESU–B chamber and is connected to it via a 4-way cross, which is the further connected to the pumping system mentioned in section 2.2.3. A motorized butterfly valve (Pro-axis) enables isolation from the pumps and adjusting the pumping capacity. The other two ports of the cross are used to attach Brewster windows through which the laser beams can enter both the chambers.

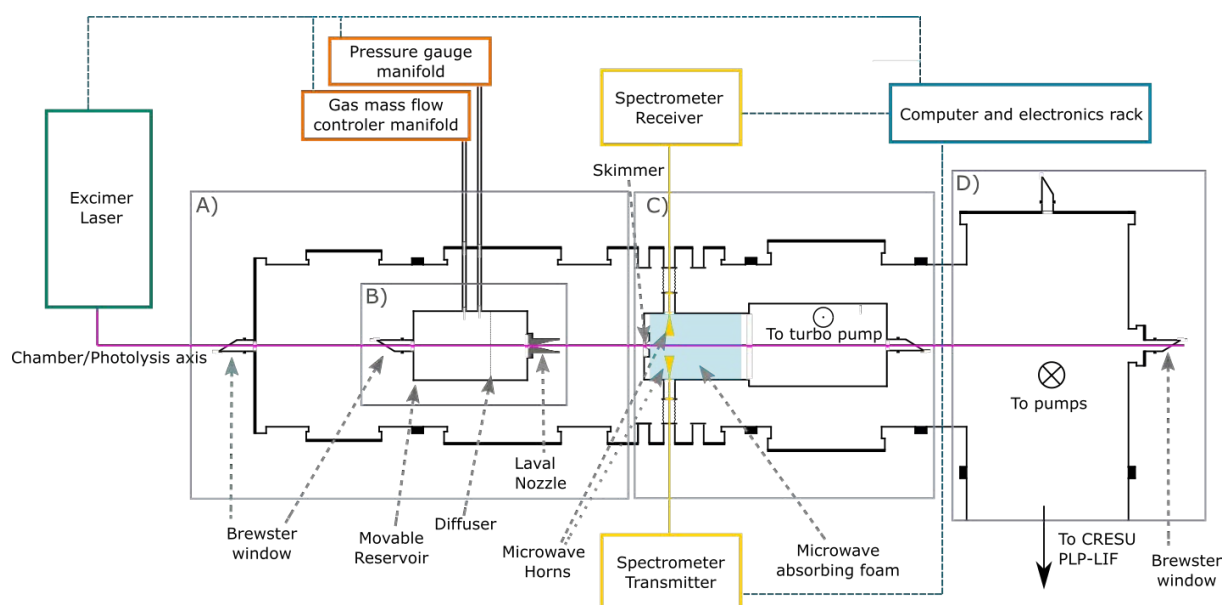


Figure 2.2.6: CRESUChirp chamber schematic showing the different regions: (A) Chamber region where the reaction takes place and from where the excimer laser enters, (B) Reservoir which is fitted with a nozzle, (C) Skimmer chamber which is pumped by a turbo pump, (D) 4-way cross which is connected to the pumps and the CRESU–B chamber. Image adapted from Théo Guillaume.

The 3 m long (11 L) reservoir inside the CRESU–Chirp chamber is movable and is installed on a translation table. The reservoir position can be adjusted within the uniform flow length of the nozzle, attached on the reservoir, to choose the duration of the uniform flow over which the molecules are probed by the chirped–pulse Fourier transform microwave (CP-FTMW) spectrometer. The reservoir, similar to the one in the CRESU–B chamber, is Teflon coated and has a Teflon-coated aluminium diffusing plate (170 mm in diameter and 3 mm thick fitted with hundreds of 6 mm diameter holes

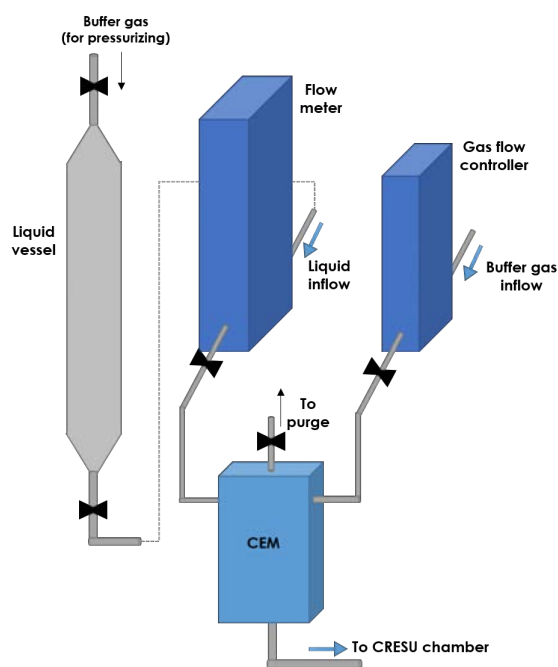
spread as a grid, and one larger hole, 30 mm diameter, allowing for the laser beam to pass through the reservoir).

A secondary chamber, as shown in section C of Figure 2.2.6, was designed and incorporated into the CRESU–Chirp chamber and will be described in detail in the thesis of Omar Abdelkader Khedaoui. This chamber is fitted on the CRESU–Chirp chamber axis, pumped by a turbomolecular pump (Osaka Vacuum TGkine3300M) and is fitted with a 4 mm skimmer on owith a 4mm skimmer at the front and a Brewster window at the back.

Multiple capacitance gauges (Brooks XacTorr CMX0) allow for precise measurement of the reservoir and chamber pressures essential for the establishment of reproducible CRESU conditions/flows. Another series of mass flow controllers are used for the flow of gases: Brooks SLA5800 series (100 SLM), Brooks GF series (20 SCCM–1SLM) F series.

2.3 Liquid flow controller

The liquid flow system used for the flow of liquid samples in this work is detailed in this section. The setup consists of a Coriolis liquid flow meter (Bronkhorst mini CORI-FLOW ML120V00)



(a) Liquid setup schematic



(b) Image of the liquid setup line.

Figure 2.3.1: The liquid flow system, including a flow meter, gas flow controller, and a CEM, used for introducing the liquid reactants in this work.

that introduces a metered flow of liquid sample into an Controlled Evaporation Mixer (CEM) (Bronkhorst W-202A-222-K), followed by controlled dilution with a buffer gas via a thermal mass flow controller (Bronkhorst EL-FLOW Prestige). The schematic and the picture showcasing the liquid line connections are shown in Figure 2.3.1.

The Coriolis flow meter is the most crucial part of this setup, as it allows us to flow in accurate small liquid flows, as low as 0.1 g/h. The Coriolis flow meter contains a tube powered by a fixed vibration which changes when a fluid (gas/liquid) passes through it due to a change in the mass flow momentum. This will result in the tube twisting leading to a phase shift which is then measured and a linear output is derived proportional to liquid mass flow. The flow meter is quite sensitive to vibrations and hence is fitted on four rubber anti-vibration pads.

While the typical procedure for calibration of the flow meter is performed at the factory, an additional in-house calibration was done under laboratory conditions to confirm the flows being used. For this procedure, the CEM was removed from the line and the outflow (of propanol) was collected into a beaker where the liquid collected was carefully measured using a weighing scale. A key point to be noted is that the flow meter does not have a valve and its only role is to measure the flow, and the reading is then communicated to the CEM where the valve is adjusted accordingly. For the calibration process, propanol was flown for set period of time (3–5 minutes) and the flow measured with the flow meter during that time. This mass was then compared with the expected mass based on the measured flow rate from flow meter in FlowPlot software (10 points/second) throughout course of experiment. The Figure 2.3.2 shows the measured mass against the expected mass which gives a fit with a slope of 1.008 ± 0.008 .

2.4 Radical Generation

The focus of this thesis is to study the kinetics and branching ratios of reactions involving radicals, CN radicals in particular, especially given their relevance for low-temperature environments both in the interstellar medium and planetary atmospheres. Some of the most commonly used techniques to generate radicals *in-situ* are microwave discharge, flash vacuum pyrolysis, and photolysis— the method of choice in this work. Flash photolysis was developed by Norrish and Porter who won the Nobel Prize in 1967 for this method. In this method, a flash lamp was used to generate the transient species from a precursor which allowed them to then measure the kinetics, as the photolysis via the flash lamp marked the start of the process/reaction. The flash lamp has since been replaced by pulsed lasers

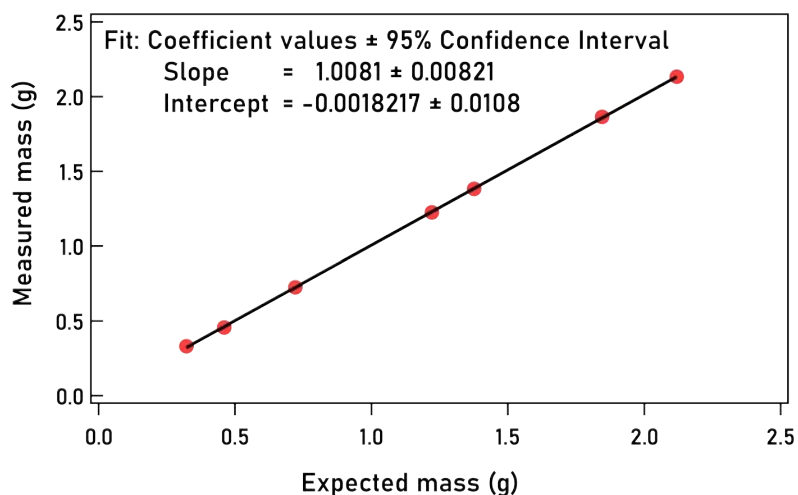


Figure 2.3.2: Liquid flow meter calibration: Measured mass of propanol against the expected mass, which was measured by the area under the curve for the flow rate against time.

because of their advantages like narrow line widths, high repetition rates, high energies, and short pulse durations. In this work, an excimer laser (Coherent LPXPro 210) which enters the chamber via a Brewster window is the source to generate radicals via photolysis at 10 Hz for the LIF measurements and at 100 Hz for the measurements using chirped-pulse microwave spectroscopy.



Figure 2.4.1: Precursor/ICN vessel, fitted with a glass frit, used to flow in the precursor with a buffer gas flowing in from the top.

A few of the precursors that can be photolysed to generate CN radicals, the species of interest in this work, are BrCN (at 193 nm), ICN (at 248 nm or 266 nm) and C₂N₂ (at 193 nm). ICN was photolysed

at 248 nm for the experiments detailed in this thesis. ICN is a solid compound and was placed on a glass frit in a 30 cm long glass vessel, shown in Figure 2.4.5. A buffer gas was then flowed in which allowed for the precursor vapour to enter the CRESU chamber. A rough estimation of the precursor flow can be made based on the known vapour pressure of the precursor and the flows being used which ensured that the pseudo–first order conditions were always obtained.

2.4.1 UV-Visible spectrometer setup

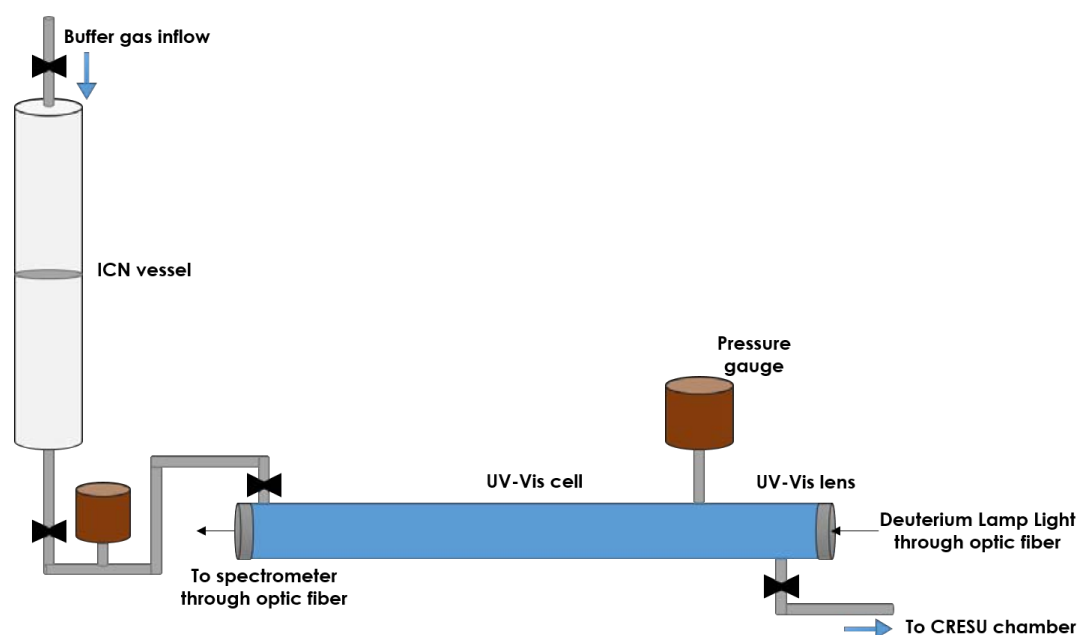


Figure 2.4.2: Schematic for the UV-Vis spectrometer setup integrated with the precursor (ICN) vessel to measure the precursor concentration going into the main CRESU flow.

Knowing the exact concentration of precursor, which can then be used to calculate the CN radical concentration based on the known absorption cross-sections, is not needed when operating under pseudo–first order conditions to measure the overall rate coefficients. The only requirement is for the radical concentration to be less than the other reactant concentration by a factor of 100 or more.

As will be discussed in section 2.5, laser–induced fluorescence is an extremely sensitive technique to measure the radicals and can be used to follow the initial CN radical concentration over time to obtain the kinetic rate coefficient. In the case of experiments with chirped–pulse microwave spectroscopy, the sensitivity is limited under the high–pressure CRESU conditions and the CN radical concentration is equal to the sum of concentrations of all the potential products. A need for accurately measuring and optimising the ICN concentration was felt.

To have an accurate measurement of the amount of ICN being put into the flow, a UV-Visible

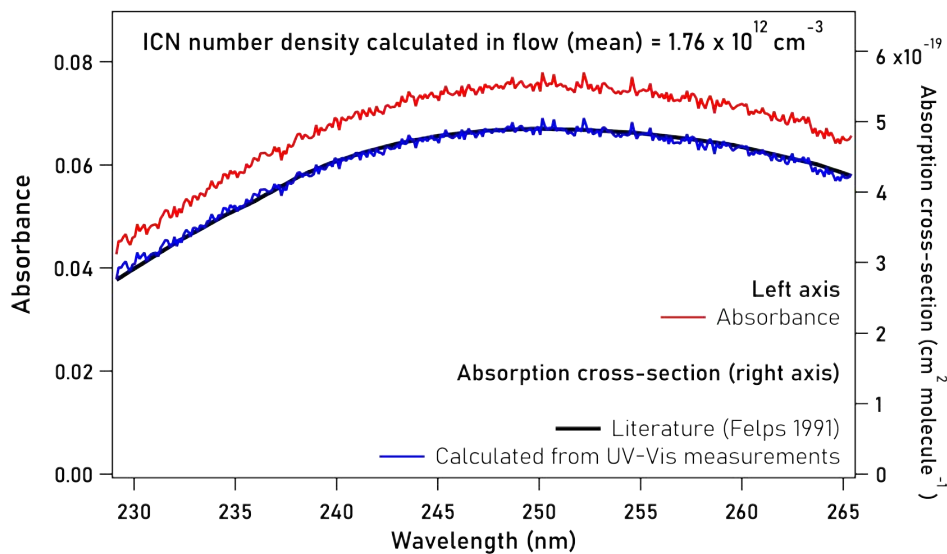


Figure 2.4.3: Output from the Igor Pro code showing the absorbance measured for ICN on the left-axis and a comparison of literature absorption cross-section with the absorption-cross section calculated using the measured absorbance.

spectrometer was set up as shown in Figure 2.4.3. ICN vapour is carried by a controlled buffer gas flow and the pressure within the vessel (measured using an MKS Baratron Gauge type 626) is adjusted by means of a valve down stream. The returning vapour flow was passed through a UV-Vis absorption cell. ICN has a well reported [Felps et al., 1991] absorption spectrum over 200–600 nm wavelength range which was used to calculate the ICN concentration flowing into the main chamber using the Beer Lambert law.

The UV-Vis cell is a 63 cm long, 3.5 cm diameter stainless steel cylinder and has quartz windows at its two ends, followed by collimating lenses. The light source (Ocean Insight DH2000-DUV) has two lamps, a deuterium lamp and a halogen lamp to cover a complete range of 190–2500 nm transmitted via an optic fibre (QP600-2-XSR). On the other end, another optic fibre is used to transmit the light, after the absorption by the compound (ICN in this case) in the cell, to a Maya2000-Pro spectrometer fitted with an Ocean Optics H5 grating to provide a resolution of 0.16 nm. This system provides an absolute measurement of the precursor injected into the CRESU flow. The UV-vis measured concentrations differed from those calculated using the reported vapour pressure of ICN at room temperature, and the pressure of the precursor cell by up to a factor of 2–5. These differences probably come from to the cooling of the ICN due to its sublimation and pumping.

The intensity (I_o) of the deuterium lamp source over the wavelength range 190–250 nm and the background/stray intensity (I_{off}) with the lamp off was measured using the Ocean View software. The

intensity measurement (I) when ICN is flowing through the UV-Vis cell was then input into the Beer Lambert law

$$\ln((I - I_{\text{off}})/(I_0 - I_{\text{off}})) = \sigma Nd$$

where σ is the ICN absorption cross-section measured by Felps et al. [1991], d is the length of UV-Vis cell and N is the number density of the species. The number density calculated was averaged over the measured wavelength range of 200–250 nm, which provided the ICN density in the UV-Vis cell. This value was used to estimate the “real” vapour pressure of ICN, which was then input into the flow calculations to measure the ICN number density in the main CRESU flow. The Igor pro code that was used for this analysis is provided in the Appendix. Using the measured ICN number density, the measured laser fluence inside the chamber at 248 nm and the absorption cross-section (and quantum efficiency of 1) of ICN, the number density of CN radicals generated could be estimated. An example for the same is shown in Table 2.4.1.

The ICN vessel was modified for the CN + propene chirped–pulse experiment, where higher CN concentrations were sought. A custom-built silicone heating pad (Omicron Technologies) with a thermocouple, shown in Figure 2.4.4, was set up which could be fitted around the ICN vessel allowing us to maintain the temperature was typically set to one degree above the room temperature.

Table 2.4.1: Parameters of the laser and CN radicals generated at 248 nm (100 Hz for the chirped–pulse experiments).

ICN density (cm^{-3})	Absorption cross-section (cm^2)	Measured power (W)	Beam area (cm^2)	Laser fluence (photons $\text{cm}^2 \text{ pulse}^{-1}$)	Generated radical density (cm^{-3})
2×10^{12}	4.7×10^{-19}	1.4	0.2826	6.2×10^{16}	5.8×10^{10}



Figure 2.4.4: The heating pad apparatus used with the ICN vessel along with the controller.

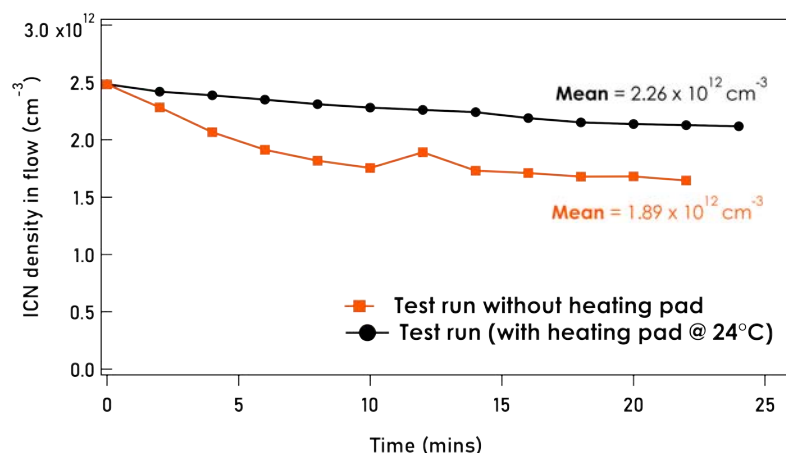


Figure 2.4.5: ICN concentration stability over time with (black filled circles) and without (orange filled squares) the heating pad.

As indicated earlier, there was a possibility of ICN cooling, so a comparison between the ICN concentrations with and without the heating pad measured with the UV-Vis setup was made, shown in Figure 2.4.5. While the measurements do not vary significantly, the heating pad was used for the chirped-pulse experiments given the slight advantage both in terms of the ICN concentration and stability.

2.5 Laser Induced Fluorescence Spectroscopy

Laser induced fluorescence (LIF) spectroscopy, coupled with pulsed-laser photolysis, is a powerful and sensitive technique used to study radicals and atoms. It is based on a chemical species being

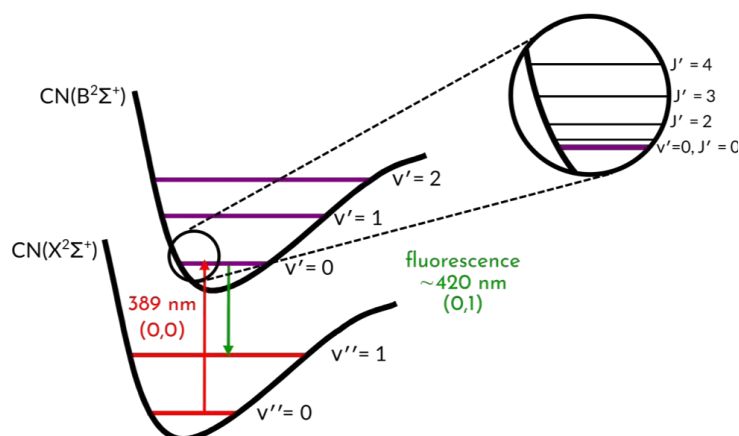


Figure 2.5.1: The $\text{CN } B^2\Sigma^+(v'=0) \leftarrow X^2\Sigma^+(v''=0)$ laser induced fluorescence scheme utilised for the laboratory detection of CN radicals in this work. The red upward arrow represents the laser excitation wavelength utilised to excite CN to its first electronically excited state. The green downward arrow represents the off-resonant fluorescent emission. Figure credit: Ilsa R. Cooke

excited to a higher energy level by resonant absorption of a photon from a laser beam, followed by spontaneous emission of light which can be measured by a photodetector. The absorption takes place from a distinct ro-vibrational level within the lower electronic (ground) state of the chemical species (radical) to a distinct level within an electronically excited state, and the energy of the photon is tuned to match the energy difference between these two levels. Emission from the excited quantum state can then take place to lower lying energy levels via allowed transitions governed by quantum selection rules. The fluorescence scheme utilised for laboratory based LIF detection of CN radicals in this work is illustrated in Figure 2.5.1.

LIF detection has multiple advantages over absorption spectroscopy. First, the LIF signal is observed against a dark background giving it an excellent detection sensitivity. Second, as the fluorescent emission takes place in random directions, it can be collected at various angles with respect to the collimated laser beam thus providing a unique capability of achieving two- and three-dimensional images. Third, it is possible to learn about the individual transitions from the excited state to the various lower levels of the target species by dispersing the fluorescence signal. Finally, the delay between the excitation and detection events allows the possibility of exploring the processes the excited species undergoes in the intervening time.

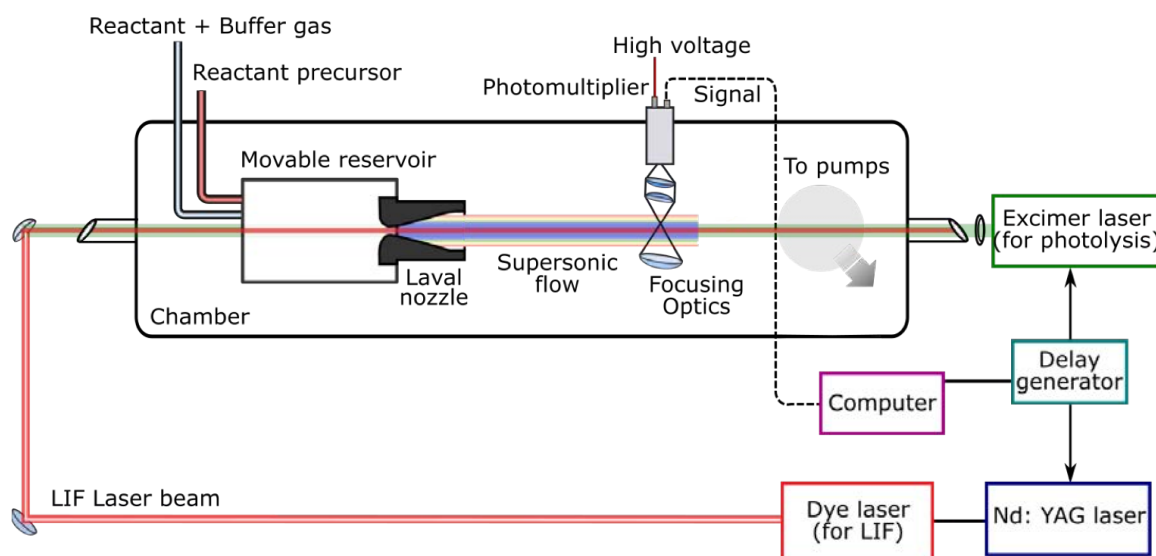


Figure 2.5.2: Schematic of a CRESU apparatus configured for the study of neutral–neutral reactions using laser-induced fluorescence, based on the setup at the Université de Rennes. The reactant, buffer gas, and radical reactant precursor are delivered to the reservoir via a series of flow controllers. The gas mixture enters the chamber through the Laval nozzle, through which expansion produces a uniform supersonic flow. Radicals are produced in the supersonic beam by photolysis of a precursor using radiation from a fixed frequency pulsed excimer laser and are detected by LIF that is excited using tunable radiation from a dye laser. Image from Cooke and Sims [2019]

2.5.1 PLP–LIF setup available at Rennes

A schematic of the CRESU apparatus, CRESU–B chamber as mentioned earlier in section 2.2.3, configured for its use with laser induced fluorescence spectroscopy is shown in Figure 2.5.2.

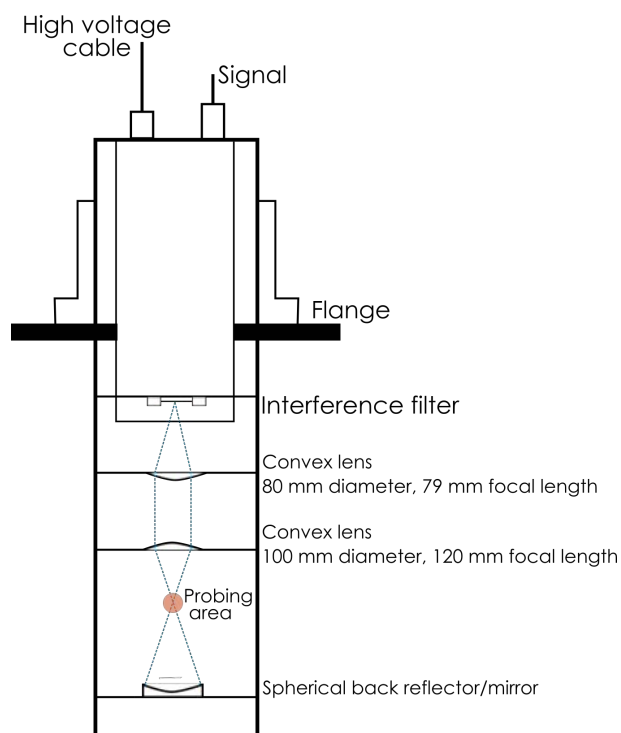


Figure 2.5.3: Optics setup utilised to focus the fluorescence onto the photomultiplier tube (not to scale). The blue dotted lines indicate the focusing action of the optics.

The CRESU PLP–LIF setup at Rennes was adapted to study the CN radical and is explained here. A Laser Analytical Systems (LDL 20505) dye laser equipped with a single 2400 lines/mm grating was operated with 0.2% mixture of Exciton Exalite 389 dye in 1,4-dioxane. The dye laser was pumped by the frequency-tripled output of a Nd:YAG laser (Continuum, Powerlite Precision II) at 355 nm (~ 200 mJ) and could be tuned in the range 378–395 nm, with a peak around 389 nm where pulse energies in the range of 50–70 μ J was measured. The dye laser radiation excites the CN radical into the (0,0) band of the $X^2\Sigma^+ \leftarrow B^2\Sigma^+$ electronic transition at ~ 388.3 nm, as shown in Figure 2.5.1. A narrowband interference filter centered at 420 nm (Ealing Optics, 10 nm FWHM) was used with a photo-multiplier tube (PMT, Thorn EMI 6723) to select the off-resonant fluorescence into the first vibrational level of the ground state via the (0,1) band. A CN ro-vibrational spectrum recorded with the dye laser in the range 387.5–388.9 nm in the CRESU flow at 83 K is shown in Figure 2.5.4 in comparison with a simulation obtained at 83 K using the PGOPHER software [Western, 2017] using parameters from Brooke [2014].

2.5.2 Data acquisition and analysis

The system is synchronised via a Stanford Research Systems (SRS) delay generator model 535 (DG 535), coupled to a custom pulse generator which is used to generate trigger commands for the lasers and to trigger the oscilloscope (Tektronix TDS 3032B) data acquisition, used for visualising and optimising the signals. The delays are mostly constant except for the laser delays, which can be changed by the user or by the program via PC commands. The trigger pulses from the DG 535 and commands (target wavelength for dye lasers, start/stop for the excimer) are communicated to the lasers from the PC via BNC cables. The signal measured by the photomultiplier tube is processed by a SRS Gated Integrator (SR250) that creates the gate, integrates and communicates the result to the PC via a SR245 Computer Interface (explained later in this section).

The CN radical is generated via ICN photolysis at 248 nm radiation from a KrF excimer laser, as explained in section 2.4 at 10 Hz, the repetition rate is limited by the Nd:YAG laser. A HeNe laser is used to establish the laser/reaction axis along which both the excimer and dye lasers were aligned. To scan the decay of the signal, a pair of laser pulses is required for every time point. The start of the reaction is marked by the initiation of ICN photolysis/excimer laser pulse. This is followed by the dye laser pulse which induces the fluorescence, measured with the photomultiplier tube, which is proportional to the radical concentration. Thus, the dye laser trigger provides a time stamp for the

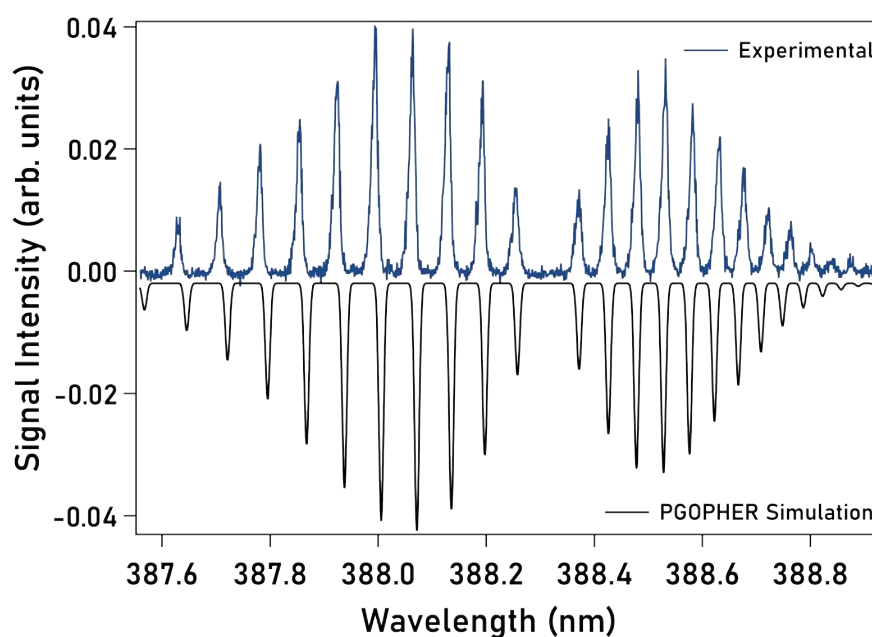


Figure 2.5.4: CN spectrum recorded under CRESU conditions at 83 K, shown in blue, in comparison with the simulation at 83 K using PGOPHER Western [2017]

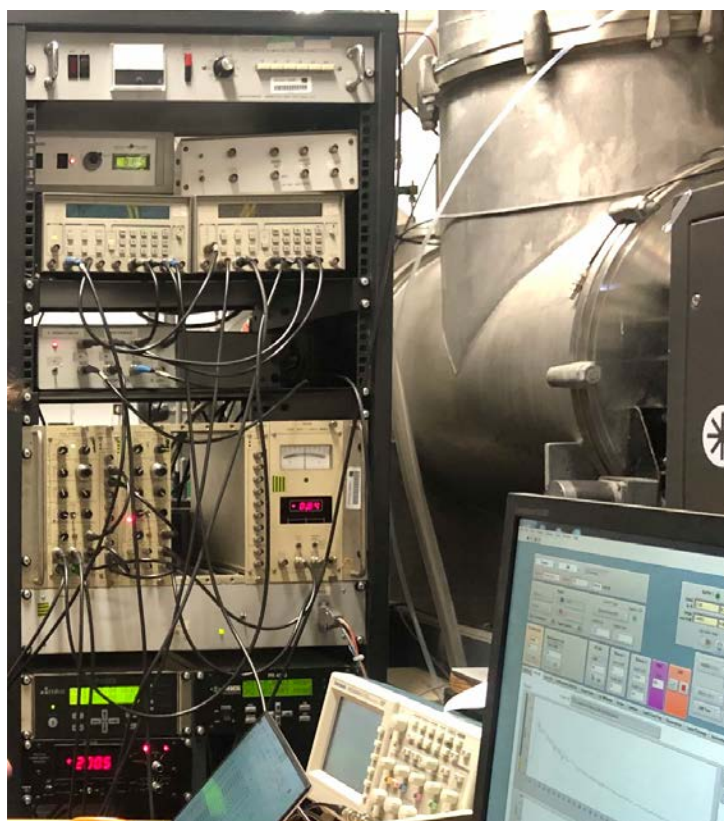


Figure 2.5.5: Picture of the electronics rack used for the PLP–LIF experiments.

radical concentration measurement. The LIF signals were recorded by a gated integrator and a boxcar averager (Stanford Research Systems), an example of which is shown in Figure 2.5.6.

The excimer laser pulse often causes a high peak on the photomultiplier tube because of its very high intensity, and possible reflections from the metal surfaces. A metal cone baffle is placed inside the chamber after the Brewster window from where the excimer laser enters to reduce some scattering, though not completely. This scatter, and also the scatter from the LIF/dye laser cause a non-linear response from the PMT and this part of the recorded signal cannot be used. This scatter signal looks like the sharp dip in the blue waveform as shown in Figure 2.5.6.

The dye laser pulse generates a short lived fluorescence (60–80 ns) from the CN radical, which shows up in the blue trace shown in Figure 2.5.6. The fluorescence signal, in red in Figure 2.5.6, is recorded and integrated by using an optimal gate length. The integrated value of the signal, proportional to the radical concentration, is communicated to the LabVIEW program. A background signal to establish a baseline is measured by triggering 10 dye laser pulses before the excimer laser is triggered. This measured signal from these pulses establishes the background signal, and can be subtracted later from the signal from the radical. To record the time dependence of the CN radical depletion during the

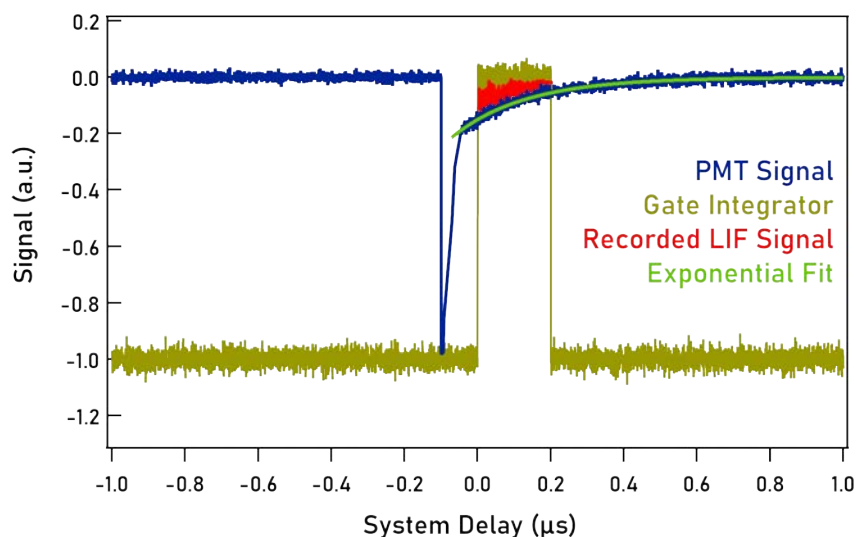


Figure 2.5.6: PMT and LIF signals, as collected during an LIF experiment (using simulated data).

reaction, delays between the excimer and the dye laser pulses in the range of zero to hundreds of μs , both operating at 10 Hz, are used.

The LIF signal decays were averaged typically 5–10 times for each delay (between the excimer and dye laser pulses) time point. A series of delays in the range -5 – $400 \mu\text{s}$ can then be used to obtain the time dependent LIF signal from the CN radical which can be fit to single exponential decays.

2.6 Chirped-pulse microwave spectroscopy

The most sensitive and widely used detection methods in gas-phase physical chemistry studies, including the laser-induced fluorescence technique used in this work, often face serious challenges in relating signal intensities to actual concentrations of reaction products. While photo-ionization mass spectrometry, especially used in conjunction with synchrotron radiation sources, can be used to overcome this challenge, isomer-specific measurements with this technique are quite difficult due to similar photo-ionisation energies and lack of photoionisation spectra of reaction products and transient species.

Rotational spectroscopy is one of the most powerful structural tools in physical chemistry as it can provide a high degree of molecular specificity, allowing unambiguous assignment of species, including isomers, that possess at least a modest permanent electric dipole. Given the power of this technique, rotational spectroscopy has also been the most successful method in the recent decades to detect species in the interstellar medium due to the advent of radio telescopes and improvements in radio-

frequency technology.

The molecules explored in this work are asymmetric tops— polyatomic molecules with three different moments of inertia, one about each perpendicular axis passing through the centre of gravity. The different rotational energy levels are quantized and the transitions/spectra can be analysed to provide accurate information on bond lengths and angles, and on energy barriers to internal rotation. Study of internal rotation is one of the most active areas within microwave spectroscopy. For molecules which consist of two groups connected by a single bond, the groups can rotate with respect to one another about the single bond and the barrier height for this rotation leads to A and E torsional states.

SPCAT/SPFIT is a program suite developed by Pickett [1991] which can be used to predict spectra of molecules at different temperatures using ‘initial guesses’ of rotational constants and dipole moments and to fit the observed spectra. The fits can be used to make better guesses for the rotational constants, including distortion constants and hyperfine components. This program was used in this work to predict the spectra of key molecules at low temperatures and will be discussed in Chapter 6.

Traditional cavity-based microwave spectrometers depend on tuning the resonant cavities to the specific rotational lines of the species. In addition, by scanning at such high resolution, acquiring the spectrum for a range of frequencies or multiple frequencies can be very slow. Pate and co-workers [Brown et al., 2008] developed chirped-pulse – Fourier Transform Microwave (CP-FTMW) spectroscopy which allows one to scan large bandwidths in the microwave region, with the possibility of collecting tens of GHz of a broadband spectrum in $< 40 \mu\text{s}$. In this technique, a broadband linear frequency sweep polarises a gas sample, after which a free induction decay (FID) is detected,

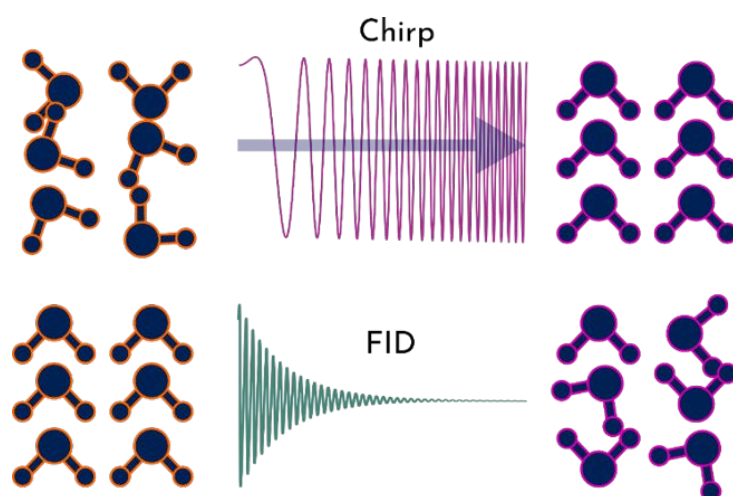


Figure 2.6.1: Visual representation of the principle of chirped-pulse microwave spectroscopy or the effect of chirped microwave radiation on molecular species. Figure credit: Ilsa R. Cooke

shown in Figure 2.6.1. The FID can then be Fourier transformed to produce a broadband frequency spectrum. This technique employs digital technology making it highly repeatable, stable, and fast. This spectroscopy technique has also been expanded into the (sub)millimetre region using frequency multiplication techniques and/or a heterodyne receiver to down–convert the FID back to the microwave region on the backend.

The chirped–pulse FTMW (CP–FTMW) spectrometer consists of three basic components: (i) chirped microwave pulse generation, (ii) microwave excitation pulse and molecular beam sample interaction region, and (iii) FID detection. The FID is the characteristic decay back to equilibrium of a sample polarized by an external electric field, and is described by the optical Bloch equations [Allen and Eberly, 1987]. The FID describes the decay of coherence within a polarized system, which includes the rate of decay by collisional rotational inelastic energy transfer, as well as elastic or phase changing collisions [Schwendeman, 1978]. The FID decay constant, and hence the linewidth of a signal has pressure and Doppler broadening components. The conditions under which the molecules were probed in this work—inside the skimmer chambers, where the pressure is low (around $\sim 8 \mu\text{bar}$), were in the limit where Doppler broadening/decay is the dominant dephasing mechanism. The shape of the FID in this case is no longer dominated by the pressure decay rate. When using single frequency ($\pi/2$) pulses under these conditions, the signal intensity is proportional to the number of molecules as described in Hearne et al. [2020]. The $\pi/2$ pulses are modelled from the Bloch equations such that the $\pi/2$ pulses excite all the molecules in the system to a higher level, compared to π pulses which will excite all particles in the first half time, and de–excites in the second half such that so all particles are in lower level.

2.6.1 Setup developed at Rennes

A new E-band spectrometer in the range 60–90 GHz was designed and constructed, incorporating numerous advances in millimetre wave technology that had not been available to previous spectrometers operating in this frequency range. The spectrometer details have been published in Hays et al. [2020] and will be provided in detail in Théo Guillaume’s thesis. A schematic of the electronics is shown in Figure 2.6.2.

For the transmitter side, shown at the top in Figure 2.6.2, an arbitrary waveform generator (AWG, Keysight M8195A, 64 GS/s) is used to produce frequencies in the range of 1–16 GHz. The up–conversion of the signal is done in a mixer (Marki M11850H) using a phase–locked dielectric

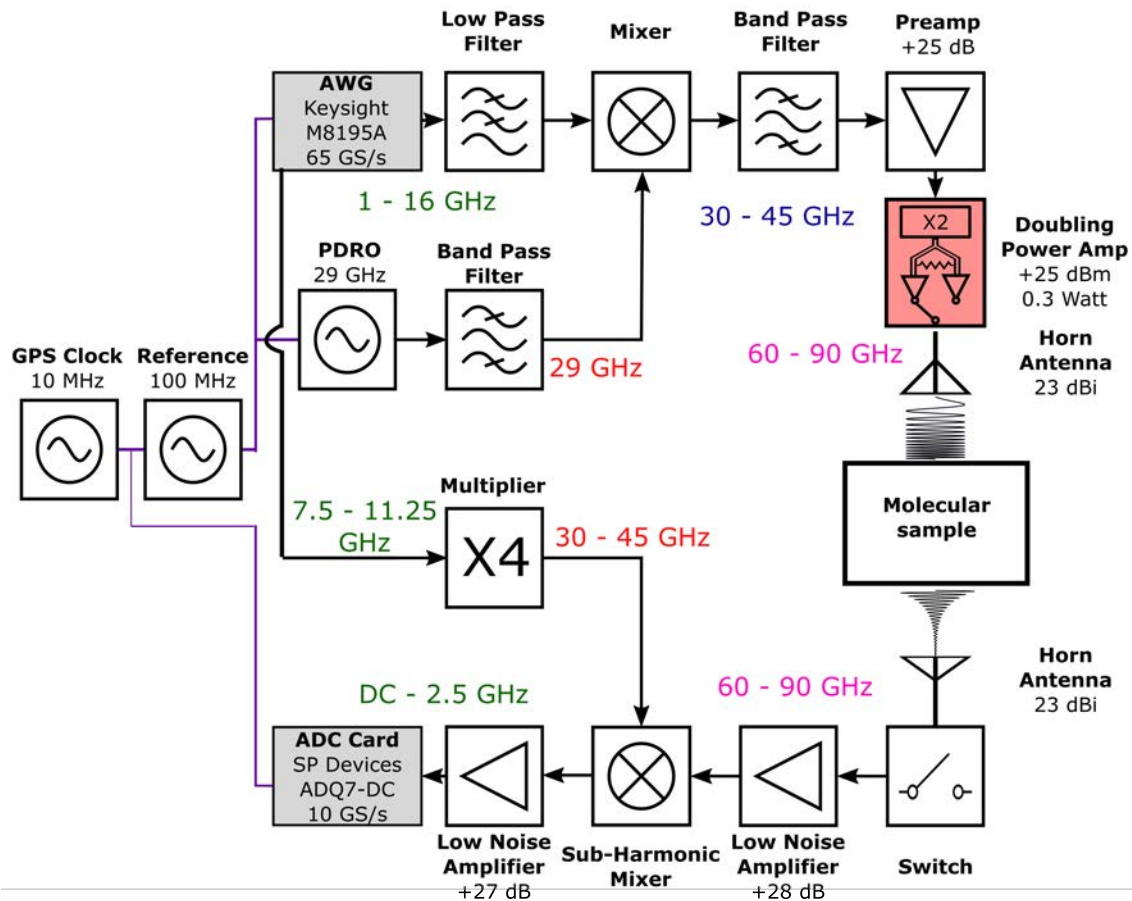


Figure 2.6.2: Schematic of the E-band spectrometer used in this work with the digitizer in as the acquisition device. Image from Hays et al. [2020].

resonator oscillator (PDRO, Microwave Dynamics PLO-2070–29.00) operating at 29 GHz as the local oscillator (LO) source. The upper sideband is then selected using a broadband high-pass filter (Reactel 9HS-X30/45G- K11R) before entering the preamplifier (Quinstar QPW-205020525-J0). This signal is then input into a Quinstar integrated system (QBM-609025E0U0R) that includes a passive frequency doubler to bring the frequency range to 60–90 GHz (Quinstar QPM-75002E), a waveguide splitter (Quinstar QJH-EUFBZIL), two millimeter wave power amplifiers (Quinstar QPW-60752530-C2W0 and Quinstar QPW-75902530-C2W0), and a waveguide switch (Quinstar QWZ-ET2800). Two amplifiers are used, one for the 60–75 GHz range and the other operating between 75–90 GHz, which can be switched manually via an electro-mechanical switch. The amplifiers are controlled via TTL signals for fast turn-on and turn-off times of less than 20 ns. Both amplifiers output about 300 mW of RF (radio frequency) power over each band. The microwave radiation is output through a 23 dBi gain horn antenna (Quinstar QWH-EPRR00).

The receiver system, shown at the bottom in Figure 2.6.2, begins with an identical horn antenna (Quinstar QWH-EPRR00) followed by a variable attenuator that attenuates signals by up to 30 dB

(Quinstar QAL-E00000), for monitoring pulse power while performing experiments. The signal then enters a fast single pole-single throw PIN switch operating in the 60–90 GHz range (Millimeter Wave Products 911E/387TTL). The switch has a 10 ns 10%–90% rise time to either transmission or isolation, with around 3 dB insertion loss across the band, and over 30 dB of isolation. This switch is crucial to protect the millimeter wave low-noise amplifier (LNA), from the initial polarizing pulse. The LNA (Millitech LNA-12-02,350) has (28 ± 4) dB of gain across the 60–90 GHz range and has a 3 dB noise figure, rising to 4.5 dB below 67 GHz. The low-noise amplifier is followed by a subharmonic mixer (Virginia Diodes WR12SHM), which has a dual sideband conversion loss of 6 dB with a 3 dB bandwidth of DC-15 GHz at the intermediate Frequency (IF) port. The output from the IF (Intermediate frequency) is further amplified using a LNA with 25 dB of gain and a 2.5 dB noise figure (Miteq AFS4-0 0,101,800-25-S-4). The choice of the LO source is determined by whether an oscilloscope or a digitizer card is used to record the heterodyned signal. A PDRO operating at 37.5 GHz (Microwave Dynamics PLO-2070-37.50) or the second channel of the AWG sent through a quadrupler (Quinstar QMM-38,150,504 J) provides an LO between 30–45 GHz.

A digitizer is used for data acquisition during the experiment, while an oscilloscope (Tektronix DPO 71604C) is used for troubleshooting and characterization of the instrument. The digitizer is a Teledyne SP Devices ADQ7DC-PCIE card running at 10 GS/s with a 2.5 GHz 3 dB bandwidth. The oscilloscope and digitizer are triggered by pulses from an AWG marker channel. The switch and pulsed amplifiers are controlled by a BNC 577 digital pulse/delay generator (DDG), which is triggered by another marker channel on the AWG. The timing for each cycle of the experiment is conducted in a manner to protect the low noise receiver from the intense polarizing pulse, so that the polarizing pulse does not damage the LNA. Most of the system, particularly the AWG, the PDROs, and the oscilloscope, is synchronized to a 100 MHz oven-controlled crystal oscillator (Precision Test Systems GPS10-eR-50) which is locked to a GPS-disciplined Rb clock (Stanford Research Systems FS740) operating at 10 MHz. The higher-frequency 100 MHz signal is used to improve phase stability and the digitizer and the DDG are synchronized to the 10 MHz clock.

The spectrometer is mounted on two independent 1.15 m high aluminium tables, one each for the receiver and transmitter sides, shown in Figure 2.6.3. The electronics are mounted on heat-sink blocks maintained at a constant temperature of $(25 \pm 0.1)^\circ\text{C}$ by a water chiller (ACCEL series 250 PHP) in order to maintain the stability of the components through long experiments. The metal plate with the electronics are then placed on an optical breadboard via an optical post assembly to permit a fine alignment of the waveguide for coupling with the chamber.

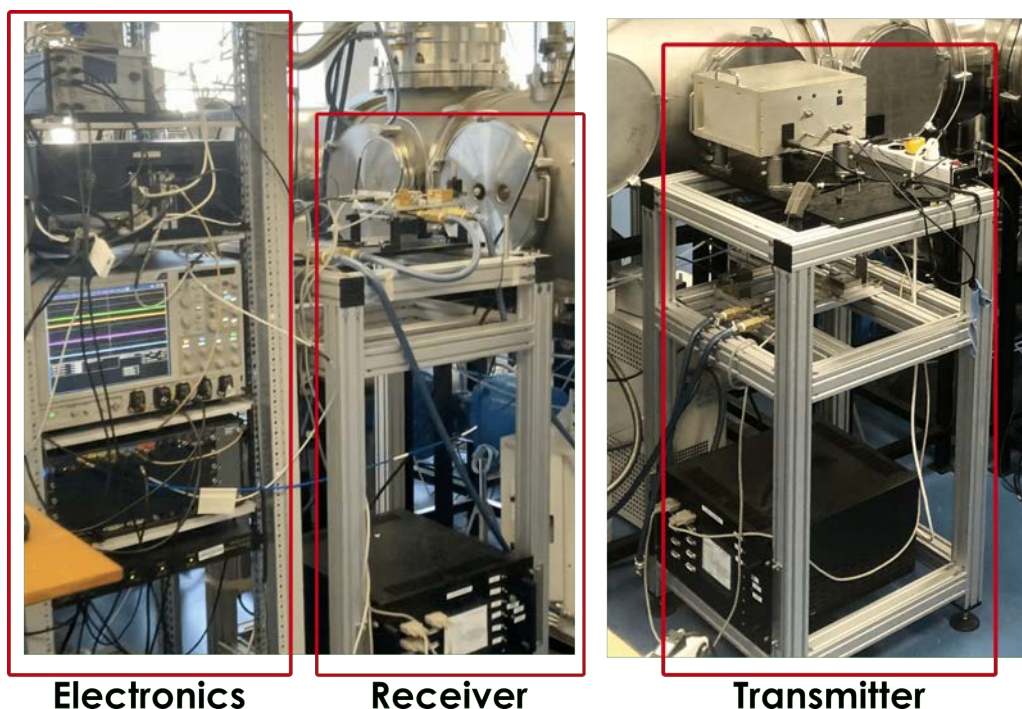


Figure 2.6.3: CRESUCHIRP E-band setup developed at Université de Rennes.

The coupling of the spectrometer inside the secondary chamber, shown in section C of Figure 2.6.3, is achieved using waveguide bulkheads connected to ~ 150 mm long waveguides, which have the horn antennas mounted at the ends. The vacuum seal between the chamber and air is achieved by a homemade 100 micron thick Teflon sheet windows clamped between the two waveguide flanges. Gaskets shaped for waveguide flanges (SAS Industries Inc., 1056-7407) are used to create vacuum seals between individual waveguide elements. In this configuration, the distance between each horn is about 10 cm and can probe the skimmed flow. The interior of the skimmer chamber is lined with 2 cm millimetre-wave absorptive foam (Eccosorb HR-10 Laird) to reduce reflections of the microwave radiation from the metal surfaces, which can cause significant noise in the data.

2.6.2 Data acquisition

The complete acquisition protocol and details on its optimisation will be explained in the theses of Théo Guillaume and Omar Abdelkader Khedaoui. The addition of the secondary expansion has helped improved the sensitivity achievable with the spectrometer, and an example of the same is provided in the Appendix A6. Here, I will explain the acquisition scheme used for studying the products from the reaction of CN + propene, which is presented in Chapter 6. A key point to note is that the reaction takes place under CRESU conditions, shown in section A shown in Figure 2.2.6, and the reaction products formed are skimmed into a secondary expansion, section C in Figure

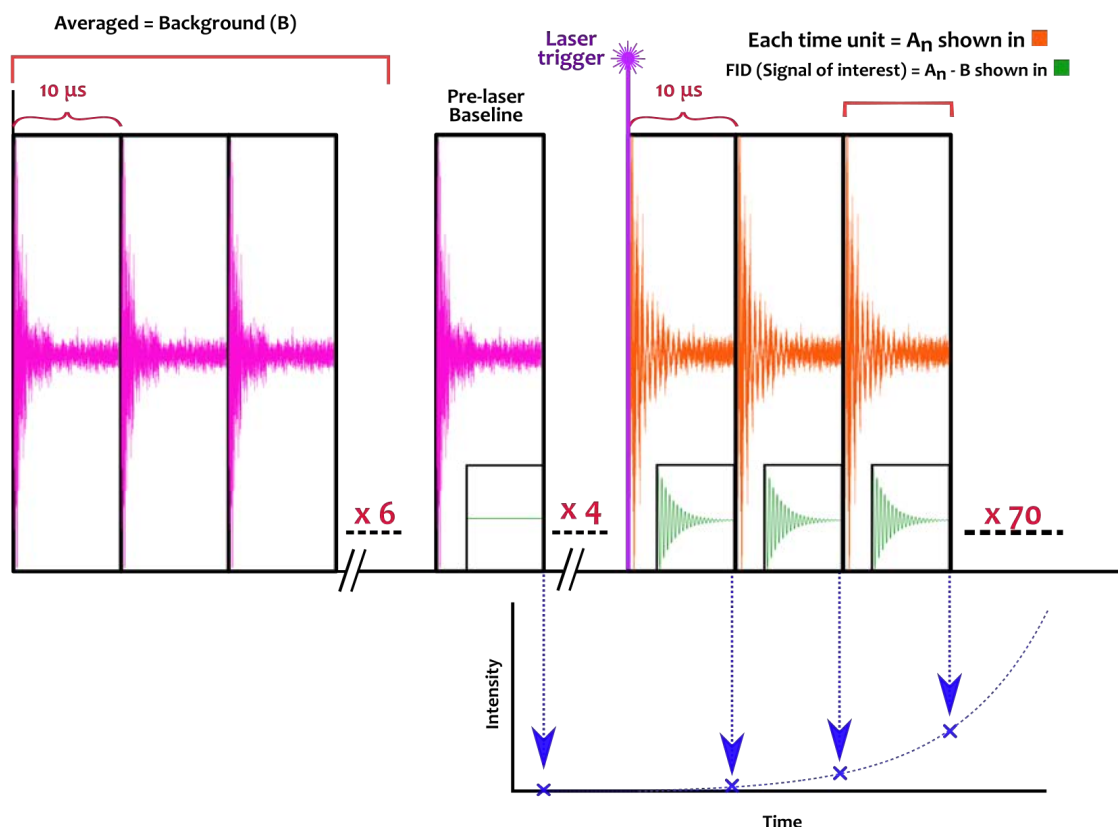


Figure 2.6.4: Schematic of the data acquisition scheme for measuring laser-produced products in the skimmer chamber formed via reaction or photolysis. The insets show the time-domain data when the pre-laser frames are averaged and subtracted from the remaining frames.

2.2.6, where they are then detected. The excimer laser pulse marks the start of the reaction, and as the uniform CRESU flow enters the skimmer chamber, a time dependence can be obtained.

A 50–300 ns long excitation microwave pulse (chirp/single frequency) generated by the AWG is transmitted through the horn antenna. During this time, the switch on the receiver side blocks the pulse to protect the highly sensitive receiver electronics. This pulse excites the species of interest, and as the free induction decay (FID) begins, the switch is triggered to be in transmitting mode to record this signal from the receiver side. The complete frame consisting of the excitation pulse, trigger for the switch, trigger for the laser (if needed) and the FID signal is 10 μs long. A series of 80 frames are used to record the time dependence of the possible products from the reaction, as shown in Figure 2.6.4. The data is recorded on the ADC card, where up to 100,000 acquisitions of the complete set of frames are recorded and averaged. Further analysis of the different frames was performed using the Igor Pro software and is explained in detail in section 2.6.3.

Similar to the LIF experiments, the excimer laser generates the CN radical and marks the start of the reaction. As shown in Figure 2.6.4, 10 frames collected before the laser pulse were used to establish

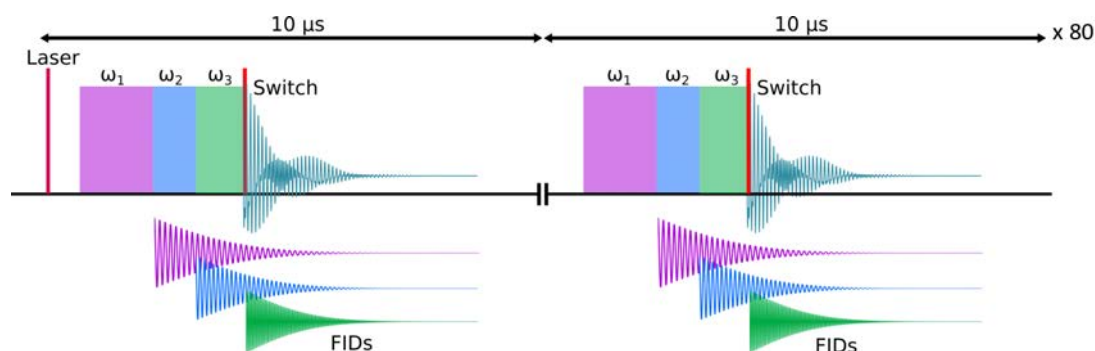


Figure 2.6.5: Schematic of the multicolour pulses which allow us to monitor the various species at the same time as the FID collected has a combination of the FIDs from the different species. Figure credit: Ilsa R. Cooke

the baseline, as no products are present in the flow before the laser pulse. More information about the analysis of the data collected will be presented in section 2.6.3.

While the principle of chirped-pulse experiments is to send in a broadband chirp, this also distributes the power of the spectrometer over a wide range of frequencies. To overcome this, single frequency pulses to measure single species and “multicolour” pulses, based on Broderick et al. [2018], to measure multiple species were used. The multicolour pulses, shown in Figure 2.6.5, are designed with multiple single frequency pulses corresponding to the most intense rotational transitions for the different products to detect multiple possible reaction products simultaneously. This allows us to monitor signal arising for a number of the predicted product species during a single scan, three shown in Figure 2.6.5, once the switch was in transmitting mode. The length of each pulse was optimised to be in $\pi/2$ conditions for maximum signal based on Rabi cycle principle [Park et al., 2011], as the signal intensity depends on the dipole moment of the species and the electric field strength generated under the conditions used in the skimmer chamber.

2.6.3 Data analysis

The data collected was post-processed using an Igor Pro (Igor Pro 8, Wavemetrics) routine developed by Théo Guillaume and Brian M Hays. The signal is collected in the time-domain, which can then be Fourier transformed to obtain the spectrum in frequency domain. The time-domain data, however, are not completely clean and have noise due to reflections, and spurs from clocks and LO bleed-through. In order to clean the spectra, a filtering scheme is applied to remove the coherent noise, similar to the way the mismatched ADCs were removed from spectra taken with another digitizer [Hernandez-Castillo et al., 2016]. The sum of the parasitic sine waves from electronic spurs, which,

are present at all times forms a repeating pattern in the noise that can be collected from the frames and used as a filter to remove fluctuations. The Fourier transform of this time-domain data can then be used for analysis. Not all noise can be removed by this procedure, however, and some a lot spurious content from mixing with clocks or impure LOs is also observed in our data. In most cases, these spur frequencies are well separated from the frequencies of species we are interested in and hence do not interfere.

As explained in section 2.6, the intensity of the FID is directly proportional to the amount of the species, which in turn can be linked to the intensity of the frequency-domain line. The peak heights of the spectral lines in the Fourier transforms over the various frames, shown in Figure 2.6.4, can then be used to follow the species/reaction products over time. Typically, six out of the ten frames before the laser trigger are averaged and used as background, which are subtracted from the frames containing molecular signal, while the remaining four pre-laser frames are used to establish the baseline signal for the signal/species intensity. The remaining frames can then be used to observe the time dependence of the species. Given the size of the frames, a time resolution of $10 \mu\text{s}$ was used to follow the reaction. The repetition rate of the experiment is limited at 100 Hz due to the excimer laser used. So, each set of frames was repeated at 100 Hz and averaged up to 100,000 times to reach a higher signal-to-noise ratio.

Chapter 3

Theoretical calculations

3.1 Introduction

The synergy between theory and experiments has aided, and often accelerated, progress in a wide variety of fields. The focus of this thesis is to understand reaction kinetics at low temperatures, where several fundamental quantum theories get tested. Quantum chemistry has benefited from the increased availability and accessibility to advanced mathematical tools via softwares like GAMESS [Schmidt et al., 1993], Gaussian [Frisch et al., 2016], MOLPRO [Werner et al., 2012], CFOUR [Stanton et al., 2010], ORCA [Neese, 2012], among others.

The computational chemistry software package Gaussian (Gaussian09 [Frisch et al., 2009]) is used in this thesis. This software is based on the fundamental laws of quantum mechanics and can be used to predict a range of molecular properties of chemical species, and reaction paths in a wide variety of chemical environments.

3.2 Quantum Mechanics

The postulates of quantum mechanics form the rigorous foundation for the process of predicting the observable chemical properties using first principles. *Ab initio* quantum chemistry methods are computational calculations that attempt to solve the electronic Schrödinger equation to yield useful physio-chemical information such as electron densities, energies and other properties of the molecular system. Analytical solution of the Schrödinger equation, however, is only possible for a small number

of relatively simple systems, and hence most systems of interest to chemists use chemical models based on either involve approximations or on intuitive concepts.

There are two major components when performing the computations: level of theory and a basis set. A level of theory/model introduces the methodology which includes certain approximations to the fundamental quantum chemistry postulates, including the Hamiltonian/energy operator, to extend its practical utility. A basis set is a set of mathematical functions using which the quantum mechanical wavefunction for a molecular system is constructed.

3.2.1 Levels of theories used

Most of the chemical models used in this thesis are based on Density Functional Theory (DFT), which is based on the modification of the Hamiltonian/energy functional in the Schrödinger equation to electron probability density and includes an approximate treatment of electron correlation.

- B3LYP: This is a “Becke, 3-parameter, Lee–Yang–Parr” exchange-correlation functional [Becke, 1993]. The major advantage is a significant increase in computational accuracy, compared to simple Hartree-Fock based methods, without a major increase in computing time. However, it has certain limitations in terms of producing acceptable results in case of weak hydrogen bonding, and torsional interactions.
- M06-2X: This method was introduced by Zhao and Truhlar [2008] as a hybrid meta exchange-correlation functional, and is better at modelling non-covalent interactions than B3LYP. It still has limited applications for high-spin systems.

For some calculations in Chapter 4, the coupled cluster method, CCSD(T) [Cizek, 1969, Purvis and Bartlett, 1982, Scuseria et al., 1988, Scuseria and Schaefer, 1989] is used. This method starts with the Molecular Orbital theory/method and then adds the correction for the electron correlation. For thermochemistry calculations, CBS-QB3 [Montgomery et al., 1999, 2000], a composite method, is used.

3.2.2 Basis sets used

Physically, a basis set specifies the region of space each electron in the chemical system is restricted in. Larger basis sets have fewer constraints on this region of space for the electrons, and since the probability of finding an electron is finite for any region of space, larger basis sets provide more accurate

results. This may however be computationally expensive. So, selection of basis sets was done carefully based on the molecular system of interest. The basis sets used in this thesis are:

- cc-pVTZ: It is a type of correlation-consistent split-valence basis set and has two (*double-zeta*) basis functions for each valence orbital [Kendall et al., 1992]. The 'aug' can be used to add one diffuse function on each atom [Woon and Dunning, 1993].
- 6-311G: It is a type of split-valence basis set [Krishnan et al., 1980, McLean and Chandler, 1980].

3.3 Parameters/Quantities computed in this work

3.3.1 Geometry optimisation

Geometry optimisation is based on minimising the energy of the structure to reach an “optimised” structure with the least strain. This process is achieved by the software via altering the input parameters like bond length, bond angle and torsion angle, such that the starting structure moves towards a local minimum, which may or may not be a global minimum on a potential surface.

3.3.2 Potential Energy Surface Calculations

A Potential Energy Surface (PES) describes the energy of a molecular system, a collection of atoms, in terms of certain geometrical parameters, generally the positions of the atoms. For a reaction, a PES represents a unique energy “landscape” formed by each geometry of the atoms of molecules in a chemical reaction. By characterising the PES, one can locate the minimum energy shape of the molecules involved and also to computing the rates of reaction.

Stationary points are defined where the first derivative of the energy with respect to geometry remains zero, represented as

$$\frac{\partial E}{\partial r} = 0 \quad (3.3.1)$$

for all r , where r is a geometric parameter. These include maxima, minima, transition state (first-order saddle point) and higher-order saddle points.

In the mapped contour surface below the 3D plot in Figure 3.3.1, the blue dot represents a local

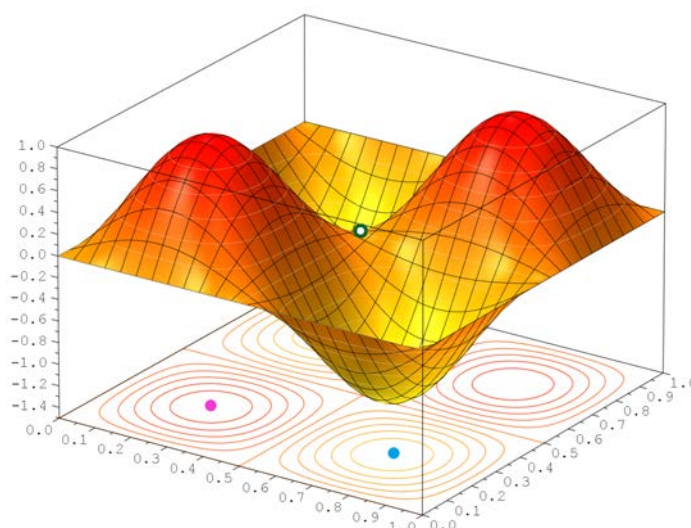


Figure 3.3.1: An illustration of a potential energy surface.

minimum which satisfies the condition:

$$\frac{\partial^2 E}{\partial^2 r} > 0 \quad (3.3.2)$$

The pink dot is a local maximum which represents a transition state, where the double derivative of energy function is less than zero,

$$\frac{\partial^2 E}{\partial^2 r} < 0 \quad (3.3.3)$$

The green outlined dot on the 3D surface is a saddle point. .

Intrinsic Reaction Coordinate (IRC) calculations can also be performed to verify the reaction path as it allows one to follow the minimum energy reaction pathway in a mass-weighted Cartesian coordinates between the transition state of a reaction and its reactants and products.

3.3.3 Thermochemistry

Gaussian also outputs the enthalpy and Gibbs free energy for a reaction as the free energy differences between the optimised minima on a PES can be used to predict reaction thermochemistries. In the CBS-QB3 composite method, the total electronic energy plus the internal thermal energy, which comes directly from the frequency part of the output, can be used to calculate the enthalpies of the reaction channels. This was used for the possible reaction pathways for the reaction between CN and methanol.

Chapter 4

Low temperature reaction kinetics of CN radical with methanol

Modified from: Gupta, D., Cheikh Sid Ely, S., Cooke, I., et al., J Phys Chem A, 123, 9995

4.1 Introduction

Methanol (CH_3OH) is considered to be one of the simplest and most abundant complex organic molecules (COMs) by astronomers and has been detected in various astrophysical environments. Methanol was first detected in Sagittarius A and B2 [Ball et al., 1970] and has since been detected in various sources including galactic H II regions [Batra et al., 1987], prestellar cores [Bizzocchi et al., 2014, Vastel et al., 2014], ISM clouds [Turner, 1998], protostellar sources [Kristensen et al., 2010, van Dishoeck et al., 1995], protoplanetary disks [Walsh et al., 2016], and comets [Biver et al., 2000, Wollenhaupt et al., 2000], with temperatures ranging from 30–300 K. The abundance of methanol is one of the highest among the COMs, as high as 3×10^{-5} with respect to H_2 in some sources [Herbst and van Dishoeck, 2009].

Accurate kinetic measurements (either experimental or theoretical) of the various formation and destruction routes of methanol at a range of temperatures are essential to model the abundance of methanol in various astrophysical environments. Studying the reactivity of methanol at low temperatures can also aid our understanding of the formation of other complex, and potentially prebiotic molecules. A major destruction route for many neutral COMs, including methanol, is via their reactions with radicals such as CN, which is ubiquitous in space.

The rate coefficients for the reactions of methanol with other radicals such as OH [Ocaña et al., 2019] and C(³P) [Shannon et al., 2014] have been measured experimentally using the CRESU technique and were found to remain rapid at low temperatures relevant to the cold ISM. The CN radical has been found in many astronomical sources [Dutrey et al., 1997, Henkel et al., 1988, Hily-Blant et al., 2008, Jefferts et al., 1970], and CN chemistry has been shown to play an important role in Titan’s atmosphere [Gautier et al., 2011, Vuitton et al., 2007, Wilson and Atreya, 2003]. Thus, the reaction with CN radicals is a feasible destruction route for methanol in a range of low temperature environments that remains unexplored. One of the possible products of this reaction, the methoxy radical (CH₃O), has been detected in the cold source Barnard 1b [Cernicharo et al., 2012a] (12–15 K), and there has been a significant discussion concerning its abundance compared to its isomer, hydroxymethyl radical (CH₂OH), which has not been detected yet. In the low-temperature conditions of Barnard 1b, non-thermal mechanisms must be invoked if methoxy formation is expected to occur on dust grains, as CH₃O and CH₂OH cannot thermally desorb from ice surfaces at these temperatures. However, ice-phase experiments on the photodissociation of methanol suggest the CH₂OH isomer is favoured, and therefore, it has been suggested that the methoxy radical abundance could be explained by its formation in the gas-phase [Antinolo et al., 2016]. In particular, the reaction between methanol and the OH radical has been discussed as a source of CH₃O/CH₂OH, but the branching ratio into the two channels has not yet been fully characterised [Antinolo et al., 2016, Ocaña et al., 2019, Shannon et al., 2013].

To the best of our knowledge, no previous experiments have been published for the reaction of CN radicals with methanol below room temperature. The earliest study at room temperature was conducted by Sayah et al. [1988] who performed flow-tube experiments using photodissociation of C₂N₂ at 193 nm as their source of CN radicals. They determined a rate coefficient of $(1.2 \pm 0.2) \times 10^{-10} \text{ cm}^3 \text{ s}^{-1}$ which is different by an order of magnitude from a later study by Janssen and Herschberger [2015], who report a value of $(1.03 \pm 0.10) \times 10^{-11} \text{ cm}^3 \text{ s}^{-1}$ at room temperature. Janssen and Herschberger [2015] used photolysis of ICN at 266 nm to produce the CN radicals and studied the reaction using time-resolved infrared diode laser absorption spectroscopy, allowing them also to investigate the reaction products.

Here, the rate coefficients for the reaction of methanol with the CN radical over a wide temperature range of 17–296 K using the CRESU technique are presented. First the experimental and theoretical methodologies used in these measurements are detailed followed by the rate coefficients and their dependence on temperature, and a discussion of the implications of the results and their astrophysical

importance is given. These measurements can be input into astrochemical models in order to assess the importance of the reaction as a destruction route for methanol at various temperatures.

4.2 Experimental Methodology and Results

4.2.1 Experimental Measurements

The kinetics of the reaction between the CN radical and methanol was monitored by following the decay of the CN radical using the Pulsed-Laser Photolysis – Laser Induced Fluorescence (PLP–LIF) technique in the temperature range 17–296 K. The low temperatures were achieved using the CRESU technique, as described in Chapter 2, configured for the study of neutral-neutral reaction kinetics using PLP–LIF as shown in Figure 2.5.2. A dilute mixture (typically <1%) of methanol (<0.2%) and radical precursor, ICN, (<0.01%) in a buffer gas (He, Ar, or N₂) expands isentropically from a high-pressure region (reservoir), into a low-pressure region (chamber) through a convergent-divergent Laval nozzle to generate a cold supersonic flow that is uniform in temperature and density. Different nozzle designs, listed in Appendix A1, were used to achieve a variety of temperatures and densities, characterised using impact pressure measurements. The high density of the molecules (10^{16} – 10^{17} cm⁻³) in the flows ensure that enough collisions take place to maintain thermal equilibrium.

Two methods were used to perform the experiments as the first set of measurements at room temperature, undertaken by a previous doctoral student Sidaty Chiekh Sid Ely, deviated significantly from previous measurements made by Sayah et al. [1988]. In the first method, referred to as EM I from hereon, gas mixtures were made in a Teflon coated stainless steel container by careful control of the partial pressures of methanol vapour and the buffer gas. Different concentrations of methanol could be obtained by varying the pressure of the buffer gas. A solid sample of ICN was placed on a frit (porous glass) in a glass vessel and introduced into the chamber via a controlled flow of buffer gas (~200 sccm). The fourth harmonic output of a Nd:YAG laser (Spectra Physics GCR 190) at 266 nm was used to photo-dissociate ICN and produce CN radicals largely in the $v=0$ level of the $X^2\Sigma^+$ ground vibrational state. In the second method, referred to as EM II hereinafter, a Coriolis liquid flow controller assembly (Bronkhorst mini CORI-FLOWTM M14), as described in section 2.3, was used to introduce methanol into the flow. The CN radicals, in this case, were generated via photodissociation of ICN at 248 nm using a KrF excimer laser (Coherent LPXPro 210) at a laser fluence in the reaction zone of ~ 25 mJ cm⁻². Photodissociation of ICN at 248 nm produces CN

radicals primarily ($\geq 93\%$) in the $\nu=0$ level of the $X^2\Sigma^+$ state [O'Halloran et al., 1987] and rapid rotational relaxation is ensured by frequent collisions due to the high density of the buffer gas.

In both the methods, the LIF/fluorescence signal for the CN radical was then recorded by excitation into the (0,0) band of the $B^2\Sigma^+ \leftarrow X^2\Sigma^+$ electronic transition at 388.3 nm using a dye laser (Laser Analytical Systems, LDL 20505, operating with 0.2% mixture of Exciton Exalite 389 dye in 1,4-dioxane) pumped by the frequency-tripled output of a Nd:YAG laser (Continuum, Powerlite Precision II) at a wavelength of 355 nm. A narrowband interference filter centered at 420 nm (Earling Optics) was used with a photo-multiplier tube (PMT, Thorn EMI 6723) to select the off-resonant fluorescence into the first vibrational level of the ground state via the (0,1) band. As the start of the reaction is marked by the initiation of ICN photolysis, delays in the range of zero to hundreds of μs between the excimer and the LIF laser pulses, both operating at 10 Hz, allowed us to record the time dependence of the CN radical depletion during the reaction. The LIF signals were recorded by a gated integrator and a boxcar averager (Stanford Research Systems). The LIF signal decays were averaged typically 5–10 times.

The absorption cross section of ICN has been reported as $3 \times 10^{-19} \text{ cm}^2$ at 266 nm [Myer and Samson, 1970] and $4.7 \times 10^{-19} \text{ cm}^2$ at 248 nm [Felps et al., 1991]. Given the density of ICN in the gas flow was $\sim 10^{12} \text{ cm}^{-3}$, only 1–2% of the precursor was dissociated at the laser fluence used (35 mJ/cm^2), yielding an estimated maximum CN ($X^2\Sigma^+$) concentration of $1.4 \times 10^{10} \text{ cm}^{-3}$, lower than the concentration

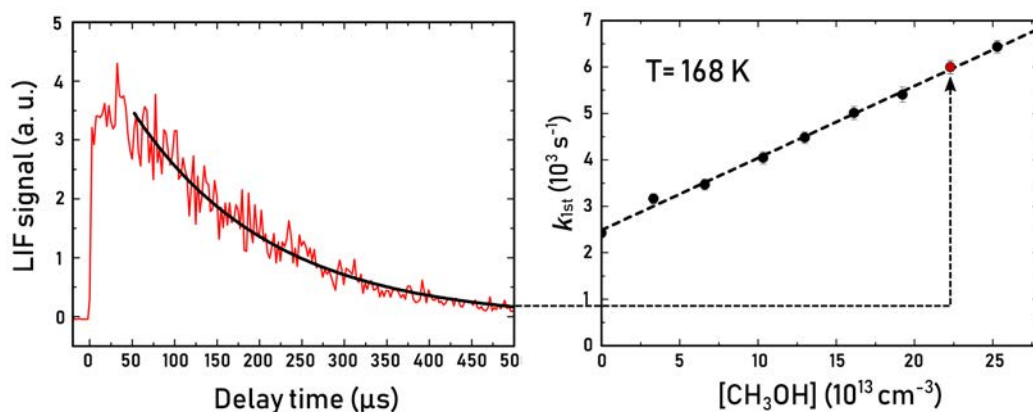


Figure 4.2.1: LIF signal, in red, recorded for the reaction between methanol and CN radical in the left panel for a temperature of 168 K, fit to a single exponential decay function (black solid line). The right panel shows the second-order kinetics plot where the pseudo-first order rate coefficients are plotted against the methanol concentrations. The black line shows the fit yielding the second-order bimolecular rate coefficient. The red point corresponds to the k_{1st} obtained from the decay shown in the left panel at a methanol density of $2.22 \times 10^{14} \text{ cm}^{-3}$.

of methanol used by a factor of at least 100, ensuring pseudo-first order conditions for all the experiments.

4.2.2 Experimental Results

A typical LIF decay trace and second order plot obtained at temperature 168 K are shown in Figure 4.2.1. LIF measurements were also taken at negative time delays to establish a pre-trigger baseline, as seen in Figure 4.2.1. The fit is only made after 10–50 μs so as to allow enough time for rotational relaxation of CN and for the photomultiplier tube to recover from the excimer laser scatter. The nonzero intercept in the second order plot, shown in the right panel of Figure 4.2.1, is due to the loss of CN by diffusion out of the probed beam area and by reaction with the precursor and/or impurities in the buffer gas. As the laser alignment and other external factors may change over periods of days,

Table 4.2.1: Rate Coefficients for the Reaction of the CN Radical with Methanol Measured at Different Temperatures, with the Associated Experimental Parameters^a

T (K)	Buffer gas	Total density (10^{16} cm^{-3})	Range of $[\text{CH}_3\text{OH}]$ (10^{13} cm^{-3})	No. of exp. points	Rate coefficient k ($10^{-11} \text{ cm}^3 \text{ s}^{-1}$)
17 ^c	He	4.89	0.90–6.50	9	7.4 ± 1.2
24 ^b	He	18.30	0.00–8.94	8	5.82 ± 0.63
	He	18.30	0.00–5.81	10	6.82 ± 0.77
					6.1 ± 0.6
36 ^b	He	5.28	0.00–3.64	7	5.4 ± 0.6
53 ^b	Ar	20.20	0.00–6.72	7	3.7 ± 0.5
72 ^b	N ₂	5.79	0.00–6.22	9	3.2 ± 0.4
83 ^c	N ₂	4.88	0.97–9.74	12	3.37 ± 0.84
	N ₂	4.88	0.96–9.01	6	2.96 ± 1.30
					3.3 ± 0.7
97 ^b	Ar	15.45	0.00–12.14	8	3.2 ± 0.4
141 ^b	Ar	6.95	0.00–16.89	8	1.6 ± 0.2
168 ^b	Ar	9.01	0.00–25.28	9	1.6 ± 0.2
294 ^b	N ₂	15.15	1.07–20.92	8	1.49 ± 0.18
296 ^b	N ₂	14.30	0.00–27.46	9	1.45 ± 0.18
296 ^b	N ₂	32.00	0.00–41.46	9	1.48 ± 0.19
296 ^c	N ₂	9.02	10.51–52.57	5	1.72 ± 0.18
296 ^c	N ₂	11.69	6.84–34.19	5	1.66 ± 0.52
					1.6 ± 0.2

^aQuoted uncertainties are calculated using the standard error evaluated from the second order plot, multiplied by the appropriate Student's t factor for 95% confidence, and then combined with an estimated systematic error of 10%. Entries in bold are variance weighted mean values of rate coefficients at the same temperature, calculated using statistical uncertainties only, where the resulting uncertainty is then combined in quadrature with an estimated systematic error of 10%. ^bExperiments performed using EM I. ^cExperiments performed using EM II.

the intercepts of different second-order plots are not necessarily constant. Therefore, we derive the second-order rate coefficient for each temperature from the readings taken on a given day rather than taking all of the k_{1st} values at that temperature. These were fit to exponential functions which yielded the pseudo-first order reaction coefficients, shown in Figure 4.2.1. The second order plots for all the temperatures performed by EM II are provided in the Appendix A3.

Linear plots of the pseudo-first order rate coefficients versus the methanol concentration were then used to calculate the second-order rate coefficient. The non-zero intercept in the second order plot, shown in the lower panel of Figure 4.2.1, is due to the loss of radical concentration from factors such as radical diffusion out of the probed beam area. The procedure was repeated for multiple temperatures using different Laval nozzles. The experimental parameters and rate coefficients measured for each temperature are summarised in Table 4.2.1.

The upper limit for the concentration of methanol is an important experimental constraint imposed due to the formation of methanol dimers, which could interfere with the experimental measurement. The range of methanol densities used to calculate the second-order rate coefficient for each temperature, as mentioned in Table 4.2.1, was based on the tests where first-order rate coefficients were measured over a large range of methanol density. The second-order plots were then carefully observed for if and when the plot deviated from linear behaviour, which would indicate potential formation of dimers. This is shown in Figure 4.2.2, where the pseudo- k_{1st} was measured at 83 K and

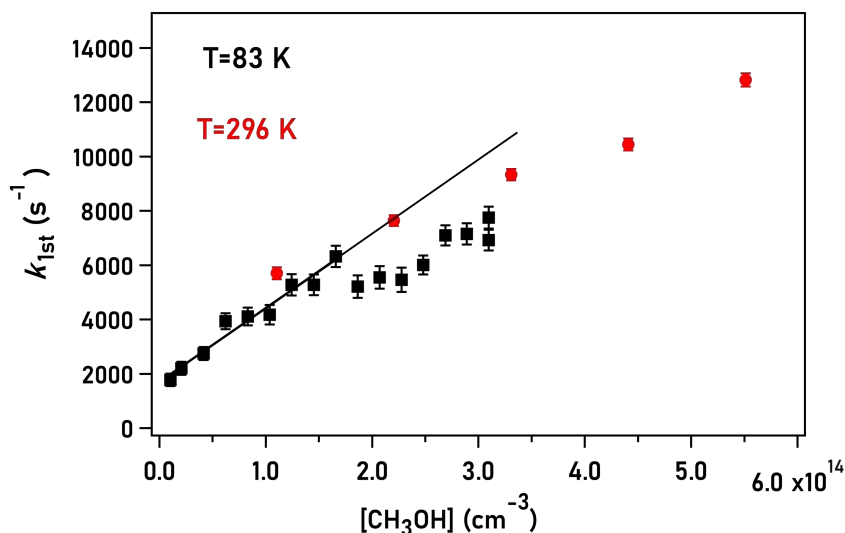


Figure 4.2.2: Measurement of pseudo-first order rate coefficient as a function of methanol as a test for clustering of methanol at 83 K in black, with a buffer gas density of $4.9 \times 10^{16} \text{ cm}^{-3}$ and 296 K in red, with a buffer gas density of $9 \times 10^{16} \text{ cm}^{-3}$. The solid black line for the data at 83 K is used to stress on the deviation from linear behaviour.

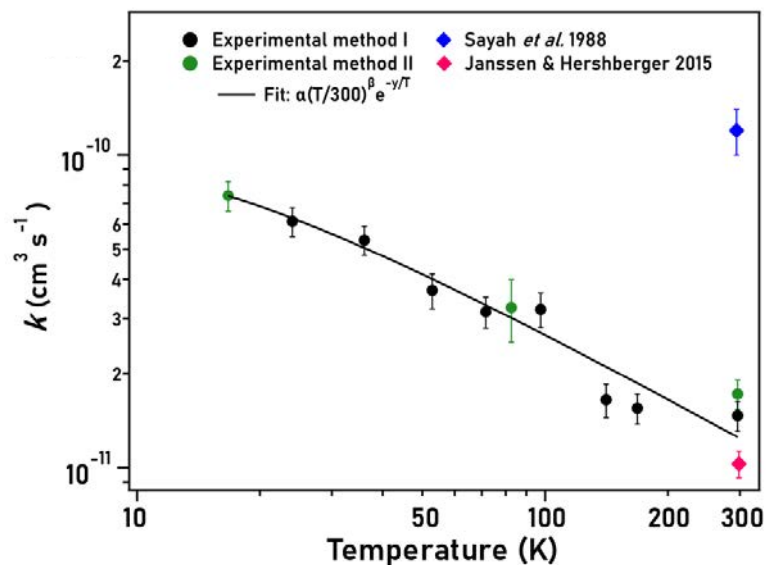


Figure 4.2.3: Rate coefficients for the reaction of CN radicals with methanol displayed on log-log scale as a function of temperature. The filled black circles are the experiments performed with the CRESU setup using EM I and the filled green circles are the experiments using EM II. The blue diamond represents the work of Sayah et al. [1988] and the magenta diamond represents the work of Janssen and Hershberger [2015]. The modified Arrhenius fit: $\alpha(T/300)^\beta e^{-\gamma/T}$ with the fitting parameters: $\alpha = (1.39 \pm 0.06) \times 10^{-11}$, $\beta = -0.40 \pm 0.08$ and $\gamma = -13.6 \pm 3.6$, where the errors are 1σ .

room temperature (296 K) using nitrogen as the buffer gas. The methanol concentration at which deviation from linear-behaviour starts to occur is dependent on the nature of the buffer gas and its temperature and density, occurring at lower values for low temperatures and high densities created by the Laval nozzles. In the Figure 4.2.2, a deviation can be noted above $1 \times 10^{14} \text{ cm}^{-3}$ for 83 K, so all the measurements at temperatures below 100 K were taken at methanol densities below $1 \times 10^{14} \text{ cm}^{-3}$ as shown in Table 4.2.1. No deviation from linear behaviour was seen at room temperature, shown in Figure 4.2.2, even at densities as high as $5 \times 10^{14} \text{ cm}^{-3}$ which is the highest density used for room temperature measurement in this work.

The experimentally measured rate coefficients over the temperature range $T=17\text{--}296 \text{ K}$ are well fit by the modified Arrhenius equation $k(T) = 1.39 \times 10^{-11} (T/300 \text{ K})^{-0.4} \exp(-13.6 \text{ K}/T)$ and are shown in Figure 4.2.3 along with the rate coefficients measured at room temperature from two previous studies.

The experimentally obtained rate coefficient at room temperature was also used to make a semi-empirical prediction as suggested by Faure et al. [2009] based on long range capture theory. The polarizabilities of CN and CH_3OH , $2.26 \times 10^{-24} \text{ cm}^3$ [Faure et al., 2000] and $3.29 \times 10^{-24} \text{ cm}^3$ [David R. Lide, 2004], and their ionization potentials, 13.60 eV and 10.85 eV [David R. Lide, 2004] respectively, were input into the formula mentioned in Chapter 1. The values for $k_{15\text{K}}$ and $k_{40\text{K}}$ along

with the rate coefficient obtained at room temperature ($k_{296\text{K}}$) were then analytically interpolated by the standard 3-parameter modified Arrhenius fit $k(T) = \alpha(T/300\text{ K})^\beta \exp(-\gamma\text{ K}/T)$ and is shown in comparison with the experimental values in Figure 4.2.4.

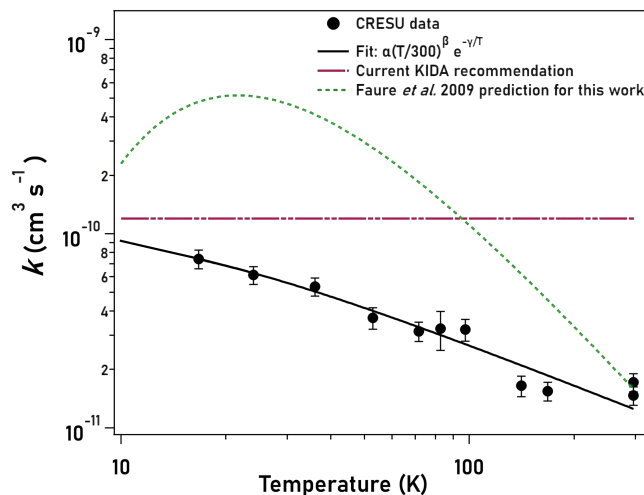
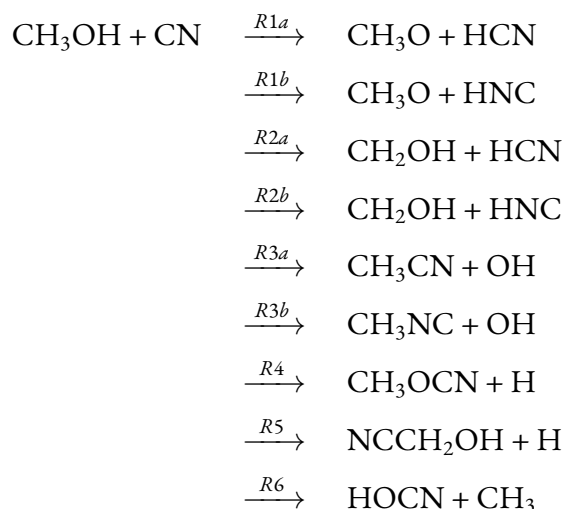


Figure 4.2.4: The CRESU experimental data (black filled circles) fit with a modified Arrhenius equation (black solid line) and the prediction based on the room temperature value from this work using capture theory from Faure et al. [2009] (green dashed line). The current KIDA recommendation for this reaction is shown in pink

4.3 Theoretical Methodology and Results

4.3.1 Theoretical Calculations



Electronic structure calculations were performed to optimise the stationary points for the different channels of the reaction of the CN radical with methanol using Gaussian09 [Frisch et al., 2009]. Only

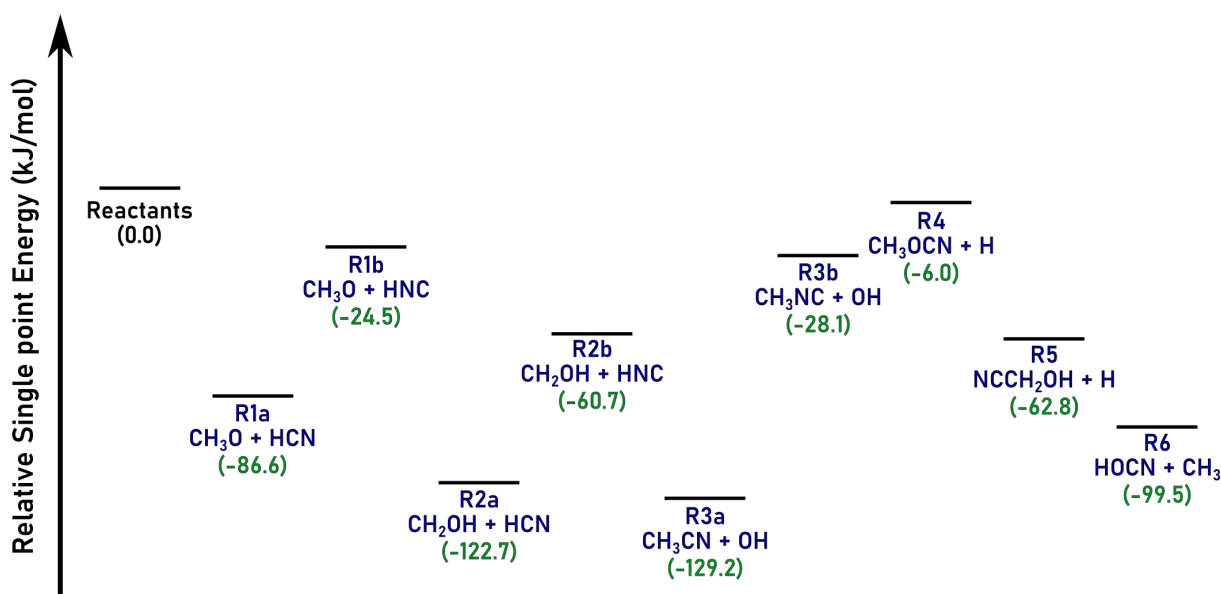


Figure 4.3.1: Relative reaction energy (in kJ mol^{-1}) calculated at CCSD(T)/aug-cc-pVTZ//CCSD/aug-cc-pVTZ for the product channels considered in this work.

exothermic channels were considered as viable reaction channels at such low temperatures and are shown here:

High accuracy single point energies were calculated using CCSD(T)/aug-cc-pVTZ for all the structures (reactants and products) following optimisation of their geometries at CCSD/aug-cc-pVTZ. The difference between the single point energies of the products and reactants was used to calculate the changes in energy for all the reaction channels, and are provided in Figure 4.3.1. The parameters of the optimised structures are given in Appendix A7.1. The standard reaction enthalpy $\Delta H_r^\circ(298.15 \text{ K})$ for each channel was also calculated, as explained by Ochterski [2000], using the composite CBS-QB3 method. Attempts to locate the transition states and possible complexes for obtaining a complete potential surface were made using DFT methods- M062X and B3LYP levels of theory.

Table 4.3.1: Reaction Enthalpies $\Delta H_r^\circ(298.15 \text{ K})$, in kJ mol^{-1} , Calculated for Each Channel Using CBS-QB3 Compared with the Enthalpy Values Calculated from the Values Provided in the Active Thermochemical Table Ver. 1.22 e74a

	R1a	R1b	R2a	R2b	R3a	R3b	R4	R5	R6
CBS-QB3	-90.9	-31.2	-126.0	-66.3	-127.6	-28.1	-23.2	-76.6	-111.0
ATcT (1.22e)	-99.3	-36.2	-137.5	-74.4	-138.4	-35.2			-118.4

4.3.2 Theoretical Results

The reaction enthalpies $\Delta H_r^\circ(298.15 \text{ K})$ were obtained at CBS-QB3, which is a composite method used widely [Ess and Houk, 2005, Guner et al., 2003, Somers and Simmie, 2015] to obtain accurate energies of molecules and radicals. The values obtained were compared with enthalpy values calculated using the active thermochemical table (ATcT) [Ruscic and Bross, 2019, Ruscic et al., 2004, 2005] and are shown in Table 4.3.1. ATcT has been developed by Ruscic and coworkers and is based on statistical analysis to produce a self-consistent thermochemical network. The reaction enthalpies for the various channels follow the same trend across the different methods, with channel R3a being the most exothermic, followed by R2a, R6, and R1a.

4.4 Discussion

Figure 4.2.3 shows the experimentally obtained values of the rate coefficient from this work as a function of temperature, compared with the two previous studies measured at room temperature. The CRESU results have been fit to the modified Arrhenius equation and show a dependence $k(T) = 1.26 \times 10^{-11} (T/300 \text{ K})^{-0.7} \exp(-5.4 \text{ K}/T) \text{ cm}^3 \text{ s}^{-1}$. The work by Sayah et al. [1988] at room temperature yielded a value of $1.2 \times 10^{-10} \text{ cm}^3 \text{ s}^{-1}$, which was different from the value obtained here using EM I by an order of magnitude. Following this, a secondary method for CN radical generation and for creating methanol/buffer gas mixtures (EM II) was used to confirm the measurements made using EM I (particularly those at room temperature), and to reduce the likelihood of systematic errors. A room temperature rate coefficient was measured using EM II that agrees within error to that obtained using EM I. The current results are further supported by the work of Janssen and Hershberger [2015] who obtained a rate coefficient of $(1.03 \pm 0.10) \times 10^{-11} \text{ cm}^3 \text{ s}^{-1}$ at room temperature, which is in reasonably good agreement with the value reported here of $(1.6 \pm 0.2) \times 10^{-11} \text{ cm}^3 \text{ s}^{-1}$. It is unclear why the value measured by Sayah et al. [1988] is faster than these three essentially independent measurements by an order of magnitude.

The difference between the ionization potential of methanol and the electron affinity of CN radical is 6.98 eV, which is well below the 8.75 eV semi-empirical limit proposed by Ian Smith and colleagues [Smith et al., 2006] for the existence of a non-submerged barrier to reaction. This suggests the reaction between the CN radical and methanol will be rapid even at low temperatures, with a rate coefficient greater than $\sim 10^{-10} \text{ cm}^3 \text{ s}^{-1}$ at 10 K, consistent with what was observed in this study. Faure et al.

[2009] provided a semi-empirical model which combines room temperature kinetics data with a long-range capture method to predict rate coefficients for neutral–neutral reactions at low temperature. For reactions with rate coefficients greater than $10^{-11} \text{ cm}^3 \text{ s}^{-1}$ at room temperature, a fit ($k(T) = \alpha(T/300 \text{ K})^\beta \exp^{-\gamma/T}$) is proposed to be valid at temperatures as low as 5 K. A plot obtained using the model is shown in Figure 4.2.4. This method, however, over-predicts the rate coefficient, suggesting that the reaction is not controlled by long-range attractive forces even at the lowest temperatures where measurements have been performed. It appears likely that submerged barriers are playing an important role in determining the low temperature reactivity.

The reaction enthalpies $\Delta H_r^\circ(298.15 \text{ K})$ obtained using CBS-QB3 and ATcT, shown in Table 4.3.1, show a reasonable agreement. The reaction enthalpies for R4 and R5 could not be calculated from ATcT due to missing values for NCCH_2OH and CH_3OCN in the active thermochemical table. The reaction channels R1a, R2a, R3a, and R6 are the most thermodynamically favored product channels of the studied reaction. Similar trends were also found from the reaction energies calculated using the difference between the single point CCSD(T)/aug-cc-pVTZ energies of the reactants and products. The HNC channels for both R1 and R2 were found to have lower stabilisation energies compared to the HCN analogues, which is expected as HCN is more stable than HNC. Preliminary calculations performed at B3LYP/aug-cc-pVTZ to identify the saddle points for the reaction channels suggest that the channels R3a, R3b, and R4 have very high (zero-point corrected) barriers of 83.6, 134.7, and 227.9 kJ mol^{-1} , respectively, making them unlikely to take place in low temperature environments. Preliminary calculations for the complexes for the reaction channels R1a and R2a were also optimised at (U)-M062X/aug-cc-pVDZ. Only a single (submerged) transition state, however, could be located for channel R1a at (U)-M062X/cc-pVTZ. Intrinsic reaction coordinate calculations are necessary, however, to confirm the potential surface along the same.

To the best of the author's knowledge, this is the first set of kinetics data published for this reaction at low temperatures, which makes it useful for atmospheric and astrochemical models. The Kinetics Database for Astrochemistry, KIDA (homepage: <http://kida.obs.u-bordeaux1.fr/>, accessed August 2021) [Talbi and Wakelam, 2011, Wakelam et al., 2012], currently uses the rate coefficient measured by Sayah et al. [1988] over the whole temperature range of 10–300 K, which is significantly different from what is observed experimentally both here and by Janssen and Hershberger [2015]. Furthermore, the reaction is assumed to proceed in equal ratios via channels 1a ($\text{CH}_3\text{O} + \text{HCN}$) and 2a ($\text{CH}_2\text{OH} + \text{HCN}$). Janssen and Hershberger measured the CH_2OH channel as the dominant reaction product at room temperature, with only 8% into the methoxy channel, based on isotopic experiments. Models

using the room temperature rate coefficient reported in KIDA, therefore, over-predict both the rate of CH_3O formation and its yield relative to the CH_2OH isomer. The product branching ratios for this reaction have not been measured below room temperature, so it is unknown whether the reaction will be a significant source of methoxy (CH_3O) under dense cloud conditions.

Other destruction routes for methanol with the OH radical [Ocaña et al., 2019] and the $\text{C}(^3P)$ [Shannon et al., 2014] radical have been reported to have rate coefficients approaching $10^{-10} \text{ cm}^3 \text{ s}^{-1}$ at 10 K. A similar rate coefficient for the reaction of CN with methanol further establishes the role of this reaction as a significant destruction route for methanol in cold interstellar clouds where both these species have been detected. The room temperature rate coefficient reported here is an order of magnitude lower than the current value in KIDA, suggesting that astrochemical networks involving warm gas temperatures (e.g., hot cores models) may over-predict the destruction of methanol. Use of the current KIDA-recommended rate coefficients may also lead to over-prediction of the abundance of the methoxy radical, which is thought to be a precursor to more complex organic molecules like dimethyl ether and methyl formate [Balucani et al., 2015]. Astrochemical models assuming the current KIDA rate coefficients ($6.0 \times 10^{-11} \text{ cm}^3 \text{ s}^{-1}$ into both the CH_3O and CH_2OH channels) should be updated to reflect these new laboratory data. Janssen and Herschberger's [Janssen and Herschberger, 2015] room temperature branching ratio should be used at $T < 300 \text{ K}$ until low temperature measurements have been made.

4.5 Conclusion

The CRESU technique coupled with PLP–LIF has been employed to show that the reaction between the CN radical and methanol has a negative temperature dependence in the temperature range 17–296 K, well-characterised by the modified Arrhenius equation $k(T) = 1.29 \times 10^{-11} (T/300 \text{ K})^{-0.7} \exp(-5.5 \text{ K}/T)$. The present measurements vary significantly from the room temperature value of Sayah et al. [1988] which is currently the value recommended by the KIDA database [Talbi and Wakelam, 2011] for all temperatures between 10 and 300 K. While this experiment has yielded the overall rate coefficient for the reaction of the CN radical with methanol, the PLP–LIF technique is unable to provide product-specific rate coefficients or branching ratios. Electronic structure calculations revealed that the reaction channels involving CN substitution have high barriers, making them unlikely to occur at low temperatures. The H atom abstraction routes are likely to be the dominant reaction channels under cold ISM conditions, forming the isomers CH_2OH and CH_3O .

More calculations are needed to locate and confirm the submerged saddle points for other channels for the reaction of the CN radical with methanol, followed by theoretical kinetics calculations. The new setup integrating chirped-pulse broadband microwave spectroscopy with continuous flow CRESU developed in Rennes, as described in Chapter 2, has the ability to identify the products from this reaction and will provide the branching ratios for the reaction channels at low temperatures. The current sensitivity of this setup, however, is limited currently especially for radical products. The reaction between methanol and the CN radical is an interesting system to be studied with this setup to explore the distribution between the CH_3O and CH_2OH channels given their relevance to astrochemistry.

Chapter 5

Low temperature reaction kinetics of CN radical with aromatic molecules: benzene and toluene

Modified from: Cooke, I. R., Gupta, D., Messinger, J. P., & Sims, I. R. 2020, *Astrophys J*, 891, L41 & Messinger, J. P., Gupta, D., Cooke, I. R., Okumura, M., & Sims, I. R. 2020, *J Phys Chem A*, 124, 7950.

The work on CN + toluene also appears in “Messinger, J. P. H. (2021). *Spectroscopy and Kinetics of Atmospheric and Astrochemical Reactions* (Doctoral dissertation, California Institute of Technology”

5.1 Introduction

This work was motivated by the discovery of benzonitrile (C_6H_5CN) in a nearby cold molecular cloud (Taurus, TMC-1), which marked the first detection of an aromatic species in the interstellar medium by radio astronomy [McGuire et al., 2018]. Benzonitrile has been proposed as a tracer of benzene, which may be a low-temperature precursor to more complex polycyclic aromatic hydrocarbons (PAHs). PAHs are widely accepted to exist in the ISM owing to their characteristic infrared emission features. The recent discovery of cyano-naphthalenes [McGuire et al., 2021] is the only specific detection within this class of molecules with radio astronomy. However, due to their structural similarities, the exact chemical origins of the IR bands remain elusive [Lovas et al., 2005]. It has been

suggested that PAHs make up as much as 10–25% of interstellar carbon budget [Chiar et al., 2013, Dwek et al., 1997]. Understanding the origin of PAHs can help answer fundamental questions about their role in forming interstellar dust as well as potentially prebiotic material that may be incorporated into new planetary systems.

The cyclization of benzene (or the phenyl radical), the smallest aromatic ring, has been suggested as a bottleneck to the formation of these large aromatics at low temperatures [Cherchneff et al., 1992, Kaiser et al., 2015, Tielens and Charnley, 1997]. However, benzene itself is difficult to detect as it has no permanent dipole moment and hence is invisible to radio astronomy. While benzene has been detected in the ISM through infrared observations of a single weak absorption feature (the ν_4 bending mode near $14.85 \mu\text{m}$) in a handful of sources [Cernicharo et al., 2001, Kraemer et al., 2006, Malek et al., 2011], absorption due to Earth's atmosphere limits its observation to bright IR-sources using space-based infrared telescopes (e.g. the Spitzer Space Telescope and the Infrared Space Observatory). Instead, it was suggested that benzonitrile (dipole moment = 4.5 D) might be used as a chemical proxy for benzene in the cold, starless ISM, as it is expected to form via the barrierless, exothermic neutral-neutral reaction between CN and benzene [Trevitt et al., 2010, Woods et al., 2002]. If linked to benzene, benzonitrile may be used to constrain the early stages of the aromatic chemistry in the ISM.

CN radical has long been known to be abundant in the interstellar medium (ISM), where it was first detected in 1940s [Adams, 1941, McKellar, 1940], and in the atmosphere of Titan, one of Saturn's moons, where it leads the formation of nitrile compounds, including $\text{C}_2\text{H}_3\text{CN}$ and HC_3N [Loison et al., 2015, Wilson and Atreya, 2004, Yung et al., 1984]. At the low temperatures found in these environments, reactions between CN and other compounds, as has been shown for many hydrocarbons [Sims et al., 1993], are very relevant and thus must be included in gas-phase models. Reactions between CN and hydrocarbons can proceed through either an abstraction or an addition mechanism [Cooke and Sims, 2019] and a number of cyano-containing molecules linked to these reactions have been found in ISM [Belloche et al., 2014, Broten et al., 1978].

On Titan, benzene has been detected by Cassini Ion Neutral Mass Spectrometer (INMS) [Waite et al., 2005], along with other aromatics like toluene [Magee et al., 2009] which has been detected in its upper atmosphere, with models suggesting that it has a high abundance in the lower atmosphere as a product of the fast association reaction between C_6H_5 and CH_3 [Loison et al., 2019]. The temperature ranges from 80-200 K in Titan's atmosphere, and given the presence of CN on Titan,

the reactions of CN with both benzene and toluene are also of interest in this temperature range.

Rate coefficients for the reaction between CN and benzene have been previously measured using PLP–LIF at 295, 165 and 105 K by Trevitt et al. [2010], who found $k(T)$ to be relatively constant, ranging from $3.9\text{--}4.9 \times 10^{-10} \text{ cm}^3 \text{ s}^{-1}$. They attribute the lack of temperature dependence to a reaction mechanism that proceeds without an energy barrier in the entrance channel and likely forms an addition complex; which is supported by theoretical calculations of the reaction potential energy surface [Balucani et al., 1999, Lee et al., 2019, Woon, 2006]. In addition to the overall rate coefficients, Trevitt et al. [2010] measured the products of the reaction at room temperature using synchrotron VUV photoionization mass spectrometry.

Here, we report rate coefficients for the reaction of benzene with the CN radical over a wide temperature range of 15–295 K using the CRESU technique. These rate coefficients can be input into astrochemical models to assess the importance of the reaction as a production route for benzonitrile and therefore the robustness of benzonitrile as a chemical proxy for benzene at various temperatures in the ISM.

Other aromatic nitriles may also serve as proxies for undetected aromatic compounds in the ISM, as the addition of the cyano moiety gives these compounds large dipole moments making them visible to radio astronomy. The identification of additional specific aromatic compounds would significantly constrain models of PAH formation in the ISM. However, little is known about the reaction of CN with other aromatic molecules and whether these reactions also result in the formation of nitrile compounds.

Trevitt et al. [2010] also studied the reaction between CN and toluene ($\text{C}_6\text{H}_5\text{CH}_3$), a benzene ring with a methyl substitution, which remains the sole measurement of the rate coefficient for this reaction. They studied this reaction at 105 K and found a rate coefficient of $(1.3 \pm 0.3) \times 10^{-10} \text{ cm}^3 \text{ s}^{-1}$ using pulsed laser photolysis–laser induced fluorescence (PLP–LIF) measurements in conjunction with a pulsed Laval nozzle. This rate coefficient is a factor of 3 lower than the rate coefficients measured for the CN + benzene reaction measured in the same study, suggesting that the structure of aromatic molecules can play a significant role in the reaction rates. Furthermore, they observed non-exponential decays of CN at room temperature in the presence of toluene and were therefore unable to measure a rate coefficient, in contrast with their measurements of benzene under the same conditions. They suggested that this could be due to dissociation of the products back to the CN + toluene reactants, and that further studies would be necessary to better understand these results.

The difference between the rate coefficients of the CN + benzene and CN + toluene reactions would seem to suggest that the structure of an aromatic compound can play a role in the reaction dynamics. This highlights the importance of investigating whether nitrile compounds may be formed from the reactions of CN with larger, more complex aromatic compounds, and of verifying the reliability of using cyano-substituted compounds as a proxy for larger aromatic species. To that end, we have conducted measurements of the CN + toluene reaction rate coefficient between 16 and 294 K to gain further insight into this reaction, especially at the low temperatures relevant to the ISM and Titan. Furthermore, we have computed stationary points on the potential energy surface (PES) of the CN + toluene reaction to better understand the possible products and mechanism of this reaction.

5.2 Experimental Methodology and Results

5.2.1 Experimental Measurements

The kinetics of the reaction between the CN radical, and benzene and toluene was measured using Pulsed-Laser Photolysis-Laser Induced Fluorescence (PLP-LIF). The low gas temperatures were achieved using the CRESU technique, which has been described in detail in Chapter 2. A dilute mixture (typically <0.1%) of benzene (Sigma Aldrich, Anhydrous 99.8%)/toluene (Sigma-Aldrich, 99.9%) and ICN, the CN radical precursor used in this set of experiments, in a buffer gas (He (99.995%), Ar (99.998%), or N₂ (99.995%); Air Liquide) was expanded isentropically through a Laval nozzle to generate a cold supersonic flow. A wide range of temperatures were obtained by careful manipulation of the physical dimensions of the nozzle, the buffer gas used, and the flow conditions/pumping capacity.

A Controlled Evaporation and Mixing system (Bronkhorst CEM) was used to introduce the required reactant (benzene/toluene) into the flow, described in detail in section 2.4.1. The CN radicals were generated by photodissociation of ICN (Acros Organics, 98%) at 248 nm and the LIF/fluorescence signal from the CN radical was recorded at 10 Hz, similar to as explained in subsection 4.2.1.

The experiments were performed under pseudo-first order conditions with benzene/toluene in excess. The UV absorption cross-section of ICN at 248 nm has been measured as $4.7 \times 10^{-19} \text{ cm}^2$ Felps et al. [1991]. For the density of ICN used in the gas flow ($\sim 10^{12} \text{ cm}^{-3}$), there is an estimated CN ($X^2\Sigma^+$) concentration of $< 1 \times 10^{10} \text{ cm}^{-3}$, which is lower than the concentration of benzene/toluene by at least a factor of one hundred. The LIF signal decays were recorded for 140–200 μs following

the firing of the photolysis laser to capture the fast CN decay in the presence of benzene. LIF measurements were also taken at negative time delays ($5 \mu\text{s}$ before the excimer laser fires) to establish a pre-trigger baseline. a single exponential decay function was fit to the LIF data after $\geq 10 \mu\text{s}$ to allow enough time for rotational relaxation of CN and for the photomultiplier tube to recover from scatter due to the excimer laser. The LIF signals were averaged typically 5 times and fit to single exponential decays starting $\geq 10 \mu\text{s}$ after photolysis to allow for rotational thermalization of CN, yielding pseudo-first order rate coefficients, k_{1st} . The LIF decay traces were recorded for the CN decay in the presence of at least eight different concentrations of benzene/toluene. Plots of k_{1st} versus the reactant (benzene/toluene) concentration were the fit with a weighted linear regression to calculate the second-order rate coefficient. The procedure was repeated for various temperatures using different Laval nozzles. The experimental parameters and the measured rate coefficients with their uncertainties are summarized in Table 5.2.1 for CN + benzene and in Table 5.2.2 for CN + toluene.

5.2.2 Experimental Results

5.2.2.1 CN + Benzene

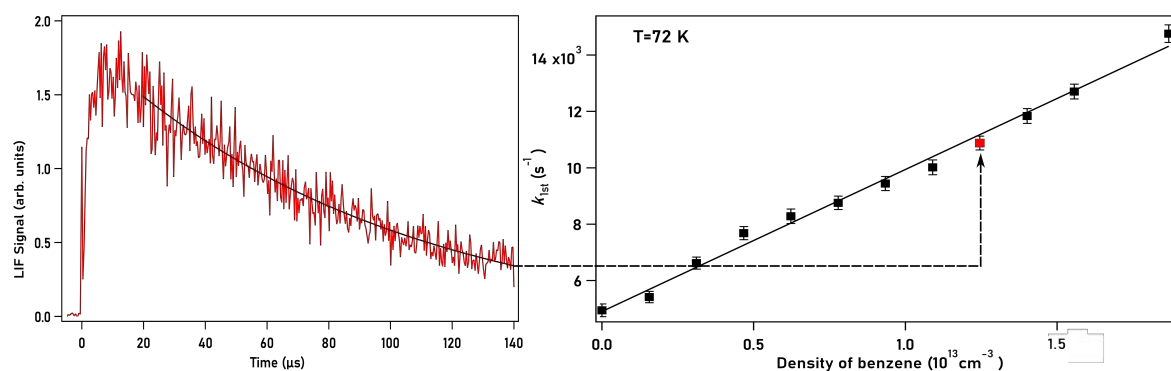


Figure 5.2.1: Kinetics data obtained using PLP–LIF in continuous CRESU flows for a temperature of 72 K. The left panel shows CN radical LIF signal decay of $\text{CN}(B^2\Sigma^+ \rightarrow X^2\Sigma^+)$ at a benzene density of $1.6 \times 10^{13} \text{ cm}^{-3}$ fit with a single exponential decay function (black line). The right panel shows the second–order kinetics plot where the pseudo-first order rate coefficients are plotted against the benzene concentration. The black line shows the fit yielding the second-order bimolecular rate coefficient. The red point corresponds to the k_{1st} obtained from the decay shown in the left panel.

Figure 5.2.1 shows an example CN LIF decay trace and second order kinetics plot, obtained at 72 K. The second order plots for all the temperatures, as listed in Table 5.2.1, are provided in the Appendix. The non-zero intercept observed in the second order plots (e.g. in the right panel of Figure 5.2.1) is due to other losses of CN, a combination of CN diffusion out of the probed beam area and reaction

with ICN and/or other impurities in the buffer gas.

Table 5.2.1: Rate coefficients for the reaction of the CN radical with benzene measured at different temperatures, with the associated experimental parameters^a

T (K)	Buffer gas	Total density (10^{16} cm^{-3})	Range of $[\text{C}_6\text{H}_6]$ (10^{12} cm^{-3})	No. of exp. points	Rate coefficient k ($10^{-10} \text{ cm}^3 \text{ s}^{-1}$)
15	He	5.02	2.19–19.7	13	5.45 ± 0.90
			2.19–17.5	14	5.36 ± 0.86
					5.4 ± 0.6
17	He	4.85	2.03–14.2	13	4.5 ± 0.7
24	He	4.85	2.08–22.8	11	5.1 ± 0.7
36	He	5.31	1.48–14.8	11	5.37 ± 0.70
		5.27	1.47–20.6	14	5.49 ± 0.94
		5.27	1.47–14.7	11	5.18 ± 0.77
					5.3 ± 0.6
72	He	6.01	1.54–24.6	14	5.47 ± 0.63
		6.01	3.00–16.5	12	5.12 ± 0.73
					5.4 ± 0.6
83	N_2	4.61	2.06–16.5	8	3.89 ± 0.70
			2.04–24.6	12	3.85 ± 0.62
					3.9 ± 0.4
110	Ar	2.71	1.66–19.9	11	4.2 ± 0.6
200	N_2	5.27	2.52–20.2	13	3.7 ± 0.8
294	N_2	7.04	1.52–76.1	9	3.47 ± 0.40
293	N_2	9.78	1.53–76.6	9	3.45 ± 0.39
		18.5	2.21–69.6	8	3.33 ± 0.54
293	He	5.27	6.25–37.5	9	3.98 ± 0.57
	He	6.92	2.03–81.3	10	3.35 ± 0.46
	He	9.39	2.16–63.4	6	4.08 ± 0.55
295	He	9.10	1.50–74.8	9	4.02 ± 0.46
					3.6 ± 0.4

^a Quoted uncertainties are calculated using the standard error evaluated from the second order plot, multiplied by the appropriate Student's t factor for 95% confidence, and then combined in quadrature with an estimated systematic error of 10%. Entries in bold are the variance weighted mean values of rate coefficients measured at the same temperature, where the standard error on the mean is combined in quadrature with an estimated systematic error of 10%.

The number of points and the range of benzene concentration used for each nozzle are shown in Table 5.2.1. The upper limit for the concentration of benzene is determined by an experimental constraint imposed due to the formation of benzene dimers, which could cause the rate coefficients to be underestimated. This effect is particularly significant at low temperatures, where dimerization occurs at much lower reactant concentrations than at room temperature. [Hamon et al., 2000] measured the rate coefficients for dimerization of benzene in helium. They found that the onset of significant complex formation at 16 K occurred when $[\text{C}_6\text{H}_6] \geq 1 \times 10^{14} \text{ cm}^{-3}$ which is consistent

with our measurements of the pseudo- k_{1st} as a function of benzene densities, as shown in Figure 5.2.2. Based on this, we obtain the bimolecular rate coefficients by fitting benzene concentrations $< 2.5 \times 10^{13} \text{ cm}^{-3}$, except for at room temperature, where the fit concentrations are $< 1 \times 10^{14} \text{ cm}^{-3}$.

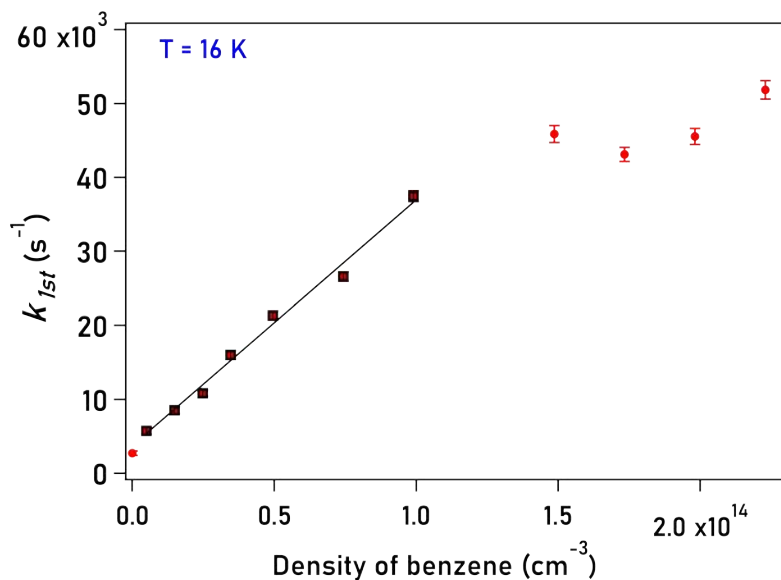


Figure 5.2.2: Measurement of pseudo-first order rate coefficient as a function of benzene density as a test for clustering of benzene at 16 K. The black hollow boxes show the measurements show a linear behaviour and could be used for the linear fit (black line) to provide the second-order rate coefficient at this temperature. (These test measurements were not used in the final analysis; a different nozzle with a lower density was used for the low temperature (15 K) measurements.)

Care was taken to ensure photodissociation of C_6H_6 was negligible during the kinetics experiments

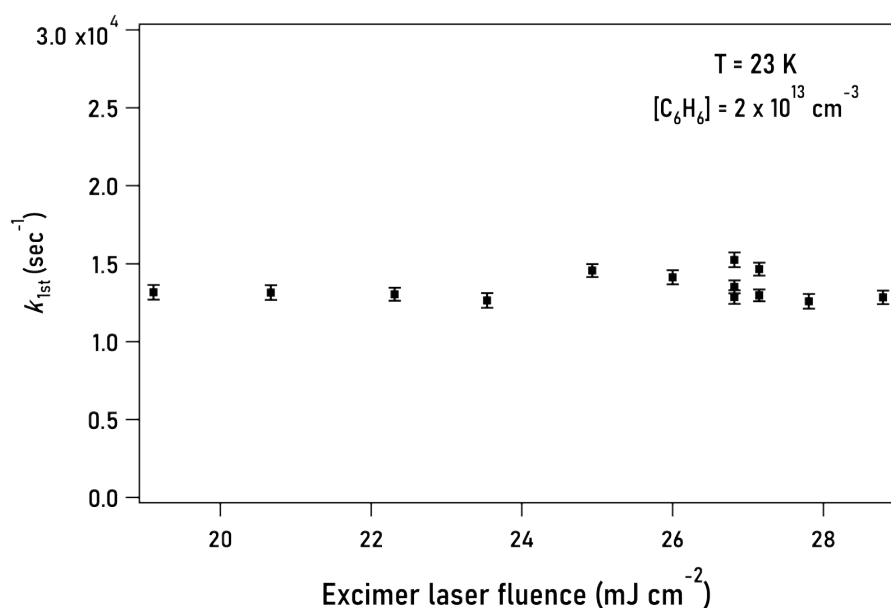


Figure 5.2.3: The pseudo- k_{1st} for the reaction between CN and benzene at 23 K with $[\text{benzene}]$ at $2 \times 10^{13} \text{ cm}^{-3}$ shown as a function of varying excimer laser (248 nm) fluence.

as reaction between the phenyl radical and CN is expected to be rapid. The absorption cross section for benzene at 248 nm is $1.4 \times 10^{-19} \text{ cm}^2$ [Nakashima and Yoshihara, 1982] yielding a maximum phenyl radical concentration of less than 10^{10} cm^{-3} at the laser fluence used of $\sim 25 \text{ mJ cm}^{-2}$. [Kovács et al., 2009] have suggested the possibility of two-photon absorption via the $^1B_{2u}$ state, leading to dissociation of benzene; they found a high total absorption cross section for the second photon of $2.8 \times 10^{-17} \text{ cm}^2$. For the highest benzene concentration used here ($\sim 1 \times 10^{14} \text{ cm}^{-3}$) and with the laser fluence used, all photolysis of benzene occurs by two-photon dissociation. The resulting phenyl radical concentration is too low ($< 1\%$) to affect the kinetics of the reaction. The concentrations of the phenyl radical are even lower in reality due to quenching of the excited $^1B_{2u}$ state by the buffer gas. To experimentally verify this, we measured the first-order rate coefficient at $T = 23 \text{ K}$ and $[\text{C}_6\text{H}_6] = 2 \times 10^{13} \text{ cm}^{-3}$ while varying the excimer laser fluence over the range of 19–30 mJ cm^{-2} and found that k_{1st} remained constant, as shown in Figure 5.2.3. This behaviour showed that at the benzene concentrations and the laser fluence (25 mJ cm^{-2}) used in this work, the effect of benzene photodissociation on the reaction kinetics was not significant.

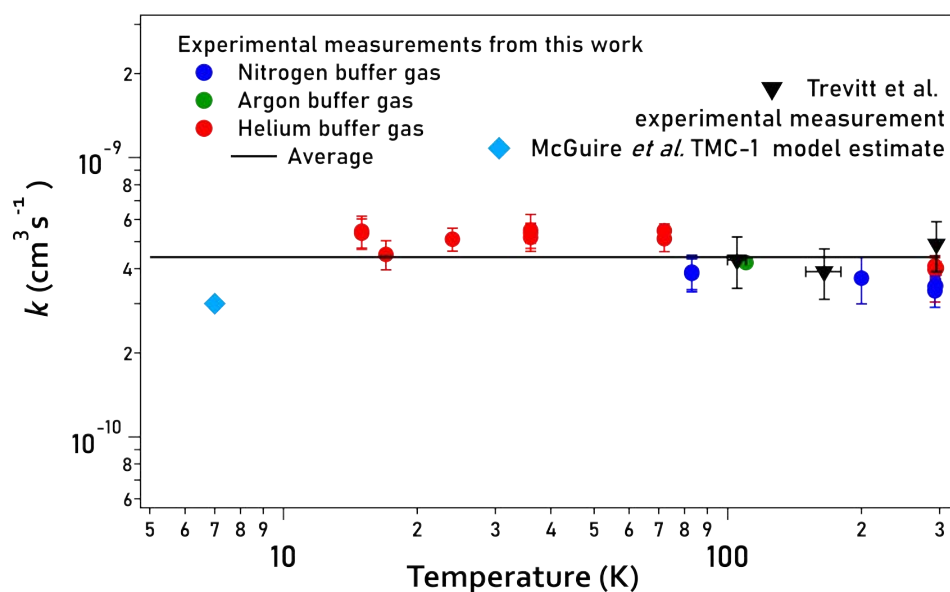


Figure 5.2.4: Rate coefficients for the reaction of the CN radical with benzene as a function of temperature displayed on a log-log scale. The circles are the data taken here using the continuous CRESU in Rennes, with helium buffer gas in red, nitrogen in blue and argon in green. The black diamonds are the data taken by Trevitt et al. [2010] using a pulsed CRESU. The cyan triangle shows the estimated rate coefficient used by McGuire et al. [2018] to model the abundance of benzonitrile in TMC-1 at 7 K. The black horizontal line shows the mean value over the temperature range.

The second-order rate coefficients were derived from the slopes of the weighted linear-least squares regressions to the 2nd-order kinetics plots and are shown in Table 5.2.1 along with their uncertainties,

which are calculated using 95% confidence limits calculated by multiplying the standard error by the appropriate factor from the two-sided Student's t -distribution, and combined with an estimated 10% systematic error. The measured rate coefficients over the temperature range $T = 15$ – 295 K are shown in Figure 5.2.4 along with the rate coefficients measured by Trevitt et al. [2010] and the rate coefficient used by McGuire et al. [2018] to model the abundance of benzonitrile in TMC-1. Within the experimental uncertainty the measured rate coefficient for the $\text{CN} + \text{C}_6\text{H}_6$ reaction remains essentially constant between 15–295 K. The weighted average of all of the rate coefficients between 15–295 K is $(4.4 \pm 0.2) \times 10^{-10} \text{ cm}^3 \text{ s}^{-1}$.

5.2.2.2 CN + Toluene

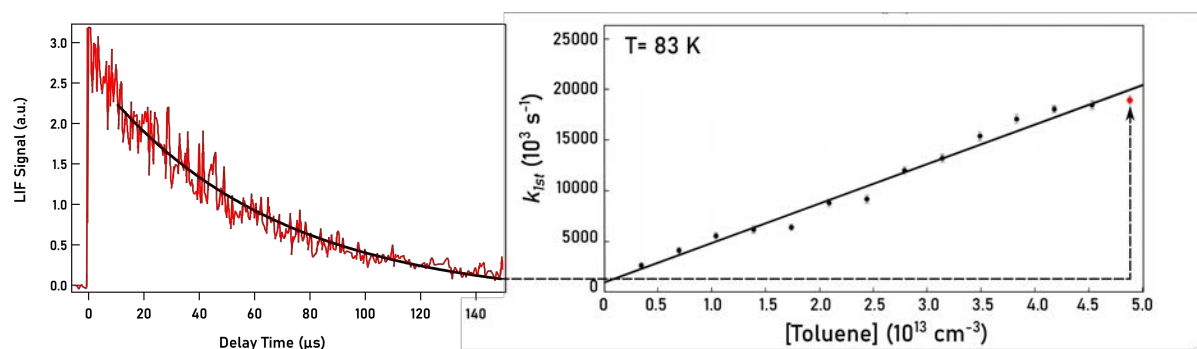


Figure 5.2.5: Kinetics data for the $\text{CN} + \text{toluene}$ obtained using PLP–LIF in continuous CRESU flows for a temperature of 83 K. The left panel shows LIF signal decay of $\text{CN}(B^2\Sigma^+ \rightarrow X^2\Sigma^+)$ at a toluene density of $4.8 \times 10^{13} \text{ cm}^{-3}$ fit with a single exponential decay function (black line). The right panel shows the second-order kinetics plot where the pseudo-first order rate coefficients are plotted against the toluene concentration. The black line shows the fit yielding the second-order bimolecular rate coefficient. The red point corresponds to the k_{1st} obtained from the decay shown in the left panel.

LIF decay of CN for the reaction between CN and toluene at 83 K and the second-order plot can be seen in Figure 5.2.5. The non-zero intercepts seen on the second-order plots, similar to what was seen in Figure 5.2.1, arise from the loss of CN via side chemistry and diffusion out of the region probed by LIF. Results of the experiments between 15 and 294 K are shown in Table 5.2.2 and Figure 5.2.6. At least nine points with varying toluene concentrations were taken for each measurement under pseudo-first-order conditions, with toluene in excess. Formation of toluene dimers at high toluene densities, especially at the lowest temperatures, can lead to wrong results for the kinetics. This therefore imposes an upper limit on the toluene concentration used in experiments in order to minimize any effect of the reaction between CN and toluene dimers on our measurements. This effect can be traced by the non-linear behavior in the second-order plots, as was shown for the case of benzene in Figure 5.2.2. Similar tests were performed for the case of toluene and the toluene density in all the measurements

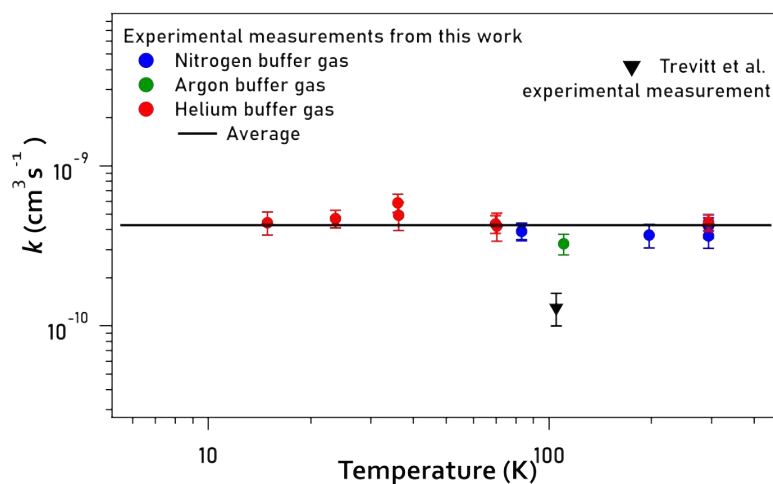


Figure 5.2.6: Rate coefficients for the reaction of the CN radical with toluene as a function of temperature displayed on a log-log scale. The circles are the data taken here using the continuous CRESU in Rennes, with helium buffer gas in red, nitrogen in blue and argon in pink. The black triangle is the datum taken by Trevitt et al. [2010] using a pulsed CRESU. The black horizontal line shows the mean value over the temperature range.

was $< 5 \times 10^{13} \text{ cm}^{-3}$, except at room temperature where the highest toluene density used was $9 \times 10^{13} \text{ cm}^{-3}$.

To test whether the photolysis of toluene at 248 nm affected our measurements, experiments were conducted varying the power of the excimer laser at 110 K, with $[\text{toluene}] = 9 \times 10^{12} \text{ cm}^{-3}$. We found no significant change in the measured pseudo first-order rate coefficients k_{1st} as a function of our laser power, as shown in Figure 5.2.7. With the excimer laser fluence of 25 mJ cm^{-2} and the toluene absorption cross section at 248 nm of $2.9 \times 10^{-19} \text{ cm}^2$ [Koban et al., 2004], we expect roughly 1% of the toluene to photolyze if the photolysis quantum yield is 1, which should not measurably affect the

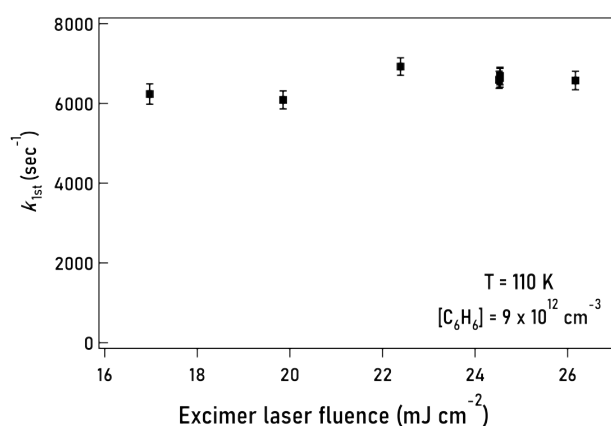


Figure 5.2.7: The pseudo- k_{1st} for the reaction between CN and toluene at 110 K with $[\text{toluene}]$ at $9 \times 10^{12} \text{ cm}^{-3}$ shown as a function of varying excimer laser (248 nm) fluence.

observed rate coefficients. Similar to benzene, it has also been suggested that two-photon absorption at 248 nm can photolyze toluene to form H atoms among other potential processes [Kovács et al., 2009], with the total absorption cross section for the second photon experimentally determined to be $1.7 \times 10^{-17} \text{ cm}^2$. For the highest toluene concentrations used ($\sim 1 \times 10^{14} \text{ cm}^{-3}$), we estimate at most $4.8 \times 10^{11} \text{ cm}^{-3}$ of toluene undergoes two-photon absorption, though it is likely much less than that, as discussed in greater detail in the discussion section 5.4.1, and is unlikely to affect the rate coefficients measured.

Table 5.2.2: Rate coefficients for the reaction of the CN radical with toluene measured at different temperatures, with the associated experimental parameters^a

T (K)	Buffer gas	Total density (10^{16} cm^{-3})	Range of [C ₆ H ₅ CH ₃] (10^{13} cm^{-3})	No. of exp. points	Rate coefficient <i>k</i> ($10^{-10} \text{ cm}^3 \text{ s}^{-1}$)
15	He	5.04	0.19-1.04	10	4.4 ± 0.7
24	He	4.83	0.18-1.95	11	4.7 ± 0.6
36	He	5.27	0.13-1.77	14	5.90 ± 0.77
	He	5.32	0.13-1.27	9	4.93 ± 0.98 5.6 ± 0.7
70	He	6.00	0.25-1.52	11	4.35 ± 0.56
	He	6.09	0.13-1.87	13	4.23 ± 0.73 4.3 ± 0.6
83	N ₂	4.63	0.35-4.88	14	3.92 ± 0.49
	N ₂	4.63	0.17-3.13	14	3.90 ± 0.44 3.9 ± 0.4
110	Ar	2.71	0.13-1.41	11	3.3 ± 0.5
197	N ₂	5.32	0.21-2.14	11	3.7 ± 0.6
294	N ₂	10.5	1.54-9.29	11	3.67 ± 0.48
	N ₂	3.75	0.95-4.76	9	4.26 ± 0.57
	N ₂	8.20	1.77-7.89	9	4.23 ± 0.53
	He	9.41	1.80-5.40	11	4.46 ± 0.53 4.2 ± 0.5

^a Quoted uncertainties are calculated using the standard error evaluated from the second order plot, multiplied by the appropriate Student's *t* factor for 95% confidence, and then combined in quadrature with an estimated systematic error of 10%. Entries in bold are the variance weighted mean values of rate coefficients measured at the same temperature, where the standard error on the mean is combined in quadrature with an estimated systematic error of 10%.

5.3 Theoretical Methodology and Results

The reaction between CN and benzene has been suggested to proceed without an energy barrier in the entrance channel and likely forms an addition complex, which is supported by theoretical calculations of the reaction potential energy surface ([Balucani et al., 1999, Lee et al., 2019, Woon, 2006]. No

further theoretical calculations on the reaction between CN and benzene were performed in this work.

Investigation of possible channels for the reaction between CN and toluene, with identification of all the stationary points is reported for the first time in this work.

5.3.1 Theoretical Calculations

Investigation of possible channels for the reaction between CN and toluene, with identification and energy calculation of all the stationary points (minima, complexes, and transition states) shown in Figure 5.3.1, was done using Gaussian 09 software [Frisch et al., 2009]. All the species, including the reaction complexes and transition states were optimized at (U)M06-2X/aug-cc-pVTZ level and zero-point corrected energies were calculated for each. In addition, intrinsic reaction coordinate (IRC) calculations were performed at (U)M06-2X/6-311G to determine the minimum energy path that the transition states followed to confirm the connection between the appropriate reactants and products.

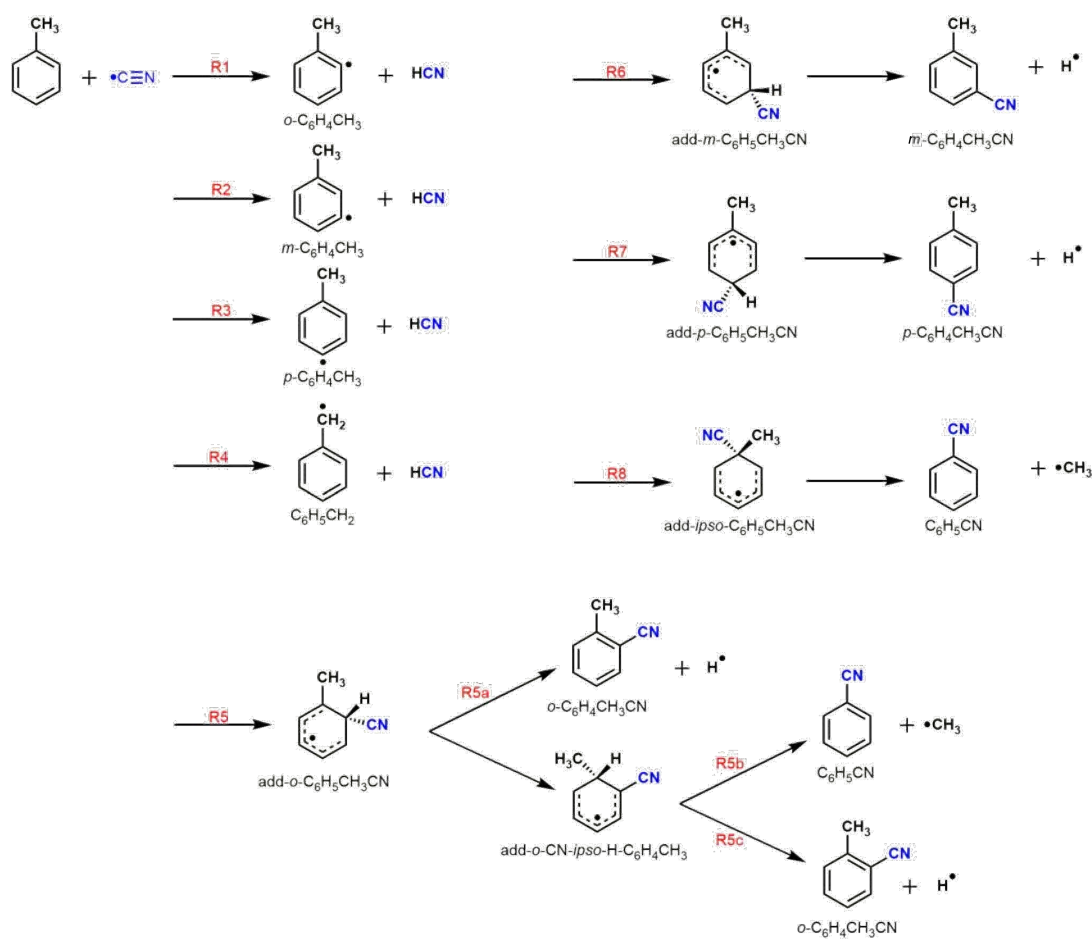


Figure 5.3.1: The reaction pathways of the CN + toluene reaction and possible products of the abstraction (R1–R4) and CN-addition (R5–R8) channels that are considered in the theoretical calculations.

Gibbs energies ($\Delta_r G^\circ$ (298 K)) for all included channels were also calculated at (U)M06-2X/aug-cc-pVTZ method. Both addition-elimination channels, leading to nitrile formation, and abstraction channels, leading to HCN formation, are considered. While reactions involving the CN radical may produce both cyano- and isocyano- compounds, only the former pathways are considered in these calculations. Previous work on the CN + benzene reaction Lee et al. [2019] showed a significant barrier (28 kJ mol^{-1}) to isocyano products, which suggests that this pathway will not be relevant in the low temperature ISM.

5.3.2 Theoretical Results

As shown in the Figure 5.3.2, stationary points (reactants, products, intermediates, transition states) for both the abstraction (R1–R4) and addition-elimination (R5–R8) channels were characterized for the reaction between CN and toluene. An additional substitution channel, leading to the formation of benzyl cyanide, was found to be exothermic at (U)M06-2X/aug-cc-pVTZ, but has a large barrier $\sim 20 \text{ kcal mol}^{-1}$, and hence will not be relevant under interstellar conditions and is excluded. The relative reaction energy (ΔU_r°) and Gibbs energy at 298 K (ΔG_r°) for all calculated product channels can be seen in Table 5.3.1. Intermediates formed from the addition of CN to the aromatic ring were

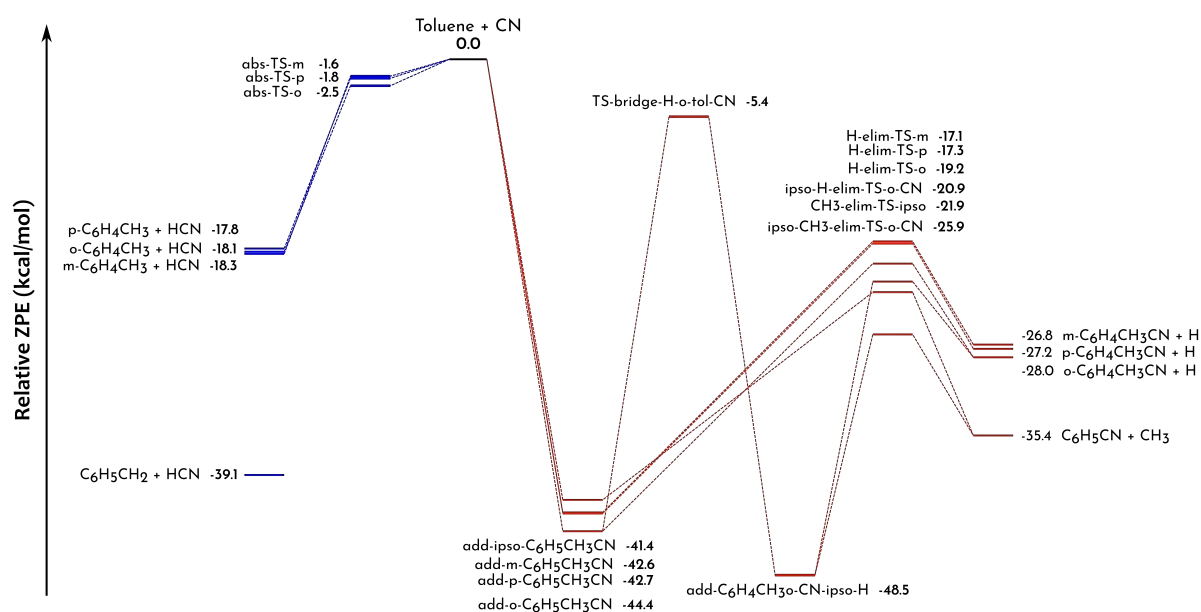


Figure 5.3.2: The stationary points for PES for the CN + toluene reaction, performed at (U)M06-2X/aug-cc-pVTZ and include zero-point energy corrections, showing the abstraction (abs-) pathways (blue) and addition-elimination (add- and elim-) pathways (red), the latter of which can undergo an internal hydrogen shift (-bridge). Note that a barrier leading to the formation of C₆H₅CH₂ + HCN could not be located despite several attempts.

Table 5.3.1: Zero-point corrected reaction energies and Gibbs energies of the reaction products calculated in this work. Note that some reaction pathways result in the same products.

Reaction channel	Products	Reaction energy ΔU_r° (kcal mol ⁻¹)	Gibbs energy $\Delta G_r^\circ(298\text{ K})$ (kcal mol ⁻¹)
R1	<i>o</i> -C ₆ H ₄ CH ₃ + HCN	-18.1	-18.1
R2	<i>m</i> -C ₆ H ₄ CH ₃ + HCN	-18.3	-18.6
R3	<i>p</i> -C ₆ H ₄ CH ₃ + HCN	-17.8	-18.2
R4	C ₆ H ₅ CH ₂ + HCN	-39.1	-38.1
R5a	=R5c; <i>o</i> -C ₆ H ₄ CH ₃ CN + H	-28.0	-23.6
R5b	=R8; C ₆ H ₅ CN + CH ₃	-35.4	-35.5
R5c	=R5a; <i>o</i> -C ₆ H ₄ CH ₃ CN + H	-28.0	-23.6
R6	<i>m</i> -C ₆ H ₄ CH ₃ CN + H	-26.8	-22.5
R7	<i>p</i> -C ₆ H ₄ CH ₃ CN + H	-27.2	-23.8
R8	=R5b; C ₆ H ₅ CN + CH ₃	-35.4	-35.5

found to form barrierlessly, subsequently followed by submerged barriers leading to the formation of stable nitrile products. This mechanism closely resembles the mechanism of benzonitrile formation from the reaction of benzene and CN, [Lee et al., 2019, Woon, 2006] although it does differ from the reaction between toluene and OH, which features both pre-reactive complexes and barriers before formation of the addition product [Zhang et al., 2019].

Abstraction pathways, shown in blue in Figure 5.3.2, were found to have slightly submerged transition states, and therefore are possible products at low temperatures. However, higher level calculations are needed to confirm these barrier values, as similar abstraction pathways from aromatic compounds have been shown to possess positive barriers [Woon, 2006, Zhang et al., 2019]. At the level of theory used, these barrier values are likely within the error of the calculations. An important point to note is that no transition state or complex could be characterized for the channel R4a despite several attempts, though we do not rule out the existence of these stationary points.

5.4 Discussion

5.4.1 Chemical Kinetics

The rate coefficients for the reaction of CN with C₆H₆, measured here between 15 and 295 K, give a weighted mean value of $(4.4 \pm 0.2) \times 10^{-10} \text{ cm}^3 \text{ s}^{-1}$ over this range. This value is consistent with those previously measured by Trevitt et al. [2010] at 295, 165 and 105 K with a pulsed CRESU apparatus and PLP-LIF, as highlighted in Figure 5.2.4. Trevitt et al. [2010] predicted the reaction would remain

rapid at even lower temperatures, as confirmed by our measurements. Similar rapid kinetics behaviour was observed for the reaction of CN with $C_6H_5CH_3$ which remained independent of temperature over the 15–294 K range, with a weighted mean value of $(4.1 \pm 0.2) \times 10^{-10} \text{ cm}^3 \text{ s}^{-1}$. Our results for this reaction differ from the measurement by Trevitt et al., who measured a rate coefficient of $(1.3 \pm 0.3) \times 10^{-10} \text{ cm}^3 \text{ s}^{-1}$ at 105 K in their LIF experiments. They used a similar LIF method to detect CN, under similar experimental conditions of total density, and CN and toluene concentrations. Since their measurements agree well with our results for the benzene system, this suggests that this discrepancy is related to the toluene system. This discrepancy and its possible reasons are discussed later in this section.

The lack of temperature dependence observed in both studies is consistent with a barrierless entrance channel and the formation of an addition complex. It has been shown both experimentally and theoretically that addition-elimination reactions between CN and unsaturated hydrocarbons typically have no barriers in their entrance channel due to the formation of intermediate radical adducts that are relatively stable [Carty et al., 2001]. In general, for this class of reactions, there is usually at least one exothermic exit channel to products. Goulay and Leone [2006] found a similarly large rate coefficient for the reaction between the ethynyl radical (C_2H) and benzene with essentially no temperature dependence between 105–298 K.

The rate coefficients presented for the reaction between CN and benzene here and those of Trevitt et al. [2010] are similar to those of Woon [2006], who used trajectory calculations to predict the rate coefficients between 50–300 K. The calculated rate coefficients ranged from $(3.15\text{--}3.5) \times 10^{-10} \text{ cm}^3 \text{ s}^{-1}$ when back reactions to re-form $CN + C_6H_6$ are excluded. Woon [2006] also investigated the pressure dependence of the reaction by including back-dissociation of the $C_6H_6\text{-CN}$ intermediate complex using a multiwell treatment and found a slight temperature dependence at 10^{-3} mbar, which converges with the high pressure limit rate coefficient by 50 K. We measured the room temperature rate coefficient at three different pressures for both nitrogen and helium buffer gases, as shown in Figure 5.2.4, and did not observe a pressure dependence. It is important to note, however, that the laboratory experiments were likely conducted within the high pressure limit. Similar tests at room temperature using N_2 and He as a buffer gas and varying the total density of the gas flow were performed for the reaction CN and toluene. We found that the rate coefficients had no pressure dependence, shown in Figure 5.2.6, implying that the reaction is either a bimolecular reaction or a termolecular reaction in the high pressure limit in our experimental conditions. Unlike the room temperature measurements of Trevitt et al., we see no evidence for non-exponential decays at any toluene concentration or total

gas density used in these experiments, and the measured rate coefficients are in good agreement with our values at all other temperatures.

Trevitt et al. observed non-exponential decays of CN at room temperature, which they suggested might be due to back-dissociation of adduct complexes. However, no such behavior was observed in this work, shown in Figure 5.4.1, suggesting that the discrepancy might have arisen from differences in the photolysis step. Trevitt et al. photolyzed their sample at a wavelength of 266 nm, with a laser fluence of 40 mJ cm^{-2} ($5.0 \times 10^{16} \text{ photons cm}^{-2}$, in a probable 3–6 ns long pulse), in contrast to the 248 nm laser beam with a fluence of 25 mJ cm^{-2} ($3.1 \times 10^{16} \text{ photons cm}^{-2}$, 22 ns long pulse) used in this work. The ICN photolysis cross sections are similar at these two wavelengths [Felps et al., 1991, Myer and Samson, 1970]. At room temperature, the toluene absorption cross section to the S1 state at 266 nm is $1.3 \times 10^{-19} \text{ cm}^2$ [Fally et al., 2009]. The S1 state fluoresces with a lifetime of 86 ns when excited at 266 nm at low pressures [Hickman et al., 1996]. At 248 nm, the cross section is larger ($2.9 \times 10^{-19} \text{ cm}^2$) [Fally et al., 2009], but the fluorescence lifetime is much shorter due to rapid internal conversion to S0, displaying approximately equal intensity 3 and 26 ns components at low pressures [Jacon et al., 1977]. As discussed above, multiphoton absorption at 248 nm of toluene is known to lead to photolysis [Kovács et al., 2009] and may additionally lead to photoionization, as the excited toluene is higher in energy than the ionization onset of toluene (8.3 eV) [Lu et al., 1992]. Both of these processes are also likely to occur in the 266 nm experiments.

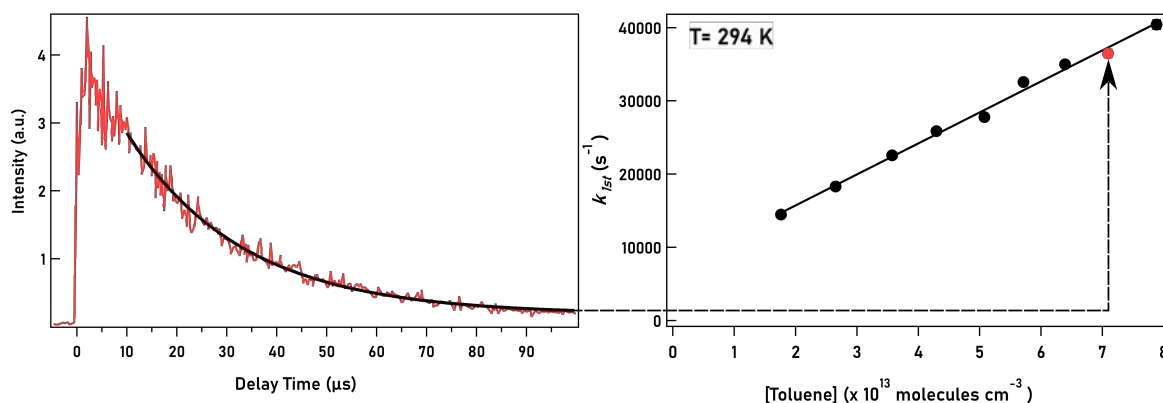


Figure 5.4.1: Experimental kinetics of the CN radical + toluene measured using PLP–LIF, at room temperature (294 K). The left panel shows LIF signal decay of $\text{CN}(B^2\Sigma^+ \rightarrow X^2\Sigma^+)$ at a toluene density of $7.1 \times 10^{13} \text{ cm}^{-3}$ fit with a single exponential decay function (black line). The right panel shows the second-order kinetics plot where the pseudo-first order rate coefficients are plotted against the toluene concentration. The black line shows the fit yielding the second-order bimolecular rate coefficient. The red filled circle corresponds to the k_{1st} obtained from the decay shown in the left panel showing decay of the CN signal and resulting second-order plot at 294 K.

The above considerations suggest that single-photon excitation of toluene is occurring at both photolysis wavelengths, but only multiphoton effects are likely to give rise to interference. Possible pathways for CN generation on the time scale of the experiment exist by either two-photon photodissociation or two-photon ionization, particularly at 266 nm by quadrupled Nd:YAG lasers. Such effects are likely to be significantly lower when toluene is excited at 248 nm light produced by an excimer, due to the longer pulse duration and rapid internal conversion of the S1 state. This is in good agreement with the experimental measurements reported here, showing no relationship between excimer power and k_{Isr} , and no evidence for non-exponential decays, as shown in Figure 5.4.1. In the experiments of Trevitt et al. at 266 nm, however, the long lifetime of the S1 state, short photolysis pulse duration, and higher laser fluence may have caused larger amounts of multiphoton absorption to occur, such that photodissociation or photoionization products could have affected their measurements for toluene. Such effects would not be observed upon 266 nm excitation of benzene, however, as 266 nm lies below the absorption threshold for the benzene S1 state; so, two-photon dissociation would have to occur by a non-resonant process.

5.4.2 Reaction products

Previous theoretical and experimental studies [Balucani et al., 1999, Lee et al., 2019, Woon, 2006] have shown that benzonitrile is the major species produced in the reaction between CN and benzene, with negligible or no production of the -NC isomer, phenylisocyanide, nor the H-abstraction product, the phenyl radical. Woon [2006] calculated the reaction potential energy surface and relative product yields and found that while the $C_6H_5CN + H$ products form exothermically and barrierlessly, there is a 25 kJ mol^{-1} barrier to form the isocyano product pair $C_6H_5NC + H$ after initial barrierless formation of the C_6H_5NC adduct, which was found to be extremely rare in master equation calculations.

Crossed beam experiments conducted under single collision conditions at much higher energies have demonstrated that the benzonitrile is the main reaction product [Balucani et al., 1999, 2000b,c]. Balucani et al. [1999] conducted crossed beam experiments at collision energies between 19.5 and 34.4 kJ mol^{-1} as well as electronic structure and RRKM calculations. Neither the C_6H_6CN adduct nor the phenylisocyanide isomer C_6H_5NC were found to contribute to the crossed beam scattering signal. It was concluded that the dominant reaction entrance channel is barrierless leading to the formation of a CN-addition complex that subsequently dissociates to form benzonitrile + H, with the C_6H_5NC product channel contributing less than 2%.

Lee et al. [2019] studied the reaction of benzene + CN indirectly using microwave discharge experiments and cavity Fourier transform microwave spectroscopy, in combination with electronic structure calculations. They found that the reaction produces benzonitrile in high yield, with <0.1% relative abundance of phenylisocyanide. Isotopic measurements confirmed that the CN bond remains intact during the product formation. In contrast to previous computations, they found formation of the *iso*-adduct requires surmounting a barrier of ~ 17 kJmol⁻¹ as well as a second barrier for H atom loss; implying that phenylisocyanide formation should be highly disfavored under low temperature conditions. While these very sensitive experiments provide important insights into possible reaction pathways, it is important to note that they were not conducted under conditions of kinetic isolation, nor at thermal equilibrium. Under these conditions it is difficult to probe any specific reaction mechanism as multiple reaction paths may contribute and it is unclear how well the product branching ratios obtained reflect those that would be obtained for the elementary reaction CN + C₆H₆ at a well-defined temperature.

Further work from Trevitt et al. [2010] on CN + benzene measured branching ratios at room temperature, using slow flow reactors in conjunction with product detection by multiplexed photoionization mass spectrometry (MPIMS) to identify species by mass and photoionization spectrum. They found that the photoionization efficiency curve at $m/z=103$ could be well fit by benzonitrile photoionization spectrum with no detectable evidence for the H-abstraction product channel, C₆H₅ + HCN, nor the -NC isomer phenylisocyanide. They were able to establish a limit of <15% product fraction for the phenyl radical channel (C₆H₅ + HCN). Low-temperature kinetics experiments, however, are still needed to identify and confirm the product channel specific rate coefficients that are critical parameters for models of astrochemical environments and planetary atmospheres.

In the same work at room temperature, Trevitt et al. found that the reaction between CN and toluene exclusively forms tolunitrile (methylbenzonitrile), with no evidence for the hydrogen abstraction channels or for benzonitrile formation. Due to the similarities in the calculated photoionization spectra of the ortho, meta, and para isomers of the tolunitrile, they were unable to distinguish the precise isomers of tolunitrile formed from this reaction. Henis and Miller [1983] also measured the products of the CN + toluene reaction, using the 254 nm photolysis of ICN and analyzing the resulting products with GC-MS, and observed both tolunitrile and a small yield (9%) of benzonitrile. While it is unclear if this benzonitrile is formed as a result of CN + toluene or side chemistry, particularly in light of its nondetection in the MPIMS experiments by Trevitt et al., our calculations do

show potential pathways to benzonitrile formation from ortho or ipso addition of CN to the aromatic ring.

In conjunction with the similarities in products measured by MPIMS for the reactions of CN with benzene and toluene, it is suggested that the major mechanism is the same for the two reactions resulting in the formation of cyano-substituted aromatic compounds. Investigation of other substituted compounds, such as xylenes or deuterium-substituted benzene, may yield further insight into whether this mechanism is general for these reactions. This will aid in future astronomical searches to improve our understanding of the formation of small aromatic rings in the ISM.

The submerged barriers found for the various channels for the CN + toluene reaction using quantum chemical calculations highlight the diversity of the products that could be formed from this reaction at low temperatures. While the abstraction channels were found to have slightly submerged barriers, calculations at a higher level of theory are necessary to correctly estimate their energies. Furthermore, the transition state(s) and/or a possible complex in the case of the hydrogen abstraction from the methyl group pathway remain to be explored further. This will also provide the accuracy necessary for master equation calculations, which would further elucidate the mechanism and product branching ratios of this reaction.

5.4.3 Astrophysical Implications

The rate coefficients measured here for the CN reaction with benzene are consistent with (albeit somewhat higher than) the value used in the astrochemical model of McGuire et al. [2018] to predict the abundance of benzonitrile in TMC-1, $k(T) = 3 \times 10^{-10} \text{ cm}^3 \text{ s}^{-1}$ (Shingledecker, private communication 2019). It is therefore unlikely that this reaction is the cause of the discrepancy between the abundance of benzonitrile in their model versus that observed in TMC-1 [McGuire et al., 2018]. The large rate coefficients observed over the full temperature range suggests that the reaction should be rapid in astronomical sources that have sufficient density of benzene and CN. Instead, the discrepancy between the observed and modeled abundances, as can be seen in Figure 5.4.2, is likely due to the underproduction of benzene; due to missing production routes and/or underestimation of the rates for those already in the reaction network.

It is likely that other radicals can add to benzene with similarly rapid rate coefficients, indicating that other benzene derivatives may be present in the cold ISM. The reaction of CH with benzene was measured by Hamon et al. [2000] at 25 K and found to be similarly rapid with a rate coefficient of 2.7

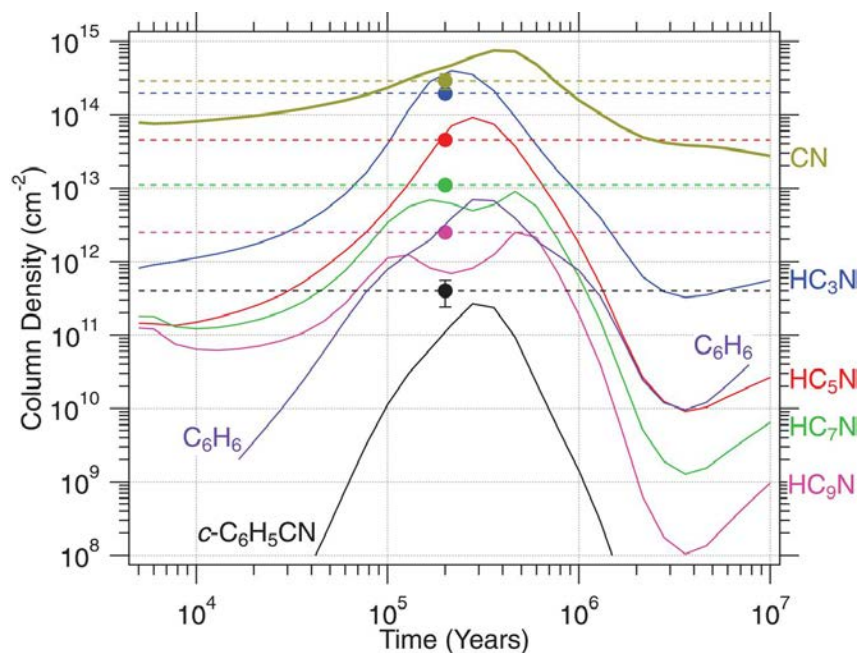


Figure 5.4.2: Modeled gas-phase column densities of benzonitrile in TMC-1 as a function of time in solid coloured lines. The dots with dashed horizontal lines show the abundances derived from observations. Reproduced from McGuire et al. [2018]. The black dot shows the measured abundance in TMC-1 and the solid line shows the modeled abundance using a rate coefficient of $3 \times 10^{-10} \text{ cm}^3 \text{ s}^{-1}$.

$\times 10^{-10} \text{ cm}^3 \text{ s}^{-1}$. Rate coefficients for the reaction of OH with benzene down to 58 K were presented in a review by Hansmann and Abel [2007] and were found to be an order of magnitude lower; however, a complete kinetics study has yet to be published. The reaction of CN with other aromatics may also be rapid and produce products with high dipole moments that could lend themselves to astronomical detection. An alternative route to benzonitrile formation could involve the radiative association reaction between the phenyl (C_6H_5) and CN radicals, which may be rapid under ISM conditions but has not yet been investigated. The reactions of CH and OH with anthracene have both been measured in CRESU flows [Goulay et al., 2006, 2005], though reactions of CN with aromatics (other than toluene done in this work) larger than benzene have not yet been studied.

The origin of the first aromatic ring, as in systems like benzene and toluene, under interstellar conditions is not well understood and is a major source of uncertainty in astrochemical models of aromatic chemistry. Jones et al. [2011] investigated benzene formation via the reaction of C_2H with 1,3-butadiene. Benzene was observed at significant fractions ($30\% \pm 10\%$) with the dominant reaction product the thermodynamically less stable isomer, hexa-1,3-dien-5-yne. However, Lockyear et al. [2015] also studied the products of this reaction using synchrotron photoionization mass spectrometry. The photoionization spectra indicated that fulvene is the major reaction product,

with a branching fraction of $\sim 60\%$. They did not detect benzene as a product and placed an upper limit on the production of benzene and hexa-1,3-dien-5-yne isomers of 45%. [Lee et al., 2019] likewise observed evidence for fulvene formation in a microwave discharge containing HC_3N (a C_2H precursor) and 1,3-butadiene. The discrepancy may be due the high collisional energy of the crossed-beam experiment, emphasizing the importance of studying reactions under both single collision and thermal conditions. The main formation route for benzene in the kida2014 network [Wakelam et al., 2015] is the dissociative recombination of C_6H_7^+ with an electron. McGuire et al. [2018] also added the reaction between $\text{C}_2\text{H} + 1,3\text{-butadiene}$ yielding benzene + H to the kida2014 network with a rate coefficient of $3 \times 10^{-10} \text{ cm}^3 \text{ s}^{-1}$. It is therefore possible that the benzene abundance in their model is overestimated since they do not account for the low (or zero) fraction of benzene likely produced by this reaction at low temperatures. In addition, 1,3-butadiene has not been detected in the ISM and thus it is unknown whether the reaction could produce significant quantities of benzene in TMC-1.

It has been argued that the reaction between C_2H and isoprene (C_5H_8 ; 2-methyl-1,3-butadiene), a barrierless reaction that produces toluene, may be a source of it at low temperatures [Dangi et al., 2013], but it is unknown whether isoprene is present in the ISM: Isoprene is not included in astrochemical databases such as the Kinetic Database for Astrochemistry [Wakelam et al., 2012] (kida.obs.u-bordeaux1.fr, accessed July 2020). Other mechanisms, such as ion-neutral reactions, may also contribute, but further investigation is necessary.

On Titan, the CN radical is mainly generated from the photolysis of HCN, which is formed through reactions of $\text{N}(^4\text{S})$ or through ion chemistry [Loison et al., 2015, Wilson and Atreya, 2004]. Once formed, CN reacts primarily with the highly abundant CH_4 to re-form HCN. This cycle can be interrupted, however, by CN reactions with other compounds, most commonly C_2H_2 or HC_3N . While this reaction has not explicitly been included in models, recent work has suggested that the concentrations of benzene and toluene in the Titan atmosphere are similar, peaking at a mole fraction of 10^{-6} at an altitude of roughly 1000 km above the surface [Loison et al., 2019]. Benzonitrile has not been detected on Titan and a photochemical model recently developed by Loison et al. [2019] to investigate the production of aromatics in the atmosphere of Titan predicted significant formation of toluene and ethylbenzene, benzonitrile was not predicted to be abundant due to efficient consumption of CN by methane. Even with the larger rate coefficients measured in this work, this is likely also the case for the products of the reaction between CN and toluene, though implementation of these results into Titan models may still be beneficial to determine if they have any influence in the atmosphere.

Astronomical searches for toluene and the tolunitrile products of the reaction between CN and toluene would test the robustness of using cyano-containing species as proxies for the unsubstituted hydrocarbons. While benzene has no permanent dipole moment, toluene has a small one (0.37 D) [Rudolph et al., 1967] and may be observable via radio astronomy, though it would have to be present in higher abundance than, say, benzonitrile, to be detectable. The use of velocity stacking, which averages the signal of multiple transitions together to increase the signal-to-noise ratio [Langston and Turner, 2007, Loomis et al., 2016, Walsh et al., 2016], may assist in searching for toluene in the ISM. While there have been no previous detections of toluene in the ISM, it has been argued that the protonated toluene ion, $C_7H_9^+$ [Douberly et al., 2008], and methyl-substituted PAHs [Joblin et al., 1996, Wagner et al., 2000] are possible carriers of the 6.2 and the 3.4 μm unidentified infrared bands, respectively. Definitive detection of toluene and related compounds, such as these, would allow us to constrain aromatic pathways and, in particular, could test the bottom-up mechanism for PAH formation, wherein small molecules, such as toluene, react progressively to form large PAHs.

In order to better understand the potential formation pathways of the products of the reaction between CN and benzene/toluene in the low-temperature ISM, more accurate measurements of the product ratios are required and, specifically, the branching ratio for the tolunitrile and potential benzonitrile products for the CN + toluene reaction. While challenging for many techniques due to the similarities of the isomers, recent developments at Rennes, as described in Chapter 2, by coupling low temperature supersonic uniform flows to microwave spectrometers [Hays et al., 2020, Hearne et al., 2020] will allow us to determine branching ratios for these reactions and others relevant for astrochemistry. As each of these compounds will have a unique rotational spectrum, this technique is well-suited for quantitatively measuring the product branching ratio of these reactions.

5.5 Conclusion

The CRESU technique, combined with PLP-LIF, has been used to measure the kinetics of the reactions of CN with benzene and toluene over the temperature range 15–295 K. We find that the rate coefficients for these reactions do not display an obvious temperature dependence over this temperature range, confirming that both the reactions, $CN + C_6H_6$ and $CN + C_6H_5CH_3$, will remain rapid at temperatures relevant to the cold ISM.

These results for the benzene reaction suggest that benzonitrile is indeed a robust chemical proxy that can be used to infer the abundance of benzene from observations made using radio astronomy. They

also indicate that the discrepancy between the observed and modeled abundances of benzonitrile in TMC-1 is likely due to missing or inaccurate kinetic data for benzene production routes. The result for the toluene reaction is higher than the only previous measurement of this rate coefficient at 105 K, for reasons that are not yet completely understood. This similarly suggests that the reactions between CN and simple aromatics proceed through a similar mechanism, which is supported by our theoretical calculations and previous product measurements. Further work, particularly on the products formed from this reaction, would be beneficial to determine their potential detectability in the ISM. The ability to detect and use cyano-substituted aromatics, which have large dipole moments, as proxies for unsubstituted aromatic compounds in the ISM would help advance our knowledge of PAH formation.

Chapter 6

Low temperature product branching ratios for the reaction of CN radical with propene

6.1 Introduction

Reaction rates of thousands of elementary reactions are essential to predict and identify the key pathways responsible for the abundances of various chemical species across the diverse astrophysical environments. Another crucial parameter to understand the chemical evolution in these extra-terrestrial environments is a quantitative measurement of the different products formed from a given reaction. The branching distribution/ratios of the product channels, combined with the overall rate coefficient, from a reaction at a range of temperatures also serves as a fundamental test of theories for prediction of rate coefficients and outcomes of reactions. Experimental measurements of product branching ratios as a function of temperature, particularly at low temperatures, however, remain rather scarce, especially for large polyatomic systems [Hickson, 2019, Osborn, 2017, Seakins, 2007, Trevitt and Goulay, 2016].

The challenge for measuring branching ratios comes from the difficulty in measuring the different product channels simultaneously. Low-temperature branching ratio measurements in the past have been based on calibrated H-atom LIF branching measurements and photoionisation mass spectrometry [Seakins, 2007, Trevitt and Goulay, 2016]. The former, being a LIF technique has sensitivity, but is limited by its inability to distinguish the branching contribution from channels where H atom(s) are not produced. Photoionisation /mass spectrometry (PIMS) techniques also

have the advantage of being sensitive, as any molecule can be ionised in the VUV with a high cross-section and ions counted individually, with no background. It is most powerful when coupled to synchrotron radiation as the photon energy tunability allows threshold photoionisation, which under certain conditions, gives access to the isomeric structures of the products through their photoionisation spectra. This technique has been applied with great success by Taatjes, Osborn, and coworkers [Osborn, 2017] for room temperature measurements, while a pulsed CRESU apparatus coupled to a quadrupole mass spectrometer at the ALS (Advanced Light Source) has been used for branching ratio measurements down to 70 K [Bouwman et al., 2013]. In most laboratories, however, the PIMS technique is unable to differentiate between isomeric species as, the photoionisation spectra/cross-sections for different isomers are either not available or very similar without the use of a synchrotron source. Chirped pulse microwave spectroscopy is a useful technique as the high specificity of rotational spectroscopy enables the differentiation of even very similar geometrical isomers Abeysekera et al. [2014a].

Chirped-pulse Fourier transform microwave (CP-FTMW) rotational spectroscopy technique combined with a pulsed CRESU reactor was developed by Abeysekera et al. [2015, 2014b], Oldham et al. [2014] to measure the product branching ratio for the reaction of CN with propyne. This remains the only quantitative measurement of branching ratio for a reaction at low temperature using chirped pulse microwave spectroscopy. Here, I present product-specific measurements for the reaction of CN with propene using the recently developed E-band spectrometer by Hays et al. [2020], described in Chapter 2.

Propene (C_3H_6) has been detected in the Taurus Molecular Cloud-1 [Marcelino et al., 2007], a well-known repository of a wide variety of hydrocarbons and aromatic species/PAHs [Cernicharo et al., 2021, McGuire et al., 2018, 2021]. Propene was also identified by Cassini's Ion Neutral Mass Spectrometer in Titan's ionosphere [Vinatier et al., 2010] and is expected to be present in Titan's lower atmosphere [Waite et al., 2007]). CN radical chemistry is well-known in low-temperature astrophysical environments, including dark clouds and planetary atmospheres [Balucani et al., 2000a, Morales et al., 2010, Sims et al., 1994]. Various groups have studied the CN + propene reaction both experimentally and theoretically [Gannon et al., 2007, Gu et al., 2008, Huang et al., 2009, Morales et al., 2010, Trevitt et al., 2009, 2010]. The possible reaction pathways from this reaction are shown in Figure 6.1.1. A rate coefficient of $(3.73 \pm 0.40) \times 10^{-10} \text{ cm}^3$ for this reaction was measured by Morales et al. [2010] at 23 K emphasising its relevance at low temperatures. No cyanopropene isomers have been detected in the interstellar medium or in Titan's atmosphere till date and understanding the

branching ratio of the different product channels from this reaction at low temperature is needed to update the astrochemical models to establish the role of this reaction in those environments.

Gannon et al. [2007] measured the H atom channel(s) using a calibrated PLP-LIF technique and

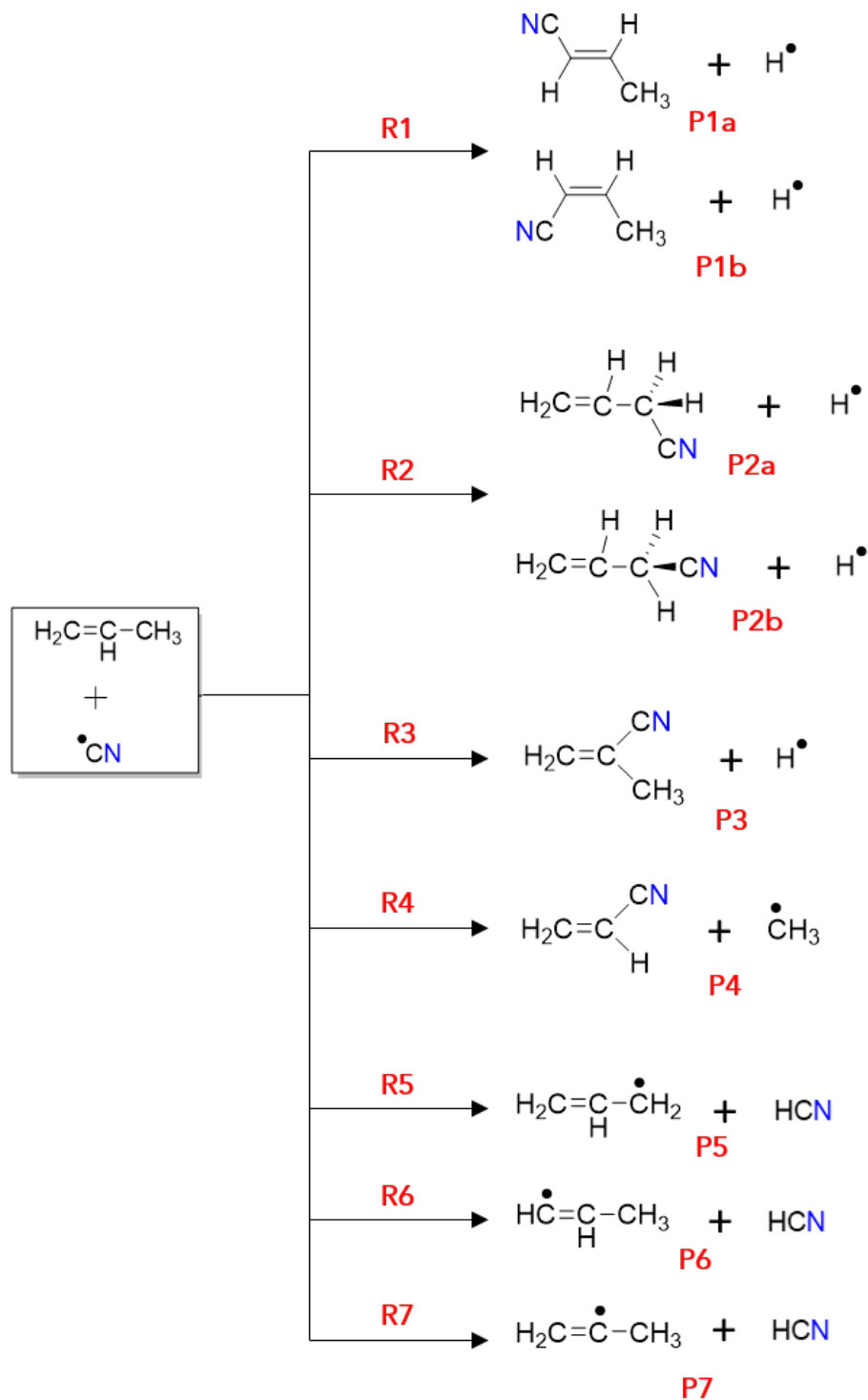


Figure 6.1.1: The reaction pathways of the CN + propene reaction and possible products of the addition-elimination (R1–R4) and abstraction (R5–R8) channels that are considered in the theoretical calculations.

found that the H-atom yields were pressure dependent and ranged from 0.478 at 2 Torr to almost zero at 200 Torr (in He buffer gas). Gannon et al. [2007] also performed quantum calculations suggesting that a $\text{CH}_3 + \text{C}_3\text{H}_3\text{N}$ exit pathway was energetically plausible and predicted a zero-pressure CH_3 elimination yield of 0.51 at 298 K. They emphasized the need for further experimental investigation to elucidate the structure(s) of the H-atom co-product and to characterize the $\text{C}_2\text{H}_3\text{CN} + \text{CH}_3$ (R4 in Figure 6.1.1) product channel.

Crossed-molecular beam (CMB) studies by Gu et al. [2008] for the reaction of CN with propene (and two d_3 propene isotopologues) at collision energies of 25.5 kJ mol^{-1} suggested that three isomers, trans 1-cyanopropene (P1a), cis 1-cyanopropene (P1b), and 3-cyanopropene (P2a/b), could be responsible (within their experimental error limits) for the experimental features they found, with the contribution from the first two being $(75 \pm 8)\%$. This was later combined with a computational study by Huang et al. [2009] where they found that the dominant pathway at collision energies $\leq 21 \text{ kJ mol}^{-1}$ was $\text{H}_2\text{CCHCN} + \text{CH}_3$ (R4) and the H-atom co-product channel contributions from 1-cyanopropene (R1) and 3-cyanopropene (R2) which is in agreement with the CMB study.

Trevitt et al. [2009, 2010] measured the products from CN reaction with propene at room temperature (4 Torr) using multiplexed time-resolved mass spectrometry with tunable synchrotron photoionisation. In the first study [Trevitt et al., 2009], the vinyl cyanide + CH_3 channel (R4 in Figure 6.1.1) was found to be the dominant pathway and the H loss pathways were assigned to 1-cyanopropene and 2-cyanopropene (R1 and R3, respectively). Further study by Trevitt et al. [2010] of this reaction at a higher experimental mass resolution and based on experimentally determined photoionisation reference spectra for the three cyanopropene isomers (P1a/b, P2a/b, and P3) revealed that vinyl cyanide + CH_3 (R4) channel was the dominant product channel with a branching ratio of (0.59 ± 0.15) and the H loss channel accounted for the remaining product yield (0.41). Of this 0.41 branching ratio for the H atom channels, the distribution among the cyanopropene isomers, however, was found to be different from their earlier study: (0.50 ± 0.12) from 1-cyanopropene (R1) and (0.50 ± 0.24) from 3-cyanopropene (R2). However, the cis/trans isomers for the 1- and 2-cyanopropene species (P1a/b and P2a/b) were not distinguishable at the photoionisation resolution of these experiments. Trevitt et al. [2010], however, concluded that there still remains some uncertainty around their assignment between the three cyanopropene ($\text{C}_4\text{H}_5\text{N}$) species due to close similarities between the photo-ionisation spectra.

These studies overall suggest the formation of 1- and 3- cyanopropene isomers as the non-H

atom channels from the $\text{CN} + \text{C}_3\text{H}_6$ reaction at room temperature. These studies were unable to distinguish between the two isomers for 1-cyanopropene and the two conformational isomers for 3-cyanopropene. Also, no study on the detection of products from this reaction is available below room temperature. In this work, the product channels of the reaction of CN with propene were explored using CP-FTMW spectroscopy in uniform supersonic flows at 35 K. Rotational spectra of the two isomers of 1-cyanopropene were also recorded and are reported here. Preliminary results for the complete potential energy surface for this reaction are also presented.

6.2 Experimental methodology and results

6.2.1 Experimental measurements

The products from the reaction between CN and propene formed under CRESU conditions at 35 K were measured using chirped pulse microwave spectroscopy. An E-band (60–90 GHz) spectrometer, as described in section 2.6.1, was used to monitor the various possible products. A dilute mixture ($\sim 0.1\%$) of propene (99.5%; Air Liquide) and ICN (Acros Organics, 98%), the CN radical precursor, in a buffer gas (Ar (99.998%)); Air Liquide) was expanded isentropically through a Laval nozzle to generate a cold supersonic flow at 35 K. All the gases, including Ar and propene were introduced into the CRESU flow using Brooks gas flow controllers. For the spectroscopic measurements, a mixture of trans and cis- crotonitrile/1-cyano propene (Sigma Aldrich, 99%) was seeded in a flow of argon (99.5%; Air Liquide) and delivered to the CRESU flow via a glass bubbler.

The reaction between CN and propene is initiated by ICN photolysis at 248 nm using a KrF excimer laser (Coherent LPXPro 210) with a laser fluence in the reaction zone of $\sim 49.5 \text{ mJ cm}^{-2}$ (6.18×10^{18} photons $\text{sec}^{-1} \text{ cm}^{-2}$). Photodissociation of ICN at 248 nm produces CN radicals primarily ($\geq 93\%$) in the $\nu=0$ level of the $X^2\Sigma^+$ state [O'Halloran et al., 1987] and rapid rotational relaxation is ensured by frequent collisions due to the high density of the buffer gas. The ICN concentration was measured using an UV-Vis spectrometer, described in section 2.4, and an estimated concentration of CN radicals in the flow was calculated similar to as shown in Table 2.4.1 to be in the range $4\text{--}8 \times 10^{10} \text{ cm}^{-3}$. The CN concentration is lower than the concentration of propene by at least a factor of one thousand, hence ensuring pseudo-first order conditions. The CRESU flow was then expanded into a secondary chamber via a 4 mm diameter wide molecular beam skimmer (Beam Dynamics, Inc.), which cools the chemical species in the flow, including the formed products, down to around ~ 5 K. The distance

between the nozzle exit and skimmer entry was maintained at 20 cm, providing an approximate hydrodynamic time of $600 \mu\text{s}$, including the region inside the nozzle after the throat. Based on the acquisition scheme provided in section 2.6.2, $\sim 500 \mu\text{s}$ of reaction time could be observed at a time step of $\sim 10 \mu\text{s}$ (as the beginning $50 \mu\text{s}$ was used to collect pre-laser background and baseline). There is also a $80\text{--}90 \mu\text{s}$ delay after the excimer laser pulse for the reaction products to enter the skimmer chamber. The chemical species were monitored using either single-frequency or multicolor pulses, explained in section 2.6.2, to follow the strongest (at 9 K) rotational transition, in $60\text{--}90 \text{ GHz}$, for each product simultaneously. 100,000 acquisitions at 100 Hz were collected in ~ 16 minutes for the reaction. Other scans which did not use the excimer laser were run at $\sim 2 \text{ kHz}$ frequency, as there was no limitation from the excimer laser.

6.2.2 Experimental results

The spectrum of propene was recorded in the range $69\text{--}71 \text{ GHz}$, and the transitions are shown in Figure 6.2.1. The Figure 6.2.1 also show the rotational transitions predicted for propene in the CDMS catalog [Müller et al., 2005] based on results presented in Craig et al. [2016], Hirota [1966], Lide Jr

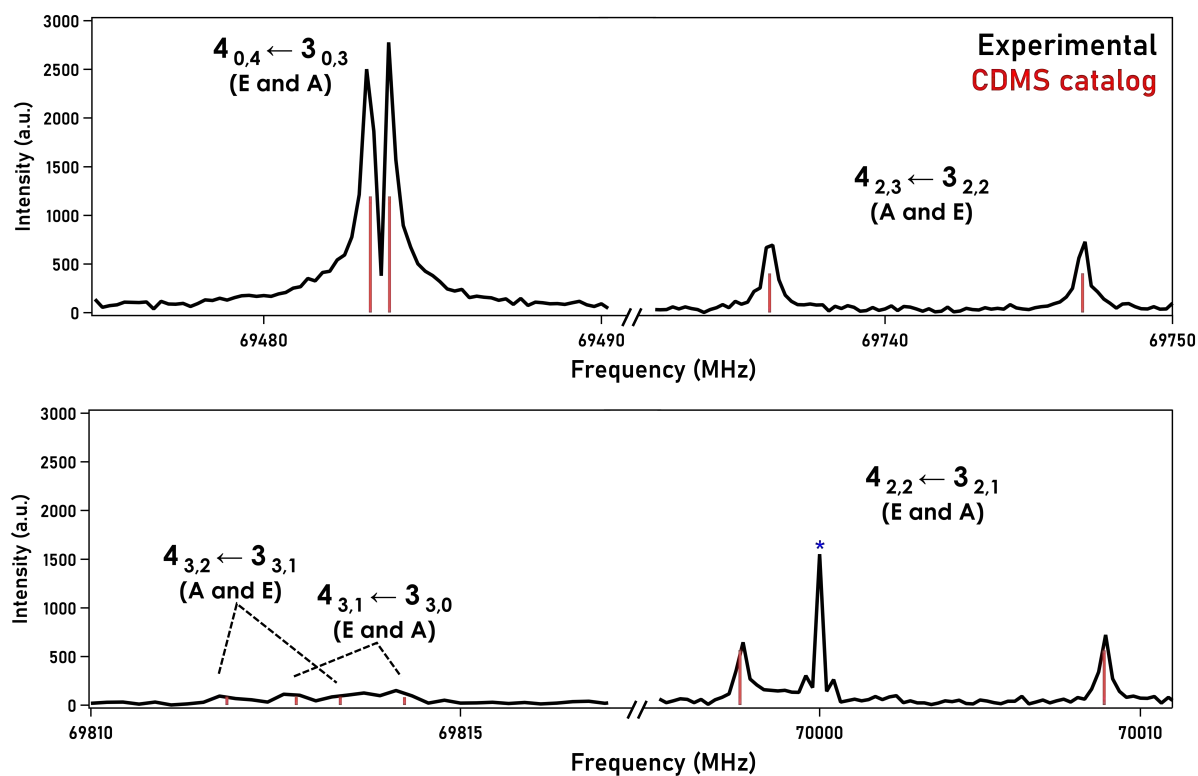


Figure 6.2.1: Propene spectrum, in black, recorded at $\sim 5 \text{ K}$ using a chirp $69\text{--}71 \text{ GHz}$ shown along with the catalog lines from CDMS, in red. The A and E components arise due to the internal rotation of the methyl group in propene. The blue asterisk represent an electronic spur.

and Mann [1957], Pearson et al. [1994], Wlodarczak et al. [1994].

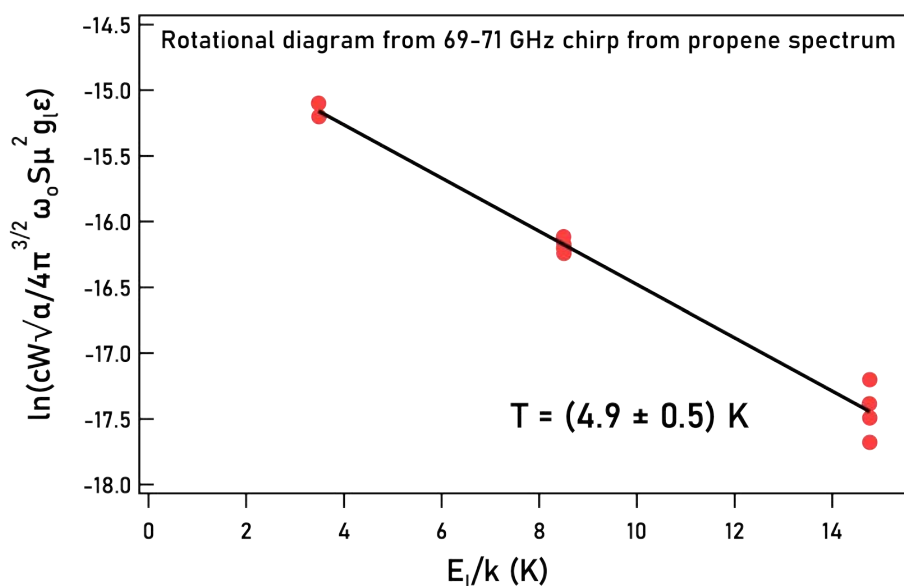


Figure 6.2.2: Rotation diagram using the line intensities of the propene spectrum in the range 69–71 GHz. The rotational temperature is calculated as the negative inverse of the slope and $T_{\text{rot}} = (4.9 \pm 0.5) \text{ K}$ was measured.

Rotation diagram analysis is a common technique used in astronomy where the intensity of the different rotational lines can be used to derive the rotational temperature (T_{rot}) of the species observed. In Figure 6.2.2, the rotational diagram using the line intensities of the different rotational transitions showed in Figure 6.2.1 gives a rotational temperature of $(4.9 \pm 0.5) \text{ K}$.

A spectrum of two of the possible products from the reaction between CN and propene– trans and cis– 1– cyanopropene, P1a and P1b respectively in Figure 6.1.1, was recorded in the range 63.85–68.85 GHz and is shown in Figure 6.2.3. The Figure 6.2.3 also shows the predicted spectral lines of the two species at 9 K using SPCAT with rotational parameters from Lesarri et al. [1995]. The VAR and INT files for the two species used are provided in the Appendix. The spectrum for the cis 1–cyanopropene shows A–E splitting, which were not included in the prediction, highlighting the larger internal rotation barrier for the methyl group in cis 1–cyano propene compared to trans 1–cyano propene.

To avoid possible reactions of the CN radical with the dimers/clusters of propene, it is essential that the concentration of propene is maintained below the dimerization limit of propene. A test was performed by following the intensity of the propene spectral line at 69483.72 MHz for a series of propene concentrations in the flow. The results are shown in Figure 6.2.4 which showed a deviation from linearity at concentrations higher than $\sim 1 \times 10^{14} \text{ cm}^{-3}$ and so the concentration of propene

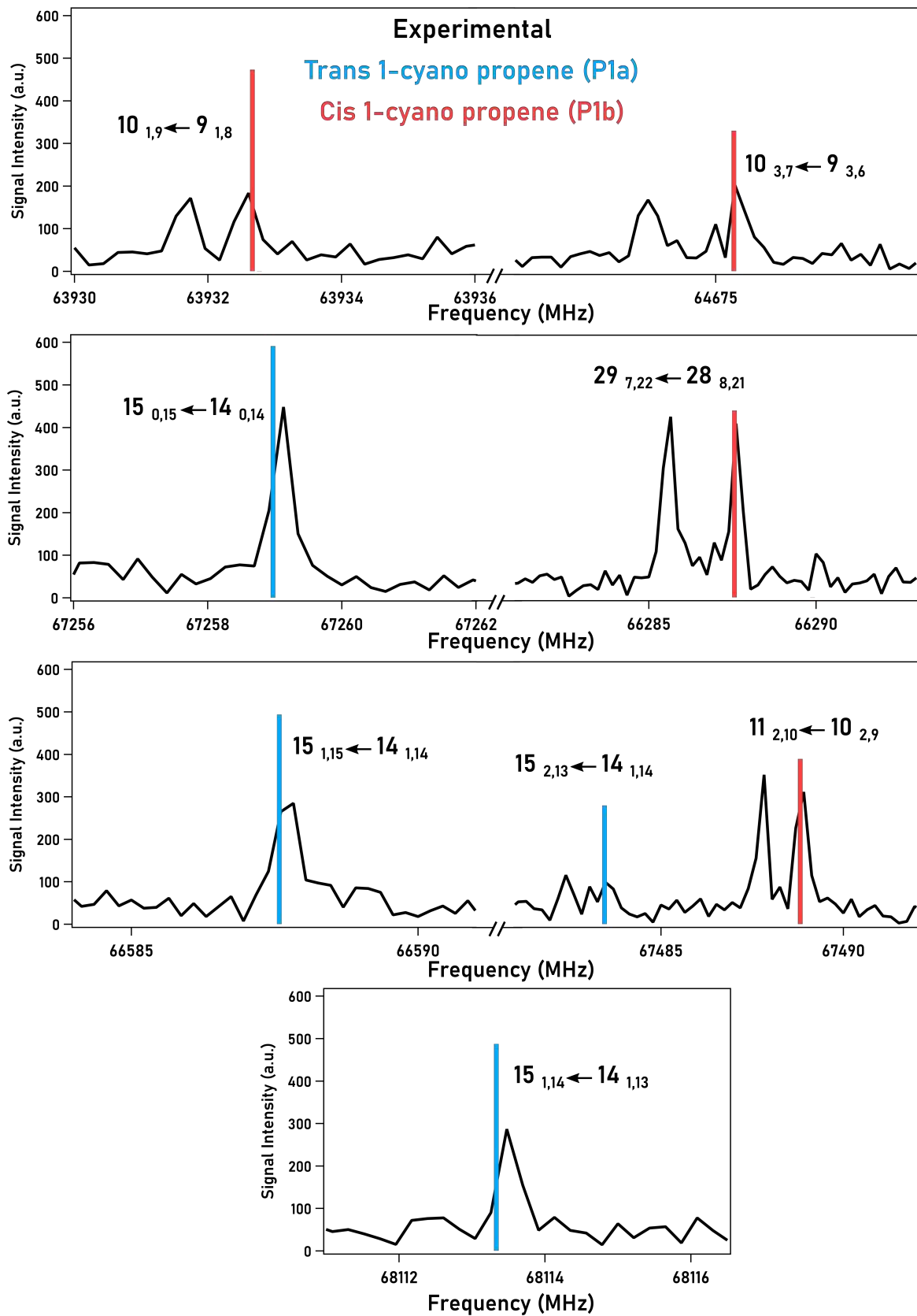


Figure 6.2.3: Spectrum obtained at ~ 5 K for a mixture of cis and trans 1-cyano propene shown along with the simulated catalog lines using SPCAT at slightly higher temperature of 9 K.

used in the reaction scans was maintained at $6 \times 10^{13} \text{ cm}^{-3}$.

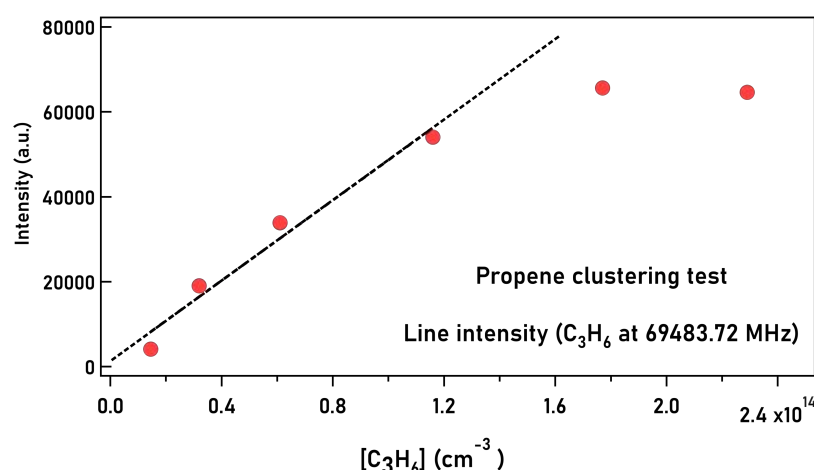


Figure 6.2.4: Measurement of propene rotational transition intensity as a function of number density of propene in the flow as a test for clustering of propene at 35 K.

As mentioned in section 2.4, the ICN concentration was measured downstream before it entered the CRESU chamber using a UV-Vis spectrometer which was used to estimate the ICN concentration in the flow. ICN could also be detected using the microwave spectrometer, and the spectrum of ICN recorded is provided in the Appendix. The estimated concentration of ICN in the flow over the ~ 16 minutes long reaction scans of CN + propene and the CN + ethene reaction, which was used as a calibration (explained later in section 6.4), is shown in Figure 6.2.5. With a laser fluence of 6.2×10^{16} photons pulse⁻¹ cm⁻² at 248 nm, a mean CN radial concentration was estimated to be 1.2×10^{10} cm⁻³ and 1.4×10^{10} cm⁻³ for the propene and ethene reaction scans respectively.

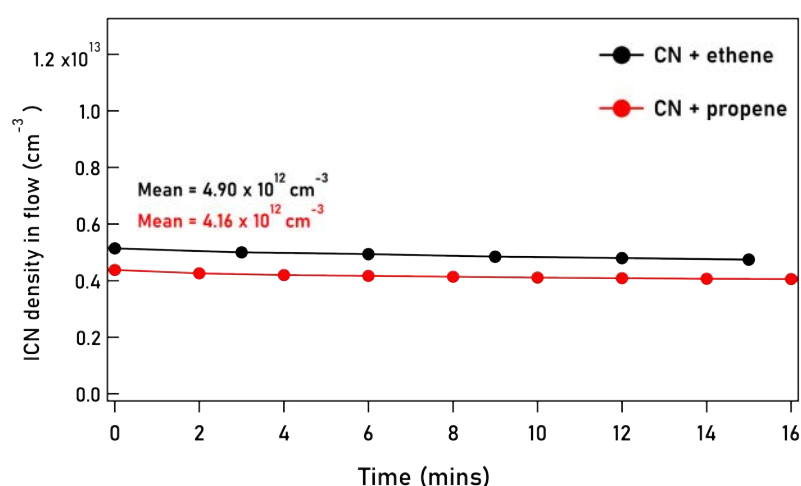


Figure 6.2.5: ICN number density in the CRESU flow during the reactions of CN with ethene and propene

The multicolor pulse technique was used to monitor the products from the reaction channels (R1—

R4). The details for the multicolor pulse used are given in Table 6.2.1. While the pulse lengths for trans/cis 1-cyanopropene and vinyl cyanide were optimized using their spectra collected from the pure samples, intuitive guesses based on their known dipole moments were made for the remaining possible products.

Table 6.2.1: Details of the multicolor pulse used for monitoring the products from the reaction CN + propene.

Chemical species	Product label	Frequency (MHz)	Duration of pulse (ns)
trans 1-cyano propene	P1a	66587.66	50 ns
cis 1-cyano propene	P1b	66285.63	90 ns
2-cyano propene	P3	66708.10	70 ns
gauche 2-cyano propene	P2b	66277.00	90 ns
cis 2-cyano propene	P2a	66362.63	110 ns
vinyl cyanide	P4	66198.36	80 ns

Figure 6.2.6 shows the spectrum recorded 350 μ s after the excimer laser pulse along with the simulated spectral lines (at 9 K) for all the three cyanopropene isomers and vinyl cyanide. The VAR and INT files used for simulating the spectra for all species are provided in the Appendix. Only one product, vinyl cyanide (P4) at 66198 MHz was observed from the reaction. Figure 6.2.7 shows the spectra feature of vinyl cyanide rising as reaction time progresses, with the delay time from the excimer laser pulse indicated on top of each trace.

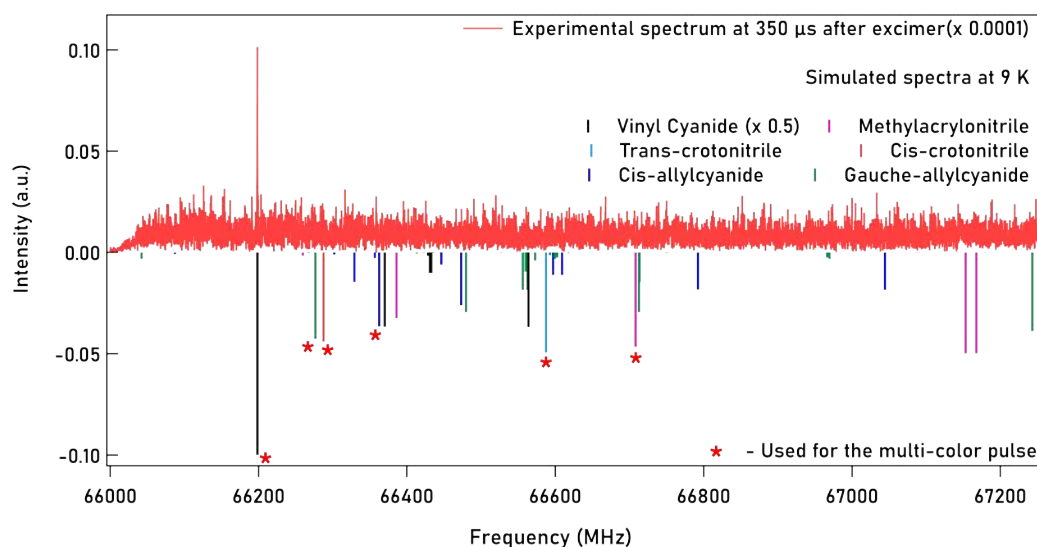


Figure 6.2.6: Spectrum recorded 350 μ s after the excimer laser pulse compared with the simulated spectra (9 K) of the products using SPCAT.

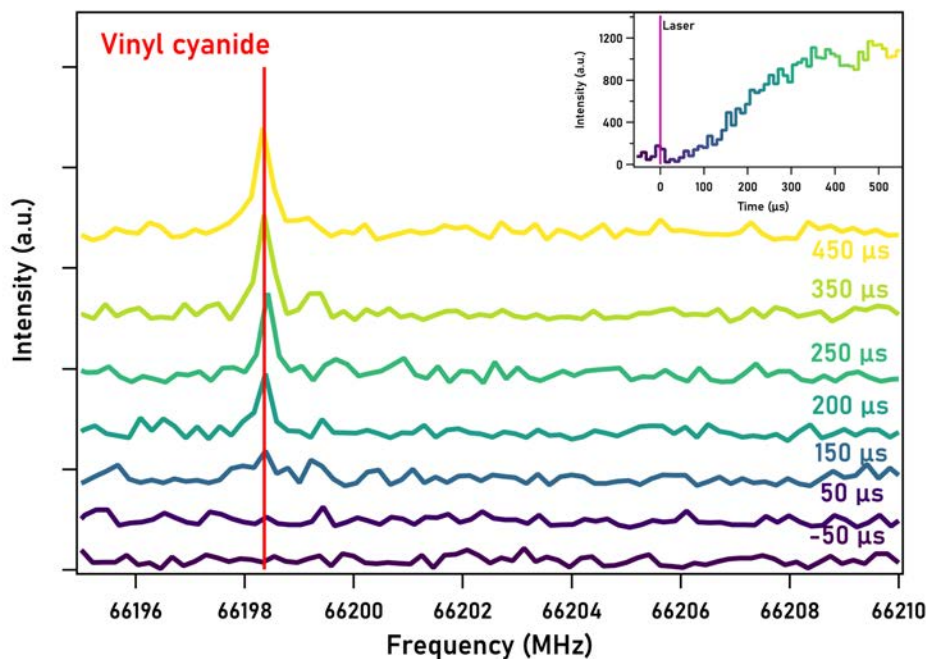


Figure 6.2.7: The rise in intensity of the rotational feature from vinyl cyanide over time from the reaction of CN + propene. The time stamps indicate the delay from the excimer laser pulse/start of reaction. The top inset shows the time dependence of the line intensity.

6.3 Theoretical methodology and results

6.3.1 Theoretical calculations

Investigation of possible channels, shown in Figure 6.1.1, for the reaction between CN and propene, with identification of all the stationary points (minima, complexes, and transition states), was done using Gaussian 09 software [Frisch et al., 2009]. All the species, including the reaction complexes and transition states were optimized at (U)B3LYP/cc-pVTZ and (U)M06-2X/cc-pVTZ levels and zero-point corrected energies were calculated for each. Both addition-elimination channels (R1–R4), leading to cyano-substituted products, and abstraction channels (R5–R7), leading to HCN formation, are considered. Reactions involving the CN radical may produce both cyano- and isocyano- species, however only the cyano-product pathways are considered in these calculations.

6.3.2 Theoretical results

A preliminary potential surface for the reaction is shown in Figure 6.3.1. All the addition-elimination channels (R1–R4) show a submerged barrier, preceded by a stable complex formation. Complete pathway schemes for each product are also provided in the Appendix A7.3. A submerged barrier of

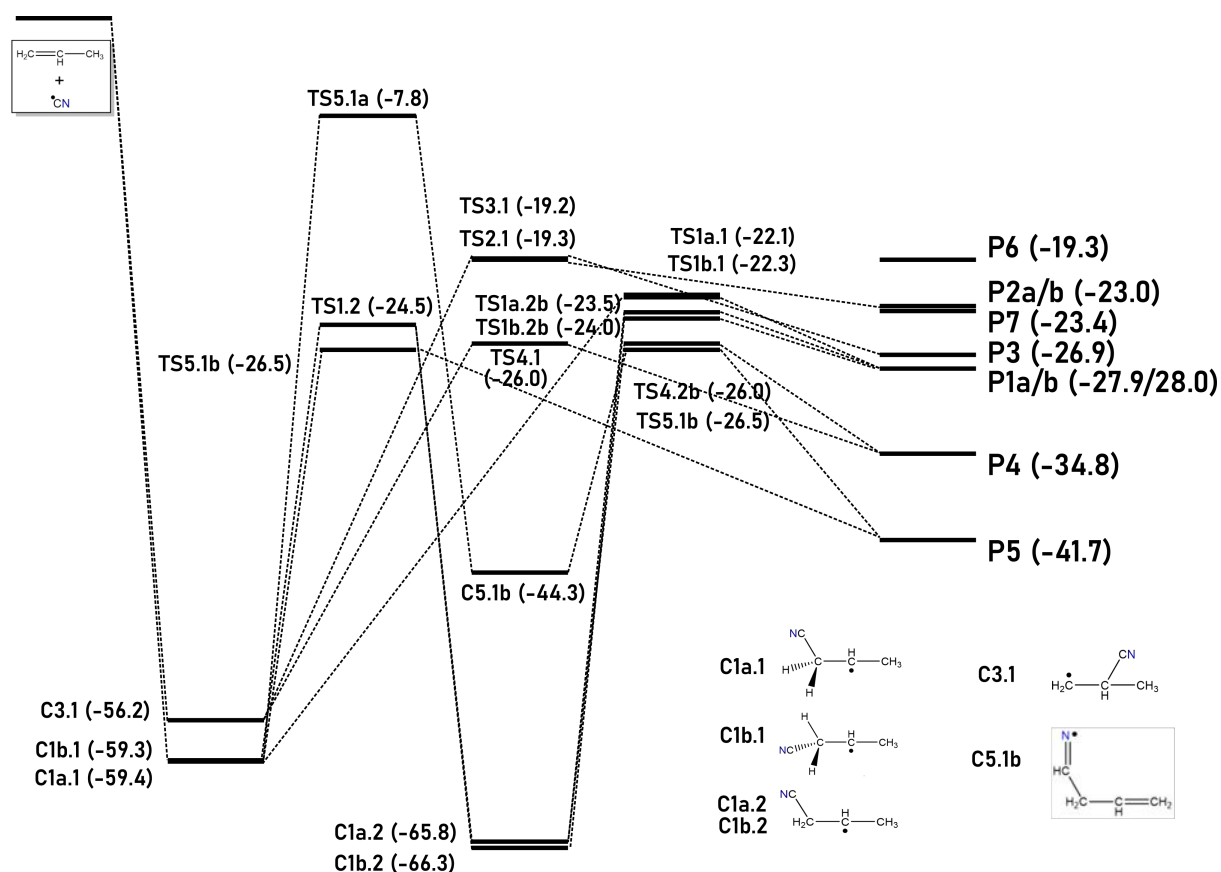


Figure 6.3.1: Potential Energy Surface the reaction of CN + propene. All energies are zero-point corrected and are given at (U)M06-2X/cc-pvTZ in kcal/mol.

-7.8 kcal/mol was found for the HCN abstraction channel R5. Transition states for other abstraction channels (P7, P8) have not yet been located.

6.4 Discussion

When using chirped pulse microwave spectroscopy, branching fractions for the different product channels can be measured by comparing the line intensities from multiple products measured at the same time. In our experiments, however, only one product was measured and so a calibration was performed using vinyl cyanide produced from the reaction of CN with ethene. For the reaction between CN and ethene, it has been suggested that the only one reaction channel takes place leading to vinyl cyanide (C₂H₃CN) and atomic hydrogen. Choi et al. [2004] suggest that H atom branching ratio for this reaction is 1, while Balucani et al. [2000c] and Trevitt et al. [2009] estimating only less than 1% and 2% contributions from the HCN channel.

Figure 6.4.1 shows the vinyl cyanide spectral line intensity over time. Since the product concentration

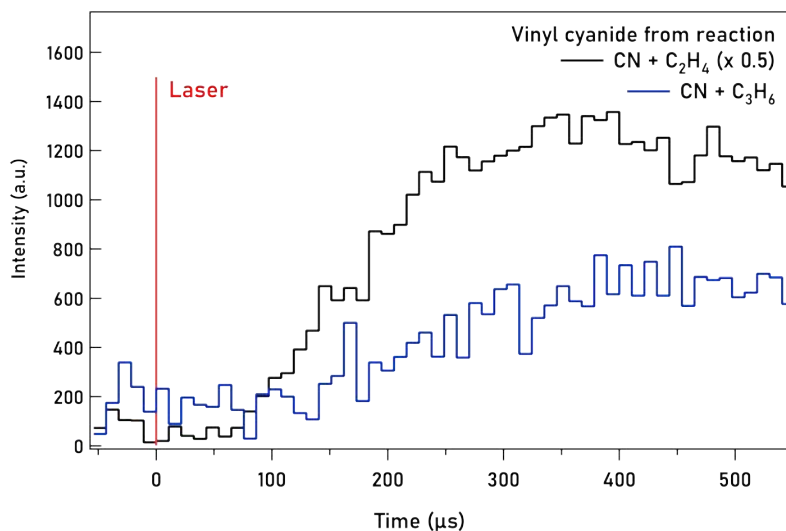


Figure 6.4.1: Vinyl cyanide rotational line intensity from the reactions of CN with ethene and propene as a function of time.

is directly proportional to the CN concentration, the effective signal intensities (signal–background) for vinyl cyanide produced from the two reactions (scaled using the CN concentration), shown in Figure 6.4.1, was used to calculate the branching fraction. The signal intensity was averaged for the time frame: 300–500 μs , providing enough time for both the reactions to have completed, while the background was averaged over the 50 μs before the excimer laser pulse.

$$\text{Branching fraction} = \frac{(\text{Signal intensity} - \text{background})_{\text{C}_3\text{H}_6 \text{ reaction}} [\text{CN}]_{\text{C}_2\text{H}_4 \text{ reaction}}}{(\text{Signal intensity} - \text{background})_{\text{C}_2\text{H}_4 \text{ reaction}} [\text{CN}]_{\text{C}_3\text{H}_6 \text{ reaction}}} \quad (6.4.1)$$

A branching fraction of (0.23 ± 0.07) was estimated for the vinyl cyanide channel (R4) from the CN + propene reaction using the expression 6.4.1. Table 6.4.1 summarises the parameters used for the calibration to calculate this branching fraction. The statistical error was estimated from the equation 6.4.1 by considering the standard deviation in the signals over the regions where the molecular signal

Table 6.4.1: Conditions and the calculated parameters for the two reaction scans, CN + C₂H₄ and CN + C₃H₆, used in this work and for calibration. Nozzle total density and 100,000 acquisitions each

Parameters	CN + C ₂ H ₄	CN + C ₃ H ₆
Reactant, C ₂ H ₄ or C ₃ H ₆ , density (cm ⁻³)	6.1×10^{13}	6.1×10^{13}
Fluence (photons cm ⁻² pulse ⁻¹)	6.2×10^{16}	6.2×10^{16}
ICN density (cm ⁻³)	4.9×10^{12}	4.2×10^{12}
CN radical concentration (cm ⁻³)	1.4×10^{11}	1.2×10^{11}
Signal–Background (a.u.)	2266.7	444.1
Branching fraction for the vinyl cyanide channel	1	0.23

and background were calculated, and the standard deviation in the CN radical concentration during the reaction, which was measured by the UV-Vis measurements.

Figure 6.2.6 shows an average of 4 scans of 100,000 acquisitions each and a signal-to-noise ratio of 8.1 was measured for vinyl cyanide. Based on the simulated intensities for the remaining products at 9 K and assuming $\pi/2$ pulse conditions were achieved, the upper limits for the branching fraction for the reaction channels (R1–R3) were estimated to be: 0.23 for 1-cyanopropene (R1)– 0.11 and 0.13 for the trans and cis isomer respectively, 0.29 for 3-cyanopropene (R2)– 0.16 and 0.13 for the cis and gauche conformer respectively, and 0.12 for 2-cyanopropene (R3).

The only spectral signature for HCN in the 60–90 GHz observable under our experimental conditions for HCN is at 88631.6 MHz (for $j= 1-0$ transition) and could not be monitored at the same time owing to the spectrometer bandwidth limitations. A separate multicolor pulse for HCN and vinyl cyanide was attempted but no signal for HCN could be conclusively found. Some contamination signal of HCN produced from ICN has been observed in previous experiments and better background subtraction will be needed to make any conclusions.

Electronic structure calculations showed submerged barriers for all the products considered during the experiments. While the R1 pathway was considered by Gannon et al. [2007], they did not take the two isomers separately into account for their calculations. They also did not explore the reaction channel R2, leading to 3-cyanopropene. Huang et al. [2009] found a barrier at CCSD(T)/cc-pVTZ//B3LYP/cc-pvTZ for the HCN abstraction channel, R5, contrary to our findings. More efforts to locate the transition states/any possible barriers for the HCN abstraction channels, R6 and R7, also need to be performed, as Huang et al. [2009] show a barrier for both these channels. Accurate energy calculations are needed and will be performed to establish the role of the HCN abstraction channels at low temperatures.

The upper limits provided for the reaction channels are based on the assumption that all the products formed would be vibrationally relaxed, however since the products explored in this work are large polyatomics, 10–atom species,– this assumption may no longer hold true. Since the excited vibrational states are not probed during the reaction, this could also contribute to the reason why these species were not seen in the recorded spectra. Gannon et al. [2007] reported that the H atom product yields were pressure dependent, but since only one nozzle was used in this measurement, which had a pressure 0.28 mbar, no comment on the pressure–dependence of this reaction from these measurements can be made at this point.

6.5 Conclusion and future outlook

The vinyl cyanide product channel (R4) was found to be a relevant channel for this reaction down to 35 K. This is the first experimental detection of vinyl cyanide from this reaction below room temperature. A branching fraction of (0.23 ± 0.07) was measured for the vinyl cyanide product channel (R4), and while the attempts to observe other products from this reaction were not successful, upper limits for all the cyanopropene isomers were established. The future direction for this work would be to achieve higher signal-to-noise ratio by taking more averages, which would also help establish more rigorous upper limits for the branching fractions. Using a different nozzle to explore the pressure dependence of this reaction will also be explored in the future. The potential surface calculations will be completed and used to obtain theoretical branching fractions for this reaction, which could help understand and verify, or otherwise, our experimental findings.

Chapter 7

Summary and future perspective

Reactions of the CN radical with a range of complex organic molecules (COMs), namely methanol, benzene, toluene, and propene, at low temperatures were explored in this work.

The rate coefficients for CN + methanol showed a negative temperature dependence, in the range 17–296 K, which is typical of what has been seen previously for other radical–neutral reactions that do not possess potential energy barriers. This shows that the reaction of methanol with the CN radical is a likely destruction route for methanol in environments where both are present. The rate coefficient obtained at room temperature strongly disagrees with a previous kinetics study by Sayah et al. [1988], which is currently available in the Kinetics Database for Astrochemistry (KIDA), and therefore used in some astrochemical models. KIDA suggests this rate coefficient over the temperature range 10–300 K which could potentially impact the modeled abundances in astrophysical environments at temperatures above ~ 50 K.

Electronic structure calculations were also performed to identify the exothermic channels, and their corresponding transition states, through which this reaction can proceed. While the exothermic channels were characterised, a complete potential energy surface could not be obtained. Two of the possible products from this reaction, CH₃O and CH₂OH, have been a topic of interest for astronomers as only methoxy (CH₃O) has been detected in the interstellar medium by Cernicharo et al. [2012b]. However, laboratory experiments have shown that only the CH₂OH isomer is released to the gas phase when icy mantles are heated [Cernicharo et al., 2012b]. This points towards possible gas-phase formation pathways, one of which is the reaction of methanol with OH [Shannon et al., 2013]. The work presented here only measured the overall rate coefficient, and future measurements

using the recently developed chirped pulse microwave spectrometer in Rennes could be used.

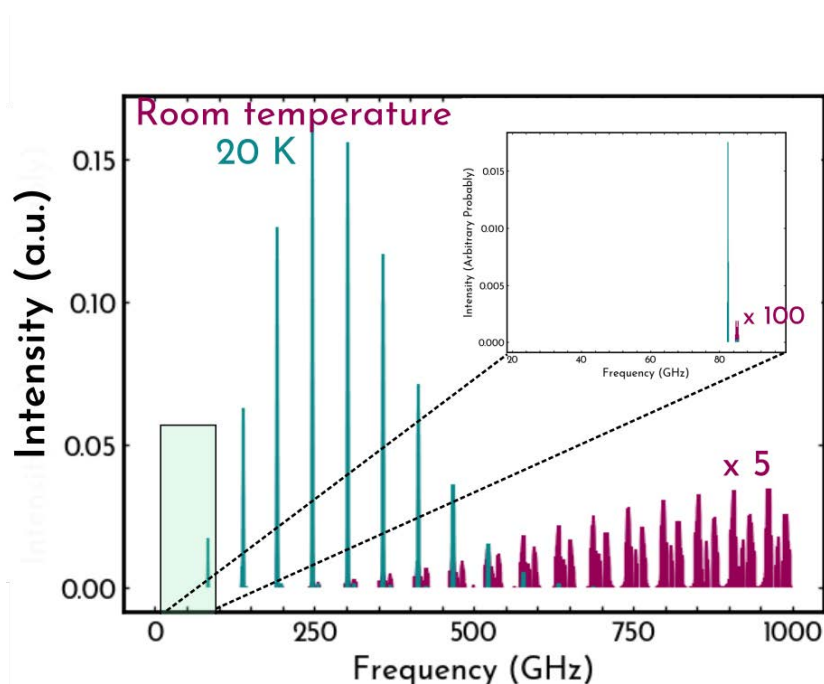


Figure 7.0.1: Simulated spectrum of methoxy (CH_3O) at 20 K and room temperature. The inset shows the spectral lines over the frequency range accessible at Rennes. Adapted Image credit: Ilsa Cooke.

The spectroscopic characterisation of the methoxy radical is well known [Endo et al., 1984], and a simulation using SPCAT in Figure 7.0.1 shows its spectrum at room temperature and at 20 K over the frequency range available at Rennes (26–40 and 60–90 GHz) [Hays et al., 2020, Hearne et al., 2020]. The spectral features around 82.46 GHz are accessible using the E-band chirped pulse spectrometer, which at low temperatures are much more intense than at room temperature, due to a shift in Boltzmann population. The spectroscopy of hydroxymethyl radical (CH_2OH), which is trickier due to rotation–tunnelling and internal rotation, has also been recently reevaluated [Chitarra et al., 2020]. Janssen and Herschberger [2015] measured CH_2OH as the dominant product channel from this reaction at room temperature, so it is exciting to investigate whether this product branching ratio changes down at low temperatures and if this reaction will be a significant source of methoxy under dense cloud conditions.

The detection of benzonitrile/cyano-benzene by McGuire et al. [2018], and since then the detection of cyano-substituted aromatics/cyclic species [McCarthy et al., 2021, McGuire et al., 2021], in the interstellar medium emphasise the importance of verifying if cyano-substituted species are indeed a robust chemical proxy to infer the abundance of their parent molecules. The low-temperature reaction kinetics for the reaction of CN radical with benzene (C_6H_6) were measured, showing that

the reaction remains rapid at the low gas temperatures found in cold dense clouds. An average rate coefficient of $(4.4 \pm 0.2) \times 10^{-10} \text{ cm}^3 \text{ s}^{-1}$ was measured with no obvious temperature dependence between 15 and 295 K. The rate coefficients of the reaction of CN radical with toluene (C_7H_8), another aromatic molecule, were measured between 15 and 294 K with an average of $(4.1 \pm 0.2) \times 10^{-10} \text{ cm}^3 \text{ s}^{-1}$ with no obvious temperature dependence, similar to benzene. This measurement, for CN + toluene reaction, is notably faster than the only previous measurement at 105 K, and while the reason for this disagreement remains unknown, the role of enhanced multiphoton effects was discussed.

The potential energy surface for the reaction, which included both abstraction and addition–elimination pathways, was explored to identify the possible pathways at low temperatures as this reaction remains rapid. Future work will expand on these calculations and use MESMER, a master equation solver program suite [Glowacki et al., 2012], to calculate theoretical branching ratio for this reaction. The cyano-substituted toluene species can be studied and measured using chirped–pulse microwave spectroscopy. This, however, will be a challenging task, as toluene has a methyl group which due to its internal rotation motion gives rise to complicated spectra for these products. It will be interesting to see how much the contribution of cyanobenzene (benzonitrile) product channel, which was identified using theoretical calculations, is from this reaction, especially at low temperatures, since benzonitrile has been detected in a series of cold sources in the ISM [Burkhardt et al., 2021b].

Further work on the products formed from this reaction, is also important to determine their potential detectability in the ISM. The ability to detect and use cyano-substituted aromatics, which have large dipole moments, as proxies for unsubstituted aromatic species in the ISM could also help advance our knowledge of PAH formation as these could provide better constraints to the astrochemical models for smaller species like benzene.

While astrochemical models still have many missing links, one of the biggest is the lack of branching ratios for reactions relevant at low temperatures. The newly developed E–band chirped pulse microwave spectrometer was used to explore the various possible product channels from the reaction of CN radical with propene. A branching fraction of (0.23 ± 0.07) was measured for the vinyl cyanide product channel ($\text{CH}_2\text{CHCN} + \text{CH}_3$), and while the attempts to observe other products from this reaction were not successful, upper limits for all the cyanopropene isomers were established. A caveat regarding vibrational relaxation on these measurements was discussed. To better constrain the upper limits for the other product channels, and their potential detection from the experimental data, the

idea of spectral stacking [Loomis et al., 2021], a commonly used technique in astronomy, will also be explored. Preliminary results on the potential energy surface characterisation were presented, and future work will aim to calculate the theoretical branching fractions using MESMER.

Future measurements for this reaction will explore the effect of pressure on this reaction. A major limitation with the current CRESU–Chirp apparatus is that very few nozzles have the right features, in terms of density, pressure and temperature, to have the best working conditions for detecting products. New nozzles are being designed by a fellow doctoral student, Omar Abdelkader Khedaoui, which could potentially help. State-of-the-art electronics have been used to achieve the best performance possible over this frequency range via the newly developed E–band spectrometer. As a new development, a rotating disk apparatus is being developed to achieve pulsed CRESU flows which will allow to reach lower pressures under CRESU conditions and open the possibility of studying this reaction at other low temperatures.

The reaction of CN with propene is only one of many reactions which could be forming complex, and even prebiotic, molecules in the interstellar conditions. Other possible reactions of the CN radical which could be studied with this technique/apparatus include benzene and cyclopentadiene. The CN radical reactions are good first choice given the high dipole moment of the possible products, but other reactions which produce products with a significant dipole moment can also be explored.

Bibliography

- Abeysekera, C., Joalland, B., Ariyasingha, N., Zack, L. N., Sims, I. R., Field, R. W., and Suits, A. G. (2015). Product branching in the low temperature reaction of CN with propyne by chirped-pulse microwave spectroscopy in a uniform supersonic flow. *The Journal of Physical Chemistry Letters*, 6(9):1599–1604.
- Abeysekera, C., Zack, L. N., Park, G. B., Joalland, B., Oldham, J. M., Prozument, K., Ariyasingha, N. M., Sims, I. R., Field, R. W., and Suits, A. G. (2014a). A chirped-pulse fourier-transform microwave/pulsed uniform flow spectrometer. ii. performance and applications for reaction dynamics. *The Journal of chemical physics*, 141(21):214203.
- Abeysekera, C., Zack, L. N., Park, G. B., Joalland, B., Oldham, J. M., Prozument, K., Ariyasingha, N. M., Sims, I. R., Field, R. W., and Suits, A. G. (2014b). A chirped-pulse fourier-transform microwave/pulsed uniform flow spectrometer. ii. performance and applications for reaction dynamics. *The Journal of chemical physics*, 141(21):214203.
- Adams, W. S. (1941). Some results with the coude spectrograph of the mount wilson observatory. *The Astrophysical Journal*, 93:11.
- Allen, L. and Eberly, J. H. (1987). *Optical Resonance and Two-Level Atoms*. Dover Publications, Inc., New York.
- Antinolo, M., Agundez, M., Jimenez, E., Ballesteros, B., Canosa, A., Dib, G. E., Albaladejo, J., and Cernicharo, J. (2016). Reactivity of OH and CH₃OH between 22 and 64 K: Modelling the gas phase production of CH₃O in Barnard 1b. 823(1).
- Bacmann, A., Lefloch, B., Ceccarelli, C., Steinacker, J., Castets, A., and Loinard, L. (2003). Co depletion and deuterium fractionation in prestellar cores. *The Astrophysical Journal Letters*, 585(1):L55.
- Ball, J. A., Gottlieb, C. A., Lilley, A. E., and Radford, H. E. (1970). Detection of Methyl Alcohol in Sagittarius. *The Astrophysical Journal*, 162:L203.
- Balucani, N., Asvany, O., Chang, A. H., Lin, S. H., Lee, Y. T., Kaiser, R. I., Bettinger, H. F., Schleyer, P. V., and Schaefer, H. F. (1999). Crossed beam reaction of cyano radicals with hydrocarbon molecules. I. Chemical dynamics of cyanobenzene (C₆H₅CN; X1A1) and perdeutero cyanobenzene (C₆D₅CN; X1A1) formation from reaction of CN(X²Σ⁺) with benzene C₆H₆(X1A1g). *Journal of Chemical Physics*, 111(16):7457–7471.
- Balucani, N., Asvany, O., Huang, L., Lee, Y., Kaiser, R., Osamura, Y., and Bettinger, H. (2000a). Formation of nitriles in the interstellar medium via reactions of cyano radicals, cn (x 2σ⁺), with unsaturated hydrocarbons. *The Astrophysical Journal*, 545(2):892.
- Balucani, N., Asvany, O., Huang, L. C. L., Lee, Y. T., Kaiser, R. I., Osamura, Y., and Bettinger, H. F.

- (2000b). Formation of nitriles in the interstellar medium via reactions of cyano radicals, $\text{cn}(x^2\sigma^+)$, with unsaturated hydrocarbons. *The Astrophysical Journal*, 545(2):892–906.
- Balucani, N., Asvany, O., Osamura, Y., Huang, L., Lee, Y., and Kaiser, R. (2000c). Laboratory investigation on the formation of unsaturated nitriles in titan's atmosphere. *Planetary and Space Science*, 48(5):447–462.
- Balucani, N., Ceccarelli, C., and Taquet, V. (2015). Formation of complex organic molecules in cold objects: The role of gas-phase reactions. *Monthly Notices of the Royal Astronomical Society: Letters*, 449(1):L16–L20.
- Batrla, W., Matthewst, H. E., Menten, K. M., and Walmsley, C. M. (1987). Detection of strong methanol masers towards galactic H II regions. *Nature*, 326:49–51.
- Becke, A. D. (1993). A new mixing of hartree–fock and local density-functional theories. *The Journal of chemical physics*, 98(2):1372–1377.
- Belloche, A., Garrod, R. T., Müller, H. S., and Menten, K. M. (2014). Detection of a branched alkyl molecule in the interstellar medium: iso-propyl cyanide. *Science*, 345(6204):1584–1587.
- Bergeat, A. and Loison, J.-C. (2001). Reaction of carbon atoms, $\text{c}(2p^2, ^3p)$ with c_2h_2 , c_2h_4 and c_6h_6 : Overall rate constant and relative atomic hydrogen production. *Phys. Chem. Chem. Phys.*, 3(11):2038–2042.
- Berne, O., Mulas, G., and Joblin, C. (2013). Interstellar $\text{c}60+$. *Astronomy & Astrophysics*, 550:L4.
- Biver, N., Bockelée-Morvan, D., Crovisier, J., Henry, F., Davies, J., Matthews, H. E., Colom, P., Gerard, E., Lis, D. C., Phillips, T. G., Rantakyro, F., Haikala, L., and Weaver, H. A. (2000). Spectroscopic Observations of Comet C/1999 H1 (Lee) with the SEST, JCMT, CSO, IRAM, and Nançay Radio Telescopes'. *The Astronomical Journal*, 120:1554–1570.
- Bizzocchi, L., Caselli, P., Spezzano, S., and Leonardo, E. (2014). Deuterated methanol in the pre-stellar core L1544. *Astronomy & Astrophysics*, 569:A27.
- Bouwman, J., Fournier, M., Sims, I. R., Leone, S. R., and Wilson, K. R. (2013). Reaction rate and isomer-specific product branching ratios of $\text{c}2\text{h}+$ $\text{c}4\text{h}8$: 1-butene, cis-2-butene, trans-2-butene, and isobutene at 79 k. *The Journal of Physical Chemistry A*, 117(24):5093–5105.
- Broadfoot, A., Atreya, S., Bertaux, J., Blamont, J., Dessler, A., Donahue, T., Forrester, W., Hall, D., Herbert, F., Holberg, J., et al. (1989). Ultraviolet spectrometer observations of neptune and triton. *Science*, 246(4936):1459–1466.
- Broderick, B. M., Suas-David, N., Dias, N., and Suits, A. G. (2018). Isomer-specific detection in the UV photodissociation of the propargyl radical by chirped-pulse mm-wave spectroscopy in a pulsed quasi-uniform flow. *Physical Chemistry Chemical Physics*, 20(8):5517–5529.
- Brooke, J. S. (2014). *Line Lists Including Intensities for Diatomic Molecules of Astronomical Interest and Remote Sensing Measurements of Greenhouse Gases*. PhD thesis, University of York.
- Brotten, N., Oka, T., Avery, L., MacLeod, J., and Kroto, H. (1978). The detection of $\text{hc}9\text{n}$ in interstellar space. *The Astrophysical Journal*, 223:L105–L107.
- Brown, G. G., Dian, B. C., Douglass, K. O., Geyer, S. M., Shipman, S. T., and Pate, B. H. (2008). A broadband fourier transform microwave spectrometer based on chirped pulse excitation. *Rev. Sci. Instrum.*, 79(5):053103.

- Burkhardt, A. M., Lee, K. L. K., Changala, P. B., Shingledecker, C. N., Cooke, I. R., Loomis, R. A., Wei, H., Charnley, S. B., Herbst, E., McCarthy, M. C., et al. (2021a). Discovery of the pure polycyclic aromatic hydrocarbon indene (c-c9h8) with gotham observations of tmc-1. *The Astrophysical Journal Letters*, 913(2):L18.
- Burkhardt, A. M., Loomis, R. A., Shingledecker, C. N., Lee, K. L. K., Remijan, A. J., McCarthy, M. C., and McGuire, B. A. (2021b). Ubiquitous aromatic carbon chemistry at the earliest stages of star formation. *Nature Astronomy*, 5(2):181–187.
- Cami, J., Bernard-Salas, J., Peeters, E., and Malek, S. E. (2010). Detection of c60 and c70 in a young planetary nebula. *Science*, 329(5996):1180–1182.
- Carlson, R. W. (1999). A tenuous carbon dioxide atmosphere on jupiter's moon callisto. *Science*, 283(5403):820–821.
- Carty, D., Le Page, V., Sims, I. R., and Smith, I. W. (2001). Low temperature rate coefficients for the reactions of CN and C₂H radicals with allene (CH₂=C=CH₂) and methyl acetylene (CH₃CCH). *Chemical Physics Letters*, 344(3-4):310–316.
- Cernicharo, J., Agúndez, M., Cabezas, C., Tercero, B., Marcelino, N., Pardo, J., and de Vicente, P. (2021). Pure hydrocarbon cycles in tmc-1: Discovery of ethynyl cyclopropenylidene, cyclopentadiene, and indene. *Astronomy and Astrophysics*, 649:L15.
- Cernicharo, J., Heras, A. M., Tielens, A. G. G. M., Pardo, J. R., Herpin, F., Guélin, M., and Waters, L. B. F. M. (2001). Infrared space observatory's discovery of C₄H₂, C₆H₂ and benzene in CRL 618. *The Astrophysical Journal*, 546(2):L123–L126.
- Cernicharo, J., Marcelino, N., Roueff, E., Gerin, M., Jiménez-Escobar, A., and Caro, G. M. (2012a). Discovery of the methoxy radical, ch3o, toward b1: dust grain and gas-phase chemistry in cold dark clouds. *The Astrophysical journal letters*, 759(2):L43.
- Cernicharo, J., Marcelino, N., Roueff, E., Gerin, M., Jiménez-Escobar, A., and Caro, G. M. (2012b). Discovery of the methoxy radical, ch3o, toward b1: dust grain and gas-phase chemistry in cold dark clouds. *The Astrophysical journal letters*, 759(2):L43.
- Cherchneff, I., Barker, J. R., and Tielens, A. G. (1992). Polycyclic aromatic hydrocarbon formation in carbon-rich stellar envelopes. *The Astrophysical Journal*, 401:269–287.
- Chiar, J. E., Tielens, A. G. G. M., Adamson, A. J., and Ricca, A. (2013). The structure, origin, and evolution of interstellar hydrocarbon grains. *The Astrophysical Journal*, 770(1):78.
- Chitarra, O., Martin-Drumel, M.-A., Gans, B., Loison, J.-C., Spezzano, S., Lattanzi, V., Müller, H. S., and Pirali, O. (2020). Reinvestigation of the rotation-tunneling spectrum of the ch2oh radical-accurate frequency determination of transitions of astrophysical interest up to 330 ghz. *Astronomy & Astrophysics*, 644:A123.
- Choi, N., Blitz, M. a., Mckee, K., Pilling, M. J., and Seakins, P. W. (2004). H atom branching ratios from the reactions of cn radicals with c₂h₂ and c₂h₄. *Chem. Phys. Lett.*, 384:68–72.
- Cizek, J. (1969). Use of the cluster expansion and the technique of diagrams in calculations of correlation effects in atoms and molecules. In *Advances in Chemical Physics*, pages 35–89.
- Cooke, I. R. and Sims, I. R. (2019). Experimental studies of gas-phase reactivity in relation to complex organic molecules in star-forming regions. *ACS Earth and Space Chemistry*, 3(7):1109–1134.

- Craig, N. C., Groner, P., Conrad, A. R., Gurusinghe, R., and Tubergen, M. J. (2016). Microwave spectra for the three $^{13}\text{C}1$ isotopologues of propene and new rotational constants for propene and its $^{13}\text{C}1$ isotopologues. *Journal of Molecular Spectroscopy*, 328:1–6.
- Cruikshank, D., Pilcher, C., and Morrison, D. (1976). Pluto: Evidence for methane frost. *Science*, pages 835–837.
- Cruikshank, D. and Silvaggio, P. (1979). Triton—a satellite with an atmosphere. *The Astrophysical Journal*, 233:1016–1020.
- Dangi, B. B., Parker, D. S., Kaiser, R. I., Jamal, A., and Mebel, A. M. (2013). A combined experimental and theoretical study on the gas-phase synthesis of toluene under single collision conditions. *Angewandte Chemie International Edition*, 52(28):7186–7189.
- David R. Lide (2004). *CRC Handbook of Chemistry and Physics: 85th edition*.
- De Graauw, T., Feuchtgruber, H., Bezaud, B., Drossart, P., Encrenaz, T., Beintema, D., Griffin, M., Heras, A., Kessler, M., Leech, K., et al. (1997). First results of iso-sws observations of saturn: detection of CO_2 , $\text{CH}_3\text{C}_2\text{H}$, C_4H_2 and tropospheric H_2O . *Astronomy and astrophysics*, 321:L13–L16.
- Doublerly, G., Ricks, A., Schleyer, P. v. R., and Duncan, M. (2008). Infrared spectroscopy of gas phase benzenium ions: Protonated benzene and protonated toluene, from 750 to 3400 cm^{-1} . *The Journal of Physical Chemistry A*, 112(22):4869–4874.
- Douglas, K., Blitz, M. A., Feng, W., Heard, D. E., Plane, J. M., Slater, E., Willacy, K., and Seakins, P. W. (2018). Low temperature studies of the removal reactions of C_2H_2 with particular relevance to the atmosphere of titan. *Icarus*, 303:10–21.
- Dutrey, A., Guilloteau, S., and Guelin, M. (1997). Chemistry of protosolar-like nebulae: The molecular content of the dm tau and gg tau disks. *Astronomy and Astrophysics*, 317:L55–L58.
- Dwek, E., Arendt, R. G., Fixsen, D. J., Soderoski, T. J., Odegard, N., Weiland, J. L., Reach, W. T., Hauser, M. G., Kelsall, T., Moseley, S. H., Silverberg, R. F., Shafer, R. A., Ballester, J., Bazell, D., and Isaacman, R. (1997). Detection and characterization of cold interstellar dust and polycyclic aromatic hydrocarbon emission from COBE observations. *The Astrophysical Journal*, 475(2):565–579.
- Encrenaz, T., Lellouch, E., Drossart, P., Feuchtgruber, H., Orton, G., and Atreya, S. (2004). First detection of CO in uranus. *Astronomy & Astrophysics*, 413(2):L5–L9.
- Endo, Y., Saito, S., and Hirota, E. (1984). The microwave spectrum of the methoxy radical CH_3O . *The Journal of chemical physics*, 81(1):122–135.
- Ess, D. H. and Houk, K. N. (2005). Activation energies of pericyclic reactions: Performance of DFT, MP2, and CBS-QB3 methods for the prediction of activation barriers and reaction energetics of 1,3-dipolar cycloadditions, and revised activation enthalpies for a standard set of hydrocarbon. *Journal of Physical Chemistry A*, 109(42):9542–9553.
- Fally, S., Carleer, M., and Vandaele, A. C. (2009). UV fourier transform absorption cross sections of benzene, toluene, meta-, ortho-, and para-xylene. *Journal of Quantitative Spectroscopy and Radiative Transfer*, 110(9-10):766–782.
- Faure, A., Vuitton, V., Thissen, R., and Wiesenfeld, L. (2009). A semiempirical capture model for fast neutral reactions at low temperature. *Journal of Physical Chemistry A*, 113(49):13694–13699.

- Faure, A., Wiesenfeld, L., and Valiron, P. (2000). Temperature dependence of fast neutral–neutral reactions: a triatomic model study. *Chemical Physics*, 254(1):49–67.
- Felps, W. S., Rupnik, K., and McGlynn, S. P. (1991). Electronic spectroscopy of the cyanogen halides. *Journal of Physical Chemistry*, 95(2):639–656.
- Fournier, M., Le Picard, S. D., and Sims, I. R. (2017). *Low-temperature chemistry in uniform supersonic flows*. Royal Society of Chemistry.
- Freeman, A. and Millar, T. (1983). Formation of complex molecules in tmc-1. *Nature*, 301(5899):402–404.
- Frisch, M. J., Trucks, G. W., Schlegel, H. B., Scuseria, G. E., Robb, M. A., Cheeseman, J. R., Scalmani, G., Barone, V., Mennucci, B., Petersson, G. A., Nakatsuji, H., Caricato, M., Li, X., Hratchian, H. P., Izmaylov, A. F., Bloino, J., Zheng, G., Sonnenberg, J. L., Hada, M., Ehara, M., Toyota, K., Fukuda, R., Hasegawa, J., Ishida, M., Nakajima, T., Honda, Y., Kitao, O., Nakai, H., Vreven, T., Montgomery, Jr., J. A., Peralta, J. E., Ogliaro, F., Bearpark, M., Heyd, J. J., Brothers, E., Kudin, K. N., Staroverov, V. N., Kobayashi, R., Normand, J., Raghavachari, K., Rendell, A., Burant, J. C., Iyengar, S. S., Tomasi, J., Cossi, M., Rega, N., Millam, J. M., Klene, M., Knox, J. E., Cross, J. B., Bakken, V., Adamo, C., Jaramillo, J., Gomperts, R., Stratmann, R. E., Yazyev, O., Austin, A. J., Cammi, R., Pomelli, C., Ochterski, J. W., Martin, R. L., Morokuma, K., Zakrzewski, V. G., Voth, G. A., Salvador, P., Dannenberg, J. J., Dapprich, S., Daniels, A. D., Ö. Farkas, Foresman, J. B., Ortiz, J. V., Cioslowski, J., and Fox, D. J. (2009). *Wallingford, USA*, 25p.
- Frisch, M. J., Trucks, G. W., Schlegel, H. B., Scuseria, G. E., Robb, M. A., Cheeseman, J. R., Scalmani, G., Barone, V., Petersson, G. A., Nakatsuji, H., Li, X., Caricato, M., Marenich, A. V., Bloino, J., Janesko, B. G., Gomperts, R., Mennucci, B., Hratchian, H. P., Ortiz, J. V., Izmaylov, A. F., Sonnenberg, J. L., Williams-Young, D., Ding, F., Lipparini, F., Egidi, F., Goings, J., Peng, B., Petrone, A., Henderson, T., Ranasinghe, D., Zakrzewski, V. G., Gao, J., Rega, N., Zheng, G., Liang, W., Hada, M., Ehara, M., Toyota, K., Fukuda, R., Hasegawa, J., Ishida, M., Nakajima, T., Honda, Y., Kitao, O., Nakai, H., Vreven, T., Throssell, K., Montgomery, Jr., J. A., Peralta, J. E., Ogliaro, F., Bearpark, M. J., Heyd, J. J., Brothers, E. N., Kudin, K. N., Staroverov, V. N., Keith, T. A., Kobayashi, R., Normand, J., Raghavachari, K., Rendell, A. P., Burant, J. C., Iyengar, S. S., Tomasi, J., Cossi, M., Millam, J. M., Klene, M., Adamo, C., Cammi, R., Ochterski, J. W., Martin, R. L., Morokuma, K., Farkas, O., Foresman, J. B., and Fox, D. J. (2016). Gaussian 16 Revision C.01. Gaussian Inc. Wallingford CT.
- Gannon, K. L., Glowacki, D. R., Blitz, M. A., Hughes, K. J., Pilling, M. J., and Seakins, P. W. (2007). H atom yields from the reactions of cn radicals with C₂H₂, C₂H₄, C₃H₆, trans-2-C₄H₈, and iso-C₄H₈. *The Journal of Physical Chemistry A*, 111(29):6679–6692.
- Gautier, T., Carrasco, N., Buch, A., Szopa, C., Sciamma-O’Brien, E., and Cernogora, G. (2011). Nitrile gas chemistry in Titan’s atmosphere. *Icarus*, 213(2):625–635.
- Ge, J., Van Eyken, J., Mahadevan, S., DeWitt, C., Kane, S. R., Cohen, R., Heuvel, A. V., Fleming, S. W., Guo, P., Henry, G. W., et al. (2006). The first extrasolar planet discovered with a new-generation high-throughput doppler instrument. *The Astrophysical Journal*, 648(1):683.
- Giacobbe, P., Brogi, M., Gandhi, S., Cubillos, P. E., Bonomo, A. S., Sozzetti, A., Fossati, L., Guilluy, G., Carleo, I., Rainer, M., et al. (2021). Five carbon-and nitrogen-bearing species in a hot giant planet’s atmosphere. *Nature*, 592(7853):205–208.

- Gibney, E. and Castelvocchi, D. (2019). Physics nobel goes to exoplanet and cosmology pioneers. *Nature*, 574(7777):162–163.
- Glowacki, D. R., Liang, C. H., Morley, C., Pilling, M. J., and Robertson, S. H. (2012). Mesmer: An open-source master equation solver for multi-energy well reactions. *J. Phys. Chem. A*, 116(38):9545–9560.
- Goulay, F. and Leone, S. R. (2006). Low-temperature rate coefficients for the reaction of ethynyl radical (c2h) with benzene. *The Journal of Physical Chemistry A*, 110(5):1875–1880.
- Goulay, F., Rebrion-Rowe, C., Biennier, L., Picard, S. D. L., Canosa, A., and Rowe, B. R. (2006). Reaction of anthracene with CH radicals: An experimental study of the kinetics between 58 and 470 k. *The Journal of Physical Chemistry A*, 110(9):3132–3137.
- Goulay, F., Rebrion-Rowe, C., Garrec, J. L. L., Picard, S. D. L., Canosa, A., and Rowe, B. R. (2005). The reaction of anthracene with OH radicals: An experimental study of the kinetics between 58 and 470k. *The Journal of Chemical Physics*, 122(10):104308.
- Gu, X., Zhang, F., and Kaiser, R. I. (2008). Reaction dynamics on the formation of 1-and 3-cyanopropylene in the crossed beams reaction of ground-state cyano radicals (cn) with propylene (c3h6) and its deuterated isotopologues. *The Journal of Physical Chemistry A*, 112(39):9607–9613.
- Guner, V., Khuong, K. S., Leach, A. G., Lee, P. S., Bartberger, M. D., and Houk, K. N. (2003). A Standard Set of Pericyclic Reactions of Hydrocarbons for the Benchmarking of Computational Methods: The Performance of ab Initio, Density Functional, CASSCF, CASPT2, and CBS-QB3 Methods for the Prediction of Activation Barriers, Reaction Energetics, and. *Journal of Physical Chemistry A*, 107(51):11445–11459.
- Hall, D., Feldman, P., McGrath, M. A., and Strobel, D. (1998). The far-ultraviolet oxygen airglow of europa and ganymede. *The Astrophysical Journal*, 499(1):475.
- Hall, D. T., Strobel, D., Feldman, P., McGrath, M., and Weaver, H. (1995). Detection of an oxygen atmosphere on jupiter’s moon europa. *Nature*, 373(6516):677–679.
- Hamon, S., Picard, S. D. L., Canosa, A., Rowe, B. R., and Smith, I. W. M. (2000). Low temperature measurements of the rate of association to benzene dimers in helium. *The Journal of Chemical Physics*, 112(10):4506–4516.
- Hansmann, B. and Abel, B. (2007). Kinetics in cold laval nozzle expansions: From atmospheric chemistry to oxidation of biomolecules in the gas phase. *ChemPhysChem*, 8(3):343–356.
- Hays, B. M., Guillaume, T., Hearne, T. S., Cooke, I. R., Gupta, D., Abdelkader Khedaoui, O., Le Picard, S. D., and Sims, I. R. (2020). Design and performance of an E-band chirped pulse spectrometer for kinetics applications: OCS – He pressure broadening. *Journal of Quantitative Spectroscopy and Radiative Transfer*, 250:107001.
- Heard, D. E. (2018). Rapid acceleration of hydrogen atom abstraction reactions of OH at very low temperatures through weakly bound complexes and tunneling. *Acc. Chem. Res.*, 51(11):2620–2627.
- Hearne, T. S., Abdelkader Khedaoui, O., Hays, B. M., Guillaume, T., and Sims, I. R. (2020). A novel ka-band chirped-pulse spectrometer used in the determination of pressure broadening coefficients of astrochemical molecules. *The Journal of Chemical Physics*, 153(8):084201.

- Henis, N. B. and Miller, L. L. (1983). Mechanism of gas-phase cyanation of alkenes and aromatics. *Journal of the American Chemical Society*, 105(9):2820–2823.
- Henkel, C., Schilke, P., and Mauersberger, R. (1988). Molecules in external galaxies - The detection of CN, C₂H, and HNC, and the tentative detection of HC₃N. *Astronomy & Astrophysics*.
- Herbst, E. and van Dishoeck, E. F. (2009). Complex Organic Interstellar Molecules. *Annual Review of Astronomy and Astrophysics*, 47(1):427–480.
- Hernandez-Castillo, A. O., Abeysekera, C., Hays, B. M., and Zwier, T. S. (2016). Broadband multi-resonant strong field coherence breaking as a tool for single isomer microwave spectroscopy. *The Journal of Chemical Physics*, 145(11):114203.
- Hickman, C. G., Gascooke, J. R., and Lawrance, W. D. (1996). The s 1–s 0 (1 b 2–1 a 1) transition of jet-cooled toluene: Excitation and dispersed fluorescence spectra, fluorescence lifetimes, and intramolecular vibrational energy redistribution. *The Journal of chemical physics*, 104(13):4887–4901.
- Hickson, K. M. (2019). Low-temperature rate constants and product-branching ratios for the c (1d)+ h₂o reaction. *The Journal of Physical Chemistry A*, 123(25):5206–5213.
- Hily-Blant, P., Walmsley, M., Pineau des Forêts, G., and Flower, D. (2008). CN in prestellar cores. *Astronomy & Astrophysics*.
- Hirota, E. (1966). Microwave spectrum of propylene. ii. potential function for the internal rotation of the methyl group. *The Journal of Chemical Physics*, 45(6):1984–1990.
- Honniball, C., Lucey, P., Li, S., Shenoy, S., Orlando, T., Hibbitts, C., Hurley, D., and Farrell, W. (2021). Molecular water detected on the sunlit moon by sofia. *Nature Astronomy*, 5(2):121–127.
- Huang, C., Kaiser, R., and Chang, A. (2009). Theoretical study on the reaction of ground state cyano radical with propylene in titan’s atmosphere. *The Journal of Physical Chemistry A*, 113(45):12675–12685.
- Irwin, P. G., Toledo, D., Garland, R., Teanby, N. A., Fletcher, L. N., Orton, G. A., and Bézard, B. (2018). Detection of hydrogen sulfide above the clouds in uranus’s atmosphere. *Nature Astronomy*, 2(5):420–427.
- Jacon, M., Lardeux, C., Lopez-Delgado, R., and Tramer, A. (1977). On the “third decay channel” and vibrational redistribution problems in benzene derivatives. *Chemical Physics*, 24(2):145–157.
- James, P. L., Sims, I. R., Smith, I. W. M., Alexander, M. H., and Yang, M. (1998). A combined experimental and theoretical study of rotational energy transfer in collisions between no($x^2\pi_{1/2}$, v=3,j) and he, ar and n₂ at temperatures down to 7 k. *The Journal of Chemical Physics*, 109(10):3882–3897.
- Janssen, E. and Hershberger, J. F. (2015). Reaction kinetics of the CN radical with primary alcohols. *Chemical Physics Letters*, 625:26–29.
- Jefferts, K., Penzias, A., and Wilson, R. (1970). Observation of the cn radical in the orion nebula and w51. *The Astrophysical Journal*, 161:L87.
- Joblin, C., Tielens, A., Allamandola, L., and Geballe, T. (1996). Spatial variation of the 3.29 and 3.40 micron emission bands within reflection nebulae and the photochemical evolution of methylated polycyclic aromatic hydrocarbons. *The Astrophysical Journal*, 458:610.

- Jones, B. M., Zhang, F., Kaiser, R. I., Jamal, A., Mebel, A. M., Cordiner, M. A., and Charnley, S. B. (2011). Formation of benzene in the interstellar medium. *Proc. Natl. Acad. Sci.*, 108(2):452–457.
- Kaiser, R. I., Parker, D. S., and Mebel, A. M. (2015). Reaction dynamics in astrochemistry: Low-temperature pathways to polycyclic aromatic hydrocarbons in the interstellar medium. *Annual Review of Physical Chemistry*, 66(1):43–67.
- Kendall, R. A., Dunning, T. H., and Harrison, R. J. (1992). Electron affinities of the first-row atoms revisited. Systematic basis sets and wave functions. *The Journal of Chemical Physics*, 96:6796–6806.
- Koban, W., Koch, J. D., Hanson, R. K., and Schulz, C. (2004). Absorption and fluorescence of toluene vapor at elevated temperatures. *Physical chemistry chemical physics*, 6(11):2940–2945.
- Kovács, T., Blitz, M. A., Seakins, P. W., and Pilling, M. J. (2009). H atom formation from benzene and toluene photoexcitation at 248 nm. *The Journal of Chemical Physics*, 131(20):204304.
- Kraemer, K. E., Sloan, G. C., Bernard-Salas, J., Price, S. D., Egan, M. P., and Wood, P. R. (2006). A post-AGB star in the small magellanic cloud observed with the spitzer infrared spectrograph. *The Astrophysical Journal*, 652(1):L25–L28.
- Krasnopolsky, V. A. (2006). A sensitive search for nitric oxide in the lower atmospheres of venus and mars: Detection on venus and upper limit for mars. *Icarus*, 182(1):80–91.
- Krishnan, R., Binkley, J. S., Seeger, R., and Pople, J. A. (1980). Self-consistent molecular orbital methods. xx. a basis set for correlated wave functions. *The Journal of chemical physics*, 72(1):650–654.
- Kristensen, L. E., van Dishoeck, E. F., van Kempen, T. a., Cuppen, H. M., Brinch, C., Jørgensen, J. K., and Hogerheijde, M. R. (2010). Methanol maps of low-mass protostellar systems: the Serpens Molecular Core. *Astronomy and Astrophysics*.
- Kuiper, G. P. (1944). Titan: a satellite with an atmosphere. *The Astrophysical Journal*, 100:378.
- Langevin, P. (1905). A fundamental formula of kinetic theory. *Ann. Chim. Phys*, 5(0365-1444):245–288.
- Langston, G. and Turner, B. (2007). Detection of ¹³C isotopomers of the molecule hc7n. *The Astrophysical Journal*, 658(1):455.
- Lee, K. L. K., McGuire, B. A., and McCarthy, M. C. (2019). Gas-phase synthetic pathways to benzene and benzonitrile: a combined microwave and thermochemical investigation. *Physical Chemistry Chemical Physics*, 21(6):2946–2956.
- Lee, Y.-T., McDonald, J., LeBreton, P., and Herschbach, D. (1969). Molecular beam reactive scattering apparatus with electron bombardment detector. *Review of Scientific Instruments*, 40(11):1402–1408.
- Lesarri, A., Cosleou, J., Li, X., Wlodarczak, G., and Demaison, J. (1995). Rotational spectra of cis and trans crotononitriles: Centrifugal distortion, hyperfine structure, internal rotation and structure. *Journal of Molecular Spectroscopy*, 172(2):520–535.
- Liang, M.-C., Lane, B. F., Pappalardo, R. T., Allen, M., and Yung, Y. L. (2005). Atmosphere of callisto. *Journal of Geophysical Research: Planets*, 110(E2).
- Lide Jr, D. R. and Mann, D. (1957). Microwave spectra of molecules exhibiting internal rotation. i. propylene. *The Journal of Chemical Physics*, 27(4):868–873.

- Lin, J. J., Zhou, J., Shiu, W., and Liu, K. (2003). Application of time-sliced ion velocity imaging to crossed molecular beam experiments. *Review of scientific instruments*, 74(4):2495–2500.
- Lockyear, J. F., Fournier, M., Sims, I. R., Guillemin, J.-c., Taatjes, C. A., Osborn, D. L., and Leone, S. R. (2015). Formation of fulvene in the reaction of c_2h_2 with 1,3-butadiene. *Int. J. Mass Spectrom.*, 378:232–245.
- Loison, J., Dobrijevic, M., and Hickson, K. (2019). The photochemical production of aromatics in the atmosphere of titan. *Icarus*, 329:55–71.
- Loison, J., Hébrard, E., Dobrijevic, M., Hickson, K., Caralp, F., Hue, V., Gronoff, G., Venot, O., and Bénilan, Y. (2015). The neutral photochemistry of nitriles, amines and imines in the atmosphere of titan. *Icarus*, 247:218–247.
- Loomis, R. A., Burkhardt, A. M., Shingledecker, C. N., Charnley, S. B., Cordiner, M. A., Herbst, E., Kalenskii, S., Lee, K. L. K., Willis, E. R., Xue, C., et al. (2021). An investigation of spectral line stacking techniques and application to the detection of hc 11 n. *Nature Astronomy*, 5(2):188–196.
- Loomis, R. A., Shingledecker, C. N., Langston, G., McGuire, B. A., Dollhopf, N. M., Burkhardt, A. M., Corby, J., Booth, S. T., Carroll, P. B., Turner, B., et al. (2016). Non-detection of hc11n towards tmc-1: constraining the chemistry of large carbon-chain molecules. *Monthly Notices of the Royal Astronomical Society*, 463(4):4175–4183.
- Lovas, F. J., McMahon, R. J., Grabow, J.-U., Schnell, M., Mack, J., Scott, L. T., and Kuczkowski, R. L. (2005). Interstellar chemistry: A strategy for detecting polycyclic aromatic hydrocarbons in space. *Journal of the American Chemical Society*, 127(12):4345–4349.
- Lu, K. T., Eiden, G. C., and Weisshaar, J. C. (1992). Toluene cation: nearly free rotation of the methyl group. *The Journal of Physical Chemistry*, 96(24):9742–9748.
- Magee, B. A., Waite, J. H., Mandt, K. E., Westlake, J., Bell, J., and Gell, D. A. (2009). Inms-derived composition of titan's upper atmosphere: analysis methods and model comparison. *Planetary and Space Science*, 57(14-15):1895–1916.
- Malek, S. E., Cami, J., and Bernard-Salas, J. (2011). The rich circumstellar chemistry of smp lmc 11. *The Astrophysical Journal*, 744(1):16.
- Marcelino, N., Cernicharo, J., Agúndez, M., Roueff, E., Gerin, M., Martín-Pintado, J., Mauersberger, R., and Thum, C. (2007). Discovery of interstellar propylene (ch_2chch_3): Missing links in interstellar gas-phase chemistry. *The Astrophysical Journal Letters*, 665(2):L127.
- McCarthy, M. C., Lee, K. L. K., Loomis, R. A., Burkhardt, A. M., Shingledecker, C. N., Charnley, S. B., Cordiner, M. A., Herbst, E., Kalenskii, S., Willis, E. R., et al. (2021). Interstellar detection of the highly polar five-membered ring cyanocyclopentadiene. *Nature Astronomy*, 5(2):176–180.
- McGuire, B. A. (2018). 2018 census of interstellar, circumstellar, extragalactic, protoplanetary disk, and exoplanetary molecules. *The Astrophysical Journal Supplement Series*, 239(2):17.
- McGuire, B. A., Burkhardt, A. M., Kalenskii, S., Shingledecker, C. N., Remijan, A. J., Herbst, E., and McCarthy, M. C. (2018). Detection of the aromatic molecule benzonitrile ($c-c_6h_5cn$) in the interstellar medium. *Science*, 359(6372):202–205.
- McGuire, B. A., Loomis, R. A., Burkhardt, A. M., Lee, K. L. K., Shingledecker, C. N., Charnley, S. B., Cooke, I. R., Cordiner, M. A., Herbst, E., Kalenskii, S., Siebert, M. A., Willis, E. R., Xue,

- C., Remijan, A. J., and McCarthy, M. C. (2021). Detection of two interstellar polycyclic aromatic hydrocarbons via spectral matched filtering. *Science*, 371(6535):1265–1269.
- McKellar, A. (1940). Evidence for the molecular origin of some hitherto unidentified interstellar lines. *Publications of the Astronomical Society of the Pacific*, 52(307):187–192.
- McLean, A. and Chandler, G. (1980). Contracted gaussian basis sets for molecular calculations. i. second row atoms, $z=11-18$. *The Journal of chemical physics*, 72(10):5639–5648.
- Montgomery, J. A., Frisch, M. J., Ochterski, J. W., and Petersson, G. A. (1999). A complete basis set model chemistry. VI. Use of density functional geometries and frequencies. *The Journal of Chemical Physics*, 110:2822–2827.
- Montgomery, J. A., Frisch, M. J., Ochterski, J. W., and Petersson, G. A. (2000). A complete basis set model chemistry. VII. Use of the minimum population localization method. *Journal of Chemical Physics*, 112:6532–6542.
- Morales, S. B., Le Picard, S. D., Canosa, A., and Sims, I. R. (2010). Experimental measurements of low temperature rate coefficients for neutral–neutral reactions of interest for atmospheric chemistry of titan, pluto and triton: Reactions of the cn radical. *Faraday discussions*, 147:155–171.
- Müller, H. S., Schlöder, F., Stutzki, J., and Winnewisser, G. (2005). The cologne database for molecular spectroscopy, cdms: a useful tool for astronomers and spectroscopists. *Journal of Molecular Structure*, 742(1-3):215–227.
- Myer, J. A. and Samson, J. A. R. (1970). Vacuum-Ultraviolet Absorption Cross Sections of CO, HCl, and ICN between 1050 and 2100 Å. *The Journal of Chemical Physics*, 52(1):266–271.
- Nakashima, N. and Yoshihara, K. (1982). Laser photolysis of benzene. v. formation of hot benzene. *The Journal of Chemical Physics*, 77(12):6040–6050.
- Neese, F. (2012). The orca program system. *Wiley Interdisciplinary Reviews: Computational Molecular Science*, 2(1):73–78.
- Nugroho, S. K., Kawahara, H., Gibson, N. P., de Mooij, E. J., Hirano, T., Kotani, T., Kawashima, Y., Masuda, K., Brogi, M., Birkby, J. L., et al. (2021). First detection of hydroxyl radical emission from an exoplanet atmosphere: High-dispersion characterization of wasp-33b using subaru/ird. *The Astrophysical Journal Letters*, 910(1):L9.
- Ocaña, A. J., Blázquez, S., Potapov, A., Ballesteros, B., Canosa, A., Antañolo, M., Vereecken, L., Albaladejo, J., and Jiménez, E. (2019). Gas-phase reactivity of ch₃oh toward oh at interstellar temperatures (11.7–177.5 k): Experimental and theoretical study. *Physical Chemistry Chemical Physics*, 21(13):6942–6957.
- Ochterski, J. W. (2000). Thermochemistry in Gaussian. *Gaussian Inc Pittsburgh PA*.
- Oldham, J. M., Abeysekera, C., Joalland, B., Zack, L. N., Prozument, K., Sims, I. R., Park, G. B., Field, R. W., and Suits, A. G. (2014). A chirped-pulse fourier-transform microwave/pulsed uniform flow spectrometer. i. the low-temperature flow system. *The Journal of chemical physics*, 141(15):154202.
- Osborn, D. L. (2017). Reaction mechanisms on multiwell potential energy surfaces in combustion (and atmospheric) chemistry. *Annual review of physical chemistry*, 68:233–260.
- Owen, T. C., Roush, T. L., Cruikshank, D. P., Elliot, J. L., Young, L. A., De Bergh, C., Schmitt, B., Geballe, T. R., Brown, R. H., and Bartholomew, M. J. (1993). Surface ices and the atmospheric composition of pluto. *Science*, 261(5122):745–748.

- O'Halloran, M. A., Joswig, H., and Zare, R. N. (1987). Alignment of cn from 248 nm photolysis of icn : A new model of the \tilde{a} continuum dissociation dynamics. *The Journal of chemical physics*, 87(1):303–313.
- Pagani, L., Daniel, F., and Dubernet, M.-L. (2009). On the frequency of nh^+ and nd . *Astronomy & Astrophysics*, 494(2):719–727.
- Park, G. B., Steeves, A. H., Kuyanov-Prozument, K., Neill, J. L., and Field, R. W. (2011). Design and evaluation of a pulsed-jet chirped-pulse millimeter-wave spectrometer for the 70–102 ghz region. *The Journal of chemical physics*, 135(2):024202.
- Pearson, J., Sastry, K., Herbst, E., and Delucia, F. (1994). The millimeter-wave and submillimeter-wave spectrum of propylene (ch_3chch_2). *Journal of Molecular Spectroscopy*, 166(1):120–129.
- Pickett, H. M. (1991). The fitting and prediction of vibration-rotation spectra with spin interactions. *Journal of Molecular Spectroscopy*, 148(2):371–377.
- Purvis, G. D. and Bartlett, R. J. (1982). A full coupled-cluster singles and doubles model: The inclusion of disconnected triples. *The Journal of Chemical Physics*, 76:1910–1918.
- Ridgway, S., Wallace, L., and Smith, G. (1976). The 800-1200 inverse centimeter absorption spectrum of jupiter. *The Astrophysical Journal*, 207:1002–1006.
- Rowe, B. R., Dupeyrat, G., Marquette, J. B., and Gaucherel, P. (1984). Study of the reactions $\text{N}^+_2 + 2\text{N}_2 \rightarrow \text{N}^+_4 + \text{N}_2$ and $\text{O}^+_2 + 2\text{O}_2 \rightarrow \text{O}^+_4 + \text{O}_2$ from 20 to 160 K by the CRESU technique. *The Journal of Chemical Physics*.
- Rudolph, H., Dreizler, H., Jaeschke, A., and Wendung, P. (1967). Mikrowellenspektrum, hinderungspotential der internen rotation und dipolmoment des toluols. *Zeitschrift für Naturforschung A*, 22(6):940–944.
- Ruscic, B. and Bross, D. H. (2019). Active Thermochemical Tables (ATcT) values based on ver. 1.122e of the Thermochemical Network, Argonne National Laboratory (2019); available at ATcT.anl.gov.
- Ruscic, B., Pinzon, R. E., Morton, M. L., Von Laszewski, G., Bittner, S. J., Nijssure, S. G., Amin, K. A., Minkoff, M., and Wagner, A. F. (2004). Introduction to active thermochemical tables: Several "Key" enthalpies of formation revisited. *Journal of Physical Chemistry A*.
- Ruscic, B., Pinzon, R. E., Von Laszewski, G., Kodeboyina, D., Burcat, A., Leahy, D., Montoy, D., and Wagner, A. F. (2005). Active Thermochemical Tables: Thermochemistry for the 21st century. In *Journal of Physics: Conference Series*.
- Sayah, N., Li, X., Caballero, J. F., and Jackson, W. M. (1988). Laser induced fluorescence studies of CN reactions with alkanes, alkenes and substituted aliphatic species. *Journal of Photochemistry and Photobiology, A: Chemistry*, 45(2):177–194.
- Schmidt, M. W., Baldridge, K. K., Boatz, J. A., Elbert, S. T., Gordon, M. S., Jensen, J. H., Koseki, S., Matsunaga, N., Nguyen, K. A., Su, S., et al. (1993). General atomic and molecular electronic structure system. *Journal of computational chemistry*, 14(11):1347–1363.
- Schwendeman, R. H. (1978). Transient Effects in Microwave Spectroscopy. *Annual Review of Physical Chemistry*, 29(1):537–558. Number: 1.
- Scuseria, G. E., Janssen, C. L., and Schaefer, H. F. (1988). An efficient reformulation of the closed-shell coupled cluster single and double excitation (CCSD) equations. *The Journal of Chemical Physics*, 89:7382–7387.

- Scuseria, G. E. and Schaefer, H. F. (1989). Is coupled cluster singles and doubles (CCSD) more computationally intensive than quadratic configuration interaction (QCISD)? *The Journal of Chemical Physics*, 90:3700–3703.
- Seakins, P. W. (2007). Product branching ratios in simple gas phase reactions. *Annu. Reports Sect. C*, 103(0):173.
- Shannon, R. J., Blitz, M. A., Goddard, A., and Heard, D. E. (2013). Accelerated chemistry in the reaction between the hydroxyl radical and methanol at interstellar temperatures facilitated by tunnelling. *Nature chemistry*, 5(9):745–749.
- Shannon, R. J., Cossou, C., Loison, J. C., Caubet, P., Balucani, N., Seakins, P. W., Wakelam, V., and Hickson, K. M. (2014). The fast $C(^3P) + CH_3OH$ reaction as an efficient loss process for gas-phase interstellar methanol. *RSC Advances*, 4(50):26342–26353.
- Sims, I. R. (2013). Tunnelling in space. *Nature chemistry*, 5(9):734–736.
- Sims, I. R., Queffelec, J. L., Defrance, A., Rebrion-Rowe, C., Travers, D., Bocherel, P., Rowe, B. R., and Smith, I. W. (1994). Ultralow temperature kinetics of neutral-neutral reactions. The technique and results for the reactions $CN+O_2$ down to 13 K and $CN+NH_3$ down to 25 K. *The Journal of Chemical Physics*, 100(6):4229–4241.
- Sims, I. R., Queffelec, J. L., Travers, D., Rowe, B. R., Herbert, L. B., Karthäuser, J., and Smith, I. W. (1993). Rate constants for the reactions of CN with hydrocarbons at low and ultra-low temperatures. *Chemical Physics Letters*, 211(4-5):461–468.
- Sims, I. R. and Smith, I. W. (1995). Gas-phase reactions and energy transfer at very low temperatures. *Annual review of physical chemistry*, 46(1):109–138.
- Smith, I. W., Sage, A. M., Donahue, N. M., Herbst, E., and Quan, D. (2006). The temperature-dependence of rapid low temperature reactions: experiment, understanding and prediction. volume 133, pages 137–156. Royal Society of Chemistry.
- Somers, K. P. and Simmie, J. M. (2015). Benchmarking Compound Methods (CBS-QB3, CBS-APNO, G3, G4, W1BD) against the Active Thermochemical Tables: Formation Enthalpies of Radicals. *Journal of Physical Chemistry A*, 119(33):8922–8933.
- Soorkia, S., Liu, C.-L., Savee, J. D., Ferrell, S. J., Leone, S. R., and Wilson, K. R. (2011). Airfoil sampling of a pulsed laval beam with tunable vacuum ultraviolet synchrotron ionization quadrupole mass spectrometry: Application to low-temperature kinetics and product detection. *Review of Scientific Instruments*, 82(12):124102.
- Stanton, J., Gauss, J., Harding, M., and Szalay, P. (2010). Cfour, a quantum chemical program package written by jf stanton, j. Gauss, ME Harding, PG Szalay with contributions from AA Auer, RJ Bartlett, U. Benedikt, C. Berger, DE Bernholdt, YJ Bomble, O. Christiansen, M. Heckert, O. Heun, C. Huber.
- Stoecklin, T., Dateo, C. E., and Clary, D. C. (1991). Rate constant calculations on fast diatom-diatom reactions. *Journal of the Chemical Society, Faraday Transactions*.
- Swings, P. and Rosenfeld, L. (1937). Considerations regarding interstellar molecules. *Astrophysical Journal*, 86:483–486.
- Talbi, D. and Wakelam, V. (2011). KIDA: The new kinetic database for astrochemistry. In *Journal of Physics: Conference Series*.

- Teolis, B. and Waite, J. (2016). Dione and rhea seasonal exospheres revealed by cassini caps and inms. *Icarus*, 272:277–289.
- Tielens, A. G. and Charnley, S. B. (1997). Is extraterrestrial organic matter relevant to the origin of life on earth? *Planetary and Interstellar Processes Relevant to the Origins of Life*. Whittet, DCB, pages 249–262.
- Tokunaga, A., Beck, S., Geballe, T., Lacy, J., and Serabyn, E. (1981). The detection of hcn on jupiter. *Icarus*, 48(2):283–289.
- Trevitt, A. J. and Goulay, F. (2016). Insights into gas-phase reaction mechanisms of small carbon radicals using isomer-resolved product detection. *Physical Chemistry Chemical Physics*, 18(8):5867–5882.
- Trevitt, A. J., Goulay, F., Meloni, G., Osborn, D. L., Taatjes, C. A., and Leone, S. R. (2009). Isomer-specific product detection of cn radical reactions with ethene and propene by tunable vuv photoionization mass spectrometry. *International Journal of Mass Spectrometry*, 280(1-3):113–118.
- Trevitt, A. J., Goulay, F., Taatjes, C. A., Osborn, D. L., and Leone, S. R. (2010). Reactions of the CN radical with benzene and toluene: Product detection and low-temperature kinetics. *Journal of Physical Chemistry A*, 114(4):1749–1755.
- Turner, B. E. (1998). The Physics and Chemistry of Small Translucent Molecular Clouds. XI. Methanol. 501:731–748.
- van Dishoeck, E. F. (2014). Astrochemistry of dust, ice and gas: introduction and overview. *Faraday Discuss.*, 168:9–47.
- van Dishoeck, E. F., Blake, G. A., Jansen, D. J., and Groesbeck, T. (1995). Molecular Abundances and Low-Mass Star Formation. II. Organic and Deuterated Species toward IRAS 16293-2422. *Astrophysical Journal*, 447(2):760–782.
- Vastel, C., Ceccarelli, C., Lefloch, B., and Bachiller, R. (2014). The origin of complex organic molecules in prestellar cores. *Astrophysical Journal Letters*, 795(1):6–11.
- Vinatier, S., Bézard, B., Nixon, C. A., Mamoutkine, A., Carlson, R. C., Jennings, D. E., Guandique, E. A., Teanby, N. A., Bjoraker, G. L., Flasar, F. M., et al. (2010). Analysis of cassini/cirs limb spectra of titan acquired during the nominal mission: I. hydrocarbons, nitriles and co₂ vertical mixing ratio profiles. *Icarus*, 205(2):559–570.
- Vuitton, V., Yelle, R. V., and McEwan, M. J. (2007). Ion chemistry and N-containing molecules in Titan's upper atmosphere. *Icarus*, 191(2):722–742.
- Wagner, D., Kim, H., and Saykally, R. (2000). Peripherally hydrogenated neutral polycyclic aromatic hydrocarbons as carriers of the 3 micron interstellar infrared emission complex: results from single-photon infrared emission spectroscopy. *The Astrophysical Journal*, 545(2):854.
- Waite, J., Young, D., Cravens, T., Coates, A., Crary, F., Magee, B., and Westlake, J. (2007). The process of tholin formation in titan's upper atmosphere. *Science*, 316(5826):870–875.
- Waite, J. H., Niemann, H., Yelle, R. V., Kasprzak, W. T., Cravens, T. E., Luhmann, J. G., McNutt, R. L., Ip, W.-H., Gell, D., De La Haye, V., et al. (2005). Ion neutral mass spectrometer results from the first flyby of titan. *Science*, 308(5724):982–986.

- Wakelam, V., Herbst, E., Loison, J. C., Smith, I. W., Chandrasekaran, V., Pavone, B., Adams, N. G., Bacchus-Montabonel, M. C., Bergeat, A., Béroff, K., Bierbaum, V. M., Chabot, M., Dalgarno, A., Van Dishoeck, E. F., Faure, A., Geppert, W. D., Gerlich, D., Galli, D., Hébrard, E., Hersant, F., Hickson, K. M., Honvault, P., Klippenstein, S. J., Le Picard, S., Nyman, G., Pernot, P., Schlemmer, S., Selsis, F., Sims, I. R., Talbi, D., Tennyson, J., Troe, J., Wester, R., and Wiesenfeld, L. (2012). A kinetic database for astrochemistry (KIDA). *Astrophysical Journal, Supplement Series*.
- Wakelam, V., Loison, J.-C., Herbst, E., Pavone, B., Bergeat, A., Béroff, K., Chabot, M., Faure, A., Galli, D., Geppert, W. D., et al. (2015). The 2014 kida network for interstellar chemistry. *The Astrophysical Journal Supplement Series*, 217(2):20.
- Walsh, C., Loomis, R. A., Öberg, K. I., Kama, M., van 't Hoff, M. L. R., Millar, T. J., Aikawa, Y., Herbst, E., Widicus Weaver, S. L., and Nomura, H. (2016). First Detection of Gas-phase Methanol in a Protoplanetary Disk. *The Astrophysical Journal Letters*, 823(1):L10.
- Werner, H.-J., Knowles, P. J., Knizia, G., Manby, F. R., and Schütz, M. (2012). Molpro: a general-purpose quantum chemistry program package. *Wiley Interdisciplinary Reviews: Computational Molecular Science*, 2(2):242–253.
- Western, C. M. (2017). Pgopher: A program for simulating rotational, vibrational and electronic spectra. *Journal of Quantitative Spectroscopy and Radiative Transfer*, 186:221–242.
- Wilson, E. H. and Atreya, S. (2004). Current state of modeling the photochemistry of titan's mutually dependent atmosphere and ionosphere. *Journal of Geophysical Research: Planets*, 109(E6).
- Wilson, E. H. and Atreya, S. K. (2003). Chemical sources of haze formation in Titan's atmosphere. *Planetary and Space Science*, 51(14-15):1017–1033.
- Wlodarczak, G., Demaison, J., Heineking, N., and Csaszar, A. (1994). The rotational spectrum of propene: internal rotation analysis and ab initio and experimental centrifugal distortion constants. *Journal of Molecular Spectroscopy*, 167(2):239–247.
- Wollenhaupt, M., Carl, S., Horowitz, A., and Crowley, J. (2000). Rate coefficients for reaction of oh with acetone between 202 and 395 k. *The Journal of Physical Chemistry A*, 104(12):2695–2705.
- Woods, P. M., Millar, T., Zijlstra, A., and Herbst, E. (2002). The synthesis of benzene in the protoplanetary nebula crl 618. *The Astrophysical Journal Letters*, 574(2):L167.
- Woon, D. E. (2006). Modeling chemical growth processes in Titan's atmosphere: 1. Theoretical rates for reactions between benzene and the ethynyl (C₂H) and cyano (CN) radicals at low temperature and pressure. *Chemical Physics*, 331(1):67–76.
- Woon, D. E. and Dunning, T. H. (1993). Gaussian basis sets for use in correlated molecular calculations. III. The atoms aluminum through argon. *The Journal of Chemical Physics*, 98:1358–1371.
- Yung, Y. L., Allen, M., and Pinto, J. P. (1984). Photochemistry of the atmosphere of titan: Comparison between model and observations. *Astrophysical Journal Supplement Series*, 55(3):465–506.
- Zhang, R. M., Truhlar, D. G., and Xu, X. (2019). Kinetics of the Toluene Reaction with OH Radical. *Research*, 2019:1–19.
- Zhao, Y. and Truhlar, D. G. (2008). The m06 suite of density functionals for main group thermochemistry, thermochemical kinetics, noncovalent interactions, excited states, and transition

elements: two new functionals and systematic testing of four m06-class functionals and 12 other functionals. *Theoretical chemistry accounts*, 120(1):215–241.

A.1 Appendix

A1 Pitot profiles of the nozzles used

He 17 K

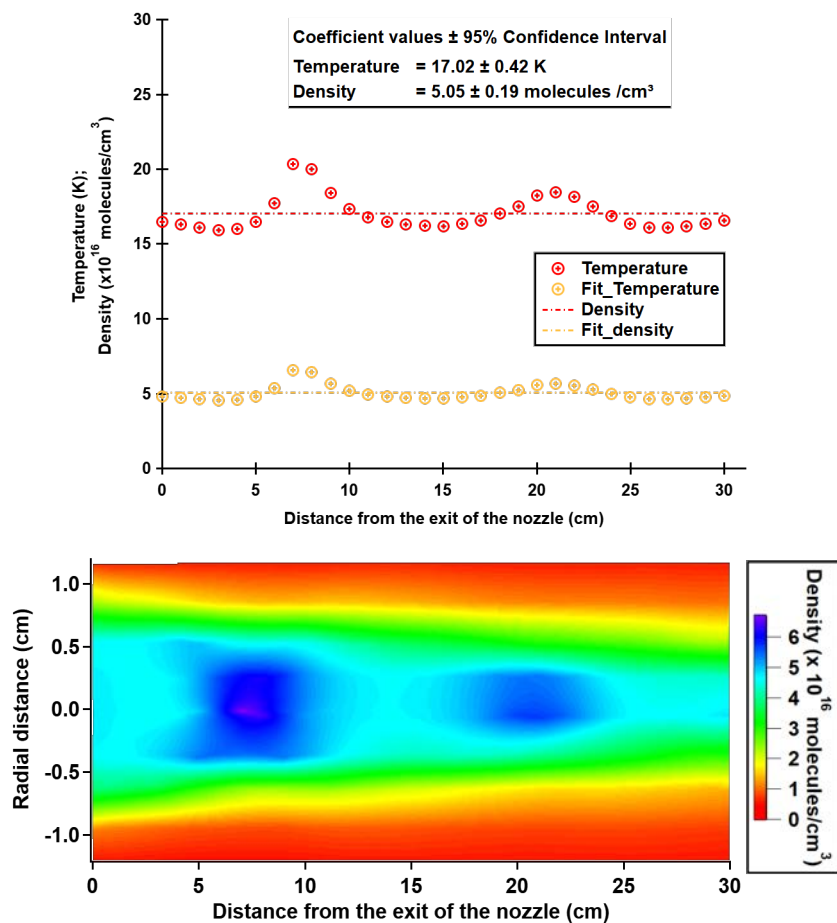


Figure A1.1: Pitot profile for 17 K nozzle with He buffer gas

He 15 K

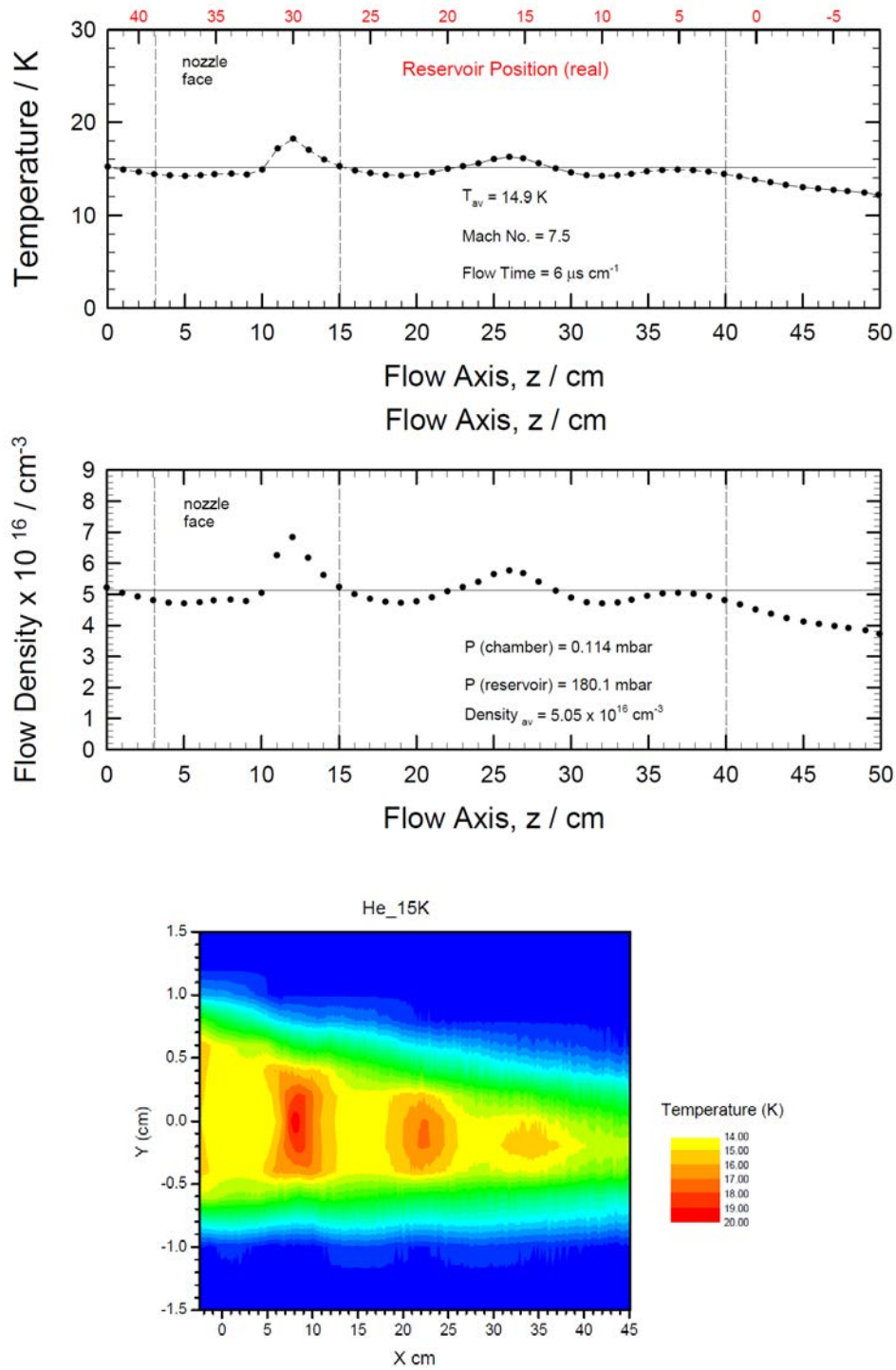
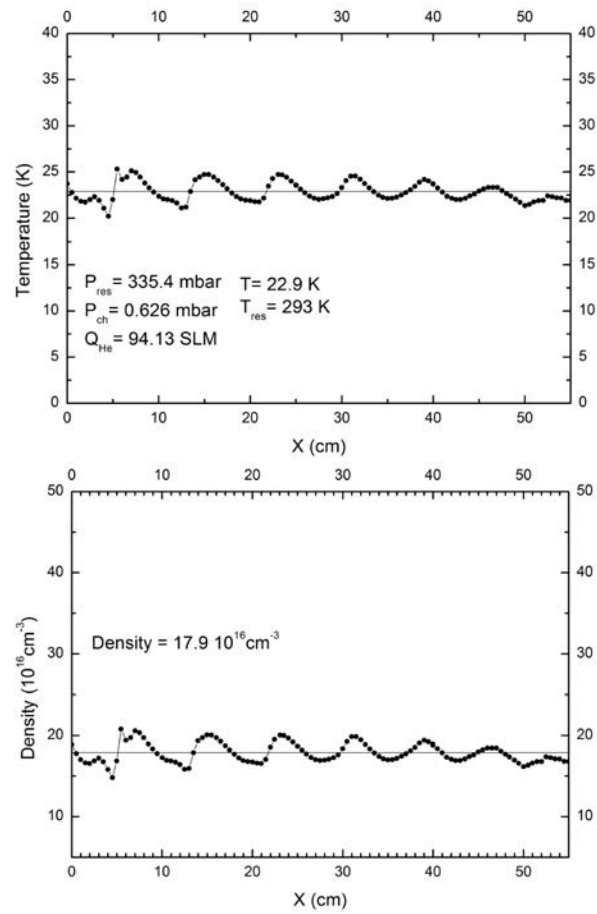


Figure A1.2: Pitot profile for 15 K nozzle with He buffer gas

He 24 K



He 6 K @ 24 K

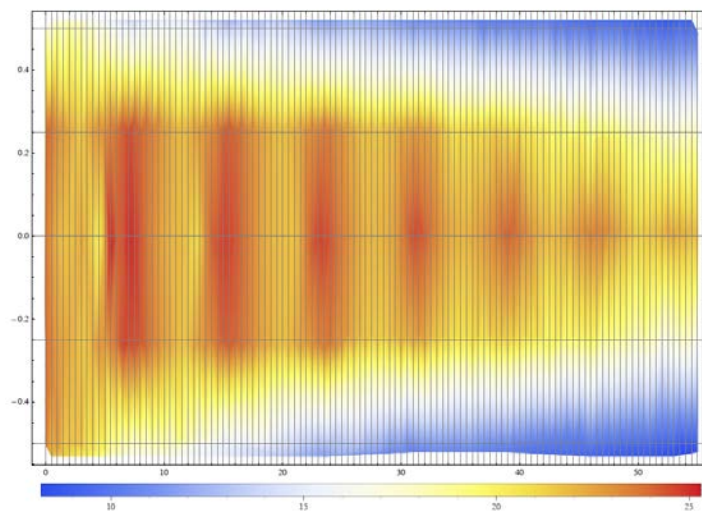
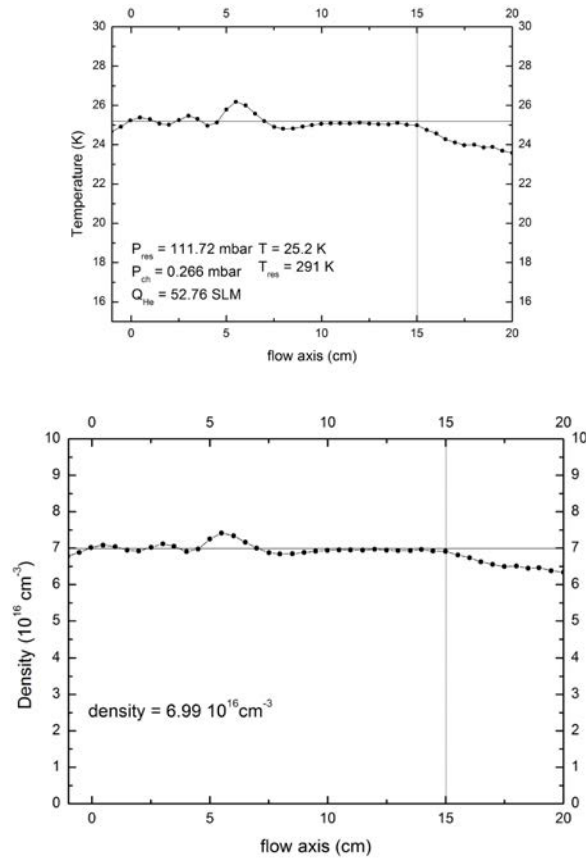


Figure A1.3: Pitot profile for 24 K nozzle with He buffer gas

He 25 K



Ar 15K @ He 25K

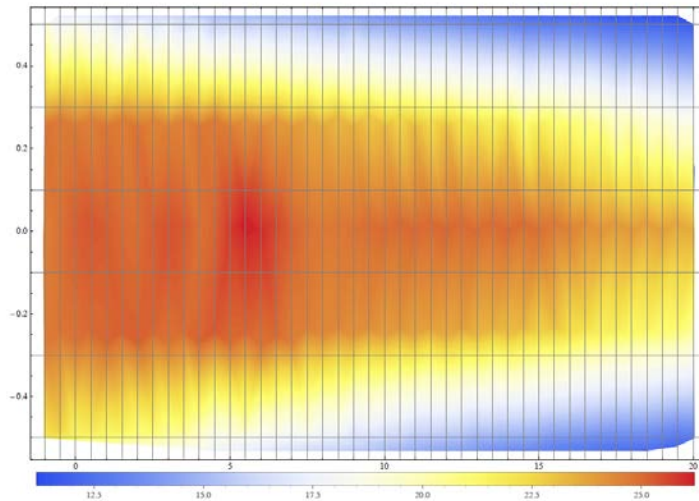


Figure A1.4: Pitot profile for 25 K nozzle with He buffer gas

Ar 35 K

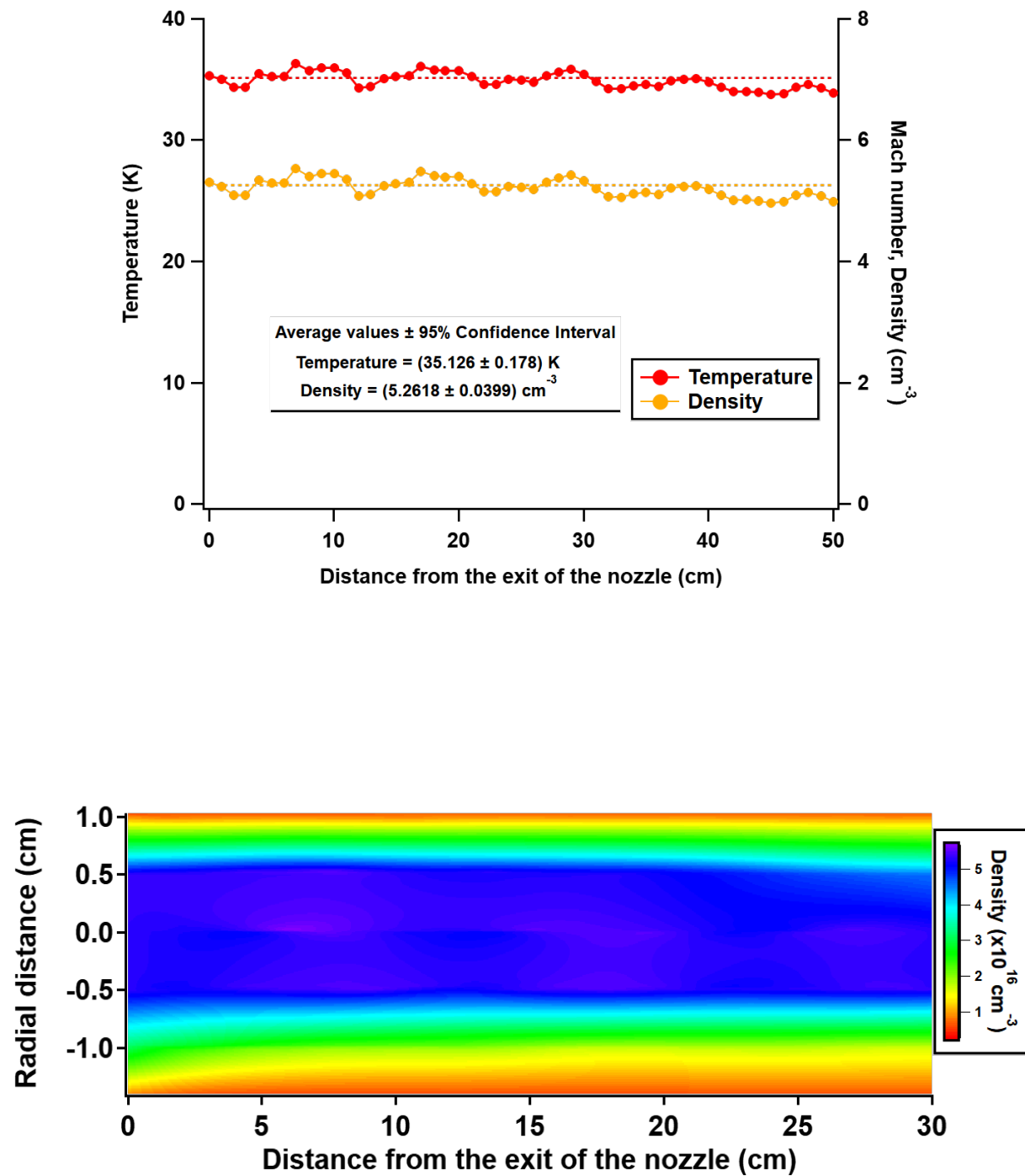
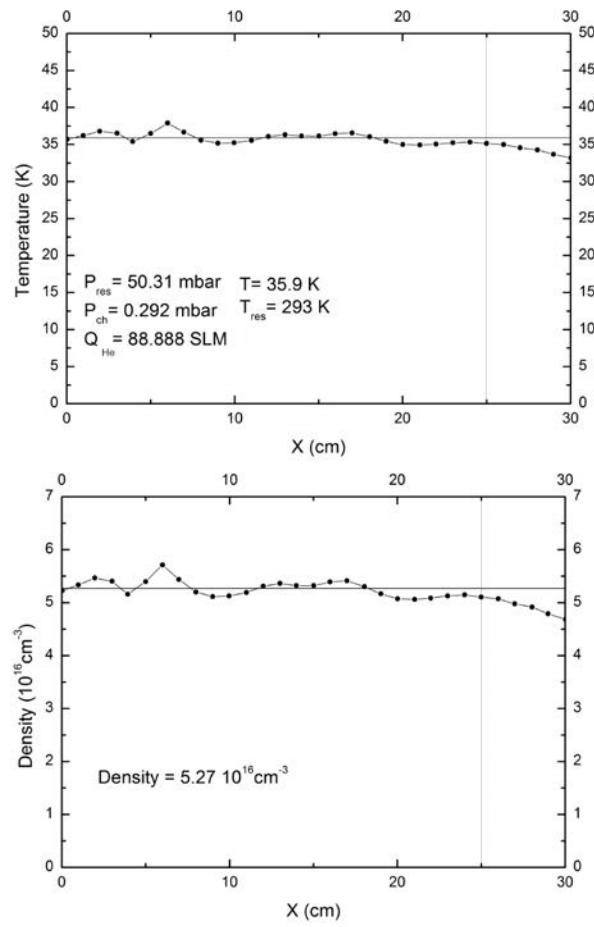


Figure A1.5: Pitot profile for 35 K nozzle with Ar buffer gas

He 36 K



He 36 K

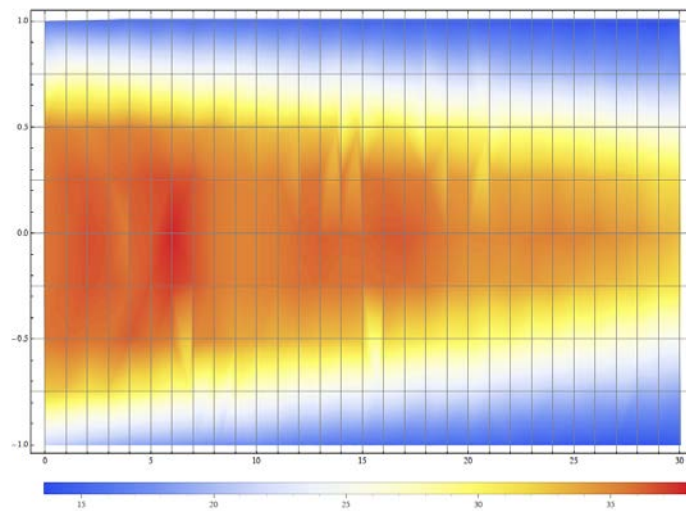


Figure A1.6: Pitot profile for 36 K nozzle with He buffer gas

Ar 53 K

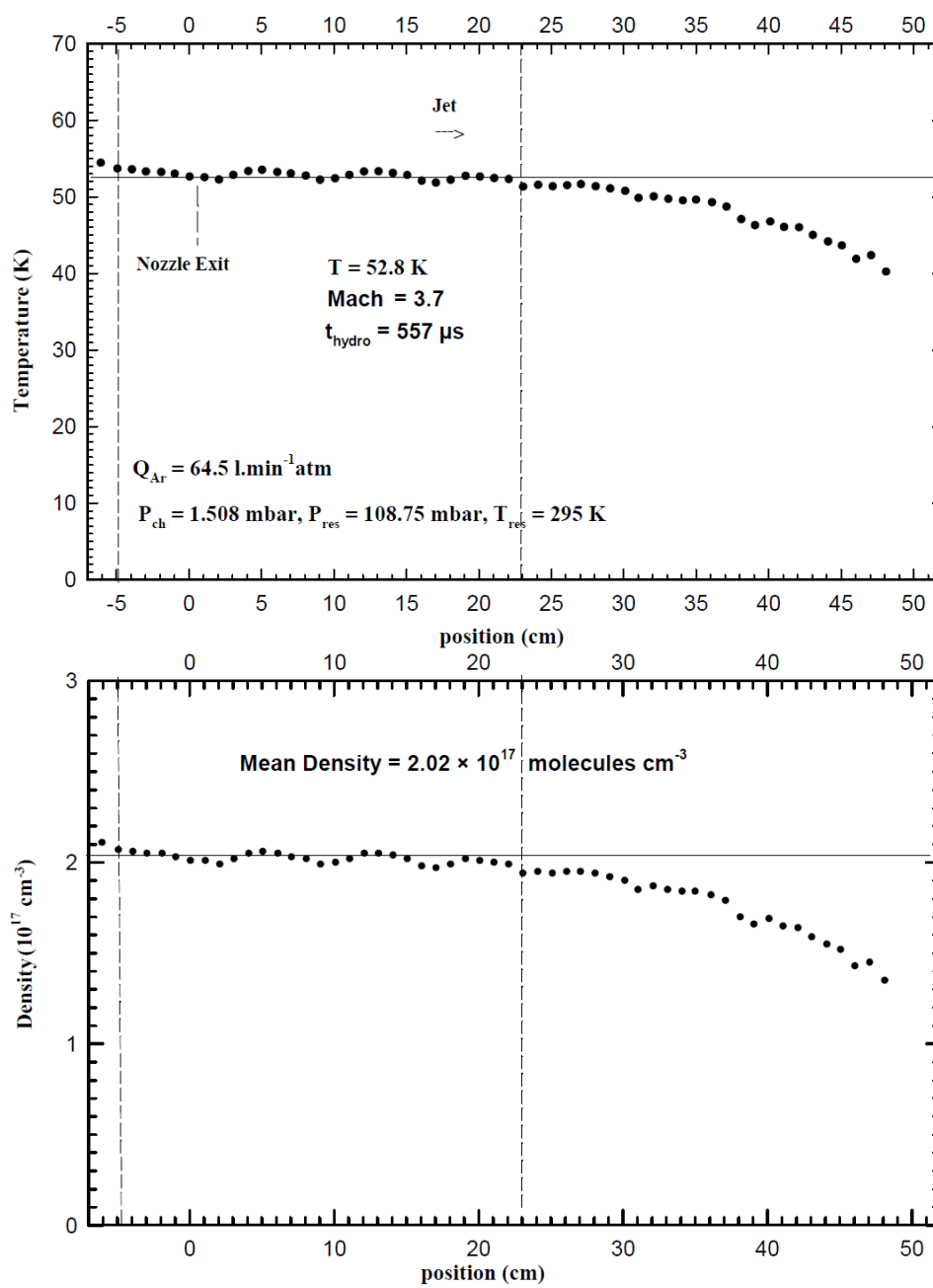
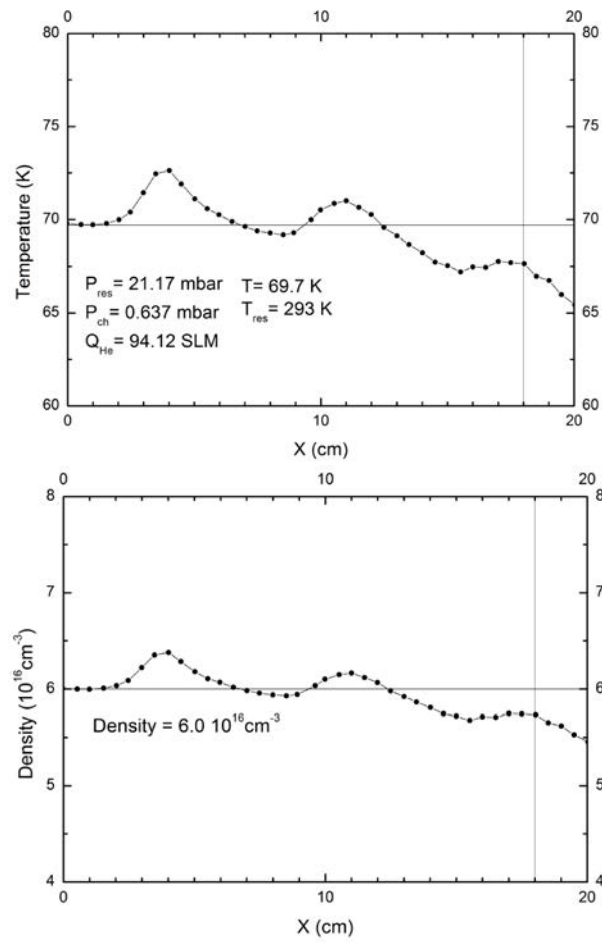


Figure A1.7: Pitot profile for 53 K nozzle with Ar buffer gas

He 72 K



Ar 50 K 0.3 @ He 71 K

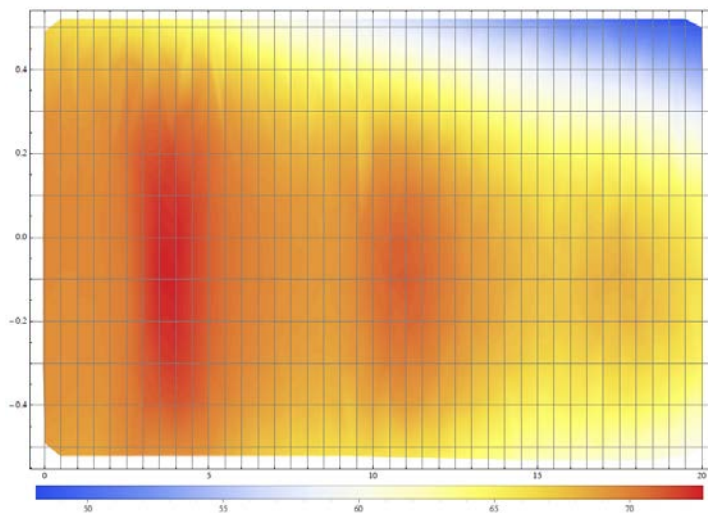
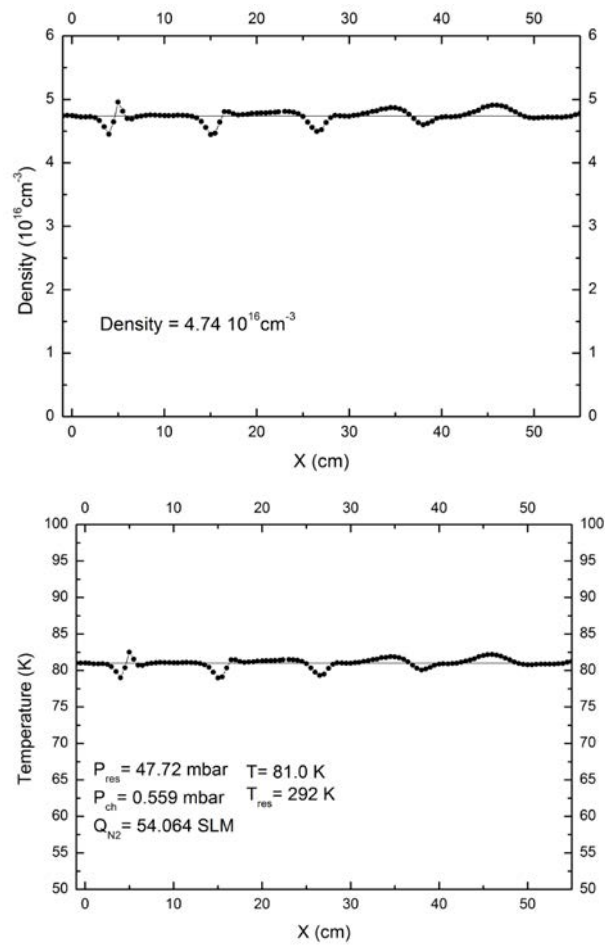
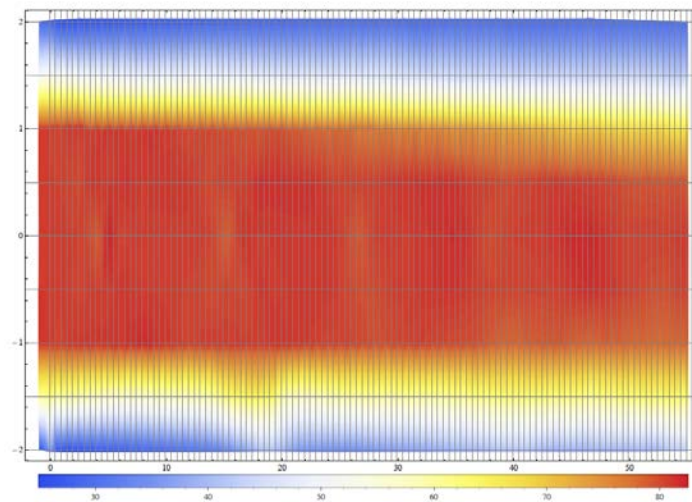


Figure A1.8: Pitot profile for 72 K nozzle with He buffer gas

N₂ 83 K**N₂ 83 K****Figure A1.9:** Pitot profile for 83 K nozzle with N₂ buffer gas

Ar 97 K

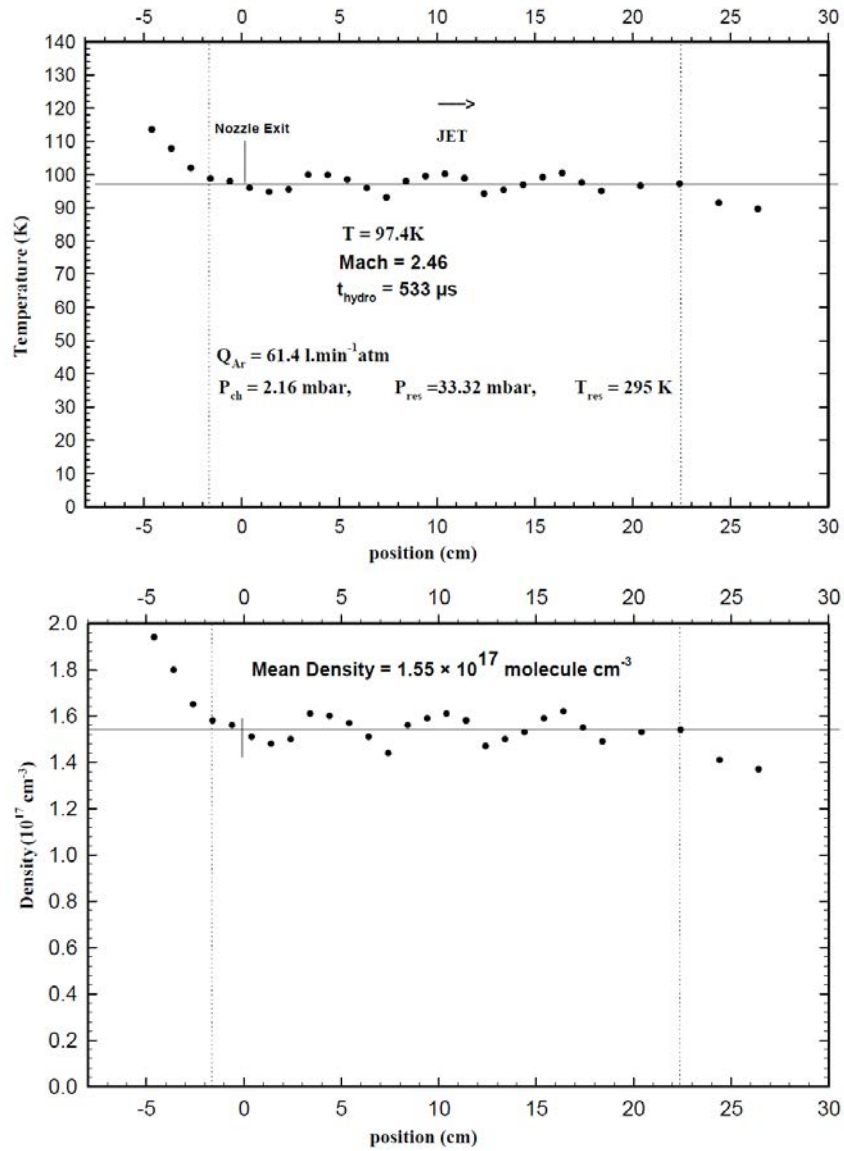
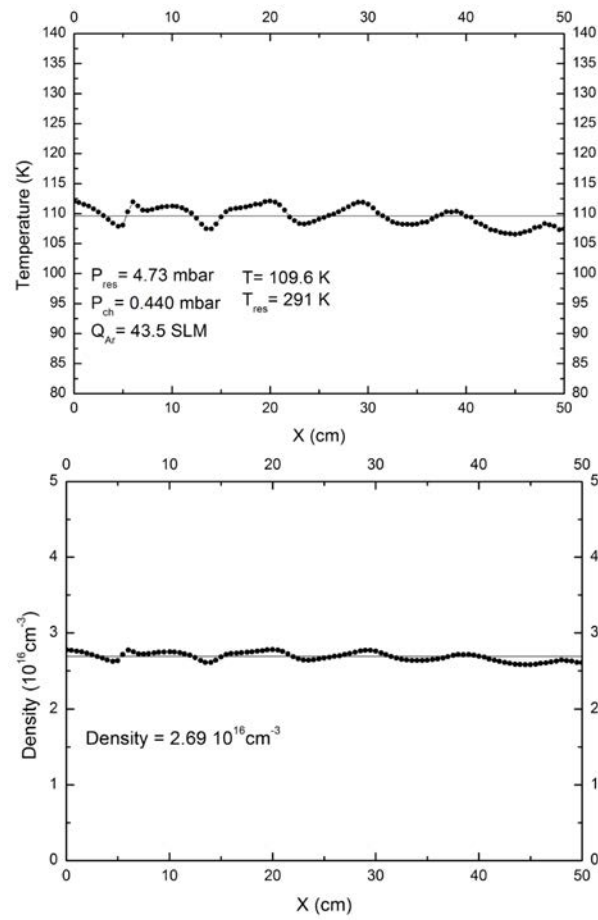


Figure A1.10: Pitot profile for 97 K nozzle with Ar buffer gas

Ar 112 K



Ar 110 K

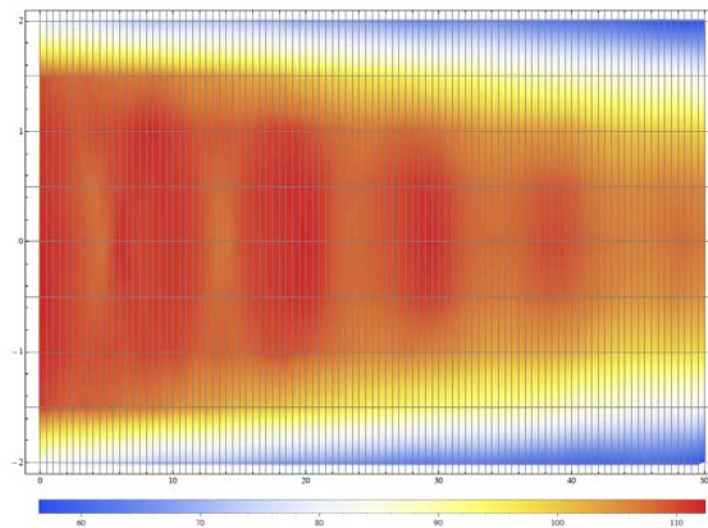


Figure A1.11: Pitot profile for 112 K nozzle with Ar buffer gas

Ar 141 K

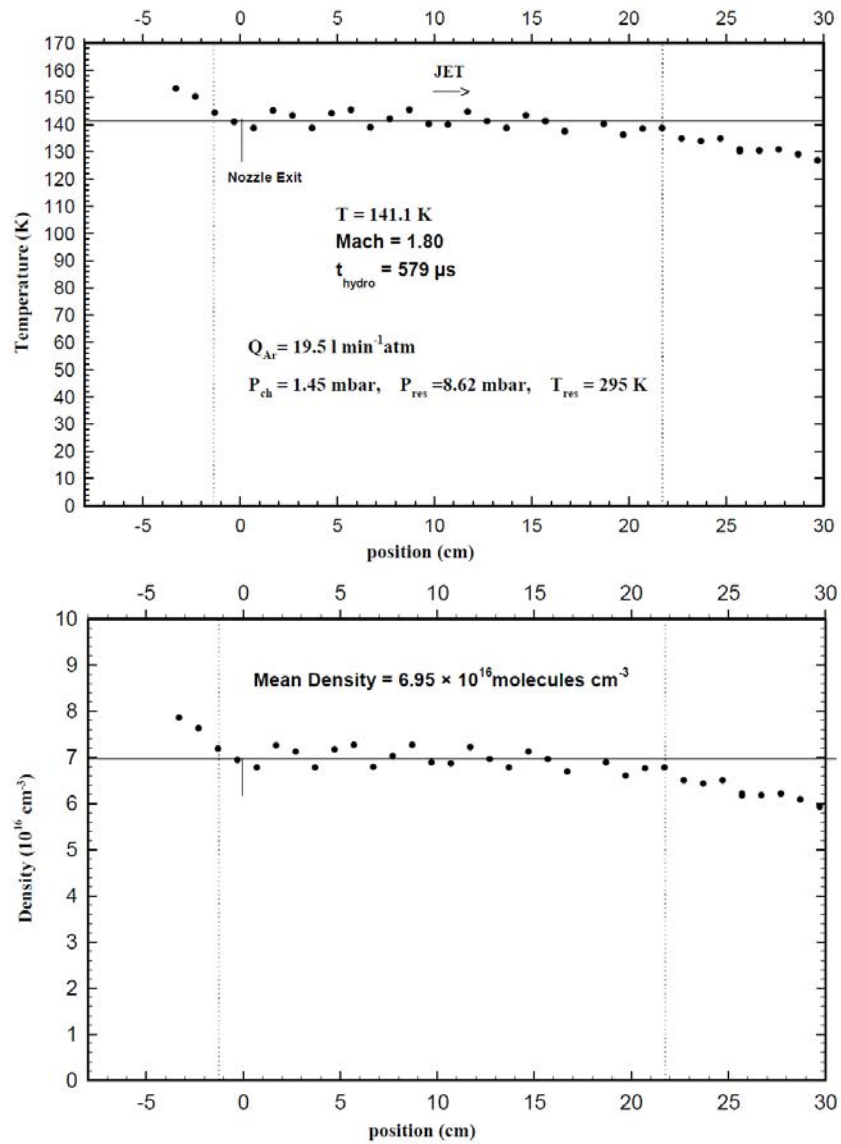


Figure A1.12: Pitot profile for 141 K nozzle with Ar buffer gas

Ar 168 K

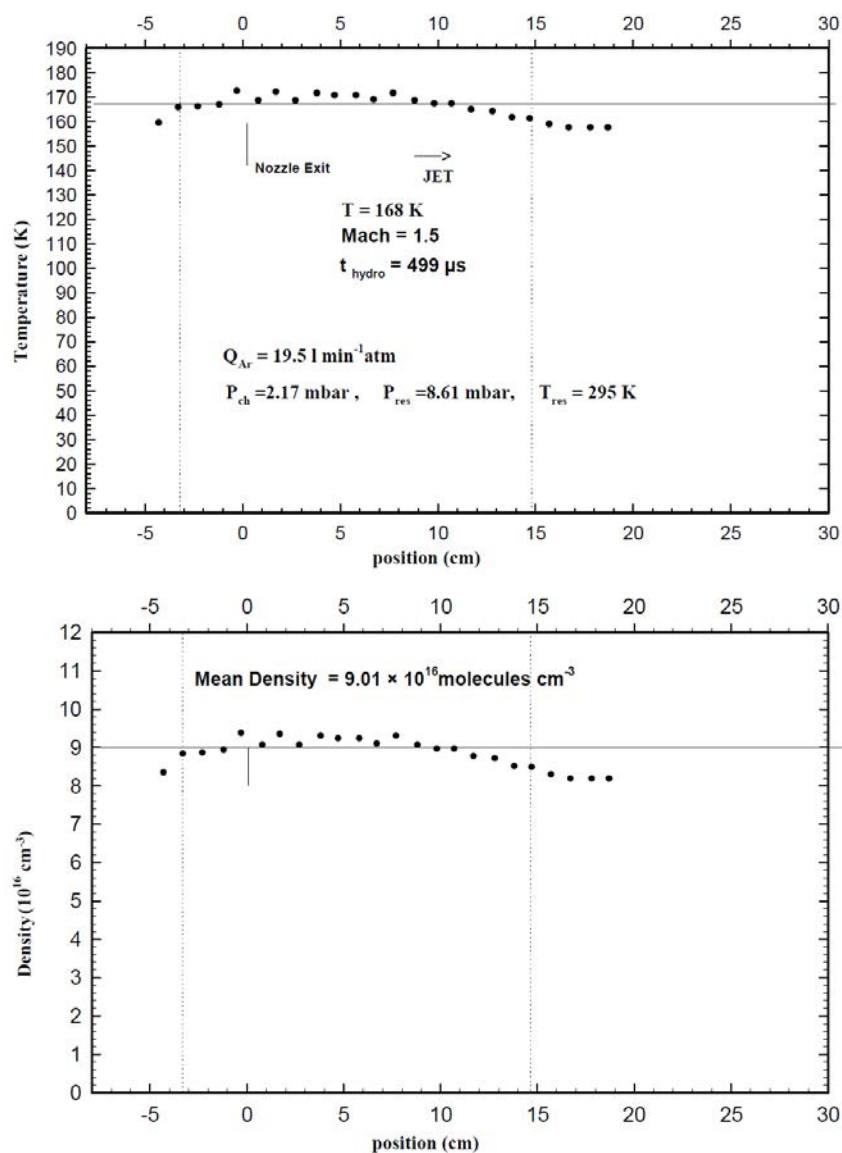


Figure A1.13: Pitot profile for 168 K nozzle with Ar buffer gas

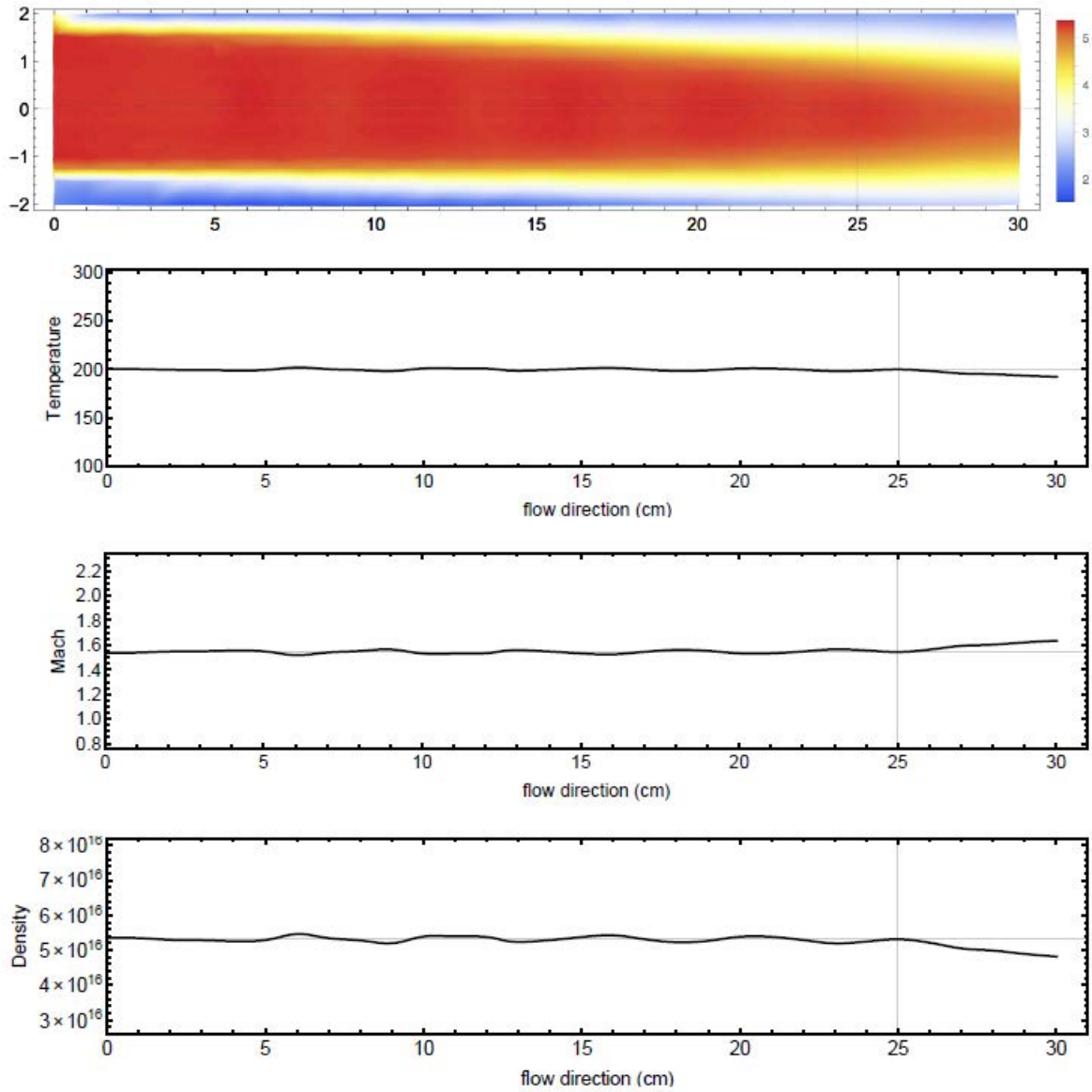
N_2 200 K

Figure A1.14: Pitot profile for 200 K nozzle with N_2 buffer gas

A2 UV-Vis spectrometer analysis

Igor Pro code for estimating ICN density in the flow

```
Function numdensity(wavelength , Io , I , Ioff , wavelength_abs ,
abscrosssec , A, B)

//gives ICN number density in the CRESU flow

//wavelength      = UV Vis wavelength file
//wavelength_abs = Literature wavelength
//A, B= wavelength values range (make sure these values are from
the higher resolution wavelength)

Wave wavelength , Io , I , Ioff , abscrosssec , wavelength_abs
variable A, B

Variable totalND , pressure_ch , buffer_total , pressure_UV , buffer_
vessel , MW, length , pressure_vessel

totalND= 5.26e16 //number density for the nozzle
pressure_ch= 0.28 //in mbar (Chamber)
buffer_total= 18.085 //in slm (Total flow through nozzle)
buffer_vessel=0.304 //slm (flow of buffer gas through precursor)

pressure_UV=75.7 //in mbar (UV cell)
pressure_vessel= 77.7 //in mbar (ICN vessel)

MW=105.92 //molar mass

//length=23 //of the Uv cell (in cm)
length=60.5 //of the Uv cell (in cm)

Variable totalnumdens

totalnumdens=6.023E+23*pressure_UV*0.000986923/(82.05745*294.15)
//molecules cm-3, pressure converted from mbar to atm
```

```

//print totalnumdens

Variable n
Wave I_int , Io_int , Ioff_int , wavelength_int , numdens

Duplicate/O Io Io_int
Duplicate/O I I_int
Duplicate/O Ioff Ioff_int
Duplicate/O abscrosssec abscrosssec_new

//Use this when the UV-Vis measurements have lower resolution
than literature absorption cross-section

//Duplicate/O wavelength_abs wavelength_int
//Interpolate2 /T=1 /I=3 /Y=I_int /X=wavelength_int wavelength , I
//Interpolate2 /T=1 /I=3 /Y=Io_int /X=wavelength_int wavelength , Io

//Use this when the UV-Vis measurements have higher resolution than
literature absorption cross-section

Duplicate/O wavelength wavelength_int
Interpolate2 /T=1 /I=3 /Y=abscrosssec_new /X=wavelength wavelength_abs ,
abscrosssec

Extract/INDX wavelength_int , indstart , wavelength_int==A //wavelength
range
Extract/INDX wavelength_int , indlast , wavelength_int==B

A=indstart [0]
B=indlast [0]

print A,B

make/O/N=(B-A+1) absorb

for (n=0;n<(numpnts(aborb));n+=1)
    absorb [n]=-log (( I_int [A+n]-Ioff_int [A+n])/( Io_int [A+n]
    -Ioff_int [A+n]))
    //print absorb [n]

```

```

endfor

display absorb vs wavelength_int[A,B]
AppendToGraph/R abscrossec_new[A,B] vs wavelength_int[A,B]
ModifyGraph lsize=1.2,rgb(abscrossec_new)=(0,0,0)
Legend/C/N=text0/A=MC
Label bottom "Wavelength□(nm)"
SetAxis left 0,*

Make/O/N=(B-A+1) numdens

for (n=0;n<numpts(numdens);n+=1)
    numdens[n]= ln((Io_int[A+n]-Ioff_int[A+n])/(I_int[A+n]-
    Ioff_int[A+n]))/(abscrossec_new[A+n]*length)
endifor

Variable actualnumdens_avg

actualnumdens_avg=mean(numdens)

print "ICN□number□density□from□UV-Vis□measurements□=□",
actualnumdens_avg

variable ICNvaporpress, ICNnumdensflow //ICNvaporpress is the c
alculated vapor pressure based on the UV cell number density measurements

ICNvaporpress = ((actualnumdens_avg/(6.023e23))*(298*83.14472
*1000)/pressure_UV)*pressure_vessel //molar density*T*R/pressure

ICNnumdensflow = (ICNvaporpress/pressure_vessel)*(buffer_vessel
/(buffer_total))*totalND

print "Expected□ICN□number□density□=□", ICNnumdensflow
print "Effective□vapor□pressure□=□", ICNvaporpress

Make/O/N=(numpts(numdens)) abscrossec_fit

for (n=0;n<numpts(numdens);n+=1)
    abscrossec_fit[n]= ln((Io_int[A+n]-Ioff_int[A+n])/(I_int

```

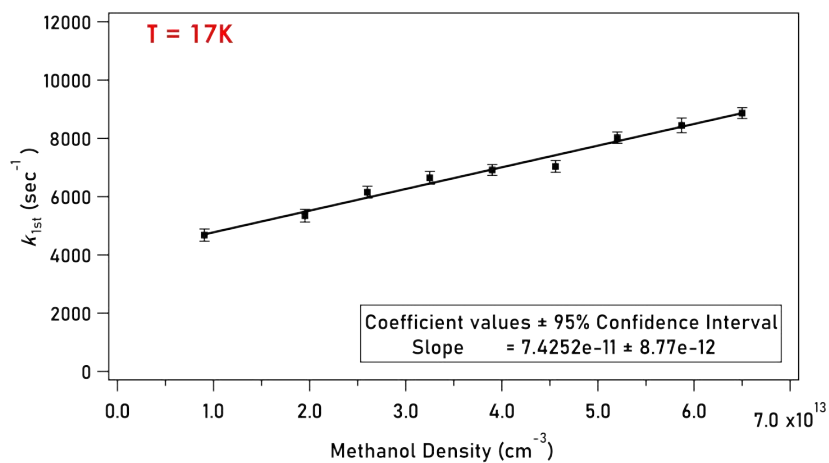
```
[A+n]-Ioff_int[A+n]))/(actualnumdens_avg*length)
endfor

AppendToGraph/R abscrossec_fit vs wavelength_int[A,B]
ModifyGraph lsize=1.2,rgb(abscrossec_fit)=(0,0,65535)
Legend/C/N=text0/A=MC

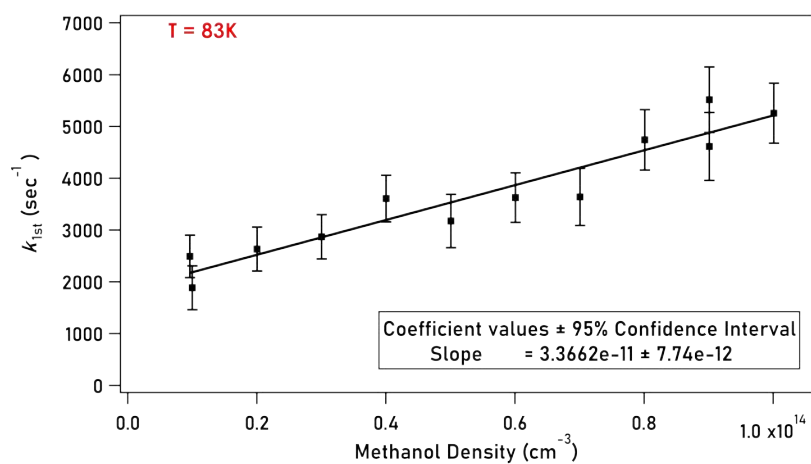
end
```

A3 Second order plots

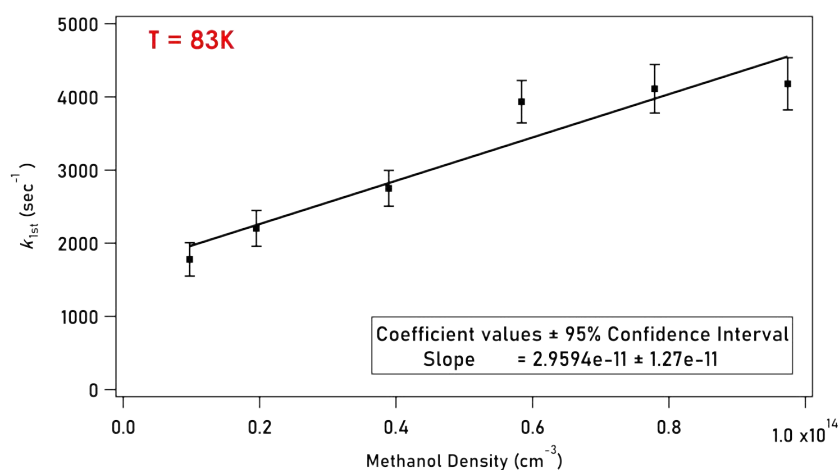
A3.1 CN + Methanol



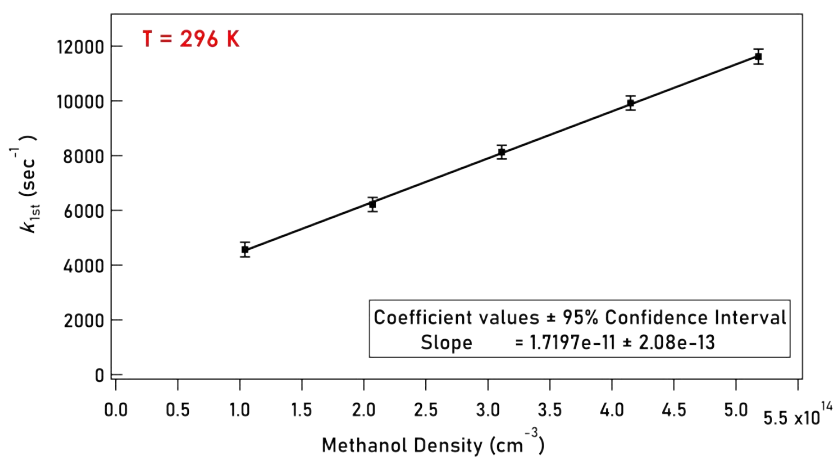
Second order plot for CN + methanol at 17 K.



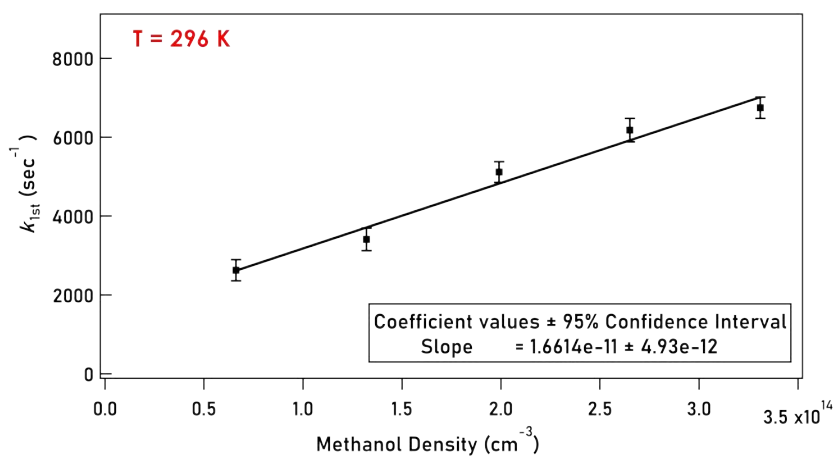
Second order plot for CN + methanol at 83 K.



Second order plot for CN + methanol at 83 K.

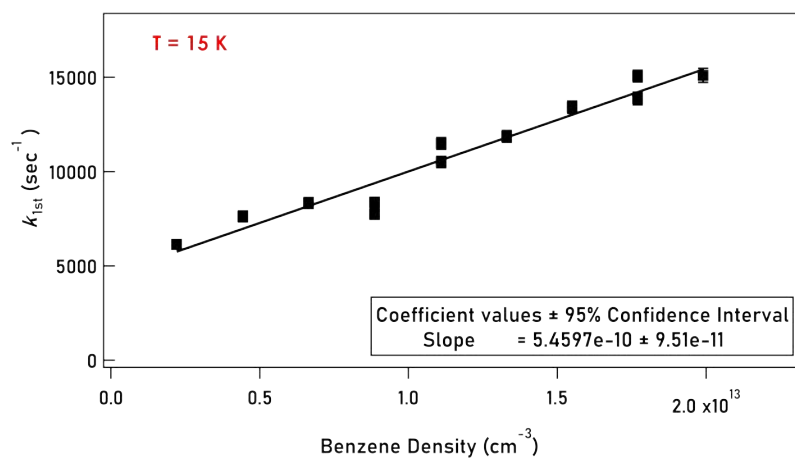


Second order plot for CN + methanol at 296 K (Room temperature).

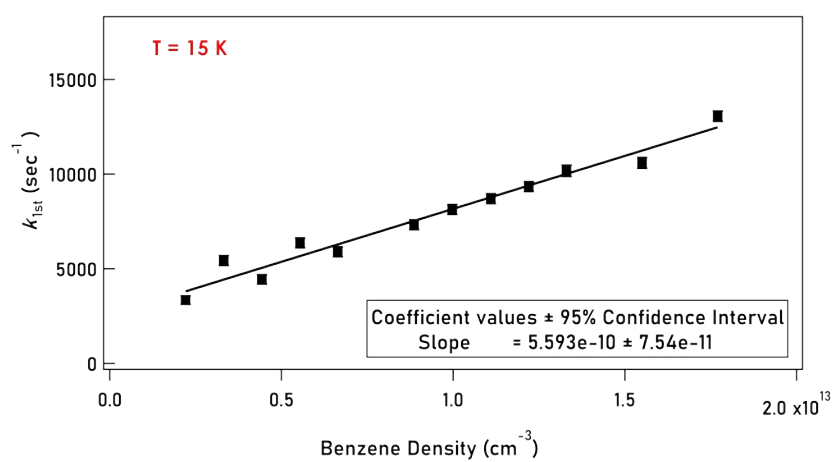


Second order plot for CN + methanol at 296 K (Room temperature).

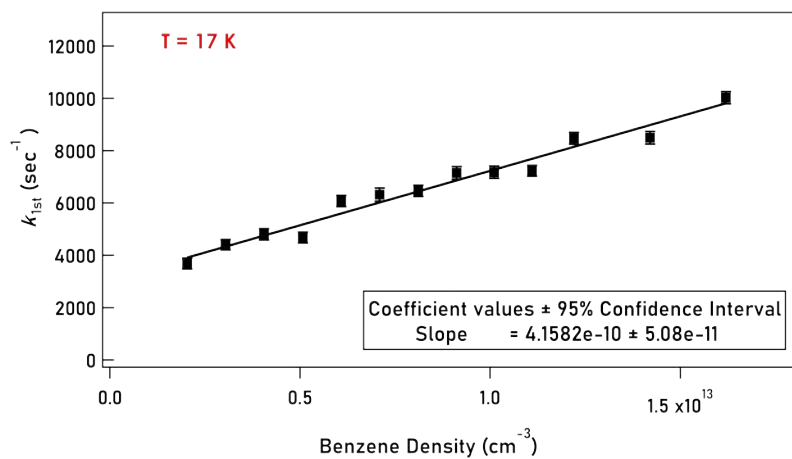
A3.2 CN + Benzene



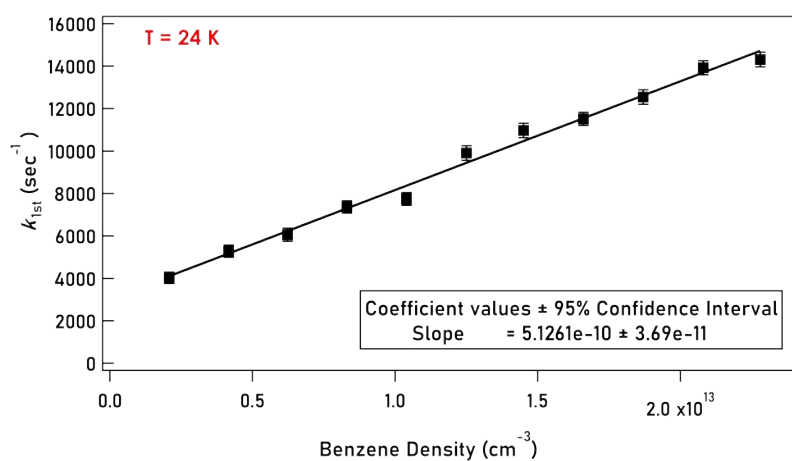
Second order plot for CN + benzene at 15 K.



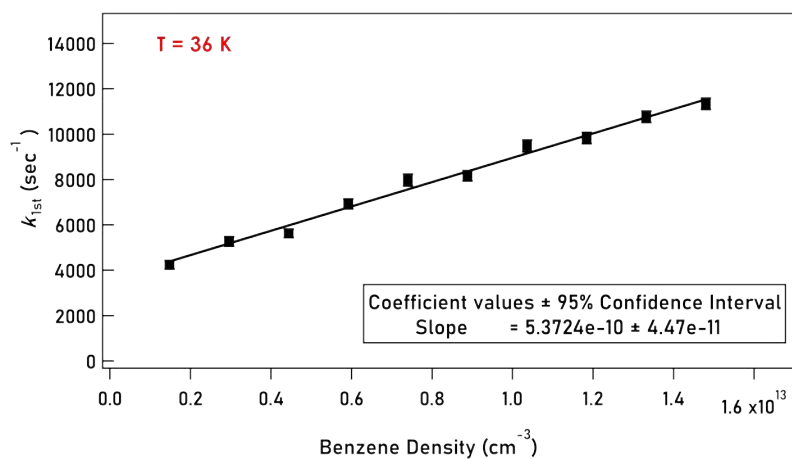
Second order plot for CN + benzene at 15 K.



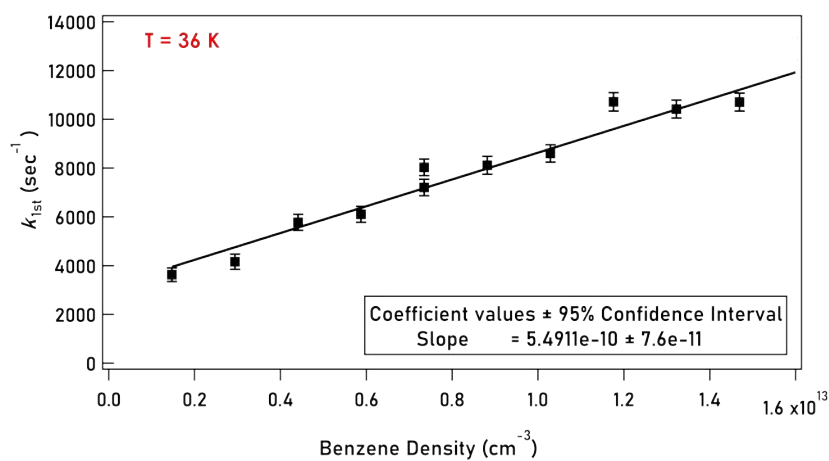
Second order plot for CN + benzene at 17 K.



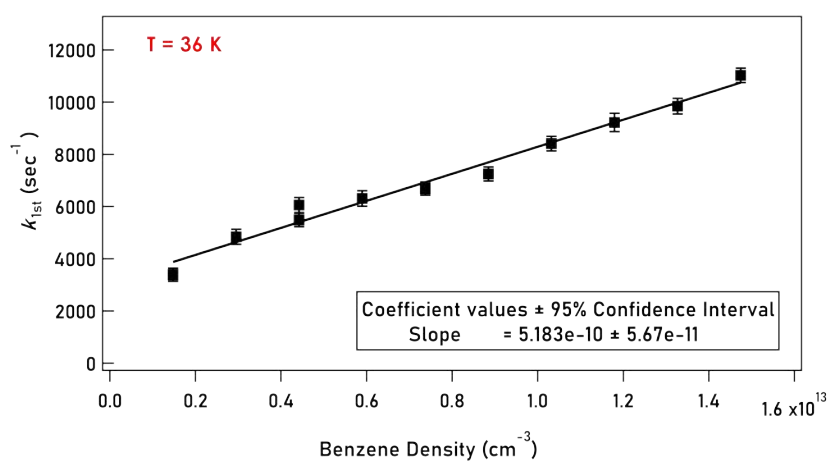
Second order plot for CN + benzene at 24 K.



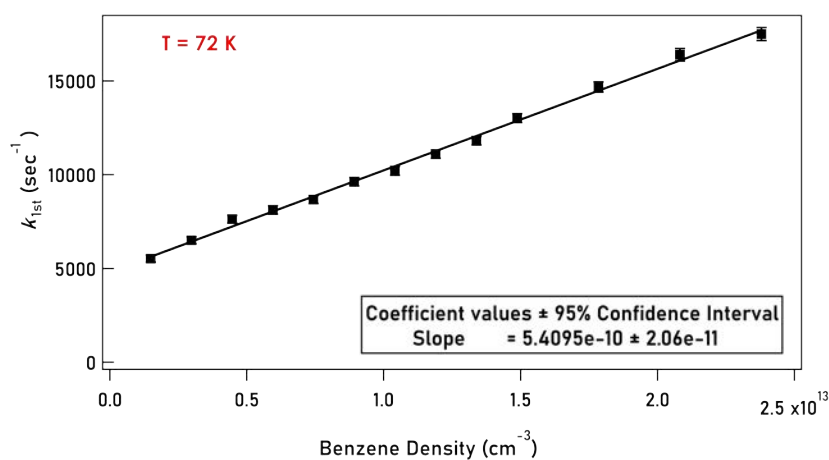
Second order plot for CN + benzene at 36 K.



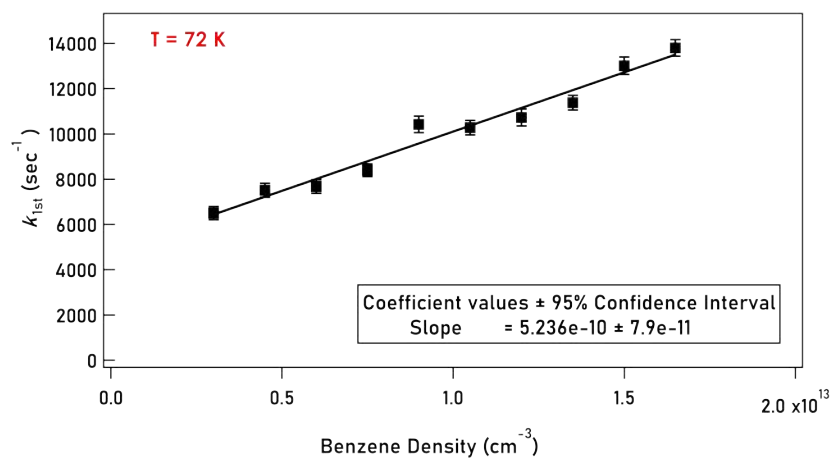
Second order plot for CN + benzene at 36 K.



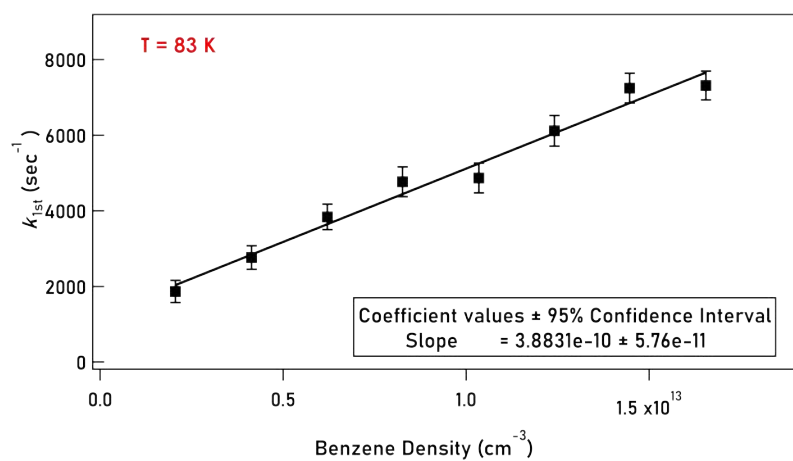
Second order plot for CN + benzene at 36 K.



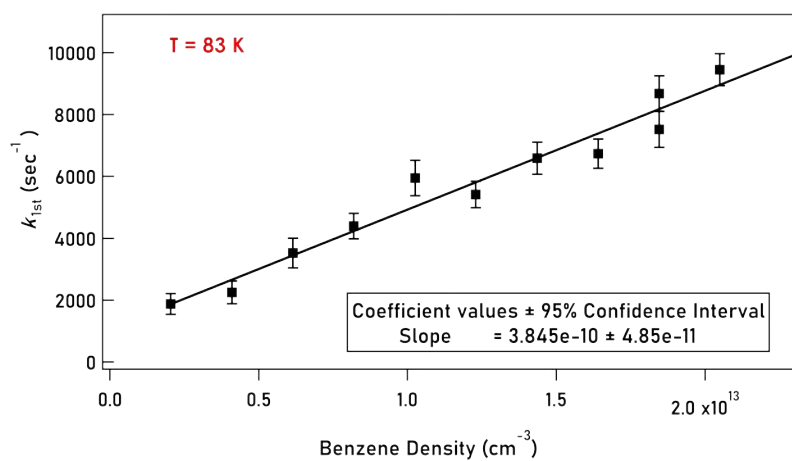
Second order plot for CN + benzene at 72 K.



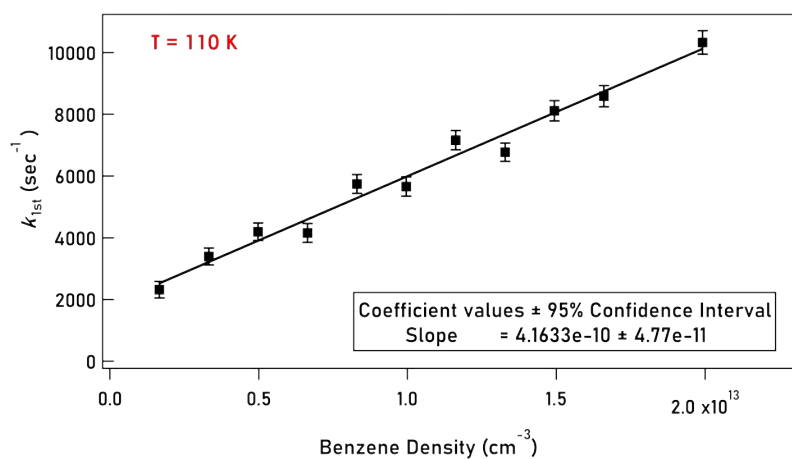
Second order plot for CN + benzene at 72 K.



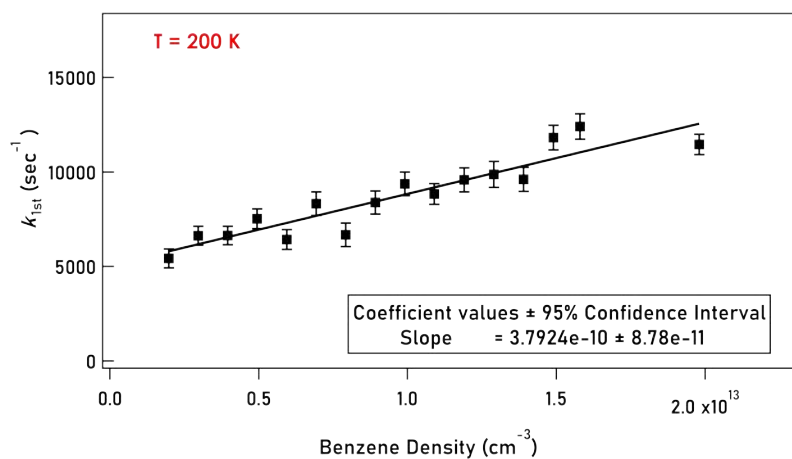
Second order plot for CN + benzene at 83 K.



Second order plot for CN + benzene at 83 K.

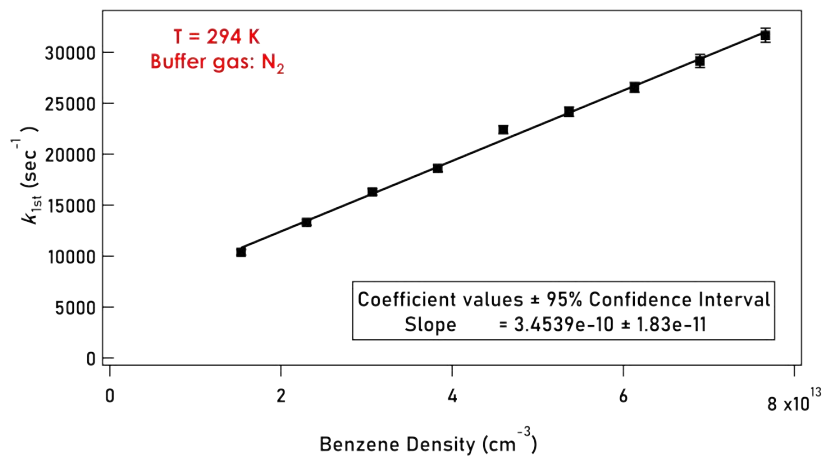


Second order plot for CN + benzene at 110 K.

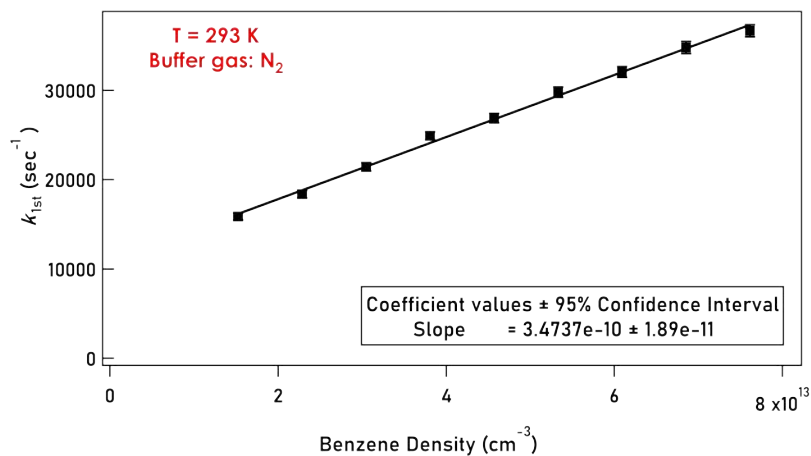


Second order plot for CN + benzene at 200 K.

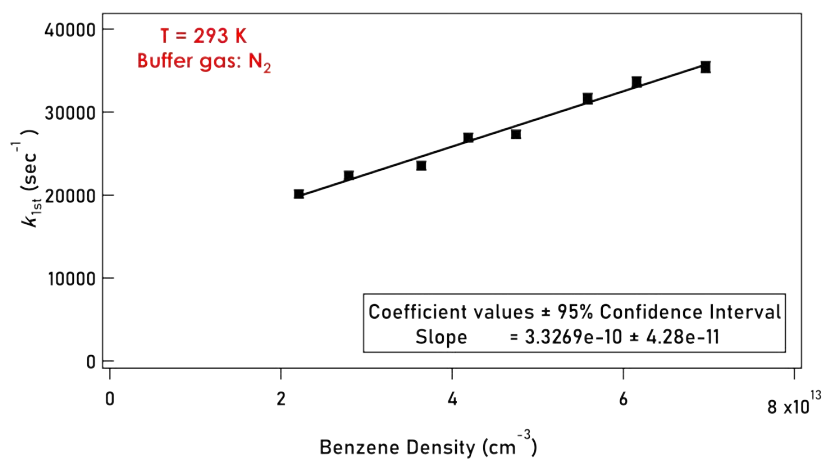
A3.3 CN + Toluene



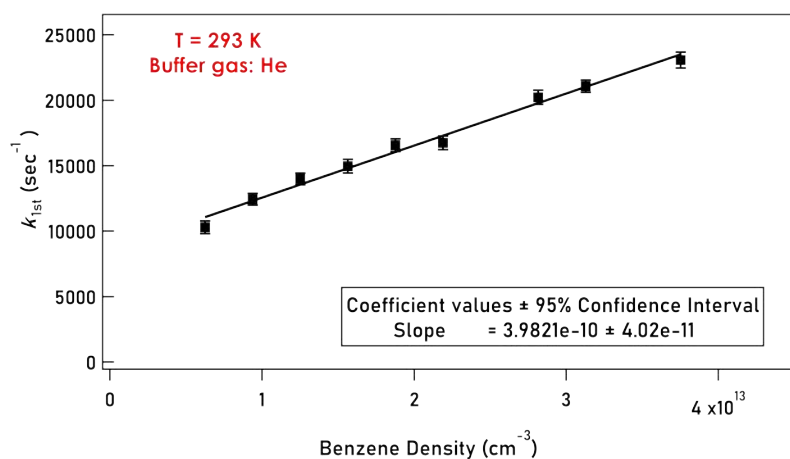
Second order plot for CN + benzene at 294 K (Room temperature), N₂ buffer gas.



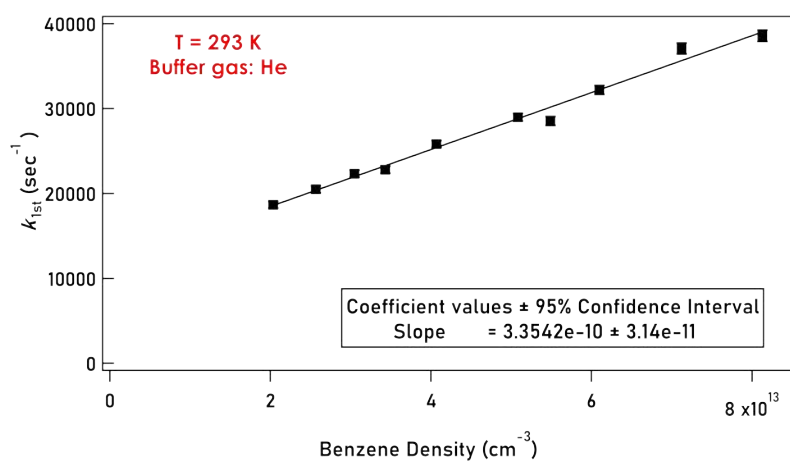
Second order plot for CN + benzene at 293 K (Room temperature), N₂ buffer gas.



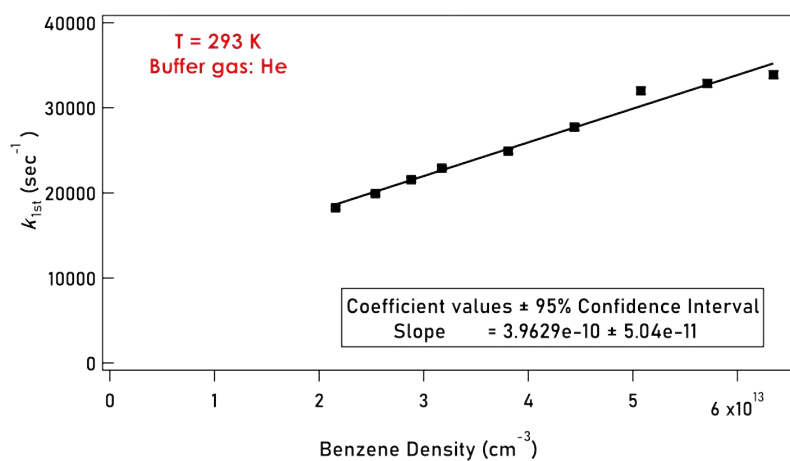
Second order plot for CN + benzene at 293 K (Room temperature), N₂ buffer gas.



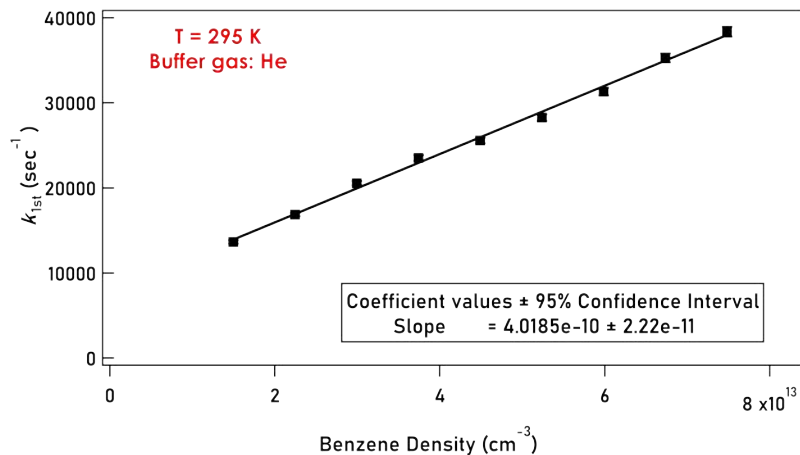
Second order plot for CN + benzene at 293 K (Room temperature), He buffer gas.



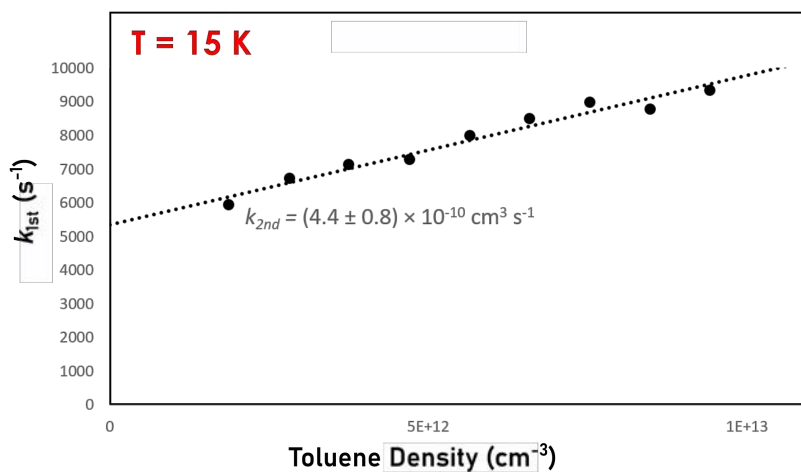
Second order plot for CN + benzene at 293 K (Room temperature), He buffer gas.



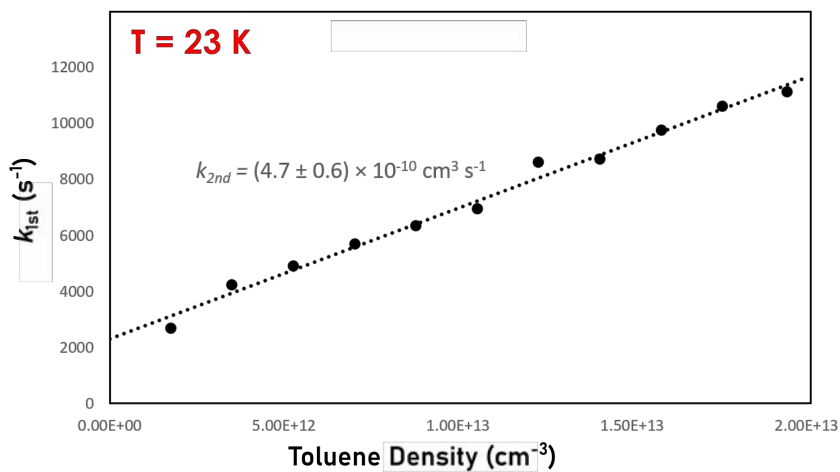
Second order plot for CN + benzene at 293 K (Room temperature), He buffer gas.



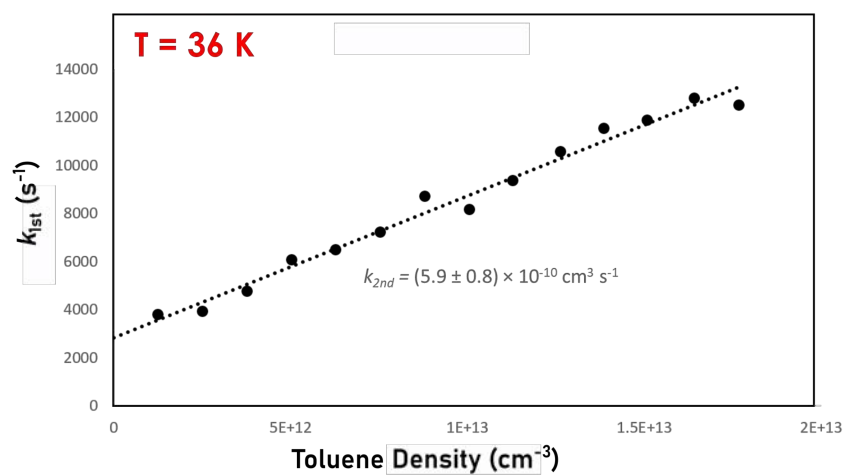
Second order plot for CN + benzene at 295 K (Room temperature), He buffer gas.



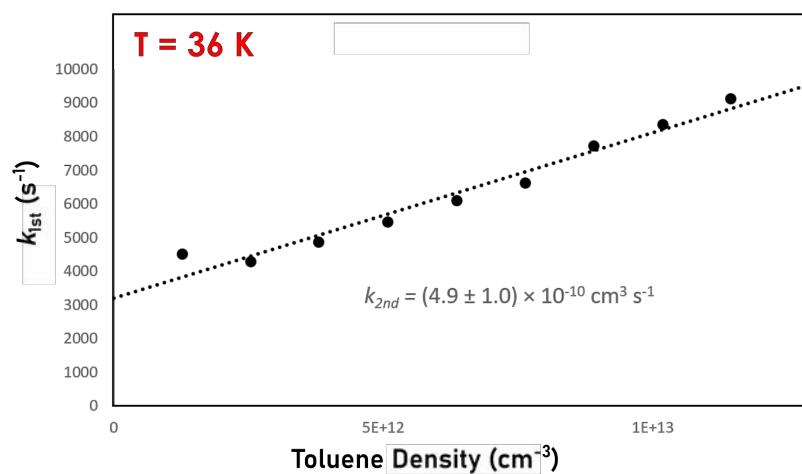
Second order plot for CN + toluene at 15 K.



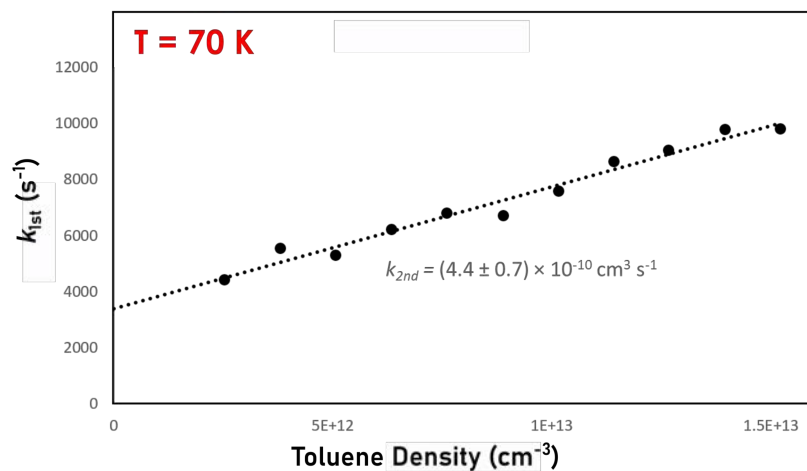
Second order plot for CN + toluene at 24 K.



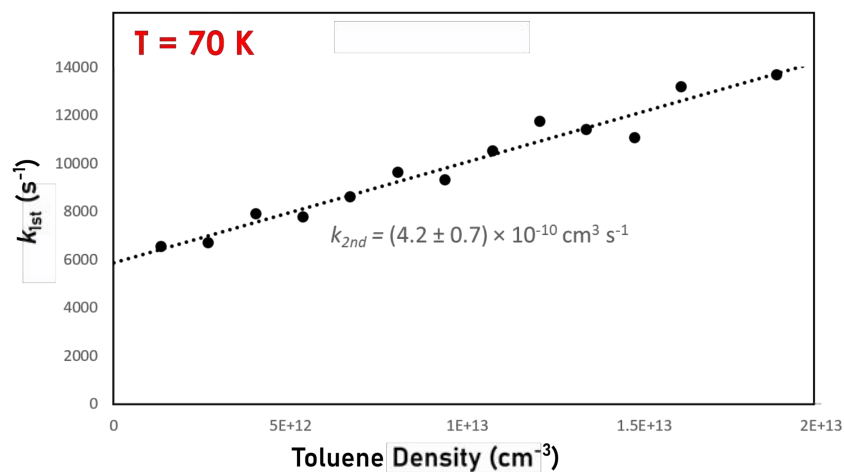
Second order plot for CN + toluene at 36 K.



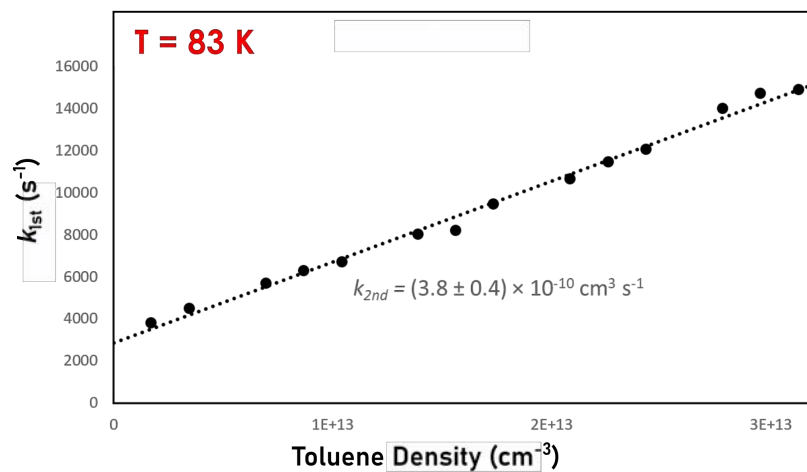
Second order plot for CN + toluene at 36 K.



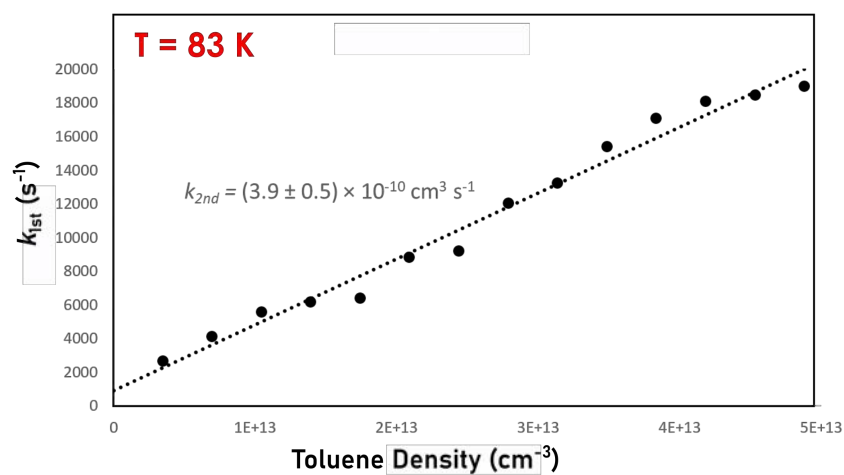
Second order plot for CN + toluene at 70 K.



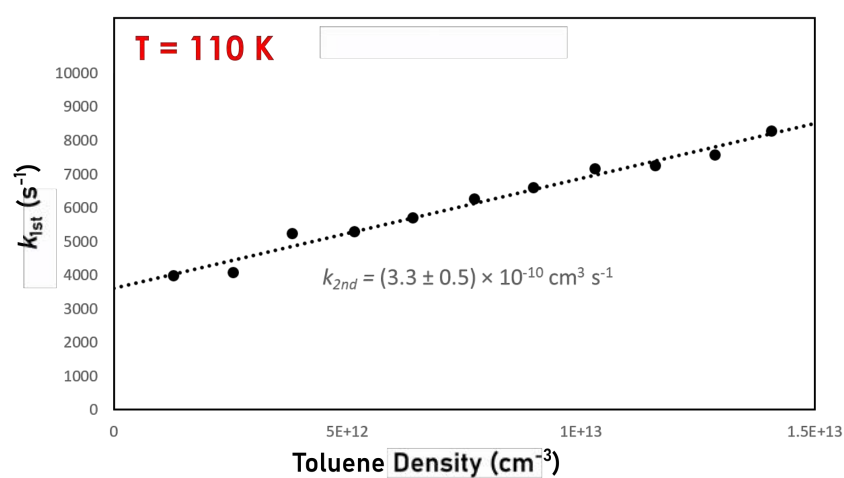
Second order plot for CN + toluene at 70 K.



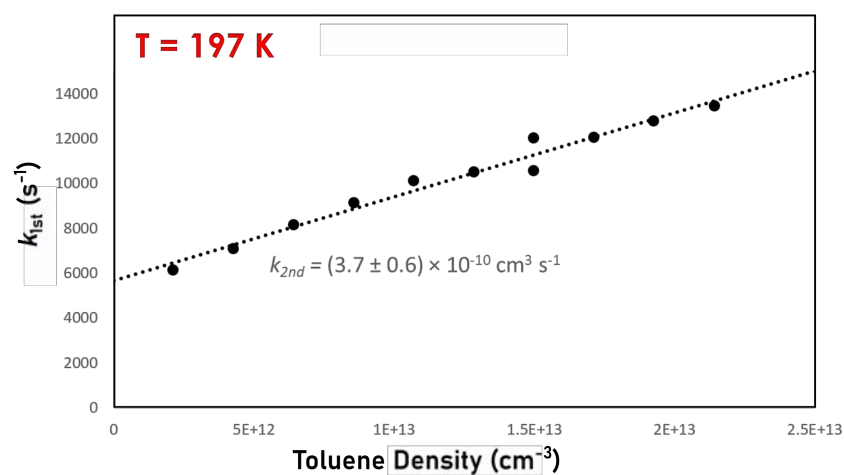
Second order plot for CN + toluene at 83 K.



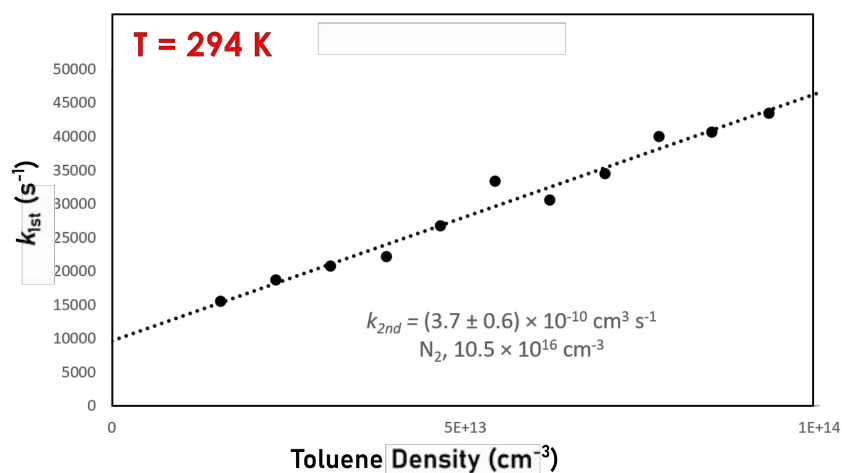
Second order plot for CN + toluene at 83 K.



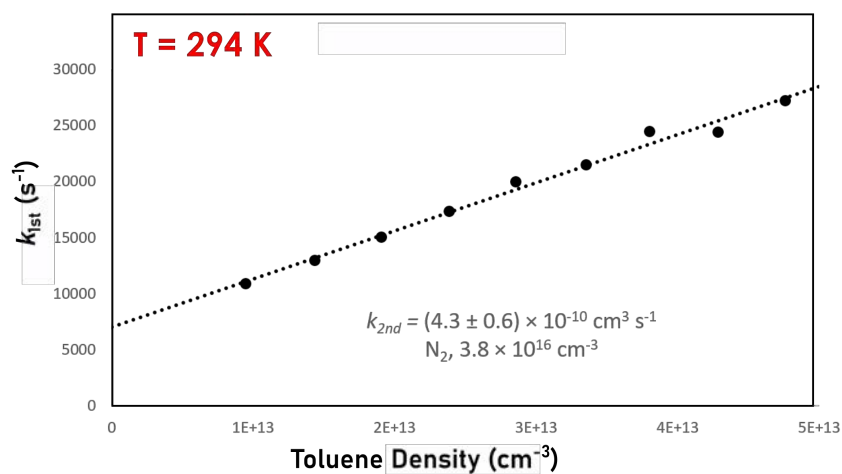
Second order plot for CN + toluene at 110 K.



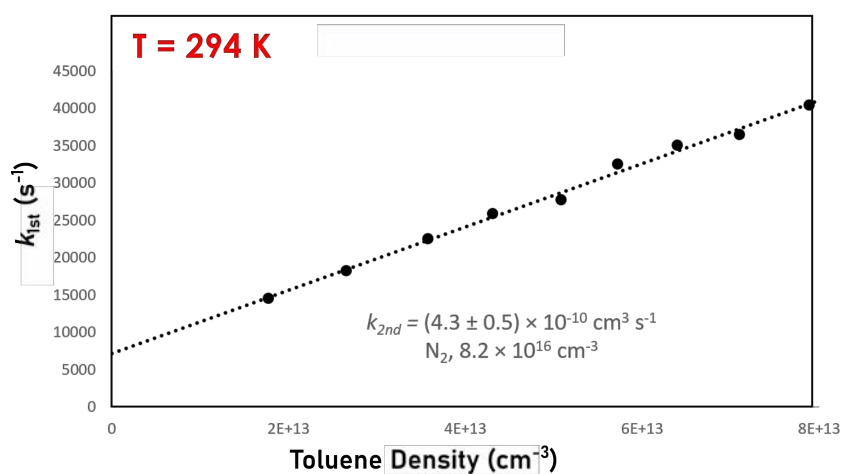
Second order plot for CN + toluene at 197 K.



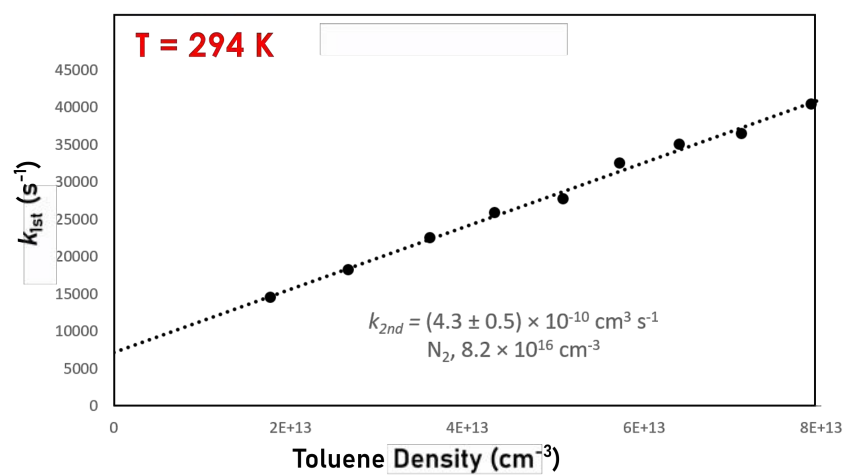
Second order plot for CN + toluene at 294 K (Room temperature), N₂ buffer gas.



Second order plot for CN + toluene at 294 K (Room temperature), N₂ buffer gas.



Second order plot for CN + toluene at 294 K (Room temperature), N₂ buffer gas.



Second order plot for CN + toluene at 294 K (Room temperature), He buffer gas.

A4 ICN spectrum and comparison

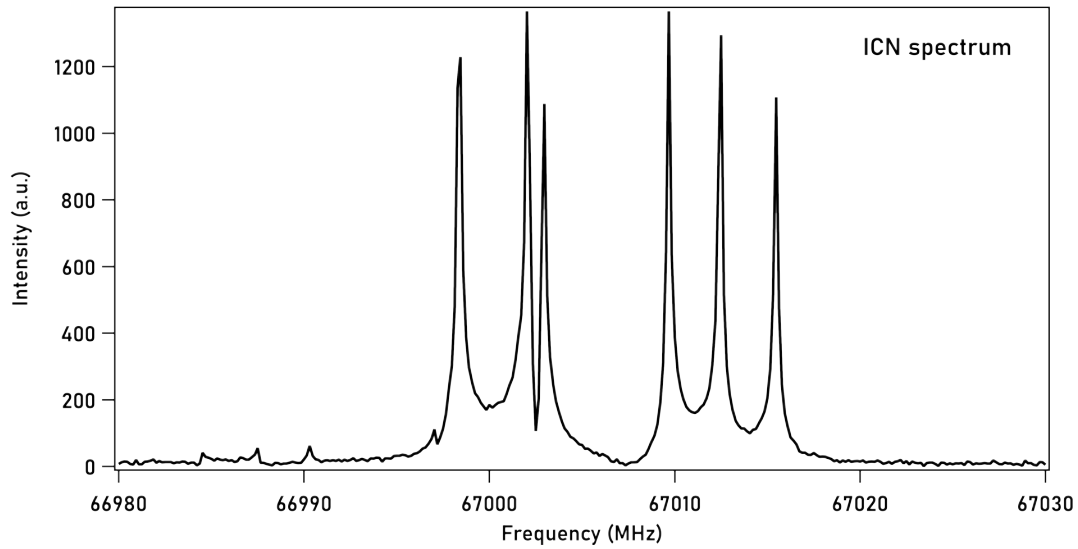


Figure A4.1: ICN microwave spectrum

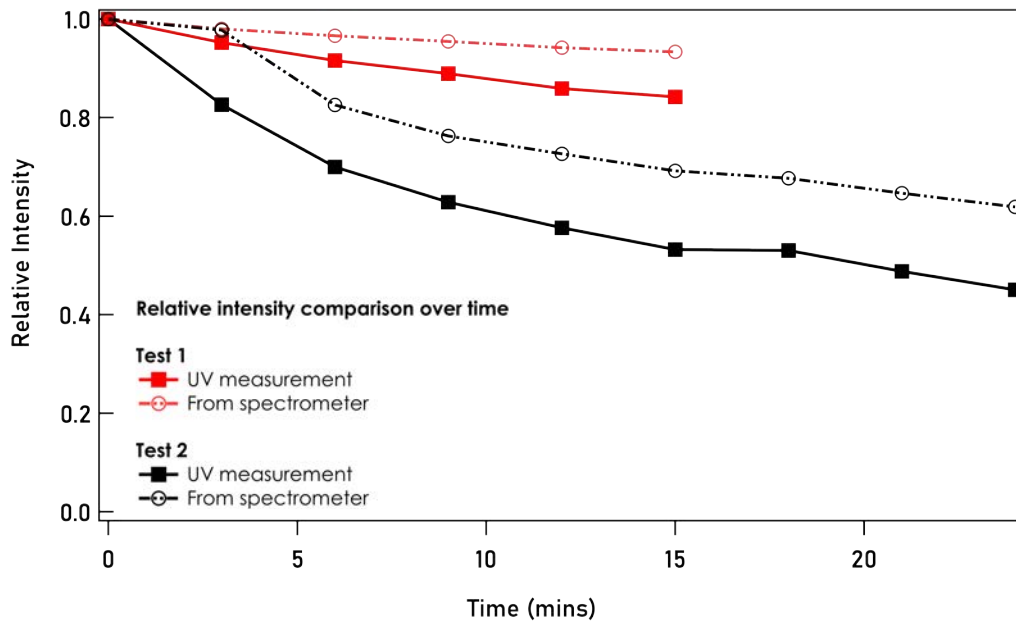


Figure A4.2: Comparison of the relative intensities measured over time for ICN in the CRESU flow measured with chirped pulse microwave spectroscopy and calculated using UV-Vis spectrometer

A5 VAR and INT files for the cyanopropene isomers

Trans 1-cyanopropene

VAR File

TRANSCROTONILE

```

11 5967 11 5 0.0000E+000 1.1000E+001
1.0000E+000 1.00000000000
a 1 1 0,50, , , , , , 0 ,
      10000 3.8054000000000010E+004 -0.000000000 /A
      20000 2.297075046224000E+003 -0.000000 /B
      30000 2.195186936220000E+003 -0.000000 /C
      200 -0.287435000000000E-003 0.0000E-03 /Delta_J
      2000 -1.573881133000000E-027 0.000000000E-27 /Delta_K
      1100 1.877211400000000E-002 -0.000000 /Delta_JK
      40100 -0.011993847000000E-021 -0.000000000E-21 /-del_J
      41000 -0.012129138000000E-021 -0.000000000E-21 /-del_K
110010000 -3.721621900000000E+000 0.00000 /chi_aa
110020000 1.820480000000000E+000 -0.000 /chi_bb

```

INT File

Trans-crotonitrile

```

0000 52023 350.6547, 0, 100, -10.0,-9.0, 100, 9.375
001 4.35
002 1.91
003 0.00

```

Cis 1-cyanopropene

VAR File

CIS-CROTONITRILE

June 18 2021

```

11 110 11 5 0.0000E+000 1.1000E+001
1.0000E+000 1.00000000000
a 1 1 0,50, , , , , , 0 ,
      10000 1.185444941000000E+004 1.000000000E+000 /A
      20000 3.524697711450000E+003 1.000000000E+000 /B
      30000 2.759742937300000E+003 1.000000000E+000 /C

```

```

200 -2.731538400000000E-003 1.00000000E+000 /-DJ
2000 -6.580159000000000E-002 1.00000000E+000 /-DK
1100 1.821065300000000E-002 1.00000000E+000 /-DJK
40100 -8.747154000000000E-004 1.00000000E+000 /-dJ
41000 -5.252616700000000E-003 1.00000000E+000 /-dK
      300 5.204930000000000E-009 1.00000000E+000 /PhiJ
      2100 -2.322000000000000E-007 1.00000000E+000 /PhiKJ
      40200 2.287820000000000E-009 1.00000000E+000 /phiJ
10010000 -1.895849000000000E+000 1.00000000E+000 /Eaa
10020000 -1.055650000000000E-001 1.00000000E+000 /Ebb
10030000 2.001365000000000E+000 1.00000000E+000 /Ecc

```

INT File

Cis-crotonitrile

```

0000 52023 452.8271, 0, 100, -10.0,-9.0, 9.375, 9.375
001 3.74
002 1.63
003 0.00

```

2-cyanopropene

VAR File

METHYLACRYLONITRILE

Tue Apr 27 16:43:01 2021

```

10 72 11 5 0.0000E+000 1.1000E+001
1.0000E+000 1.0000000000
a 1 1 0,50, , , , , , 0 ,
10000 9.291324977556440E+003 4.66236548E-003 /A
20000 4.166448682858881E+003 8.26250192E-004 /B
30000 2.924654929756764E+003 6.90669987E-004 /C
200 -7.676389874441016E-004 5.22670792E-007 /-DJ
1100 -1.389770959049683E-002 3.06113272E-006 /-DJK
2000 4.700599161140623E-003 5.40901091E-005 /-DK
40100 -2.668232996953333E-004 2.06865504E-007 /-dJ
41000 -8.686024920440348E-003 8.18225567E-006 /-dK
41100 7.496758037499224E-008 7.20280775E-009 /phiJK
42000 -5.078897253379590E-007 3.10731439E-008 /phiK
-0.1030495 -0.2811527 -0.2714869 0.1464661 -0.0689840 -0.3012532 -0.0842112 -0.5936081
-0.7437152 0.8369451 0.3108118 0.1473492 0.1450987 -0.1010872 -0.2387689 -0.0637013

```

0.2894396 0.4093451 -0.2066193 -0.7442433 0.3419929 0.6440407 0.6203302 -0.0668460
 -0.3420082 -0.1268511 -0.4087383 -0.7871693 -0.2223470 -0.1344943 0.3749455 0.3289043
 -0.3978997 0.6391557 -0.0945755 0.8942523 -0.4719640 -0.0768522 -0.0891396 0.1408744
 -0.0075963 0.3691262 -0.2068336 -0.0696206 0.3258235 0.3068415 0.2342517 -0.1204939
 -0.0402437 -0.4632691 -0.4137628 -0.5732712 -0.4421152 0.9454306 -1.0000000

INT File

Methylacrylonitrile

0000 52023 457.1044, 0, 100, -10.0, -9.0, 100, 9.375
 001 3.940
 002 0.265
 003 0.000

Cis 3-cyanopropene**VAR File**

CIS-ALLYLCYANIDE

June 18 2021

12 124 11 5 0.0000E+000 1.1000E+001 1.0000E+000 1.0000000000
 a 1 1 0,50, , , , , , 0 ,
 10000 1.132298370000000E+004 1.00000000E+000 /A
 20000 3.739346620000000E+003 1.00000000E+000 /B
 30000 2.858532640000000E+003 1.00000000E+000 /C
 200 -3.067490000000000E-003 1.00000000E+000 /-DJ
 1100 1.839000000000000E-002 1.00000000E+000 /-DJK
 2000 -5.319880000000000E-002 1.00000000E+000 /-DK
 40100 -1.015730000000000E-003 1.00000000E+000 /-dJ
 41000 -5.171700000000000E-003 1.00000000E+000 /-dK
 300 6.300000000000000E-009 1.00000000E+000 /PhiJ
 1200 -4.727000000000000E-008 1.00000000E+000 /PhiJK
 2100 -1.323700000000000E-007 1.00000000E+000 /PhiKJ
 40200 2.730000000000000E-009 1.00000000E+000 /phiJ

INT File

Cis-allylcyanide

0000 52023 442.0675, 0, 100, -10.0, -9.0, 100, 9.375
 001 3.26
 002 2.16
 003 0.00

Gauche 3-cyanopropene

VAR File

```
GAUCHE-ALLYLCYANIDE Demaison et al. 1991
  14  114   11   0   0.0000E+000   1.1000E+001
1.0000E+000 1.0000000000 Thu Oct 15 14:02:52 2020
s   1   1   0  50, , , , , , 0 ,
      10000  1.9707584000000000E+004 1.00000000E+000 /A
      20000  2.6197864800000000E+003 1.00000000E+000 /B
      30000  2.4975665700000000E+003 1.00000000E+000 /C
      200   -1.8106200000000000E-003 1.00000000E+000 /-DJ
      1100   8.0326200000000000E-002 1.00000000E+000 /-DJK
      2000   -1.2665100000000000E+000 1.00000000E+000 /-DK
      40100  -1.8745000000000000E-004 1.00000000E+000 /-dJ
      41000  2.5699000000000000E-002 1.00000000E+000 /-dK
      300   1.0044000000000000E-008 1.00000000E+000 /PhiJ
      1200  -1.9830000000000000E-007 1.00000000E+000 /PhiJK
      2100  -6.2205000000000000E-006 1.00000000E+000 /PhiKJ
      40200  3.5510000000000000E-009 1.00000000E+000 /phiJ
      41100  -2.9000000000000000E-007 1.00000000E+000 /phiJK
      42000  1.2520000000000000E-005 1.00000000E+000 /phiK
```

INT File

```
Gauche-allylcyanide
0000   000 428.1232,  0, 100, -10.0,-9.0, 100, 9.375
001   3.69
002   1.11
003   0.98
```

A6 Skimmer chamber details and comparison with CRESU

Classic

A full characterization of the post skimmer expansion was performed via Direct Simulation Monte Carlo calculations using the DS2V bird program and CFD simulations, with the fluent solver in Ansys workbench using the pressure based model. These were performed by Omar Abdelkader Khedaoui.

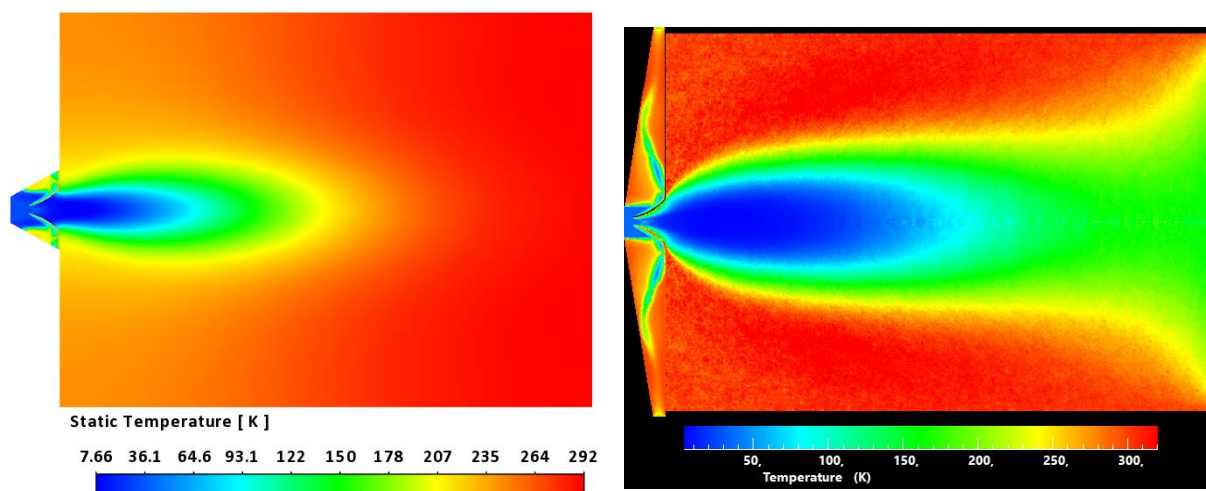


Figure A6.1: Computational simulations performed to calculate the temperature profile inside the secondary chamber, after the flow at 35 K expands. Credit: Omar Abdelkader Khedaoui.

To assess the improvement of the molecular signal with the skimmer setup, a vinyl cyanide spectrum is recorded from a 2 GHz chirp in an argon flow at 28 K under the skimmer conditions and compared to a similar spectrum under the CRESU conditions, the FIDs and the associated spectra are shown in the figure below, the results demonstrate a big improvement in the duration of the FID which last for more than 5 microseconds rather than few hundreds of nanoseconds under the CRESU conditions giving a spectrum with huge SNR of 1243 more than 18 times better than the one taken under the CRESU conditions.

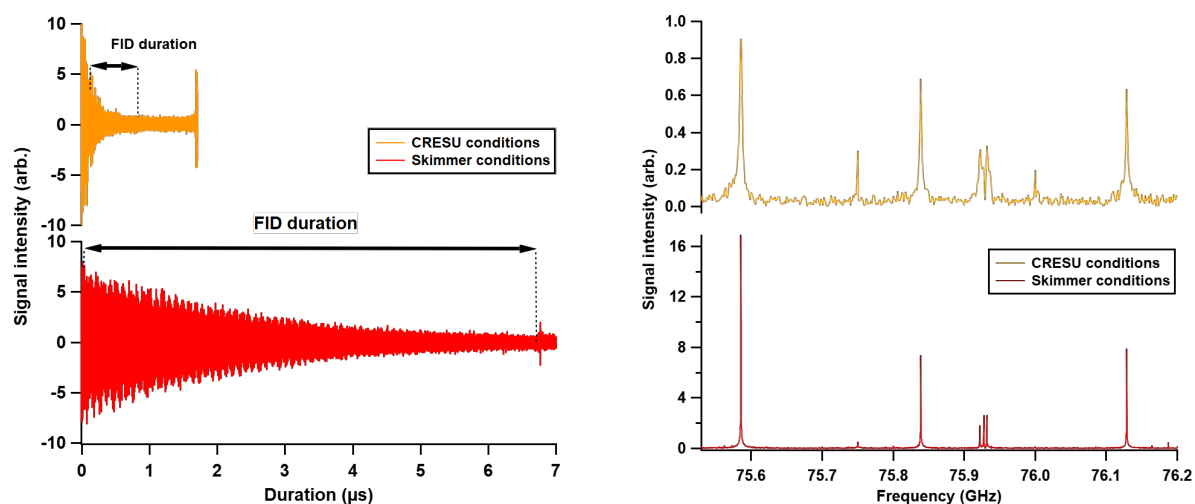
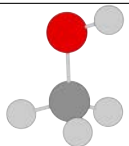
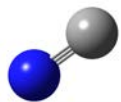
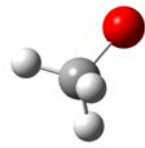
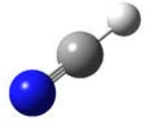
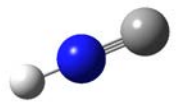


Figure A6.2: Comparison of time–domain and frequency–domain data collected with and without the secondary expansion. Credit: Omar Abdelkader Khedaoui.

A7 Optimised geometries

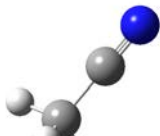
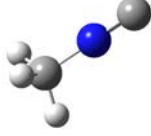
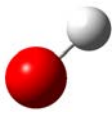
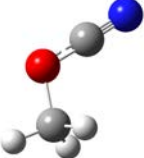
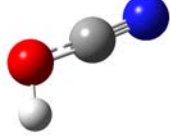
A7.1 CN + Methanol

Optimised geometries for the CN + methanol system at CCSD/aug-cc-pVTZ

							
CH₃OH				CN			
Cartesian Coordinate				Cartesian Coordinate			
Atom	X	Y	Z	Atom	X	Y	Z
C	0.667017	-0.020409	0.000002	C	0.000000	0.000000	0.535965
H	1.082822	0.984336	-0.000116	N	0.000000	0.000000	-0.625292
H	1.026149	-0.543744	0.890345				
H	1.026137	-0.543945	-0.890227				
O	-0.748423	0.121940	-0.000003				
H	-1.149827	-0.749715	0.000013				
							
CH₃O				CH₂OH			
Cartesian Coordinate				Cartesian Coordinate			
Atom	X	Y	Z	Atom	X	Y	Z
O	-0.789373	0.000031	-0.007149	C	-0.683863	0.027504	-0.056788
C	0.572731	0.000099	-0.014114	H	-1.115898	0.996037	0.14792
H	0.871384	-0.003396	1.051471	H	-1.236082	-0.884709	0.092457
H	1.003744	0.909066	-0.452187	O	0.669131	-0.125679	0.018885
H	1.003471	-0.906511	-0.457412	H	1.102109	0.729079	-0.050732
							
HCN				HNC			
Cartesian Coordinate				Cartesian Coordinate			
Atom	X	Y	Z	Atom	X	Y	Z
N	0	0	0.648707	N	0	0	0.427408
C	0	0	-0.496491	C	0	0	-0.73595
H	0	0	-1.562003	H	0	0	1.423849

A7.2 CN + Toluene

Optimised geometries for the CN + methanol system at CCSD/aug-cc-pVTZ

							
CH₃OH				CN			
Cartesian Coordinate				Cartesian Coordinate			
Atom	X	Y	Z	Atom	X	Y	Z
N	1.429488	0.000061	-0.000018	N	0.313291	-0.000165	0.000073
C	0.280888	-0.000138	0.000032	C	1.477173	0.000096	-0.00004
C	-1.173901	0.000029	-0.000009	C	-1.105393	0.000048	-0.000022
H	-1.549473	0.014954	-1.021851	H	-1.474615	-0.703026	-0.744091
H	-1.54953	-0.892314	0.498035	H	-1.474713	-0.292723	0.980884
H	-1.549332	0.877586	0.523805	H	-1.474391	0.996036	-0.236928
							
OH				CH₃OCN			
Cartesian Coordinate				Cartesian Coordinate			
Atom	X	Y	Z	Atom	X	Y	Z
O	0	0	0.108229	O	-0.410873	-0.623436	-0.000144
H	0	0	-0.865834	C	-1.503323	0.341162	0
				H	-2.4079	-0.255232	-0.00081
				H	-1.444971	0.956122	-0.894585
				H	-1.445778	0.954916	0.895468
				C	0.773339	-0.122977	0.00004
				N	1.85222	0.288939	0.000119
							
NCCH₂OH				HOCN			
Cartesian Coordinate				Cartesian Coordinate			
Atom	X	Y	Z	Atom	X	Y	Z
O	1.511419	-0.447376	-0.1087	O	-0.133385	-1.108025	0
C	0.563405	0.590257	0.038514	H	0.727166	-1.54749	0
H	0.724117	1.277626	-0.790422	N	0.048559	1.332253	0
H	0.704162	1.150055	0.967702	C	0	0.180986	0
C	-0.8263	0.110587	-0.005662				
N	-1.906279	-0.281042	-0.015217				
H	1.401687	-1.086449	0.601726				

Optimised geometries for the CN + methanol system at CCSD/aug-cc-pVTZ



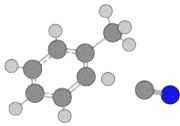
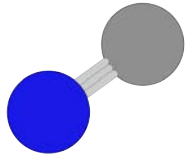
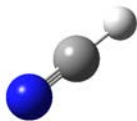
CH₃

Cartesian Coordinate			
Atom	X	Y	Z
C	0	0	0.000037
H	0	0	-1.077733
H	0	0.933444	0.538756
H	0	-0.933444	0.538756

A7.3 CN + Propene

Optimised Geometries

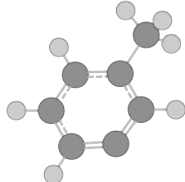
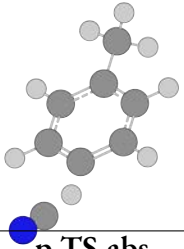
Optimised geometries for the CN + toluene system at (U)M06-2X/aug-cc-pVTZ

							
C₆H₅CH₃				o-TS-abs			
Cartesian Coordinate				Cartesian Coordinate			
Atom	X	Y	Z	Atom	X	Y	Z
C	-1.892906	-0.001998	0.007632	C	-2.104947	-1.253041	-0.0798
C	-1.191194	-1.199697	0.001838	C	-0.777722	-1.530348	0.216878
C	0.195619	-1.194122	-0.007874	C	0.098254	-0.469163	0.347791
C	0.907467	0.002748	-0.010262	C	-0.247734	0.855647	0.123912
C	0.192202	1.196248	-0.007847	C	-1.588099	1.103315	-0.166104
C	-1.195812	1.197115	0.001853	C	-2.502645	0.064079	-0.267325
H	-1.725511	-2.14032	0.001347	H	-2.820729	-2.058765	-0.16447
H	0.737149	-2.132354	-0.016823	H	-0.439307	-2.546532	0.364084
H	0.730163	2.136345	-0.016771	H	1.176	-0.683166	0.652109
H	-1.732966	2.136108	0.001387	H	-1.911276	2.124693	-0.323795
C	2.411091	0.001051	0.008269	H	-3.534888	0.284101	-0.504393
H	2.785228	-0.118345	1.026619	C	0.771804	1.955481	0.179125
H	2.81037	-0.82016	-0.585733	H	1.486361	1.787759	0.98473
H	2.810955	0.934643	-0.384032	H	1.339581	1.996293	-0.751484
H	-2.974186	-0.003989	0.012347	H	0.295768	2.922072	0.330179
				N	3.750483	-0.559347	-0.427891
				C	2.709771	-0.711141	0.046902
							
CN				HCN			
Cartesian Coordinate				Cartesian Coordinate			
Atom	X	Y	Z	Atom	X	Y	Z
N	0	0	0.531843	N	0	0	0.647167
C	0	0	-0.620484	C	0	0	-0.49487
				H	0	0	-1.560946

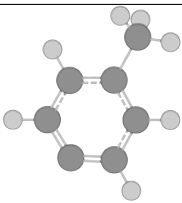
Optimised geometries for the CN + toluene system at (U)M06-2X/aug-cc-pVTZ

o-C₆H₄CH₃				m-TS-abs			
Cartesian Coordinate				Cartesian Coordinate			
Atom	X	Y	Z	Atom	X	Y	Z
C	0.938171	-0.061088	-0.003928	C	-0.20767	1.622944	-0.14558
C	0.150235	-1.188993	-0.002872	C	1.138439	1.806662	0.143007
C	-1.216947	-1.22705	-0.000114	C	1.99185	0.715211	0.220099
C	-1.882794	-0.000556	0.00267	C	1.535129	-0.584874	0.011731
C	-1.149962	1.177177	0.001239	C	0.184959	-0.77039	-0.275023
C	0.23967	1.148056	-0.002616	C	-0.642462	0.331965	-0.379912
H	-1.764283	-2.160347	-0.000858	H	-0.88919	2.459861	-0.196107
H	-2.964289	0.027362	0.004418	H	1.52013	2.803669	0.316625
H	-1.663273	2.12902	0.001313	H	3.036224	0.873281	0.459526
H	0.798815	2.076522	-0.006356	H	-0.21026	-1.766988	-0.424607
C	2.440307	-0.121999	0.002446	H	-1.726129	0.161901	-0.663879
H	2.868711	0.867651	-0.145592	C	2.476692	-1.754312	0.07577
H	2.806606	-0.514066	0.95167	H	3.252888	-1.591442	0.82191
H	2.805629	-0.779428	-0.785537	H	1.947251	-2.672423	0.323211
				H	2.968596	-1.902575	-0.886934
				C	-3.211683	-0.289229	-0.039739
				N	-4.213003	-0.690449	0.369734

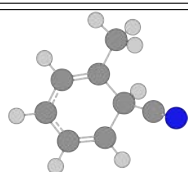
Optimised geometries for the CN + toluene system at (U)M06-2X/aug-cc-pVTZ

							
m-C₆H₄CH₃				p-TS-abs			
Cartesian Coordinate				Cartesian Coordinate			
Atom	X	Y	Z	Atom	X	Y	Z
C	0.875146	0.016561	-0.002353	C	0.795374	-0.082912	-0.397759
C	0.254736	-1.239035	-0.001823	C	0.189184	1.153648	-0.277609
C	-1.111894	-1.274628	0.000436	C	-1.1788	1.197321	-0.051083
C	-1.940832	-0.182134	0.001723	C	-1.922381	0.026342	0.085866
C	-1.315857	1.062332	0.000292	C	-1.266523	-1.199608	-0.001678
C	0.071127	1.152526	-0.00183	C	0.101644	-1.265966	-0.22713
H	-3.018398	-0.271193	0.0032	H	1.909726	-0.123292	-0.632267
H	-1.91416	1.964291	0.000412	H	0.765318	2.064076	-0.367395
H	0.539924	2.128274	-0.003416	H	-1.675507	2.156158	0.031269
C	2.37538	0.11628	0.001898	H	-1.831059	-2.116063	0.116359
H	2.700704	1.153526	-0.048133	H	0.607933	-2.219566	-0.281541
H	2.790221	-0.325837	0.90844	C	-3.406832	0.087022	0.31056
H	2.80367	-0.416851	-0.847287	H	-3.766218	-0.808813	0.813546
H	0.851213	-2.143627	-0.003278	H	-3.678731	0.953977	0.910443
				H	-3.933064	0.166858	-0.642341
				C	3.415593	-0.036611	0.010549
				N	4.462579	0.093036	0.477376

Optimised geometries for the CN + toluene system at (U)M06-2X/aug-cc-pVTZ

							
p-C₆H₄CH₃				C₆H₅CH₂			
Cartesian Coordinate				Cartesian Coordinate			
Atom	X	Y	Z	Atom	X	Y	Z
C	0.837414	0.007814	-0.004872	C	0	0	-1.828134
C	0.134946	-1.196814	-0.003618	C	0	1.204387	-1.127307
C	-1.25716	-1.219196	0.001223	C	0	1.209828	0.251146
C	-1.897447	-0.006881	0.004051	C	0	0	0.985399
C	-1.271483	1.209787	0.001261	C	0	-1.209828	0.251146
C	0.123979	1.202438	-0.003644	C	0	-1.204387	-1.127307
H	-1.821692	2.141204	0.001111	H	0	2.141081	-1.6682
H	0.661252	2.143266	-0.007886	H	0	2.147241	0.792459
C	2.342002	0.004078	0.003699	H	0	-2.147241	0.792459
H	2.73979	1.005817	-0.146768	H	0	-2.141081	-1.6682
H	2.724844	-0.36984	0.954348	C	0	0	2.390199
H	2.736305	-0.639866	-0.782416	H	0	0.926161	2.944764
H	0.683633	-2.131663	-0.007907	H	0	-0.926161	2.944764
H	-1.79764	-2.156278	0.000921	H	0	0	-2.908897

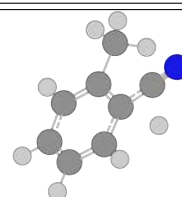
Optimised geometries for the CN + toluene system at (U)M06-2X/aug-cc-pVTZ



add-o-C₆H₅CH₃CN

Cartesian Coordinate

Atom	X	Y	Z
C	1.83322	-1.176204	-0.012016
C	0.586381	-1.467917	0.419887
C	-0.466614	-0.402565	0.568582
C	-0.027091	0.976537	0.125712
C	1.247051	1.179317	-0.292178
C	2.200525	0.140619	-0.370077
H	0.301942	-2.47783	0.679514
H	2.563654	-1.970197	-0.092311
C	-1.702379	-0.804155	-0.132544
N	-2.659976	-1.113845	-0.68093
H	1.539723	2.181553	-0.580577
H	3.201566	0.350406	-0.71442
C	-1.047692	2.060695	0.213187
H	-1.440571	2.143225	1.230688
H	-0.624311	3.02082	-0.073077
H	-1.900672	1.847372	-0.435697
H	-0.761894	-0.336393	1.629079

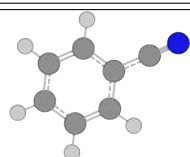


H-elim-TS-o

Cartesian Coordinate

Atom	X	Y	Z
C	1.392258	1.137085	-0.073482
C	0.029891	0.91952	-0.011342
C	-0.416727	-0.423319	0.135017
C	0.496122	-1.495601	0.024867
C	1.846949	-1.235139	-0.036529
C	2.298647	0.080619	-0.066426
H	1.756016	2.154384	-0.136667
H	-0.644172	-0.327388	1.850008
H	0.118339	-2.507812	0.033035
H	2.551577	-2.053608	-0.077834
H	3.359134	0.285149	-0.114443
C	-0.965678	2.033006	0.015246
H	-1.704626	1.920974	-0.778948
H	-1.513775	2.016336	0.961795
H	-0.477206	2.998581	-0.089558
C	-1.824507	-0.70146	-0.035353
N	-2.941003	-0.910698	-0.194196

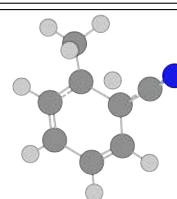
Optimised geometries for the CN + toluene system at (U)M06-2X/aug-cc-pVTZ



o-C₆H₄CH₃CN

Cartesian Coordinate

Atom	X	Y	Z
C	-0.617478	-0.653649	0
C	0.205421	-1.772849	0
C	1.587717	-1.651108	0
C	2.18265	-0.397641	0
C	1.386446	0.734366	0
H	3.258991	-0.301411	0
H	1.825128	1.722298	0
C	0	0.603678	0
C	-0.819165	1.782963	0
N	-1.488311	2.715864	0
H	2.202941	-2.540677	0
H	-0.247407	-2.755791	0
C	-2.112623	-0.771681	0
H	-2.5401	-0.282443	0.875946
H	-2.5401	-0.282443	-0.875946
H	-2.419088	-1.815048	0

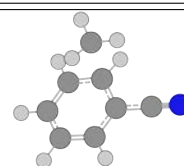
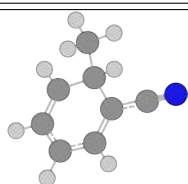


TS-bridge-H-o-tol-CN

Cartesian Coordinate

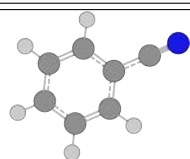
Atom	X	Y	Z
C	1.451055	1.112778	0.002315
C	0.043883	0.960567	0.100799
C	-0.479406	-0.469495	0.115691
C	0.488979	-1.546802	-0.013263
C	1.809152	-1.293271	-0.058499
C	2.316559	0.063228	-0.035129
H	1.829244	2.126961	-0.044176
H	-0.211031	0.240806	1.151458
H	0.106355	-2.555454	-0.080822
H	2.505876	-2.115238	-0.144411
H	3.380743	0.236702	-0.082377
C	-0.931922	2.077826	-0.088681
H	-0.458137	3.035061	0.120095
H	-1.307048	2.089643	-1.115653
H	-1.799664	1.970863	0.562628
C	-1.867944	-0.703043	0.002062
N	-3.004068	-0.891439	-0.074072

Optimised geometries for the CN + toluene system at (U)M06-2X/aug-cc-pVTZ



add-C₆H₄CH₃o-CN-IPSO-H				ipso-CH₃-elim-TS-o-CN			
Cartesian Coordinate				Cartesian Coordinate			
Atom	X	Y	Z	Atom	X	Y	Z
C	-1.536739	0.917667	-0.405996	C	-1.486983	0.730408	-0.763423
C	-0.042625	0.944352	-0.393591	C	-0.078243	0.748798	-0.679613
C	0.538472	-0.411055	-0.092727	C	0.568293	-0.402895	-0.166365
C	-0.237266	-1.497034	0.225276	C	-0.167408	-1.418677	0.43121
C	-1.63057	-1.404789	0.244582	C	-1.551624	-1.353116	0.44735
C	-2.261858	-0.175831	-0.088517	C	-2.205707	-0.286135	-0.176416
H	-2.034162	1.846203	-0.657829	H	-1.996493	1.548455	-1.253666
H	0.245601	-2.436824	0.456793	H	0.349896	-2.261915	0.86725
H	-2.224083	-2.269519	0.500186	H	-2.122099	-2.145295	0.910325
H	-3.342261	-0.123179	-0.090404	H	-3.286534	-0.267842	-0.209964
C	1.954948	-0.530258	-0.126776	C	1.996086	-0.464581	-0.196434
N	3.104081	-0.591253	-0.167466	N	3.144718	-0.488007	-0.219891
H	0.311936	1.259848	-1.384481	H	0.489249	1.424684	-1.303527
C	0.470964	2.003392	0.604938	C	0.224867	2.158513	0.966083
H	0.152648	1.747518	1.614798	H	-0.305727	1.628744	1.744222
H	1.558869	2.051979	0.580368	H	1.304737	2.159159	1.025162
H	0.070927	2.984078	0.349705	H	-0.241733	3.056168	0.585089

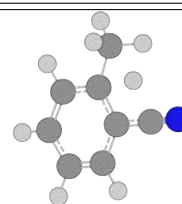
Optimised geometries for the CN + toluene system at (U)M06-2X/aug-cc-pVTZ



C₆H₅CN

Cartesian Coordinate

Atom	X	Y	Z
C	-2.165922	0.000052	0.000093
C	-1.474492	1.204054	0.000011
C	-0.089835	1.209847	-0.000102
C	0.60112	-0.000092	-0.00014
C	-0.089931	-1.209919	-0.000103
C	-1.474623	-1.20398	0.000012
H	-3.247186	0.000095	0.000402
H	-2.014715	2.140272	0.000113
H	0.461948	2.13907	-0.000273
H	0.461691	-2.139238	-0.000273
H	-2.014918	-2.140159	0.000115
C	2.037163	0.000147	0.000046
N	3.184613	-0.000098	0.000146

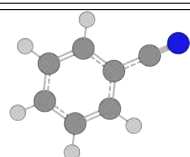


ipso-H-elim-TS-o-CN

Cartesian Coordinate

Atom	X	Y	Z
C	1.405224	1.100051	-0.03232
C	0.015786	0.889054	0.072755
C	-0.434492	-0.451821	-0.002471
C	0.463135	-1.513386	-0.009354
C	1.825741	-1.269139	-0.01589
C	2.291043	0.044099	-0.051629
H	1.770795	2.118334	-0.052801
H	0.082927	-2.52521	-0.020546
H	2.521587	-2.095652	-0.020369
H	3.354088	0.237057	-0.097412
C	-1.841507	-0.716841	-0.012544
N	-2.972282	-0.917911	-0.020684
H	-0.028268	1.028307	1.842733
C	-0.94648	2.033776	-0.113994
H	-1.172276	2.151652	-1.1754
H	-1.88303	1.855123	0.409674
H	-0.510546	2.961009	0.251589

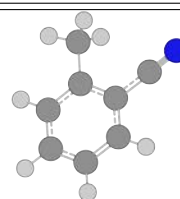
Optimised geometries for the CN + toluene system at (U)M06-2X/aug-cc-pVTZ



add-m-C₆H₅CH₃CN

Cartesian Coordinate

Atom	X	Y	Z
C	-0.18772	-0.876519	0.429048
C	-1.383636	-0.399051	0.017555
C	-1.532352	0.985154	-0.281651
C	-0.435165	1.864123	-0.175671
C	0.783683	1.437263	0.229228
C	1.017765	0.004471	0.621666
H	-0.058247	-1.928834	0.645858
H	-2.492187	1.355103	-0.613639
H	-0.5692	2.906589	-0.432741
H	1.625611	2.111835	0.292126
H	1.309141	-0.024694	1.683443
C	-2.572557	-1.303002	-0.144669
H	-3.392847	-0.974667	0.494693
H	-2.931624	-1.27866	-1.174167
H	-2.327169	-2.331704	0.109903
C	2.181911	-0.546585	-0.098014
N	3.08642	-0.975727	-0.655775

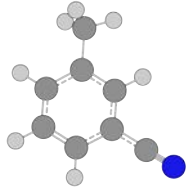
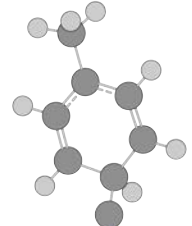


H-elim-TS-m

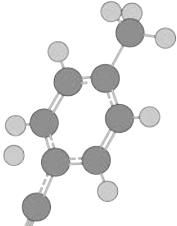
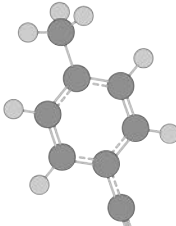
Cartesian Coordinate

Atom	X	Y	Z
C	-0.116785	-0.883809	0.038418
C	-1.418549	-0.431202	-0.011749
C	-1.648547	0.949028	-0.036208
C	-0.594921	1.855014	-0.063743
C	0.709948	1.41392	-0.014872
C	0.957473	0.032419	0.143345
H	0.099235	-1.943554	0.049383
H	-2.667791	1.312231	-0.074576
H	-0.798116	2.914313	-0.13818
H	1.54201	2.10188	-0.044771
H	1.154798	0.003708	1.857661
C	-2.573913	-1.391213	-0.047297
H	-2.231243	-2.416953	-0.164129
H	-3.15013	-1.329436	0.876652
H	-3.247572	-1.156633	-0.871008
C	2.304266	-0.460888	-0.032918
N	3.369283	-0.855025	-0.191556

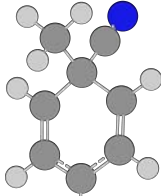
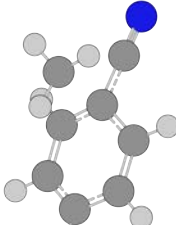
Optimised geometries for the CN + toluene system at (U)M06-2X/aug-cc-pVTZ

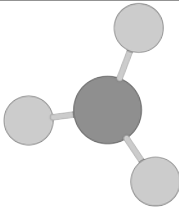
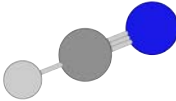
							
m-C ₆ H ₄ CH ₃ CN				add-p-C ₆ H ₅ CH ₃ CN			
Cartesian Coordinate				Cartesian Coordinate			
Atom	X	Y	Z	Atom	X	Y	Z
C	0.090404	-0.876097	-0.006932	C	0.927339	1.220768	-0.077872
C	1.403295	-0.426473	-0.008492	C	-0.387929	1.257782	-0.394073
C	1.631712	0.948555	-0.006344	C	-1.184938	0.001622	-0.625335
C	0.581328	1.85323	0.001721	C	-0.380721	-1.251616	-0.399772
C	-0.728154	1.401776	0.006027	C	0.929145	-1.208763	-0.08451
C	-0.967701	0.030855	0.001064	C	1.642635	0.011056	0.083043
H	-0.121975	-1.937074	-0.014333	H	-0.910821	2.198114	-0.496366
H	2.651477	1.313271	-0.013927	H	1.454507	2.156492	0.064712
H	0.782698	2.915377	0.001569	C	-2.400327	-0.00478	0.211256
C	2.552531	-1.39463	0.006835	N	-3.343831	-0.009454	0.861921
H	2.237244	-2.386207	-0.311282	H	-1.560062	0.001673	-1.660424
H	3.352812	-1.059785	-0.651673	H	-0.899126	-2.19416	-0.506831
H	2.967959	-1.481468	1.011925	C	3.093206	-0.007858	0.438856
C	-2.318358	-0.457429	0.000415	H	3.25611	-0.506996	1.397241
H	-1.558738	2.092698	0.009544	H	3.673941	-0.556233	-0.306468
N	-3.397403	-0.847933	0.000345	H	3.498361	0.999514	0.510665
				H	1.463451	-2.141491	0.054469

Optimised geometries for the CN + toluene system at (U)M06-2X/aug-cc-pVTZ

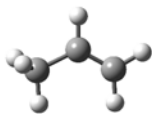
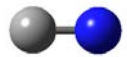
							
H-elim-TS-p				p-C ₆ H ₄ CH ₃ CN			
Cartesian Coordinate				Cartesian Coordinate			
Atom	X	Y	Z	Atom	X	Y	Z
C	0.384803	-1.216372	0.011252	C	-0.970185	1.200727	-0.005534
C	-0.989133	-1.199157	-0.037616	C	-1.683515	0.006018	-0.005797
C	-1.7043	0.00257	-0.032016	C	-0.972561	-1.193559	-0.005633
C	-0.988236	1.202043	-0.03707	C	0.409234	-1.205111	-0.002056
C	0.387119	1.217168	0.010815	C	1.108713	0.001037	0.00032
C	1.094447	0.000421	0.147935	C	0.414648	1.207136	-0.002045
H	0.933862	-2.146798	-0.004515	H	-1.506682	2.140644	-0.009651
H	-1.526635	2.139236	-0.097118	H	-1.513668	-2.13133	-0.009831
H	0.937116	2.147011	-0.00546	H	0.954613	-2.138283	-0.002744
H	1.296259	-0.002698	1.859005	C	-3.185219	-0.003468	0.00808
C	2.526507	-0.000811	-0.038085	H	-3.589777	0.989393	-0.176602
N	3.661277	-0.001892	-0.202704	H	-3.576971	-0.682233	-0.749052
C	-3.204146	-0.001315	-0.044549	H	-3.556673	-0.34503	0.975387
H	-3.589269	-0.826243	-0.642534	H	0.962436	2.138886	-0.002737
H	-3.594881	-0.120451	0.967956	C	2.543554	-0.002042	0.002706
H	-3.598425	0.931332	-0.443793	N	3.691244	-0.005211	0.004998
H	-1.529341	-2.135425	-0.098611				

Optimised geometries for the CN + toluene system at (U)M06-2X/aug-cc-pVTZ

							
add-ipso-C₆H₅CH₃CN				CH₃-elim-TS-ipso			
Cartesian Coordinate				Cartesian Coordinate			
Atom	X	Y	Z	Atom	X	Y	Z
C	-0.087289	2.302058	0	C	0.285492	-0.234545	1.222226
C	-0.069144	1.589646	1.220585	C	0.145646	0.482222	0
C	-0.069144	0.237394	1.252353	C	0.285492	-0.234545	-1.222226
C	-0.163471	-0.596792	0	C	0.285492	-1.609248	-1.207761
C	-0.069144	0.237394	-1.252353	C	0.251773	-2.307517	0
C	-0.069144	1.589646	-1.220585	C	0.285492	-1.609248	1.207761
H	-0.086877	3.381132	0	H	0.331693	0.317192	2.15045
H	-0.044298	2.138511	2.152569	H	0.331693	0.317192	-2.15045
H	-0.039398	-0.302662	2.189477	H	0.332772	-2.151409	-2.142143
H	-0.039398	-0.302662	-2.189477	H	0.251681	-3.388027	0
H	-0.044298	2.138511	-2.152569	H	0.332772	-2.151409	2.142143
C	-1.502656	-1.381397	0	C	-1.968547	0.83993	0
H	-1.5683	-2.010355	-0.886812	H	-2.104615	1.396675	0.917392
H	-1.5683	-2.010355	0.886812	H	-2.104615	1.396675	-0.917392
H	-2.32318	-0.666554	0	H	-2.305599	-0.187677	0
C	0.927105	-1.594584	0	C	0.448703	1.894963	0
N	1.761625	-2.380822	0	N	0.688139	3.016961	0

							
CH₃				HCN			
Cartesian Coordinate				Cartesian Coordinate			
Atom	X	Y	Z	Atom	X	Y	Z
C	0	0.000023	0	N	0	0	0.647167
H	0.000043	1.076044	0.000001	C	0	0	-0.49487
H	0.93197	-0.538129	0.000001	H	0	0	-1.560946
H	-0.932013	-0.538054	0.000001				

Optimised geometries for the CN + propene system at (U)M06-2X/cc-pVTZ

							
C₃H₆				CN			
Cartesian Coordinate				Cartesian Coordinate			
Atom	X	Y	Z	Atom	X	Y	Z
C	0.00000000	0.47137700	0.00000000	C	0.00000000	0.00000000	-0.62088600
C	1.28772500	0.15315800	0.00000000	N	0.00000000	0.00000000	0.53218800
C	-1.13395900	-0.50569500	0.00000000				
H	-1.77259400	-0.36559900	0.87619800				
H	-1.77259400	-0.36559900	-0.87619800				
H	-0.77596700	-1.53532500	0.00000000				
H	-0.27831300	1.52153800	0.00000000				
H	2.05940500	0.91123900	0.00000000				
H	1.61746400	-0.87929900	0.00000000				

Reaction pathways

**CH₃**

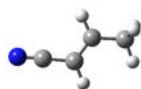
Cartesian Coordinate

Atom	X	Y	Z
C	0.00000000	0.00000000	0.00000100
H	0.00000000	1.07812100	-0.00000300
H	0.93368000	-0.53906000	-0.00000300
H	-0.93368000	-0.53906000	-0.00000300

**HCN**

Cartesian Coordinate

Atom	X	Y	Z
C	0.00000000	0.00000000	-0.49510700
H	0.00000000	0.00000000	-1.56078600
N	0.00000000	0.00000000	0.64734700

**P1a**

Cartesian Coordinate

Atom	X	Y	Z
C	0.756112	-0.580579	0
C	0	0.513467	0
C	2.245564	-0.567712	0
H	2.629836	-1.092282	0.876355
H	2.629836	-1.092282	-0.876355
H	2.636715	0.447688	0
H	0.266486	-1.54843	0
H	0.436997	1.504072	0
C	-1.428877	0.450115	0
N	-2.576667	0.412785	0

**P1b**

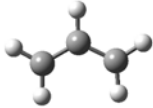
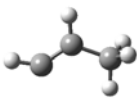
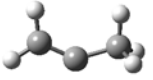
Cartesian Coordinate

Atom	X	Y	Z
C	-1.200615	0.423538	0
C	0	0.999451	0
C	-1.462127	-1.042434	0
H	-2.050839	-1.318924	0.876257
H	-2.050839	-1.318924	-0.876257
H	-0.538844	-1.617737	0
H	-2.064991	1.077944	0
H	0.112238	2.074253	0
C	1.211873	0.237368	0
N	2.185498	-0.372022	0

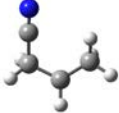
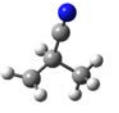
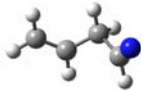
Optimised geometries for the CN + propene system at (U)M06-2X/cc-pVTZ

P2a				P3				P4			
Cartesian Coordinate				Cartesian Coordinate				Cartesian Coordinate			
Atom	X	Y	Z	Atom	X	Y	Z	Atom	X	Y	Z
C	1.039095	-0.209322	0.407598	C	0	0.416658	0	C	0	0.779205	0
C	-0.086234	0.751787	0.127481	C	-0.994937	1.297153	0	C	1.312398	0.969036	0
C	2.151189	-0.25107	-0.303901	C	1.459569	0.767954	0	H	-0.696856	1.606388	0
H	2.945244	-0.944149	-0.064346	H	1.952018	0.350913	0.878487	H	1.723106	1.968392	0
H	2.305835	0.406275	-1.1509	H	1.952018	0.350913	-0.878487	H	2.002173	0.136736	0
H	0.89413	-0.880225	1.246062	H	1.58709	1.84782	0	C	-0.580684	-0.530709	0
H	-0.208594	1.450949	0.957874	H	-2.028328	0.981858	0	N	-1.059815	-1.573816	0
H	0.124532	1.336463	-0.767846	H	-0.785624	2.358313	0				
C	-1.363457	0.058812	-0.053521	C	-0.30731	-0.990754	0				
N	-2.357816	-0.495794	-0.183827	N	-0.517301	-2.119412	0				

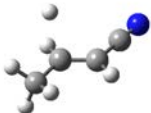
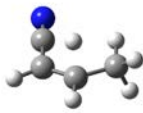
Optimised geometries for the CN + propene system at (U)M06-2X/cc-pVTZ

							
P5				P6			
Cartesian Coordinate				Cartesian Coordinate			
Atom	X	Y	Z	Atom	X	Y	Z
C	0	0	0.445774	C	0	0.449142	0
C	0	1.218605	-0.19656	C	1.299024	0.331537	0
C	0	-1.218605	-0.19656	C	-0.971277	-0.696672	0
H	0	-2.146985	0.353548	H	-1.616096	-0.65287	0.878767
H	0	-1.274245	-1.276748	H	-1.616096	-0.65287	-0.878767
H	0	0	1.53048	H	-0.445829	-1.649045	0
H	0	2.146985	0.353548	H	-0.433228	1.451506	0
H	0	1.274245	-1.276748	H	2.144766	0.999233	0
							
P7				C1a-1			
Cartesian Coordinate				Cartesian Coordinate			
Atom	X	Y	Z	Atom	X	Y	Z
C	0	0.414143	0	C	-1.09875264	0.5000972	-0.36519319
C	1.30016	0.310015	0	C	0.17834235	0.98852006	0.24639793
C	-1.177986	-0.462397	0	C	-1.71574282	-0.75169274	0.13725972
H	-1.796542	-0.284333	0.880254	H	-2.7128758	-0.89950563	-0.27193238
H	-1.796542	-0.284333	-0.880254	H	-1.11240089	-1.6280338	-0.13163525
H	-0.876517	-1.515801	0	H	-1.78555192	-0.74670677	1.22826671
H	1.947861	1.178805	0	H	-1.39125852	0.90636626	-1.32167321
H	1.7887	-0.664903	0	H	0.48385249	1.94773004	-0.16907001
				H	0.06656727	1.11741504	1.32750793
				C	1.27227027	0.02801195	0.03665601
				N	2.0907092	-0.75526913	-0.14174094

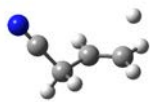
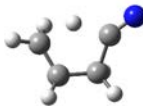
Optimised geometries for the CN + propene system at (U)M06-2X/cc-pVTZ

							
C1b-1				C1-2			
Cartesian Coordinate				Cartesian Coordinate			
Atom	X	Y	Z	Atom	X	Y	Z
C	1.15163	0.507134	-0.285917	C	-0.94901296	-0.4226854	0.40851067
C	-0.173274	1.030678	0.174588	C	0.1909151	0.52967038	0.27931749
C	1.60806	-0.852088	0.095066	C	-2.1686669	0.03737164	-0.39140797
H	2.497706	-1.140924	-0.460661	H	-1.93502486	0.09329926	-1.45371903
H	1.855675	-0.909922	1.1634	H	-2.99691294	-0.65640815	-0.25772811
H	0.829228	-1.59655	-0.084812	H	-2.49680686	1.02411507	-0.06440925
H	1.856644	1.231861	-0.664335	H	-0.633038	-1.41613882	0.09374096
H	-0.149789	1.306817	1.237608	H	0.02597915	1.58745358	0.43333812
H	-0.451837	1.930399	-0.374125	C	1.48565609	0.11662293	-0.01791193
C	-1.24705	0.045781	0.013003	N	2.55800908	-0.24267445	-0.26980143
N	-2.067689	-0.744387	-0.11393	H	-1.223608	-0.49947703	1.46633776
							
C3-1				C5-1b			
Cartesian Coordinate				Cartesian Coordinate			
Atom	X	Y	Z	Atom	X	Y	Z
C	0.39581391	0.06995234	0.4073549	C	-1.14339487	0.41819382	-0.15564507
C	0.94513871	1.34372735	-0.15327427	C	0.10906212	0.29691983	0.65974395
C	1.1333953	-1.1619046	-0.12779771	C	-2.12130985	-0.4722242	-0.1516101
H	0.71855444	-2.07755561	0.2881964	H	-3.00797784	-0.33945221	-0.75595211
H	1.04936251	-1.20600284	-1.21290372	H	-2.06709185	-1.36508321	0.45936089
H	2.18695523	-1.09423729	0.13783647	H	-1.22253287	1.30049683	-0.78376005
H	0.4687897	0.09190158	1.49716291	H	0.20696409	1.16207482	1.32189697
H	0.80291739	2.27608243	0.36961651	H	0.09516512	-0.60238718	1.27247094
H	1.2602729	1.36727121	-1.18582021	C	1.34154113	0.27016487	-0.22826203
C	-1.04141201	-0.02960806	0.09375365	N	2.20372015	-0.61819312	-0.18747202
N	-2.15492394	-0.09863738	-0.17347254	H	1.45404113	1.09337688	-0.94707301

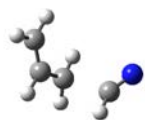
Optimised geometries for the CN + propene system at (U)M06-2X/cc-pVTZ

							
TS 1a-1				TS 1b-1			
Cartesian Coordinate				Cartesian Coordinate			
Atom	X	Y	Z	Atom	X	Y	Z
C	-0.88587498	-0.40146204	0.10657587	C	1.15208804	0.53340514	-0.13546102
C	0.11914903	0.46209004	-0.13889181	C	-0.12786498	0.95853606	-0.09545488
C	-2.32246997	-0.05716302	-0.05665015	H	2.2367991	-1.18924772	-0.75568234
H	-2.81992091	-0.77934585	-0.70626438	H	2.20483519	-0.93774597	0.9785657
H	-2.83342404	-0.09751229	0.9082648	H	0.76090717	-1.55481893	0.1568717
H	-2.45101395	0.93902009	-0.47569089	H	1.91755899	1.2870462	-0.27569196
H	-0.64108399	-1.38258814	0.49594963	C	1.60048913	-0.86828987	0.07066175
H	-0.06612494	1.40862417	-0.63069457	H	-0.45580489	1.49286978	1.68659622
H	0.25706089	1.54880062	1.4030385	H	-0.38326705	1.97932308	-0.34271271
C	1.49248003	0.05004304	-0.06096381	C	-1.22492792	0.030865	-0.04893095
N	2.59068603	-0.27972096	-0.01357481	N	-2.09710488	-0.71493205	-0.027548
							
TS 1a-2b				TS 1b-2b			
Cartesian Coordinate				Cartesian Coordinate			
Atom	X	Y	Z	Atom	X	Y	Z
C	-0.85477281	0.34616503	-0.11723802	C	-1.11743698	0.52322807	-0.08296271
C	0.15681019	-0.50351902	0.1321728	C	0.15050698	0.9712932	-0.12958173
C	-2.29336982	-0.06199694	-0.10056791	C	-1.51225382	-0.91856798	-0.05855267
H	-2.42946679	-1.01013399	0.41610401	H	-0.68943075	-1.55101588	0.26858735
H	-2.91224576	0.69365303	0.38023222	H	-2.3678958	-1.07877205	0.59482134
H	-2.65170393	-0.17348483	-1.12592289	H	-1.80366079	-1.22838003	-1.06446666
H	-0.90822562	1.33351186	1.58660209	H	-1.530936	0.85703307	1.82103628
H	-0.0287228	-1.51198405	0.47868072	H	0.37186986	2.02430022	-0.22867376
C	1.52108819	-0.11412203	0.0005487	C	1.26831407	0.09398833	-0.01253271
N	2.62420918	0.19212395	-0.10064038	N	2.16988515	-0.61340557	0.0793443
H	-0.61763383	1.32440807	-0.52070694	H	-1.90392406	1.25102398	-0.24493572

Optimised geometries for the CN + propene system at (U)M06-2X/cc-pVTZ

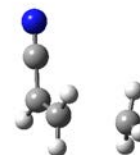
							
TS2-1				TS3-1			
Cartesian Coordinate				Cartesian Coordinate			
Atom	X	Y	Z	Atom	X	Y	Z
C	-0.97876406	-0.11079705	0.50703388	C	0.38780496	0.11926174	0.06741192
C	0.16519893	-0.79810406	-0.18538614	C	0.93501447	1.34244452	-0.08821201
C	-2.10416209	0.2396449	-0.11662408	C	1.16348547	-1.16684757	-0.09276894
H	-2.92796408	0.68284091	0.42489394	H	0.79055305	-1.93812542	0.57703902
H	-1.77780816	2.06110588	-0.85946517	H	1.06106948	-1.52719955	-1.11689795
H	-2.28434513	-0.03419114	-1.14886806	H	2.2165505	-0.99249199	0.11627723
H	-0.83216102	0.12758199	1.55325587	H	0.3144886	-0.04340221	1.89683892
H	0.34826496	-1.78057904	0.25646689	H	0.32553383	2.23350176	-0.10789312
H	-0.05763512	-0.9471711	-1.24186012	H	2.00899952	1.45293909	-0.14249884
C	1.40651692	-0.02781703	-0.07275322	C	-1.05154308	-0.00474469	-0.0005503
N	2.37127291	0.58183599	0.03170771	N	-2.18939512	-0.13227223	-0.07687848
							
TS4-1				TS5-1a			
Cartesian Coordinate				Cartesian Coordinate			
Atom	X	Y	Z	Atom	X	Y	Z
C	-0.31864001	-0.45632618	0.46344106	C	-1.29088112	0.47447293	-0.20618897
C	-0.9684379	-1.42804223	-0.22860498	C	0.03696885	1.00111292	0.21143014
C	-1.10674021	1.55321876	-0.14761188	C	-1.49906101	-0.84606517	0.10737867
H	-0.52188928	2.18768079	0.50315315	H	-2.29343398	-1.4097231	-0.36412147
H	-0.8318792	1.54545982	-1.19154887	H	0.003281	-1.11023796	-0.25403944
H	-2.1543042	1.43383164	0.08558611	H	-1.18342096	-1.23197041	1.07363155
H	-0.61435805	-0.21154725	1.47432107	H	-1.84946618	0.9720221	-0.98530982
H	-1.91911987	-1.80294834	0.11931499	H	0.35832677	1.88860709	-0.32842562
H	-0.58263686	-1.80093215	-1.16564799	H	0.09999086	1.20981663	1.2814332
C	1.03393696	-0.10497003	0.11984209	C	1.03296993	-0.15256194	-0.0453572
N	2.11192493	0.18073909	-0.15251089	N	2.16924895	-0.45432383	-0.11810631

Optimised geometries for the CN + propene system at (U)M06-2X/cc-pVTZ

**TS5-1b**

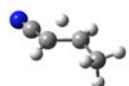
Cartesian Coordinate

Atom	X	Y	Z
C	1.2449378	0.402306	0.23201575
C	0.1028689	0.78692661	-0.54275559
C	1.97292779	-0.70134616	-0.00555757
H	2.81596371	-0.96810284	0.61515167
H	1.73553385	-1.35571661	-0.83491023
H	1.50745774	1.02699546	1.07994843
H	-0.22495207	1.81837464	-0.5125542
H	-0.06852802	0.2782241	-1.48112632
C	-1.51000024	0.04720624	0.47757765
N	-2.18580919	-0.6450041	-0.18127603
H	-1.32921632	0.50469776	1.43474142

**TS4-2b**

Cartesian Coordinate

Atom	X	Y	Z
C	-0.75140388	0.87427419	0.44758879
C	0.31900319	0.79964986	-0.37300608
C	-2.2149172	-0.83988255	-0.14048017
H	-1.5317234	-1.66452568	-0.010288
H	-2.96828825	-0.68600329	0.61758073
H	-2.45245302	-0.54459061	-1.15031823
H	-0.71859709	0.4304933	1.43217085
H	0.35401241	1.33353874	-1.31209014
C	1.42354197	-0.04808736	-0.08138187
N	2.31309279	-0.73993253	0.15053431
H	-1.5319447	1.59489035	0.25288062

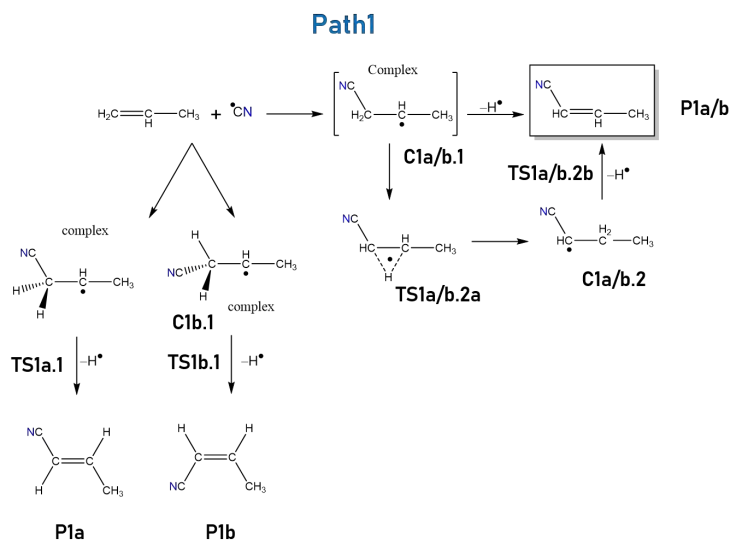
**TS1a-2a**

Cartesian Coordinate

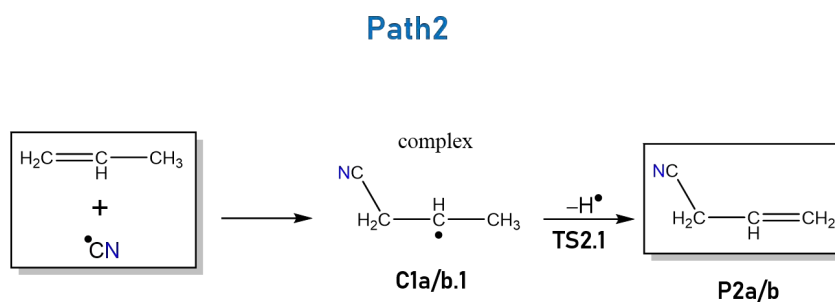
Atom	X	Y	Z
C	0.9334379	-0.45242279	-0.15150013
C	-0.18411609	0.5281902	-0.11047888
C	2.31902688	-0.00141991	0.15876817
H	2.47397177	0.0676297	1.24102921
H	3.06120291	-0.68673577	-0.245008
H	2.51073592	0.99010024	-0.25538145
H	0.6587369	-1.4962258	-0.12570153
H	0.05530289	1.56513814	0.07407252
H	0.33066801	0.14261459	-1.18992297
C	-1.52742311	0.11349816	0.03734584
N	-2.61945312	-0.24422787	0.1280146

Cartesian Coordinate

Atom	X	Y	Z

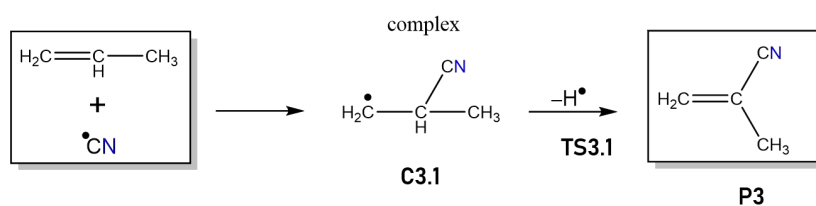


Reaction pathway: Path 1.



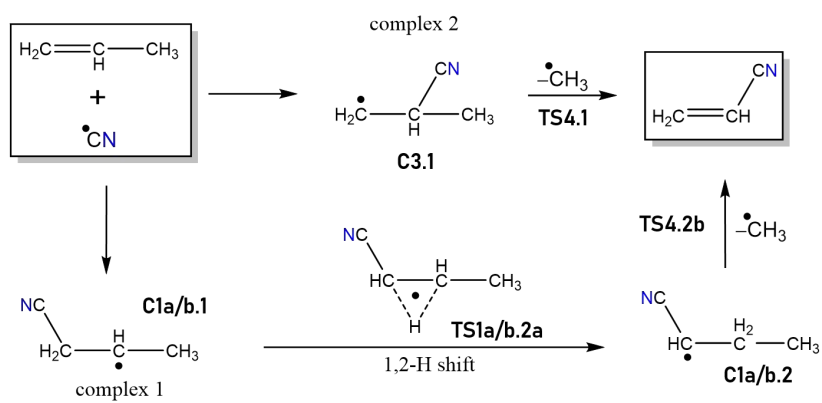
Reaction pathway: Path 2.

Path3



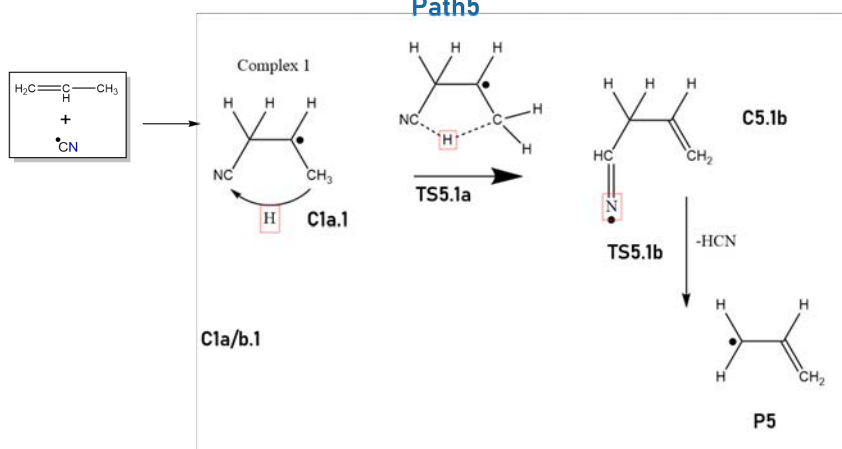
Reaction pathway: Path 3.

Path4



Reaction pathway: Path 4.

Path5



Reaction pathway: Path 5.

Annex

Résumé détaillé

L'astrochimie est un domaine interdisciplinaire relativement jeune situé au carrefour de l'astronomie, de la chimie et de la physique. L'astrochimie a été définie comme «l'étude de la formation, de la destruction et de l'excitation des molécules dans les environnements astronomiques et de leur influence sur la structure, la dynamique et l'évolution des objets astronomiques» par Alexander Dalgarno, un pionnier dans ce domaine.

Au cours des 50 dernières années environ, plus de 200 espèces chimiques différentes [McGuire et al., 2018] ont été détectées dans l'espace interstellaire, grâce à la construction d'installations radio-astronomiques de plus en plus puissantes et des progrès expérimentaux. Les différentes espèces chimiques peuvent s'avérer être un excellent outil de diagnostic des conditions physiques et des processus, y compris les densités numériques, les températures et la dynamique des gaz, dans les régions où elles sont détectées. Les molécules jouent également un rôle actif important en assistant les mécanismes de refroidissement qui sont très importants pour faciliter l'effondrement des nuages moléculaires, la formation d'étoiles et l'équilibre radiatif dans l'ISM. Une grande partie de la chimie dans l'espace se déroule à des températures et des pressions très différentes de celles de la Terre et sur des échelles de temps beaucoup plus longues, des millions d'années, par rapport aux échelles de temps terrestres. Cependant, du point de vue d'un chimiste, l'espace interstellaire fournit un environnement unique pour étudier le comportement moléculaire dans des conditions extrêmes. Cette combinaison fait de l'astrochimie un domaine de recherche fascinant et dynamique pour les chimistes, les astronomes et les physiciens.

Ce riche inventaire chimique contient de nombreuses espèces pouvant être considérées comme exotiques selon les normes terrestres. La plupart des molécules dans ces environnements ne sont pas grosses selon les normes de la chimie terrestre. Elles possèdent généralement entre 2 et 12 atomes [McGuire et al., 2018], mais il existe également quelques fullerènes (60 et 70 atomes) [Berne et al., 2013, Cami et al., 2010]. Quelques découvertes récentes comprennent des espèces légèrement plus grosses comme le cyano-cyclopentadiène (12 atomes) [McCarthy et al., 2021], le benzonitrile (13 atomes) [Burkhardt et al., 2021b, McGuire et al., 2018], l'indène (17 atomes) [Burkhardt et al.,

McGuire, B. A. (2018). *The Astrophysical Journal Supplement Series*, 239(2):17.

Cami, J., et al. (2010). *Science*, 329(5996):1180–1182.

Berne, O. et al. (2013). *Astronomy & Astrophysics*, 550:L4.

McCarthy, M. C., et al. (2021). *Nature Astronomy*, 5(2):176–180.

McGuire, B. A., et al. (2018). *Science*, 359(6372):202–205.

Burkhardt, A. M., et al. (2021). *Nature Astronomy*, 5(2):181–187.

2021a, Cernicharo et al., 2021] et le cyano naphthalène (19 atomes) [McGuire et al., 2021]. Le nuage moléculaire du Taureau (TMC-1) est une région de formation d'étoiles particulièrement bien étudiée et se distingue par une grande variété de cyano-polyynes (HC_nN famille de molécules linéaires, $n = 3, 5, 7, 9, 11$) [Freeman and Millar, 1983, Loomis et al., 2021]. Ces détections inspirent en outre de nouvelles recherches en physique-chimie pour comprendre leurs voies de spectroscopie et leurs mécanismes de formation/destruction. Une poignée d'espèces aromatiques ont également été détectées très récemment dans TMC-1 [McCarthy et al., 2021, McGuire et al., 2018]. Le nombre d'aromatiques détecté dans l'ISM est cependant très faible (seulement environ 2% du total des détections), ce qui est étrange par rapport au Chemical Abstracts Service (CAS) où $\sim 80\%$ des 135 millions de produits composés organiques, utilisés dans les laboratoires terrestres, enregistrés contiennent au moins un tel anneau.

Les molécules exotiques provenant des environnements interstellaires incluent des ions, comme C_4H^- , HCO^+ , et une large gamme de radicaux. Il existe également dans l'ISM des espèces isotopologues, où un ou plusieurs atomes dans une molécule sont des isotopes tels que deutérium, ^{13}C , ^{15}N , ^{17}O , ^{18}O et ^{34}S , etc. De nombreuses régions interstellaires ont signalé une abondance élevée de deutérium en hydrogène, appelée fractionnement de deutérium, dans les divers isotopologues détectés, ce qui a longtemps intrigué les astronomes. Le fractionnement du deutérium dans certaines régions s'est avéré aussi élevé que 10^4 [Bacmann et al., 2003, Pagani et al., 2009] par rapport aux abondances cosmiques indiquant une chimie fascinante.

Pendant longtemps, la chimie ionique a été considérée comme le principal moteur de la chimie dans l'ISM car les ions représentent environ 15% des > 200 molécules détectées. Ceci était basé sur la connaissance des interactions à longue distance induites par les espèces ioniques (chargées), leurs permettant ainsi d'interagir dans les nuages moléculaires de densité extrêmement faible. De plus, la plupart des réactions ion-molécule n'ont pas de barrière et sont exothermiques, ce qui leur permet de se dérouler dans les environnements interstellaires froids. Au cours des deux dernières décennies, cependant, le rôle des réactions neutres-neutres a été établi [Heard, 2018, Morales et al., 2010, Ocaña

-
- Cernicharo, J. et al. (2012). *The Astrophysical journal letters*, 759(2):L43
Burkhardt, A. M. et al. (2021). *The Astrophysical Journal Letters*, 913(2):L18.
McGuire, B. A. et al. (2021). *Science*, 371(6535):1265–1269
Freeman, A. and Millar, T. (1983). *Nature*, 301(5899):402–404
Loomis, R. A. et al. (2021). *Nature Astronomy*, 5(2):188–196.
Pagani, L. et al. (2009). *Astronomy & Astrophysics*, 494(2):719–727.
Bacmann, A. et al. (2003). *The Astrophysical Journal Letters*, 585(1):L55.

et al., 2019, Sims et al., 1993] car bon nombre de ces réactions ont des constantes de vitesses élevées à basse température en raison d'une barrière immergée ou d'un mécanisme impliquant des complexes stables.

De loin, l'une des atmosphères les plus explorées après celle de la Terre a été celle de Titan. Titan est la plus grande lune de Saturne et possède une atmosphère dense principalement composée d'azote (N_2) et de méthane (CH_4) [Kuiper, 1944]. Une chimie riche est induite par le rayonnement UV/solaire et les particules lourdes chargées électriquement provenant de la magnétosphère de Saturne. La liaison N_2 est principalement rompue par ionisation dissociative dans les couches de plus haute altitude et conduit à la formation de divers nitriles tel que HCN. Le CH_4 dans l'atmosphère de Titan, d'autre part, est photodissocié par le rayonnement α de Lyman en petits hydrocarbures. Ceux-ci peuvent réagir les uns avec les autres pour former des hydrocarbures plus gros comme C_2H_2 , C_2H_4 , C_3H_6 , etc. La chimie du carbone et de l'azote, à la fois dans les phases gazeuse et aérosol, de Titan est donc d'un grand intérêt pour les astrochimistes. Les nitriles ont attiré une attention particulière dans la communauté astrobiologique car ils sont considérés comme des précurseurs de la chimie prébiotique étant donné leur capacité à former des acides aminés.

N_2 et CH_4 ont également été détectés sur Triton, une lune de Neptune, [Broadfoot et al., 1989, Cruikshank and Silvggio, 1979] et Pluton [Cruikshank et al., 1976, Owen et al., 1993]. Cela indique une éventuelle chimie du nitrile intéressante sur ces planétoïdes, et souligne l'importance d'étudier et de modéliser ces réactions à basse température.

Alors que l'astrochimie a commencé comme une sous-discipline de l'astronomie, il s'agit à présent d'un domaine interdisciplinaire florissant indépendant avec une forte interaction entre les observations, les calculs/modélisations et les expériences. Trois principaux types d'activités scientifiques sont menées sur le terrain : (i) l'identification de l'espèce, (ii) la construction et l'application de modèles chimiques, et (iii) les efforts expérimentaux et théoriques.

Les besoins des astronomes en données spectroscopiques, comprenant les spectres d'espèces exotiques et instables difficiles à isoler en laboratoire, ont déclenché de nouvelles recherches en physique-

Sims, I. R. et al. (1993). *Chemical Physics Letters*, 211(4-5):461–468.

Heard, D. E. (2018). *Acc. Chem. Res.*, 51(11):2620–2627.

Morales, S. B. et al. (2010). *Faraday discussions*, 147:155–171.

Ocaña, A. J. et al. (2019). *Physical Chemistry Chemical Physics*, 21(13):6942–6957.

Kuiper, G. P. (1944). *The Astrophysical Journal*, 100:378.

Broadfoot, A. et al. (1989). *Science*, 246(4936):1459–1466.

Cruikshank, D. and Silvggio, P. (1979). *The Astrophysical Journal*, 233:1016–1020.

Owen, T. C. et al. (1993). *Science*, 261(5122):745–748.

Cruikshank, D. et al. (1976). *Science*, 835–837

chimie. La modélisation astrochimique nécessite des informations sur divers processus chimiques pour prédire l'abondance d'une variété d'espèces chimiques. Les détections astronomiques peuvent être utilisées pour dériver les abondances de molécules dans un large éventail de régions avec des conditions physiques variables, ce qui permet d'affiner davantage les modèles astrochimiques et peut même indiquer d'autres espèces possibles dans ces environnements extraterrestres.

Étant donné que les données cinétiques et spectroscopiques pour de nombreux systèmes chimiques sont nécessaires pour des systèmes exotiques ou dans des conditions extrêmes, les chercheurs tirent souvent parti des outils quantiques informatiques disponibles. Cela comprend, mais sans s'y limiter, les fréquences de transition de rotation des espèces et les constantes de vitesse de réaction. Des modèles cinétiques astrochimiques sont utilisés pour simuler l'évolution des espèces chimiques au cours du temps dans différents environnements astrophysiques. Ils sont réalisés en intégrant un système d'équations couplées, non linéaires, de loi de vitesse différentielle. La plupart de ces modèles utilisent le réseau de réactions chimiques disponible sur des bases de données chimiques comme KIDA (<http://kida.astrophy.u-bordeaux.fr/networks.html>), Udfa (<http://udfa.ajmarkwick.net/>), ou encore NIST (<https://kinetics.nist.gov/kinetics/>).

Compte tenu de la diversité chimique et physique des environnements astrophysiques, des mesures précises de divers processus en phase glace/gaz et des surfaces gaz-grain sont nécessaires pour comprendre l'ensemble de la complexité chimique de l'ISM. La plupart des molécules interstellaires et circumstellaires gazeuses détectées ont été observées via leurs raies spectrales de rotation, qui sont enregistrées et caractérisées en laboratoire. Des bases de données spectrales comme CDMS (<http://www.astro.uni-koeln.de/site/vorhersagen/>), Splatalogue (<http://www.splatalogue.net/>), et le catalogue JPL (<http://spec.jpl.nasa.gov/home.html>), contiennent les détails de ces études expérimentales pour faciliter le processus d'attribution des raies moléculaires interstellaires.

Les coefficients de vitesse de réaction, pour chaque molécule détectée, comme mentionné dans la section ci-dessus, sont requis pour la modélisation astrochimique. Les mesures expérimentales peuvent également aider à prédire la possible présence d'autres molécules dans l'ISM. Étant donné que les théories fondamentales de la chimie quantique, sur lesquelles sont basées les estimations théoriques, peuvent être testées aux basses températures pertinentes pour l'ISM, les mesures expérimentales constituent un étalon-or.

L'objectif de cette thèse est de comprendre la chimie neutre en phase gazeuse de molécules complexes dans l'ISM. Des études en laboratoire à basse température pour explorer les réactions du radical CN

pertinentes aux environnements interstellaires ont été réalisées à l'aide de la technique CRESU couplée d'une part à la technique PLP-LIF (pulsed laser photolysis -laser induced fluorescence) et d'autre part au CPFT-mmW (chirped pulsed Fourier transform millimeter wave spectroscopy).

La technique PLP-LIF a révolutionné l'étude des coefficients de vitesse de réaction car elle permet de suivre l'évolution de très faible concentration d'espèces radicalaires (réactifs) au cours du temps. Ces mesures peuvent être utilisées pour mesurer la constante de vitesse globale.

Les coefficients de vitesse pour la réaction du radical CN avec le méthanol, le benzène et le toluène ont été mesurés de 296 K à 16 K en utilisant la technique PLP-LIF en suivant la concentration de radicaux CN au cours du temps. Une dépendance négative à la température a été observée pour la réaction du méthanol avec le radical CN, présentée au chapitre 4, typique de ce qui a été vu précédemment pour d'autres réactions radicalaires neutres qui ne possèdent pas de barrières d'énergie potentielle. Les mesures s'écartent considérablement des valeurs actuellement dans la base de données cinétique pour l'astrochimie (KIDA) qui sont utilisées dans divers modèles astrochimiques et des recommandations pour les valeurs mises à jour sont fournies. Le chapitre 5 couvre les mesures de cinétique de réaction de deux molécules aromatiques, le benzène et le toluène, avec le radical CN et montre que ces réactions restent rapides jusqu'à 16 K. Les implications interstellaires potentielles de ces mesures à la lumière de la détection récente de cyano-benzène substitué dans le milieu interstellaire sont discutés.

Les coefficients de vitesse pour CN + méthanol ont montré une dépendance négative de la température, de 17 à 296 K, typique de ce qui a été observé précédemment pour d'autres réactions radical-neutres qui ne possèdent pas de barrières énergétiques potentielles. Cela montre que la réaction du méthanol avec le radical CN est une voie de destruction probable pour le méthanol dans des environnements où les deux sont présents. Le coefficient de vitesse obtenu à température ambiante est fortement en désaccord avec une étude cinétique précédente de Sayah et al. [1988], qui est actuellement disponible dans la base de données Kinetics for Astrochemistry (KIDA), et donc utilisée dans certains modèles astrochimiques. KIDA suggère ce coefficient de vitesse sur la plage de températures de 10 à 300 K, ce qui pourrait potentiellement avoir un impact sur les abondances modélisées dans les environnements astrophysiques à des températures supérieures à ~ 50 K.

Des calculs de structure électronique ont également été effectués pour identifier les chemins exothermiques et leurs états de transition correspondants, à travers lesquels cette réaction peut se dérouler. Alors que les voies exothermiques ont été caractérisées, une surface d'énergie potentielle

complète n'a pas pu être obtenue. Deux des produits possibles de cette réaction, CH_3O et CH_2OH , ont été un sujet d'intérêt pour les astronomes car seul le méthoxy (CH_3O) a été détecté dans le milieu interstellaire par Cernicharo et al. [2012]. Cependant, des expériences en laboratoire ont montré que seul l'isomère CH_2OH est libéré dans la phase gazeuse lorsque les manteaux glacés sont chauffés [?]. Cela indique des voies possibles de formation en phase gazeuse, dont l'une est la réaction du méthanol avec OH [Shannon et al., 2013]. Le travail présenté ici n'a mesuré que le coefficient de vitesse global, et de futures mesures utilisant le spectromètre à ondes millimétriques chirpées récemment développé à Rennes pourraient être utilisées.

La caractérisation spectroscopique du radical méthoxy est bien connue [Endo et al., 1984]. Une simulation utilisant SPCAT montre son spectre autour de 82,46 GHz est accessible à l'aide du spectromètre à ondes millimétriques chirpées en bande E, qui à basse température est beaucoup plus intense qu'à température ambiante, en raison d'un déplacement de la population de Boltzmann. La spectroscopie du radical hydroxyméthyle (CH_2OH), qui est plus délicate en raison de la rotation-tunnel et rotation interne, a également été récemment réévaluée [Chitarra et al., 2020]. Janssen and Hershberger [2015] a mesuré CH_2OH comme voie de produit dominant de cette réaction à température ambiante, il est donc intéressant d'étudier si ce rapport de ramification diminue à basse température et si cette réaction est une source importante de méthoxy dans des conditions de nuages denses.

La détection de benzonitrile/cyano-benzène par McGuire et al. [2018], et depuis lors la détection d'aromatiques/espèces cycliques cyano-substituées [McCarthy et al., 2021, McGuire et al., 2021], dans le milieu interstellaire soulignent l'importance de vérifier si des espèces cyano-substituées sont en effet un marqueur chimique robuste pour déduire l'abondance de leurs molécules mères. La cinétique de réaction à basse température pour la réaction du radical CN avec le benzène (C_6H_6) a été mesurée, montrant que la réaction reste rapide aux basses températures des nuages de gaz denses froids. Un coefficient de vitesse moyen de $(4,4 \pm 0,2) \times 10^{-10} \text{ cm}^3 \text{ s}^{-1}$ a été mesuré sans dépendance évidente de la température entre 15 et 295 K. Les coefficients de vitesse de réaction du radical CN avec le toluène (C_7H_8), une autre molécule aromatique, ont été mesurés entre 15 et 294 K avec une moyenne de (4,1

Cernicharo, J. et al. (2012). *The Astrophysical journal letters*, 759(2):L43.

Shannon, R. J. et al. (2013). *Nature chemistry*, 5(9):745–749

Endo, Y. et al. (1984). *The Journal of chemical physics*, 81(1):122–135.

Chitarra, O. et al. (2020). *Astronomy & Astrophysics*, 644:A123.

Janssen, E. and Hershberger, J. F. (2015). *Chemical Physics Letters*, 625:26–29

McGuire, B. A., et al. (2018). *Science*, 359(6372):202–205.

McGuire, B. A. et al. (2021). *Science*, 371(6535):1265–1269

McCarthy, M. C., et al. (2021). *Nature Astronomy*, 5(2):176–180.

$\pm 0,2) \times 10^{-10} \text{ cm}^3 \text{ s}^{-1}$ sans dépendance évidente de la température, similaire au benzène. Cette mesure, pour la réaction CN + toluène, est plus rapide que la seule mesure précédente à 105 K, et bien que la raison de ce désaccord reste inconnue, le rôle des effets multiphotoniques a été discuté.

La surface d'énergie potentielle pour la réaction, qui comprenait à la fois des voies d'abstraction et d'addition-élimination, a été explorée pour identifier les voies possibles à basse température car cette réaction reste rapide. Les travaux futurs développeront ces calculs et utiliseront MESMER, une suite de programmes de résolution d'équations maîtresses [Glowacki et al., 2012], pour calculer le rapport de branchement théorique pour cette réaction. Les espèces de toluène cyano-substituées peuvent être étudiées et mesurées en utilisant la spectroscopie rotationnelle. Ceci, cependant, sera une tâche difficile, car le toluène a un groupe méthyle qui, en raison de son mouvement de rotation interne, donne lieu à des spectres compliqués pour ces produits. Il sera intéressant de voir dans quelle mesure la contribution du canal produit du cyanobenzène (benzonitrile), qui a été identifiée à l'aide de calculs théoriques, provient de cette réaction, en particulier à basse température, puisque le benzonitrile a été détecté dans une série de sources froides dans l'ISM [Burkhardt et al., 2021b].

Des travaux supplémentaires sur les produits formés à partir de cette réaction sont également importants pour déterminer leur détectabilité potentielle dans l'ISM. La capacité de détecter et d'utiliser des aromatiques cyano-substitués, qui ont des moments dipolaires importants, en tant que marqueurs pour les espèces aromatiques non substituées dans l'ISM pourrait également aider à faire progresser nos connaissances sur la formation de HAP, car ils pourraient fournir de meilleures contraintes aux modèles astrochimiques pour les espèces plus petites comme le benzène.

De nombreuses réactions se déroulent via plusieurs chemins, et la connaissance des différents produits de ces réactions multicanaux est cruciale pour reproduire avec précision des environnements astrophysiques complexes. Bien que les modèles astrochimiques aient encore de nombreux chaînons manquants, l'un des plus importants est le manque de rapports de branchement pour les réactions pertinentes à basse température. Les mesures du rapport de branchement sont très difficiles car plusieurs produits doivent être détectés avec une haute sensibilité en même temps. La technique de mesure LIF peut être appliquée pour mesurer la présence et la cinétique de croissance de produits particuliers [Bergeat and Loison, 2001, Douglas et al., 2018, Gannon et al., 2007]. Cependant, elle ne peut pas être utilisée directement pour ces mesures car les signaux de fluorescence ne peuvent pas

Glowacki, D. R. et al. (2012). *The Journal of Physical Chemistry A*, 116(38):9545–9560

Gannon, K. L. et al. *The Journal of Physical Chemistry A*, 111(29):6679–6692.

Bergeat, A. and Loison, J.-C. (2001). *Physical Chemistry Chemical Physics*, 3(11):2038–2042.

fournir de valeurs de concentration. Ainsi, ces mesures ont été couplées à une réaction d'étalonnage pour déterminer les concentrations absolues des canaux de produits.

La deuxième partie de cette thèse s'est concentrée sur l'étude des rapports de branchement spécifiques de la réaction du radical CN avec le propène à 35 K. Ces expériences ont été réalisées en utilisant le spectromètre à ondes millimétriques chirpées en bande E récemment développé et intégré avec la technique CRESU permettant la détection d'un canal de produit, qui est la première mesure du genre pour cette réaction en dessous de la température ambiante. Les résultats de cette réaction sont présentés au chapitre 6 avec la future orientation de cette étude. Un rapport de $(0,23 \pm 0,07)$ a été mesurée pour le canal de produit de l'acrylonitrile ($\text{CH}_2\text{CHCN} + \text{CH}_3$), et bien que les tentatives pour observer d'autres produits de cette réaction n'aient pas abouti, les limites supérieures pour tous les isomères du cyanopropène ont été établies. Une mise en garde concernant la relaxation vibrationnelle sur ces mesures a été discutée. Pour mieux contraindre les limites supérieures des autres canaux produits, et leur détection potentielle à partir des données expérimentales, l'idée d'empilement spectral [Loomis et al., 2021], une technique couramment utilisée en astronomie, sera également explorée. Des résultats préliminaires sur la caractérisation de la surface d'énergie potentielle ont été présentés, et les travaux futurs viseront à calculer les fractions de branchement théoriques à l'aide de MESMER.

Les futures mesures de cette réaction exploreront l'effet de la pression sur cette réaction. Une limitation majeure de l'appareil CRESU-Chirp actuel est que très peu de tuyères ont les bonnes caractéristiques, en termes de densité, de pression et de température, pour avoir les meilleures conditions de travail pour détecter les produits. De nouvelles tuyères sont en cours de conception par un collègue doctorant, Omar Abdelkader Khedaoui, ce qui pourrait potentiellement aider. Une électronique de pointe a été utilisée pour obtenir les meilleures performances possibles sur cette gamme de fréquences via le spectromètre à bande E nouvellement développé. Un appareil à disque rotatif est en cours de développement pour obtenir des flux CRESU pulsés qui permettront d'atteindre des pressions plus basses dans des conditions CRESU et ouvriront la possibilité d'étudier cette réaction à de plus basses températures.

Low Temperature Kinetics of the Reaction Between Methanol and the CN Radical

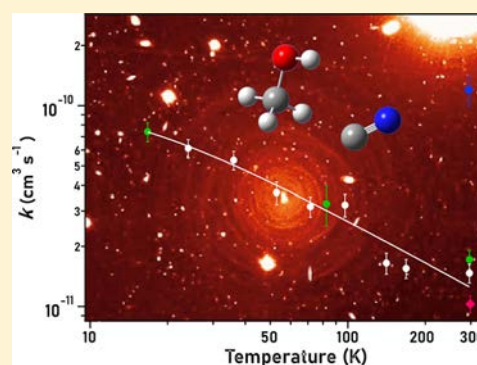
Published as part of *The Journal of Physical Chemistry virtual special issue "F. Javier Aoiz Festschrift"*.

Divita Gupta, Sidaty Cheikh Sid Ely, Ilsa R. Cooke,^{1b} Théo Guillaume, Omar Abdelkader Khedaoui,^{1b} Thomas S. Hearne, Brian M. Hays, and Ian R. Sims^{*1b}

Univ Rennes, CNRS, IPR (Institut de Physique de Rennes) - UMR 6251, F-35000 Rennes, France

Supporting Information

ABSTRACT: Methanol (CH₃OH) is considered by astronomers to be the simplest complex organic molecule (COM) and has been detected in various astrophysical environments, including protoplanetary disks, comets, and the interstellar medium (ISM). Studying the reactivity of methanol at low temperatures will aid our understanding of the formation of other complex and potentially prebiotic molecules. A major destruction route for many neutral COMs, including methanol, is via their reactions with radicals such as CN, which is ubiquitous in space. Here, we study the kinetics of the reaction between methanol and the CN radical using the well-established CRESU technique (a French acronym standing for Reaction Kinetics in Uniform Supersonic Flow) combined with Pulsed-Laser Photolysis–Laser-Induced Fluorescence (PLP-LIF). Electronic structure calculations were also performed to identify the exothermic channels through which this reaction can proceed. Our results for the rate coefficient are represented by the modified Arrhenius equation, $k(T) = 1.26 \times 10^{-11} (T/300 \text{ K})^{-0.7} \exp(-5.4 \text{ K}/T)$, and display a negative temperature dependence over the temperature range 16.7–296 K, which is typical of what has been seen previously for other radical–neutral reactions that do not possess potential energy barriers. The rate coefficients obtained at room temperature strongly disagree with a previous kinetics study, which is currently available in the Kinetics Database for Astrochemistry (KIDA) and therefore used in some astrochemical models.



1. INTRODUCTION

The interstellar medium is host to a rich chemistry that produces a variety of species, including those with six or more atoms that have been named complex organic molecules (COMs).¹ While the abundance of many COMs in the gas-phase has been explained by their formation and desorption from icy dust grain surfaces,^{2–4} COMs have also been detected in very cold (<10 K) environments where thermal desorption from ices is prohibited, suggesting a possible role of gas-phase formation routes at these low temperatures.^{5–7}

For a long time, reactions between two neutral species had not been considered to play a major role at the low temperatures and densities of the interstellar medium (ISM). Over the past couple of decades, however, the importance of neutral–neutral reactions has become well established as many of these reactions are barrierless, involve an initial weakly bound complex, or proceed through submerged barriers, meaning that many of these reactions continue at a sufficiently fast rate even at low temperatures.^{8–12} Given the difficulty in performing gas-phase kinetics experiments and theoretical calculations at low temperatures, kinetics data for most of the reactions expected to take place in interstellar and planetary environments are missing. In the absence of low temperature

data, many models either extrapolate from the room temperature rate coefficients or take the value as measured at room temperature over the whole temperature range, often down to 10 K.^{7,13}

Methanol was first detected in Sagittarius A and B2¹⁴ and has since been detected in various sources including galactic H II regions,¹⁵ prestellar cores,^{16,17} ISM clouds,¹⁸ protostellar sources,^{19,20} protoplanetary disks,²¹ and comets.^{22,23} The abundance of methanol is one of the highest among the COMs, as high as 3×10^{-5} with respect to H₂ in some sources.¹ Explaining the abundance of methanol in these sources requires accurate kinetic measurements (either experimental or theoretical) of the various routes involved in both its formation and destruction.

Rate coefficients for bimolecular reactions are often measured under pseudo-first-order conditions, in which the concentration of one of the neutral species (usually a stable molecule) must be accurately known. Given the low saturated vapor pressure of most COMs below 200 K, kinetics studies of

Received: September 5, 2019

Revised: October 15, 2019

Published: October 24, 2019

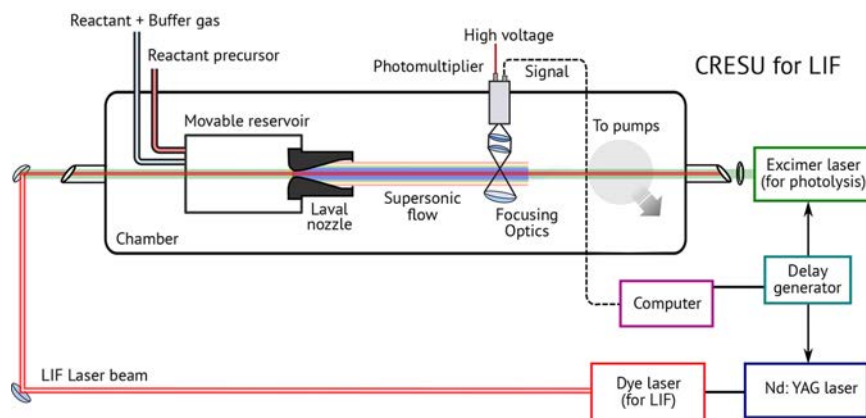


Figure 1. Schematic of the CRESU setup at Université de Rennes 1, used for the study of the kinetics of the reaction of methanol with the CN radical. The reactant gas mixture expands through a Laval nozzle from the high-pressure reservoir into the low-pressure chamber, creating a uniform supersonic flow. An excimer laser is used for the generation of the CN radicals, and a dye laser pumped by the third harmonic of a pulsed Nd:YAG laser is used for LIF and is aligned along the path of the flow and the excimer laser. A photomultiplier tube along with the corresponding optics is used to record the fluorescence signal. The laser timings and delays are controlled using a delay generator. Reprinted from ref 41. Copyright 2019 American Chemical Society.

their reactivity at low temperature can be difficult. Gas cooling by collisions with cold walls in cryogenically cooled cells can only be used down to about 200 K, except for certain light species like CO where lower temperatures can be achieved, before condensation on the cell walls causes large uncertainties in the gas concentration.^{24,25} Free jet expansions have been used extensively in spectroscopy to produce cold gas; however, the density and temperature vary strongly along the beam making them unsuitable for kinetics measurements. The CRESU technique, an essentially wall-less cooling method, allows precise control over these parameters (CRESU: Cinétique de Réaction en Ecoulement Supersonique Uniforme, a French acronym standing for Reaction Kinetics in Uniform Supersonic Flow). It involves an expansion of gas from a high-pressure region to a low-pressure region through a particular type of convergent-divergent nozzle called a Laval nozzle. This expansion results in a beam of cold gas that is uniform in velocity, temperature, and density typically for several tens of centimeters. Rowe and co-workers²⁶ developed the use of CRESU flows to study gas-phase kinetics, and this technique has since been used to characterize many ion-neutral reactions,^{27–31} neutral–neutral reactions,^{8,12,32–36} and collisional energy transfer processes.^{37–40} A detailed summary of the reactions studied using the CRESU technique was published recently.⁴¹

Radical-neutral reactions are thought to be an important destruction route for gas-phase methanol at low temperatures. The rate coefficients for the reactions of methanol with other radicals such as OH³⁶ and C(3P)⁴² have been measured experimentally using the CRESU technique and were found to remain rapid at low temperatures relevant to the cold ISM. The CN radical has been found in many astronomical sources,^{43–46} and CN chemistry has been shown to play an important role in Titan's atmosphere.^{47–49} Thus, the reaction with CN radicals is a feasible destruction route for methanol in a range of low temperature environments. One of the expected products of this reaction, the methoxy radical (CH₃O), has been detected in the cold source Barnard 1b,⁵⁰ and there has been a significant discussion concerning its abundance compared to its isomer, hydroxymethyl radical (CH₂OH), which has not been detected yet. In the low-temperature

conditions of Barnard 1b, non-thermal mechanisms must be invoked if methoxy formation is expected to occur on dust grains, as CH₃O and CH₂OH cannot thermally desorb from ice surfaces. However, ice-phase experiments on the photodissociation of methanol suggest the CH₂OH isomer is favored, and therefore, it has been suggested that the methoxy radical abundance could be explained by its formation in the gas-phase.⁵¹ In particular, the reaction between methanol and the OH radical has been discussed as a source of CH₃O/CH₂OH, but the branching ratio into the two channels has not yet been fully characterized.^{12,36,51}

To the best of our knowledge, no previous experiments have been published for the reaction of CN radicals with methanol below room temperature. The earliest study at room temperature was conducted by Sayah and co-workers⁵² who performed flow-tube experiments using photodissociation of C₂N₂ at 193 nm as their source of CN radicals. They determined a rate coefficient of $(1.2 \pm 0.2) \times 10^{-10} \text{ cm}^3 \text{ s}^{-1}$ which is different by an order of magnitude from a later study by Janssen and Hershberger,⁵³ who report a value of $(1.03 \pm 0.10) \times 10^{-11} \text{ cm}^3 \text{ s}^{-1}$ at room temperature. Janssen and Hershberger used photolysis of ICN at 266 nm to produce the CN radicals and studied the reaction using time-resolved infrared diode laser absorption spectroscopy, allowing them also to investigate the reaction products.

Here, the rate coefficients for the reaction of methanol with the CN radical over a wide temperature range of 16.7–296 K using the CRESU technique are presented. First the experimental and theoretical methodologies used in these measurements are detailed followed by the rate coefficients and their dependence on temperature, and a discussion of the implications of the results and their astrophysical importance is given. These measurements can be input into astrochemical models in order to assess the importance of the reaction as a destruction route for methanol at various temperatures.

2. EXPERIMENTAL METHODOLOGY

The kinetics of the reaction between the CN radical and methanol were measured using the Pulsed-Laser Photolysis–Laser-Induced Fluorescence (PLP-LIF) technique. The low temperatures, down to 16.7 K, were achieved using the

CRESU technique, which has been described in detail in previous publications,^{37,41,54} and will only be described in brief here. Figure 1 shows a schematic of the CRESU technique configured for the study of neutral–neutral reaction kinetics using PLP-LIF.⁴¹ A dilute mixture (typically <1%) of the reactant and radical precursor in a buffer gas (He, Ar, or N₂) expands isentropically from a high-pressure region (reservoir) into a low-pressure region (chamber) through a convergent-divergent Laval nozzle to generate a cold supersonic flow that is uniform in temperature and density. Given the high density of the molecules (10^{16} – 10^{17} cm⁻³) in the flow, collisions between the molecules ensure thermal equilibrium is maintained, typically for tens of centimeters. A wide range of temperatures can be reached by careful manipulation of the physical dimensions of the nozzle (in particular the throat diameter), the buffer gas used, and the flow conditions/pumping capacity, which varies the pressure in the reservoir and in the chamber. Characterizing the flow temperature is essential to study chemical kinetics and was performed using impact pressure measurements⁵⁴ for each nozzle prior to undertaking kinetics experiments.

Two methods were used to perform the experiments, as the first set of measurements at room temperature deviated significantly from previous measurements made by Sayah and co-workers.⁵² In the first method, hereon referred to as EM I, gas mixtures were made in a Teflon coated stainless steel container by careful control of the partial pressures of methanol vapor and the buffer gas. Different concentrations of methanol could be obtained by varying the pressure of the buffer gas. A solid sample of ICN was placed on a frit (porous glass) in a glass vessel and introduced into the chamber via a controlled flow of buffer gas (~200 sccm). The fourth harmonic output of a Nd:YAG laser (Spectra Physics GCR 190) at 266 nm was used to photodissociate ICN (Acros Organics, 98%) at a laser fluence in the reaction zone of ~35 mJ cm⁻², producing CN radicals largely in the $\nu = 0$ level of the $X^2\Sigma^+$ state. In the second method, referred to as EM II hereinafter, a Controlled Evaporation and Mixing system (CEM) was used to introduce methanol into the flow. A stainless steel vessel containing methanol was pressurized with nitrogen, and a flow of liquid methanol was passed via a Coriolis liquid flow meter (Bronkhorst mini CORI-FLOW ML120 V00) into an evaporator (Bronkhorst W-202A-222-K) and was mixed with a controlled flow of buffer gas via a thermal mass flow controller (Bronkhorst EL-FLOW Prestige). The CN radicals were generated by photodissociation of ICN (Acros Organics, 98%) at 248 nm using a KrF excimer laser (Coherent LPXPro 210) at a laser fluence in the reaction zone of ~25 mJ cm⁻². Photodissociation of ICN at this wavelength also produces CN radicals primarily (>93%) in the $\nu = 0$ level of the $X^2\Sigma^+$ state.⁵⁵ At both wavelengths, rapid rotational relaxation is assured by collisions with the cold, dense buffer gas.

In both methods, the LIF/fluorescence signal was then recorded by excitation in the (0,0) band of the $B^2\Sigma^+ - X^2\Sigma^+$ electronic transition at 388.3 nm using a dye laser (Laser Analytical Systems, LDL 20505, operating with 0.2 g/L mixture of Exciton Exalite 389 dye in 1,4-dioxane) pumped by the frequency-tripled output at 355 nm of a Nd:YAG laser (Continuum, Powerlite Precision II). A narrow band interference filter centered at 420 nm (Ealing Optics) was used with a photomultiplier tube (PMT, Thorn EMI 6723) to select the off-resonant fluorescence into the first vibrational

level of the ground state via the (0,1) band. As the start of the reaction is marked by the initiation of ICN photolysis, delays in the range of zero to hundreds of microseconds between the excimer and the LIF laser pulses, both operating at 10 Hz, allowed us to record the time dependence of the CN radical depletion during the reaction.

The experiments were performed under pseudo-first-order conditions with methanol in excess. The absorption cross section of ICN has been reported as 3×10^{-19} cm² at 266 nm⁵⁶ and 4.7×10^{-19} cm² at 248 nm.⁵⁷ Given the density of ICN in the gas flow (~ 10^{12} cm⁻³), an estimated maximum CN ($X^2\Sigma^+$) concentration of ~ 1×10^{10} cm⁻³ in either condition (EM I or EM II) was obtained at the laser fluences used, which is lower than the concentration of methanol used by a factor of at least 100.

The LIF signals were recorded by a gated integrator (Stanford Research Systems) at 200 evenly spaced time delays and were averaged typically 5–10 times. These were fit to single exponential decays, yielding pseudo-first-order rate coefficients. Linear plots of these pseudo-first-order rate coefficients versus the methanol concentration were then used to calculate the second-order rate coefficient. The procedure was repeated for multiple temperatures using different Laval nozzles. The experimental parameters and rate coefficients measured for each temperature are summarized in Table 1.

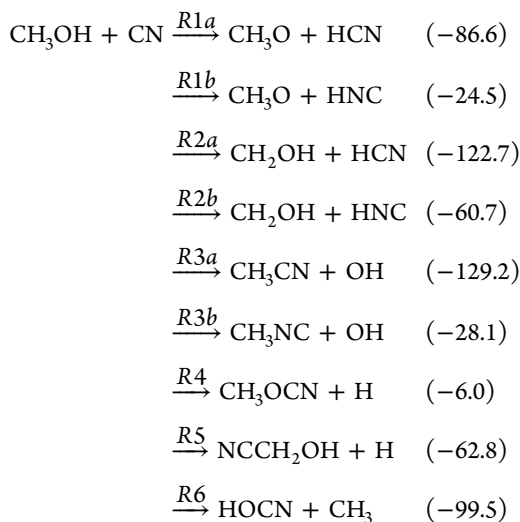
Table 1. Rate Coefficients for the Reaction of the CN Radical with Methanol Measured at Different Temperatures, with the Associated Experimental Parameters^a

<i>T</i> (K)	buffer gas	total density (10 ¹⁶ cm ⁻³)	range of [CH ₃ OH] (10 ¹³ cm ⁻³)	no. of exptl points	rate coefficient <i>k</i> (10 ⁻¹¹ cm ³ s ⁻¹)
16.7	He ^c	4.89	0.90–6.50	9	7.4 ± 1.2
24	He ^b	18.30	0.00–8.94	8	5.82 ± 0.63
	He ^b	18.30	0.00–5.81	10	6.82 ± 0.77
					6.1 ± 0.6
36	He ^b	5.28	0.00–3.64	7	5.4 ± 0.6
52.8	Ar ^b	20.20	0.00–6.72	7	3.7 ± 0.5
71.5	N ₂ ^b	5.79	0.00–6.22	9	3.2 ± 0.4
82.6	N ₂ ^c	4.88	0.97–9.74	12	3.37 ± 0.84
	N ₂ ^c	4.88	0.96–9.01	6	2.96 ± 1.30
					3.3 ± 0.7
97.4	Ar ^b	15.45	0.00–12.14	8	3.2 ± 0.4
141	Ar ^b	6.95	0.00–16.89	8	1.6 ± 0.2
168	Ar ^b	9.01	0.00–25.28	9	1.6 ± 0.2
296	N ₂ ^b	15.15	1.07–20.92	8	1.49 ± 0.18
	N ₂ ^b	14.30	0.00–27.46	9	1.45 ± 0.18
	N ₂ ^b	32.00	0.00–41.46	9	1.48 ± 0.19
	N ₂ ^c	9.02	10.51–52.57	5	1.72 ± 0.18
	N ₂ ^c	11.69	6.84–34.19	5	1.66 ± 0.52
					1.6 ± 0.2

^aQuoted uncertainties are calculated using the standard error evaluated from the second order plot, multiplied by the appropriate Student's *t* factor for 95% confidence, and then combined with an estimated systematic error of 10%. Entries in bold are variance weighted mean values of rate coefficients at the same temperature, calculated using statistical uncertainties only, where the resulting uncertainty is then combined in quadrature with an estimated systematic error of 10%. ^bExperiments performed using EM I. ^cExperiments performed using EM II.

3. THEORETICAL METHODOLOGY

Electronic structure calculations were performed to optimize the stationary points for the different channels of the reaction of the CN radical with methanol using Gaussian09.⁵⁸ Only exothermic channels were considered as viable reaction channels at such low temperatures and are shown here:



High accuracy single point energies were calculated using CCSD(T)^{59,60}/aug-cc-pVTZ^{61,62} for all the structures (reactants and products) following optimization of their geometries at CCSD^{59,63–65}/aug-cc-pVTZ. The difference between the single point energies of the products and reactants was used to calculate the changes in energy for all the reaction channels, and are provided in parentheses next to each channel in kJ mol⁻¹. The parameters for the optimized structures are given in the [Supporting Information](#). The standard reaction enthalpy $\Delta H_r^\circ(298.15 \text{ K})$ for each channel was also calculated, as explained by Ochterski,⁶⁶ using the composite CBS-QB3^{67,68} method.

4. RESULTS

A typical LIF decay trace and second order plot obtained at temperature 168 K are shown in [Figure 2](#). LIF measurements were also taken at negative time delays to establish a pretrigger baseline, as seen in [Figure 2](#). The fit is only made after 10–50 μs so as to allow enough time for rotational relaxation of CN and for the photomultiplier tube to recover from the excimer laser scatter. The nonzero intercept in the second order plot, shown in the lower panel of [Figure 2](#), is due to the loss of CN by diffusion out of the probed beam area and by reaction with the precursor and/or impurities in the buffer gas. As the laser alignment and other external factors may change over periods of days, the intercepts of different second-order plots are not necessarily constant. Therefore, we derive the second-order rate coefficient for each temperature from the readings taken on a given day rather than taking all of the k_{first} values at that temperature.

The weighted means of these multiple readings are then calculated for each temperature are shown in [Table 1](#) along with their uncertainties, calculated using 95% confidence limits of the standard error from the two-sided Student's t -distribution. The experimentally measured rate coefficients over the temperature range $T = 16.7\text{--}296 \text{ K}$ are well fit by the modified Arrhenius equation $k(T) = 1.26 \times 10^{-11} (T/300$

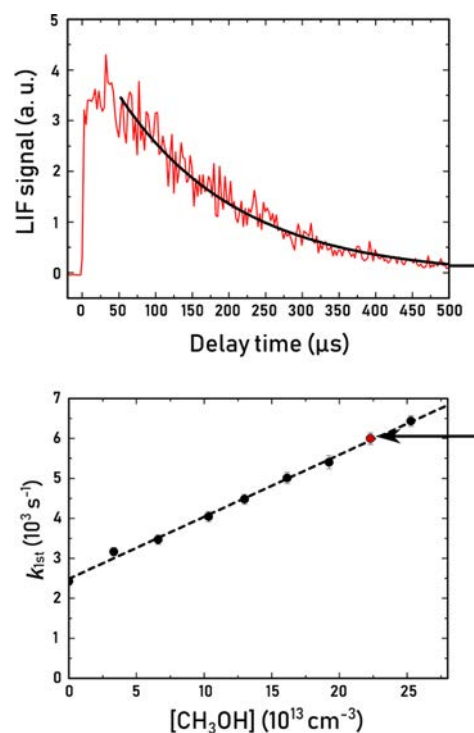


Figure 2. Typical kinetics plot obtained using PLP-LIF at a temperature of 168 K in continuous CRESU flow. The upper panel shows the LIF signal decay of CN ($B^2\Sigma^+ \rightarrow X^2\Sigma^+$) at a methanol density $2.22 \times 10^{14} \text{ cm}^{-3}$ fitted to a single exponential decay function. The lower panel shows the second order plot where the pseudo-first order rate coefficients are plotted against the methanol concentration. The slopes of the second order plots yield the rate coefficients as shown in [Table 1](#).

$\text{K})^{-0.7} \exp(-5.4\text{K}/T) \text{ cm}^3 \text{ s}^{-1}$ and are shown in [Figure 3](#) along with the rate coefficients measured at room temperature from two previous studies.

The upper limit for the concentration of methanol is an important experimental constraint imposed due to the formation of methanol dimers, which could interfere with the experimental measurement. The range of methanol densities used to calculate the second-order rate coefficient for each temperature, as mentioned in [Table 1](#), was based on the tests where first-order rate coefficients were measured over a large range of methanol density and a careful observation of when the first-order plot deviated from linear behavior, which would indicate the loss of pseudo-first-order conditions due to formation of dimers. The methanol concentration at which this deviation starts to occur is dependent on the nature of the buffer gas and its temperature and density, occurring at lower values for low temperatures and high densities.

The reaction enthalpies $\Delta H_r^\circ(298.15 \text{ K})$ were obtained at CBS-QB3, which is a composite method used widely^{69–71} to obtain accurate energies of molecules and radicals. The values obtained were compared with enthalpy values calculated using the active thermochemical table (ATcT)^{72–74} and are shown in [Table 2](#). ATcT has been developed by Ruscic and co-workers and is based on statistical analysis to produce a self-consistent thermochemical network. The reaction enthalpies for the various channels follow the same trend across the different methods, with channel R3a being the most exothermic, followed by R2a, R6, and R1a.

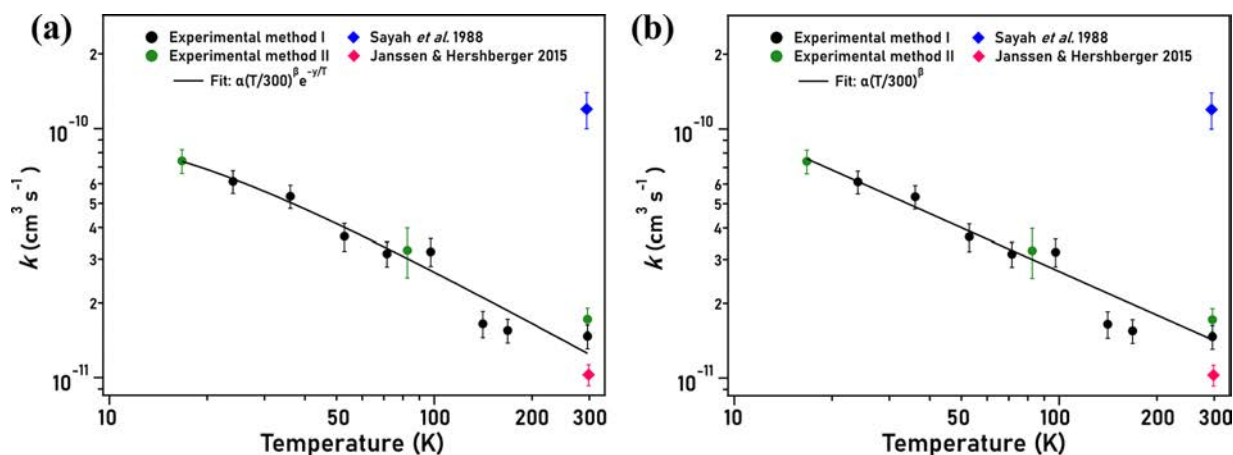


Figure 3. Rate coefficients for the reaction of the CN radical with methanol displayed on a log–log scale as a function of temperature. The filled black circles are the experiments performed with the CRESU setup using EM I, and the filled green circles are the experiments using EM II. The blue diamond represents the work of Sayah et al., and the magenta diamond represents the work of Janssen and Hershberger. (a) Modified Arrhenius fit, $\alpha(T/300 \text{ K})^{\beta} e^{-\gamma/T}$ with the fitting parameters ($\pm 95\%$ confidence limits): $\alpha = (1.26 \pm 0.43) \times 10^{-11} \text{ cm}^3 \text{ s}^{-1}$, $\beta = (-0.72 \pm 0.33)$, and $\gamma = (5.4 \pm 12)$. (b) Modified Arrhenius fit with $\gamma = 0$, $\alpha(T/300)^{\beta}$ with the fitting parameters: $\alpha = (1.42 \pm 0.31) \times 10^{-11} \text{ cm}^3 \text{ s}^{-1}$ and $\beta = (-0.58 \pm 0.09)$.

Table 2. Reaction Enthalpies $\Delta H_r^{\circ}(298.15 \text{ K})$, in kJ/mol, Calculated for Each Channel Using CBS-QB3 Compared with the Enthalpy Values Calculated from the Values Provided in the Active Thermochemical Table Ver. 1.22 e^{74a}

	R1a	R1b	R2a	R2b	R3a	R3b	R4	R5	R6
CBS-QB3	-90.9	-31.2	-126.0	-66.3	-127.6	-28.1	-23.2	-76.6	-111.0
ATcT (1.22e)	-99.3	-36.2	-137.5	-74.4	-138.4	-35.2			-118.4

^aThe reaction enthalpies for R4 and R5 could not be calculated as the species CH_3OCN and NCCH_2OH are missing from the thermochemical network of ATcT ver. 1.22 e.

5. DISCUSSION

Figure 3 shows the experimentally obtained values of the rate coefficient from this work as a function of temperature, compared with the two previous studies measured at room temperature. The CRESU results have been fit to the modified Arrhenius equation (Kooij fit) in Figure 3a and show a dependence $k(T) = 1.26 \times 10^{-11} (T/300 \text{ K})^{-0.7} \exp(-5.4 \text{ K}/T) \text{ cm}^3 \text{ s}^{-1}$. The CRESU data was also fit using the $\alpha(T/300 \text{ K})^{\beta}$ expression, which is shown in Figure 3b, and follows the curve $k(T) = 1.42 \times 10^{-11} (T/300 \text{ K})^{-0.6} \text{ cm}^3 \text{ s}^{-1}$. The work by Sayah et al.⁵² at room temperature yielded a value of $1.2 \times 10^{-10} \text{ cm}^3 \text{ s}^{-1}$, which was different from the value obtained here using EM I by an order of magnitude. Following this, a secondary method for CN radical generation and for creating methanol/buffer gas mixtures (EM II) was used to confirm the measurements made using EM I (particularly those at room temperature), and to reduce the likelihood of systematic errors. A room temperature rate coefficient was measured using EM II that agrees within error to that obtained using EM I. The current results are further supported by the work of Janssen and Hershberger⁵³ who obtained a rate coefficient of $1.03 \times 10^{-11} \text{ cm}^3 \text{ s}^{-1}$ at room temperature, which is in good agreement with the value reported here of $(1.6 \pm 0.2) \times 10^{-11} \text{ cm}^3 \text{ s}^{-1}$. It is unclear why the value measured by Sayah et al. is faster than these three essentially independent measurements by an order of magnitude.

The difference between the ionization potential of methanol and the electron affinity of CN radical is 6.98 eV, which is less than the 8.75 eV semiempirical limit proposed by Ian Smith and colleagues⁷⁵ for the existence of a nonsubmerged barrier to reaction. This suggests the reaction between the CN radical

and methanol will be rapid even at low temperatures, with a rate coefficient greater than $\sim 10^{-10} \text{ cm}^3 \text{ s}^{-1}$ at 10 K, consistent with what was observed in this study.

Faure et al.⁷⁶ provided a semiempirical model which combines room temperature kinetics data with a long-range capture method to predict rate coefficients for neutral–neutral reactions at low temperature. For reactions with rate coefficients greater than $10^{-11} \text{ cm}^3 \text{ s}^{-1}$ at room temperature, a fit ($k(T) = \alpha(T/300 \text{ K})^{\beta} e^{-\gamma/T}$) is proposed to be valid at temperatures as low as 5 K. A plot obtained using the model is shown in Figure 4. The method along with the parameters used are provided in Tables S1 and S2 in the Supporting Information. This method, however, overpredicts the rate coefficient, suggesting that the reaction is not controlled by long-range attractive forces even at the lowest temperatures where measurements have been performed. It appears likely that submerged barriers are playing an important role in determining the low temperature reactivity.

The reaction enthalpies $\Delta H_r^{\circ}(298.15 \text{ K})$ obtained using CBS-QB3 and ATcT, shown in Table 2, show a reasonable agreement. The reaction enthalpies for R4 and R5 could not be calculated from ATcT due to missing values for NCCH_2OH and CH_3OCN in the active thermochemical table. The reaction channels R1a, R2a, R3a, and R6 are the most thermodynamically favored product channels of the studied reaction. Similar trends were also found from the reaction energies calculated using the difference between the single point CCSD(T)/aug-cc-pVTZ energies of the reactants and products. The HNC channels for both R1 and R2 were found to have lower stabilization energies compared to the HCN analogues, which is expected as HCN is more stable than

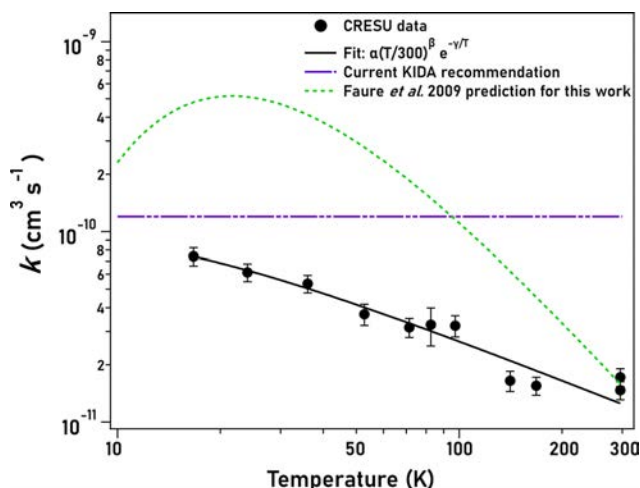


Figure 4. CRESU experimental data (black filled circles) fit with a modified Arrhenius equation (black solid line), $k(T) = 1.26 \times 10^{-11} (T/300 \text{ K})^{-0.7} \exp(-5.5 \text{ K}/T) \text{ cm}^3 \text{ s}^{-1}$, and the prediction, $k(T) = 1.80 \times 10^{-11} (T/300 \text{ K})^{-2.1} \exp(-44.6 \text{ K}/T) \text{ cm}^3 \text{ s}^{-1}$, based on the room temperature value from this work using capture theory model from Faure *et al.*⁷⁶ (green dashed line). The current KIDA recommendation for this reaction is shown in purple.

HNC. Preliminary calculations performed at B3LYP/aug-cc-pVTZ to identify the saddle points for the reaction channels suggest that the channels R3a, R3b, and R4 have very high (zero-point corrected) barriers of 83.6, 134.7, and 227.9 kJ mol⁻¹, respectively, making them unlikely to take place in low temperature environments. These preliminary calculations were likely of an insufficiently high level to locate the submerged saddle points for the reaction channels R1 and R2, indicating the need for more accurate *ab initio* methods.

To the best of authors' knowledge, this is the first set of kinetics data published for this reaction at low temperatures, which makes it useful for atmospheric and astrochemical models. The Kinetics Database for Astrochemistry, KIDA (homepage: <http://kida.obs.u-bordeaux1.fr/>, accessed July 2019),^{77,78} currently uses the rate coefficient measured by Sayah *et al.* over the whole temperature range of 10–300 K, which is significantly different from what is observed experimentally both here and by Janssen and Hershberger.⁵³ Furthermore, the reaction is assumed to proceed in equal ratios via channels 1a (CH₃O + HCN) and 2a (CH₂OH + HCN). Janssen and Hershberger measured the CH₂OH channel as the dominant reaction product at room temperature, with only 8% into the methoxy channel, based on isotopic experiments. Models using the room temperature rate coefficient reported in KIDA, therefore, overpredict both the rate of CH₃O formation and its yield relative to the CH₂OH isomer. The product branching ratios for this reaction have not been measured below room temperature, so it is unknown whether the reaction will be a significant source of methoxy under dense cloud conditions.

A new technique combining Chirped-Pulse Fourier-Transform Microwave (CP-FTMW) spectroscopy with CRESU flows, named Chirped-Pulse in Uniform Flow (CPUF), has been used to measure the channel-specific rate coefficients for the CN + propyne reaction at low temperature.⁷⁹ This technique can aid in understanding which reaction channels may be dominant at low temperatures. An E-band (~60–90 GHz) spectrometer has been developed in Rennes that will

allow the investigation of the products formed in the reaction between the CN radical and methanol as some rotational lines corresponding to CH₃O and CH₂OH fall within this frequency range.

Other destruction routes for methanol with the OH radical³⁶ and the C(³P)⁴² radical have been reported to have rate coefficients approaching 10⁻¹⁰ cm³ s⁻¹ at 10 K. A similar rate coefficient for the reaction of CN with methanol further establishes the role of this reaction as a significant destruction route for methanol in cold interstellar clouds where both these species have been detected. The room temperature rate coefficient reported here is an order of magnitude lower than the current value in KIDA, suggesting that astrochemical networks involving warm gas temperatures (e.g., hot cores models) may overpredict the destruction of methanol. Use of the current KIDA-recommended rate coefficients may also lead to overprediction of the abundance of the methoxy radical, which is thought to be a precursor to more complex organic molecules like dimethyl ether and methyl formate.⁶ Astrochemical models assuming the current KIDA rate coefficients (6.0 × 10⁻¹¹ cm³ s⁻¹ into both the CH₃O and CH₂OH channels) should be updated to reflect these new laboratory data. Janssen and Hershberger's⁵³ room temperature branching ratio should be used at $T < 300$ K until low temperature measurements have been made.

6. CONCLUSION AND FUTURE OUTLOOK

The CRESU technique coupled with PLP-LIF has been employed to show that the reaction between the CN radical and methanol has a negative temperature dependence in the temperature range 16.7–296 K, well-characterized by the modified Arrhenius equation $k(T) = 1.29 \times 10^{-11} (T/300 \text{ K})^{-0.7} \exp(-5.5 \text{ K}/T)$. The present measurements vary significantly from the room temperature value of Sayah *et al.* which is currently the value recommended by the KIDA database for all temperatures between 10 and 300 K. While this experiment has yielded the overall rate coefficient for the reaction of the CN radical with methanol, the PLP-LIF technique is unable to provide product-specific rate coefficients or branching ratios. Electronic structure calculations revealed that the reaction channels involving CN substitution have high barriers, making them unlikely to occur at low temperatures. The H atom abstraction routes are likely to be the dominant reaction channels under cold ISM conditions, forming the isomers CH₂OH and CH₃O. More calculations are needed to locate the submerged saddle points for other channels for the reaction of the CN radical with methanol, followed by theoretical kinetics calculations. A new setup integrating chirped-pulse broadband microwave spectroscopy with continuous flow CRESU is being developed in Rennes and will allow the identification of the products and provide the branching ratios for the reaction channels at low temperatures.

■ ASSOCIATED CONTENT

📄 Supporting Information

The Supporting Information is available free of charge on the ACS Publications website at DOI: 10.1021/acs.jpca.9b08472.

Parameters and description of the method suggested by Faure *et al.*⁷⁶ which extrapolates the room temperature rate coefficient to lower temperatures based on long-range capture model; Cartesian coordinates of the

optimized geometries for various suggested reaction channels (PDF)

AUTHOR INFORMATION

Corresponding Author

*Email: ian.sims@univ-rennes1.fr

ORCID

Ilsa R. Cooke: [0000-0002-0850-7426](https://orcid.org/0000-0002-0850-7426)

Omar Abdelkader Khedaoui: [0000-0002-9635-5898](https://orcid.org/0000-0002-9635-5898)

Ian R. Sims: [0000-0001-7870-1585](https://orcid.org/0000-0001-7870-1585)

Author Contributions

D.G.: Experimental measurements using EM II (see text), theoretical calculations, and drafting and correction of article. S.C.S.E.: Experimental measurements using EM I. I.R.C.: Experimental measurements using EM II (see text), drafting and correction of article. T.G.: Laser setup for EM II. O.A.K.: Design, 3D printing fabrication, and testing of lowest T Laval nozzle used for EM II. T.S.H.: Construction and operation of Controlled Evaporator Mixer system for EM II. B.M.H.: Laser alignment for EM II. I.R.S.: Scientific direction of project, participation in EM I measurements, and correction of article.

Notes

The authors declare no competing financial interest.

ACKNOWLEDGMENTS

The authors would like to thank Hamza Labiad and Joey Messinger for assistance with experiments and Jonathan Courbe, Jonathan Thiévin, Didier Biet, Ewen Gallou, and Alexandre Dapp for technical support. The authors acknowledge funding from the European Union's Horizon 2020 research and innovation programme under European Research Council (ERC) Grant Agreement 695724-CRESUCHIRP, and under the Marie Skłodowska-Curie grant agreement 845165-MIRAGE. The authors are also grateful for support from the European Regional Development Fund, the Region of Brittany and Rennes Metropole. This work was supported by the CNRS/CNES programme "Physique et Chimie du Milieu Interstellaire" (PCMI).

REFERENCES

- Herbst, E.; van Dishoeck, E. F. Complex Organic Interstellar Molecules. *Annu. Rev. Astron. Astrophys.* **2009**, *47* (1), 427–480.
- Garrod, R. T.; Weaver, S. L. W.; Herbst, E. Complex Chemistry in Star-forming Regions: An Expanded Gas-Grain Warm-up Chemical Model. *Astrophys. J.* **2008**, *682*, 283–302.
- Caselli, P.; Hasegawa, T. I.; Herbst, E. Chemical Differentiation between Star-Forming Regions - The Orion Hot Core and Compact Ridge. *Astrophys. J.* **1993**, *408*, 548–558.
- Burke, D. J.; Puletti, F.; Woods, P. M.; Viti, S.; Slater, B.; Brown, W. A. Trapping and Desorption of Complex Organic Molecules in Water at 20 K. *J. Chem. Phys.* **2015**, *143*, 164704.
- Vasyunin, A. I.; Herbst, E. Reactive Desorption and Radiative Association as Possible Drivers of Complex Molecule Formation in the Cold Interstellar Medium. *Astrophys. J.* **2013**, *769* (1), 34.
- Balucani, N.; Ceccarelli, C.; Taquet, V. Formation of Complex Organic Molecules in Cold Objects: The Role of Gas-Phase Reactions. *Mon. Not. R. Astron. Soc.: Lett.* **2015**, *449* (1), L16–L20.
- Bacmann, A.; Taquet, V.; Faure, A.; Kahane, C.; Ceccarelli, C. Detection of Complex Organic Molecules in a Prestellar Core: A New Challenge for Astrochemical Models. *Astron. Astrophys.* **2012**, *541*, L12.
- Sims, I. R.; Queffelec, J. L.; Travers, D.; Rowe, B. R.; Herbert, L. B.; Karthäuser, J.; Smith, I. W. M. Rate Constants for the Reactions of CN with Hydrocarbons at Low and Ultra-Low Temperatures. *Chem. Phys. Lett.* **1993**, *211* (4–5), 461–468.
- Balucani, N.; Asvany, O.; Huang, L. C. L.; Lee, Y. T.; Kaiser, R. I.; Osamura, Y.; Bettinger, H. F. Formation of Nitriles in the Interstellar Medium via Reactions of Cyano Radicals, CN($X^2\Sigma^+$), with Unsaturated Hydrocarbons. *Astrophys. J.* **2000**, *545* (2), 892–906.
- Sabbah, H.; Biennier, L.; Sims, I. R.; Georgievskii, Y.; Klippenstein, S. J.; Smith, I. W. M. Understanding Reactivity at Very Low Temperatures: The Reactions of Oxygen Atoms with Alkenes. *Science* **2007**, *317* (5834), 102–105.
- Morales, S. B.; Bennett, C. J.; Le Picard, S. D.; Canosa, A.; Sims, I. R.; Sun, B. J.; Chen, P. H.; Chang, A. H. H.; Kislov, V. V.; Mebel, A. M.; et al. A Crossed Molecular Beam, Low-Temperature Kinetics, and Theoretical Investigation of the Reaction of the Cyano Radical (CN) with 1,3-Butadiene (C_4H_6). A Route to Complex Nitrogen-Bearing Molecules in Low-Temperature Extraterrestrial. *Astrophys. J.* **2011**, *742* (1), 26.
- Shannon, R. J.; Blitz, M. A.; Goddard, A.; Heard, D. E. Accelerated Chemistry in the Reaction between the Hydroxyl Radical and Methanol at Interstellar Temperatures Facilitated by Tunnelling. *Nat. Chem.* **2013**, *5*, 745–749.
- Millar, T. J.; Herbst, E.; Charnley, S. B. The Formation of Oxygen-Containing Organic Molecules in the Orion Compact Ridge. *Astrophys. J.* **1991**, *369*, 147–156.
- Ball, J. A.; Gottlieb, C. A.; Lilley, A. E.; Radford, H. E. Detection of Methyl Alcohol in Sagittarius. *Astrophys. J.* **1970**, *162*, L203–L210.
- Batrla, W.; Matthews, H. E.; Menten, K. M.; Walmsley, C. M. Detection of Strong Methanol Masers towards Galactic H II Regions. *Nature* **1987**, *326*, 49–51.
- Vastel, C.; Ceccarelli, C.; Lefloch, B.; Bachiller, R. The Origin of Complex Organic Molecules in Prestellar Cores. *Astrophys. J., Lett.* **2014**, *795* (1), L2.
- Bizzocchi, L.; Caselli, P.; Spezzano, S.; Leonardo, E. Deuterated Methanol in the Pre-Stellar Core L1544. *Astron. Astrophys.* **2014**, *569*, A27.
- Turner, B. E. The Physics and Chemistry of Small Translucent Molecular Clouds. XI. Methanol. *Astrophys. J.* **1998**, *501* (2), 731–748.
- van Dishoeck, E. F.; Blake, G. A.; Jansen, D. J.; Groesbeck, T. D. Molecular Abundances and Low-Mass Star Formation. II. Organic and Deuterated Species toward IRAS 16293–2422. *Astrophys. J.* **1995**, *447* (2), 760–782.
- Kristensen, L. E.; van Dishoeck, E. F.; van Kempen, T. a.; Cuppen, H. M.; Brinch, C.; Jørgensen, J. K.; Hogerheijde, M. R. Methanol Maps of Low-Mass Protostellar Systems: The Serpens Molecular Core. *Astron. Astrophys.* **2010**, *516*, A57.
- Walsh, C.; Loomis, R. A.; Öberg, K. I.; Kama, M.; van 't Hoff, M. L. R.; Millar, T. J.; Aikawa, Y.; Herbst, E.; Widicus Weaver, S. L.; Nomura, H. First Detection of Gas-Phase Methanol in a Protoplanetary Disk. *Astrophys. J., Lett.* **2016**, *823* (1), L10.
- Biver, N.; Bockelée-Morvan, D.; Crovisier, J.; Henry, F.; Davies, J. K.; Matthews, H. E.; Colom, P.; Gerard, E.; Lis, D. C.; Phillips, T. G.; et al. Spectroscopic Observations of Comet C/1999 H1 (Lee) with the SEST, JCMT, CSO, IRAM, and Nançay Radio Telescopes. *Astron. J.* **2000**, *120*, 1554–1570.
- Biver, N.; Bockelée-Morvan, D.; Crovisier, J.; Colom, P.; Henry, F.; Moreno, R.; Paubert, G.; Despois, D.; Lis, D. C. Chemical Composition Diversity among 24 Comets Observed at Radio Wavelengths. *Earth, Moon, Planets* **2002**, *90* (1–4), 323–333.
- Wollenhaupt, M.; Carl, S. A.; Horowitz, A.; Crowley, J. N. Rate Coefficients for Reaction of OH with Acetone between 202 and 395 K. *J. Phys. Chem. A* **2000**, *104* (12), 2695–2705.
- Dillon, T. J.; Hölscher, D.; Sivakumaran, V.; Horowitz, A.; Crowley, J. N. Kinetics of the Reactions of HO with Methanol (210–351 K) and with Ethanol (216–368 K). *Phys. Chem. Chem. Phys.* **2005**, *7*, 349–355.
- Rowe, B. R.; Dupeyrat, G.; Marquette, J. B.; Gaucherel, P. Study of the Reactions $N_2^+ + 2N_2 \rightarrow N_4^+ + N_2$ and $O_2^+ + 2O_2 \rightarrow O_4^+$

- + O₂ from 20 to 160 K by the CRESU Technique. *J. Chem. Phys.* **1984**, *80* (10), 4915–4921.
- (27) Rowe, B. R.; Marquette, J. B.; Dupeyrat, G.; Ferguson, E. E. Reactions of He⁺ and N⁺ Ions with Several Molecules at 8 K. *Chem. Phys. Lett.* **1985**, *113* (4), 403–406.
- (28) Marquette, J. B.; Rowe, B. R.; Dupeyrat, G.; Poissant, G.; Rebrion, C. Ion-Polar-Molecule Reactions: A CRESU Study of He⁺, C⁺, N⁺ + H₂O, NH₃ at 27, 68 and 163 K. *Chem. Phys. Lett.* **1985**, *122* (5), 431–435.
- (29) Rowe, B. R.; Canosa, A.; Le Page, V. FALP and CRESU Studies of Ionic Reactions. *Int. J. Mass Spectrom. Ion Processes* **1995**, *149–150*, 573–596.
- (30) Speck, T.; Mostefaoui, T. I.; Travers, D.; Rowe, B. R. Pulsed Injection of Ions into the CRESU Experiment. *Int. J. Mass Spectrom.* **2001**, *208* (1–3), 73–80.
- (31) Joalland, B.; Jamal-Eddine, N.; Klos, J.; Lique, F.; Trolez, Y.; Guillemin, J. C.; Carles, S.; Biennier, L. Low-Temperature Reactivity of C_{2n+1}N⁻ Anions with Polar Molecules. *J. Phys. Chem. Lett.* **2016**, *7* (15), 2957–2961.
- (32) Carty, D.; Le Page, V.; Sims, I. R.; Smith, I. W. M. Low Temperature Rate Coefficients for the Reactions of CN and C₂H Radicals with Allene (CH₂=C=CH₂) and Methyl Acetylene (CH₃CCH). *Chem. Phys. Lett.* **2001**, *344* (3–4), 310–316.
- (33) Mullen, C.; Smith, M. A. Low Temperature NH(X³Σ⁻) Radical Reactions with NO, Saturated, and Unsaturated Hydrocarbons Studied in a Pulsed Supersonic Laval Nozzle Flow Reactor between 53 and 188 K. *J. Phys. Chem. A* **2005**, *109* (7), 1391–1399.
- (34) Daugey, N.; Caubet, P.; Bergeat, A.; Costes, M.; Hickson, K. M. Reaction Kinetics to Low Temperatures. Dicarbox + Acetylene, Methylacetylene, Allene and Propene from 77 ≤ T ≤ 296 K. *Phys. Chem. Chem. Phys.* **2008**, *10*, 729–737.
- (35) Cheikh Sid Ely, S.; Morales, S. B.; Guillemin, J. C.; Klippenstein, S. J.; Sims, I. R. Low Temperature Rate Coefficients for the Reaction CN + HC₃N. *J. Phys. Chem. A* **2013**, *117* (46), 12155–12164.
- (36) Ocaña, A. J.; Blázquez, S.; Potapov, A.; Ballesteros, B.; Canosa, A.; Antiñolo, M.; Vereecken, L.; Albaladejo, J.; Jiménez, E. Gas-Phase Reactivity of CH₃OH toward OH at Interstellar Temperatures (11.7–177.5 K): Experimental and Theoretical Study. *Phys. Chem. Chem. Phys.* **2019**, *21*, 6942–6957.
- (37) James, P. L.; Sims, I. R.; Smith, I. W. M.; Alexander, M. H.; Yang, M. A Combined Experimental and Theoretical Study of Rotational Energy Transfer in Collisions between NO(X²Π_{1/2}, V = 3, J) and He, Ar and N₂ at Temperatures down to 7 K. *J. Chem. Phys.* **1998**, *109* (10), 3882–3897.
- (38) Carty, D.; Goddard, A.; Sims, I. R.; Smith, I. W. M. Rotational Energy Transfer in Collisions between CO(X¹Σ⁺, V = 2, J = 0, 1, 4, and 6) and He at Temperatures from 294 to 15 K. *J. Chem. Phys.* **2004**, *121* (10), 4671–4683.
- (39) Sánchez-González, R.; Eveland, W. D.; West, N. A.; Mai, C. L. N.; Bowersox, R. D. W.; North, S. W. Low Temperature Collisional Quenching of NO A²Σ⁺(v' = 0) by NO(X²Π) and O₂ between 34 and 109 K. *J. Chem. Phys.* **2014**, *141* (7), 074313.
- (40) Mertens, L. A.; Labiad, H.; Denis-Alpizar, O.; Fournier, M.; Carty, D.; Le Picard, S. D.; Stoecklin, T.; Sims, I. R. Rotational Energy Transfer in Collisions between CO and Ar at Temperatures from 293 to 30 K. *Chem. Phys. Lett.* **2017**, *683* (1), 521–528.
- (41) Cooke, I. R.; Sims, I. R. Experimental Studies of Gas-Phase Reactivity in Relation to Complex Organic Molecules in Star-Forming Regions. *ACS Earth Sp. Chem.* **2019**, *3* (7), 1109–1134.
- (42) Shannon, R. J.; Cossou, C.; Loison, J. C.; Caubet, P.; Balucani, N.; Seakins, P. W.; Wakelam, V.; Hickson, K. M. The Fast C(³P) + CH₃OH Reaction as an Efficient Loss Process for Gas-Phase Interstellar Methanol. *RSC Adv.* **2014**, *4* (50), 26342–26353.
- (43) Jefferts, K. B.; Penzias, A. A.; Wilson, R. W. Observation of the CN Radical in the Orion Nebula and W51. *Astrophys. J.* **1970**, *161*, L87–L89.
- (44) Henkel, C.; Schilke, P.; Mauersberger, R. Molecules in External Galaxies - The Detection of CN, C₂H, and HNC, and the Tentative Detection of HC₃N. *Astron. Astrophys.* **1988**, *201* (1), L23–L26.
- (45) Dutrey, A.; Guilloteau, S.; Gu, M. Chemistry of Protosolar-like Nebulae: The Molecular Content of the DMTau and GGTau Disks. *Astron. Astrophys.* **1997**, *317*, L55–L58.
- (46) Hily-Blant, P.; Walmsley, M.; Pineau des Forêts, G.; Flower, D. CN in Prestellar Cores. *Astron. Astrophys.* **2008**, *480* (1), L5–L8.
- (47) Wilson, E. H.; Atreya, S. K. Chemical Sources of Haze Formation in Titan's Atmosphere. *Planet. Space Sci.* **2003**, *51* (14–15), 1017–1033.
- (48) Vuitton, V.; Yelle, R. V.; McEwan, M. J. Ion Chemistry and N-Containing Molecules in Titan's Upper Atmosphere. *Icarus* **2007**, *191* (2), 722–742.
- (49) Gautier, T.; Carrasco, N.; Buch, A.; Szopa, C.; Sciamma-O'Brien, E.; Cernogora, G. Nitrile Gas Chemistry in Titan's Atmosphere. *Icarus* **2011**, *213* (2), 625–635.
- (50) Cernicharo, J.; Marcelino, N.; Roueff, E.; Gerin, M.; Jiménez-Escobar, A.; Muñoz Caro, G. M. Discovery of the Methoxy Radical, CH₃O, toward B1: Dust Grain and Gas-Phase Chemistry in Cold Dark Clouds. *Astrophys. J., Lett.* **2012**, *759*, L43.
- (51) Antiñolo, M.; Agúndez, M.; Jiménez, E.; Ballesteros, B.; Canosa, A.; Dib, G. El; Albaladejo, J.; Cernicharo, J. Reactivity of OH and CH₃OH between 22 and 64 K: Modeling the Gas Phase Production of CH₃O in Barnard 1b. *Astrophys. J.* **2016**, *823* (1), 25.
- (52) Sayah, N.; Li, X.; Caballero, J. F.; Jackson, W. M. Laser Induced Fluorescence Studies of CN Reactions with Alkanes, Alkenes and Substituted Aliphatic Species. *J. Photochem. Photobiol., A* **1988**, *45* (2), 177–194.
- (53) Janssen, E.; Hershberger, J. F. Reaction Kinetics of the CN Radical with Primary Alcohols. *Chem. Phys. Lett.* **2015**, *625*, 26–29.
- (54) Sims, I. R.; Queffelec, J. L.; Defrance, A.; Rebrion-Rowe, C.; Travers, D.; Bocherel, P.; Rowe, B. R.; Smith, I. W. M. Ultralow Temperature Kinetics of Neutral-Neutral Reactions. The Technique and Results for the Reactions CN+O₂ down to 13 K and CN+NH₃ down to 25 K. *J. Chem. Phys.* **1994**, *100* (6), 4229–4241.
- (55) O'Halloran, M. A.; Joswig, H.; Zare, R. N. Alignment of CN from 248 Nm Photolysis of ICN: A New Model of the Å Continuum Dissociation Dynamics. *J. Chem. Phys.* **1987**, *87* (1), 303–313.
- (56) Myer, J. A.; Samson, J. A. R. Vacuum-Ultraviolet Absorption Cross Sections of CO, HCl, and ICN between 1050 and 2100 Å. *J. Chem. Phys.* **1970**, *52* (1), 266–271.
- (57) Felps, W. S.; Rupnik, K.; McGlynn, S. P. Electronic Spectroscopy of the Cyanogen Halides. *J. Phys. Chem.* **1991**, *95* (2), 639–656.
- (58) Frisch, M. J.; Trucks, G. W.; Schlegel, H. B.; Scuseria, G. E.; Robb, M. A.; Cheeseman, J. R.; Scalmani, G.; Barone, V.; Mennucci, B.; Petersson, G. A. et al. *Gaussian 09*, Revision D.01; Gaussian Inc.: Pittsburgh, PA, 2013.
- (59) Purvis, G. D.; Bartlett, R. J. A Full Coupled-Cluster Singles and Doubles Model: The Inclusion of Disconnected Triples. *J. Chem. Phys.* **1982**, *76*, 1910–1918.
- (60) Pople, J. A.; Head-Gordon, M.; Raghavachari, K. Quadratic Configuration Interaction. A General Technique for Determining Electron Correlation Energies. *J. Chem. Phys.* **1987**, *87*, 5968–5975.
- (61) Kendall, R. A.; Dunning, T. H.; Harrison, R. J. Electron Affinities of the First-Row Atoms Revisited. Systematic Basis Sets and Wave Functions. *J. Chem. Phys.* **1992**, *96*, 6796–6806.
- (62) Woon, D. E.; Dunning, T. H. Gaussian Basis Sets for Use in Correlated Molecular Calculations. III. The Atoms Aluminum through Argon. *J. Chem. Phys.* **1993**, *98*, 1358–1371.
- (63) Cizek, J. Use of the Cluster Expansion and the Technique of Diagrams in Calculations of Correlation Effects in Atoms and Molecules. *Advances in Chemical Physics* **2007**, *35*–89.
- (64) Scuseria, G. E.; Janssen, C. L.; Schaefer, H. F. An Efficient Reformulation of the Closed-Shell Coupled Cluster Single and Double Excitation (CCSD) Equations. *J. Chem. Phys.* **1988**, *89*, 7382–7387.

- (65) Scuseria, G. E.; Schaefer, H. F. Is Coupled Cluster Singles and Doubles (CCSD) More Computationally Intensive than Quadratic Configuration Interaction (QCISD)? *J. Chem. Phys.* **1989**, *90*, 3700–3703.
- (66) Ochterski, J. W. *Thermochemistry in Gaussian*; Gaussian Inc.: Pittsburgh, PA, 2000.
- (67) Montgomery, J. A.; Frisch, M. J.; Ochterski, J. W.; Petersson, G. A. A Complete Basis Set Model Chemistry. VI. Use of Density Functional Geometries and Frequencies. *J. Chem. Phys.* **1999**, *110*, 2822–2827.
- (68) Montgomery, J. A.; Frisch, M. J.; Ochterski, J. W.; Petersson, G. A. A Complete Basis Set Model Chemistry. VII. Use of the Minimum Population Localization Method. *J. Chem. Phys.* **2000**, *112*, 6532–6542.
- (69) Ess, D. H.; Houk, K. N. Activation Energies of Pericyclic Reactions: Performance of DFT, MP2, and CBS-QB3 Methods for the Prediction of Activation Barriers and Reaction Energetics of 1,3-Dipolar Cycloadditions, and Revised Activation Enthalpies for a Standard Set of Hydrocarbon. *J. Phys. Chem. A* **2005**, *109* (42), 9542–9553.
- (70) Somers, K. P.; Simmie, J. M. Benchmarking Compound Methods (CBS-QB3, CBS-APNO, G3, G4, W1BD) against the Active Thermochemical Tables: Formation Enthalpies of Radicals. *J. Phys. Chem. A* **2015**, *119* (33), 8922–8933.
- (71) Guner, V.; Khuong, K. S.; Leach, A. G.; Lee, P. S.; Bartberger, M. D.; Houk, K. N. A Standard Set of Pericyclic Reactions of Hydrocarbons for the Benchmarking of Computational Methods: The Performance of Ab Initio, Density Functional, CASSCF, CASPT2, and CBS-QB3 Methods for the Prediction of Activation Barriers, Reaction Energetics, and. *J. Phys. Chem. A* **2003**, *107* (51), 11445–11459.
- (72) Ruscic, B.; Pinzon, R. E.; Morton, M. L.; Von Laszewski, G.; Bittner, S. J.; Nijssure, S. G.; Amin, K. A.; Minkoff, M.; Wagner, A. F. Introduction to Active Thermochemical Tables: Several “Key” Enthalpies of Formation Revisited. *J. Phys. Chem. A* **2004**, *108* (45), 9979–9997.
- (73) Ruscic, B.; Pinzon, R. E.; Von Laszewski, G.; Kodeboyina, D.; Burcat, A.; Leahy, D.; Montoy, D.; Wagner, A. F. Active Thermochemical Tables: Thermochemistry for the 21st Century. *J. Phys.: Conf. Ser.* **2005**, 561–570.
- (74) Ruscic, B.; Bross, D. H. *Active Thermochemical Tables (ATcT) values based on ver. 1.122e of the Thermochemical Network*; Argonne National Laboratory, 2019. Available at <https://atct.anl.gov/Thermochemical%20Data/version%201.122/index.php>.
- (75) Smith, I. W. M.; Sage, A. M.; Donahue, N. M.; Herbst, E.; Quan, D. The Temperature-Dependence of Rapid Low Temperature Reactions: Experiment, Understanding and Prediction. *Faraday Discuss.* **2006**, *133*, 137–156.
- (76) Faure, A.; Vuitton, V.; Thissen, R.; Wiesenfeld, L. A Semiempirical Capture Model for Fast Neutral Reactions at Low Temperature. *J. Phys. Chem. A* **2009**, *113* (49), 13694–13699.
- (77) Talbi, D.; Wakelam, V. K. The New Kinetic Database for Astrochemistry. *J. Phys.: Conf. Ser.* **2011**, 012029.
- (78) Wakelam, V.; Herbst, E.; Loison, J. C.; Smith, I. W. M.; Chandrasekaran, V.; Pavone, B.; Adams, N. G.; Bacchus-Montabonel, M. C.; Bergeat, A.; Béroff, K.; et al. A Kinetic Database for Astrochemistry (KIDA). *Astrophys. J., Suppl. Ser.* **2012**, *199* (1), 21.
- (79) Abeysekera, C.; Joalland, B.; Ariyasingha, N.; Zack, L. N.; Sims, I. R.; Field, R. W.; Suits, A. G. Product Branching in the Low Temperature Reaction of CN with Propyne by Chirped-Pulse Microwave Spectroscopy in a Uniform Supersonic Flow. *J. Phys. Chem. Lett.* **2015**, *6* (9), 1599–1604.



Benzonitrile as a Proxy for Benzene in the Cold ISM: Low-temperature Rate Coefficients for CN + C₆H₆

Ilsa R. Cooke¹, Divita Gupta¹, Joseph P. Messinger^{1,2}, and Ian R. Sims¹

¹Univ. Rennes, CNRS, IPR (Institut de Physique de Rennes)—UMR 6251, F-35000 Rennes, France; ian.sims@univ-rennes1.fr

²Division of Chemistry and Chemical Engineering, California Institute of Technology, Pasadena, CA 91125, USA

Received 2020 January 23; revised 2020 February 27; accepted 2020 February 27; published 2020 March 16

Abstract

The low-temperature reaction between CN and benzene (C₆H₆) is of significant interest in the astrochemical community due to the recent detection of benzonitrile, the first aromatic molecule identified in the interstellar medium (ISM) using radio astronomy. Benzonitrile is suggested to be a low-temperature proxy for benzene, one of the simplest aromatic molecules, which may be a precursor to polycyclic aromatic hydrocarbons. In order to assess the robustness of benzonitrile as a proxy for benzene, low-temperature kinetics measurements are required to confirm whether the reaction remains rapid at the low gas temperatures found in cold dense clouds. Here, we study the C₆H₆ + CN reaction in the temperature range 15–295 K, using the well-established CRESU technique (a French acronym standing for Reaction Kinetics in Uniform Supersonic Flow) combined with pulsed-laser photolysis-laser-induced fluorescence. We obtain rate coefficients, $k(T)$, in the range $(3.6\text{--}5.4) \times 10^{-10} \text{ cm}^3 \text{ s}^{-1}$ with no obvious temperature dependence between 15 and 295 K, confirming that the CN + C₆H₆ reaction remains rapid at temperatures relevant to the cold ISM.

Unified Astronomy Thesaurus concepts: Reaction rates (2081); Astrochemistry (75); Interstellar molecules (849); Interstellar medium (847); Interdisciplinary astronomy (804); Polycyclic aromatic hydrocarbons (1280); Dense interstellar clouds (371); Interstellar clouds (834)

1. Introduction

The recent discovery of benzonitrile (C₆H₅CN) in a nearby cold molecular cloud (Taurus, TMC-1) marks the first detection of an aromatic species in the interstellar medium by radio astronomy (McGuire et al. 2018). Benzonitrile has been proposed as a tracer of benzene, which may be a low-temperature precursor to more complex polycyclic aromatic hydrocarbons (PAHs). PAHs are widely accepted to exist in the interstellar medium (ISM) owing to their characteristic infrared emission features; however, due to their structural similarities, the exact chemical origins of the IR bands remain elusive (Lovas et al. 2005). It has been suggested that PAHs make up as much as 10%–25% of the interstellar carbon budget (Dwek et al. 1997; Chiar et al. 2013). Understanding the origin of PAHs can help answer fundamental questions about their role in forming interstellar dust as well as potentially prebiotic material that may be incorporated into new planetary systems.

It has been suggested that a bottleneck to the formation of these large aromatics at low temperatures is the cyclization to produce the first aromatic ring, usually benzene or the phenyl radical (Cherchneff et al. 1992; Tielens & Charnley 1997; Kaiser et al. 2015). However, benzene itself is difficult to detect as it has no permanent dipole moment and hence is invisible to radio astronomy. While benzene has been detected in the ISM through infrared observations of a single weak absorption feature (the ν_4 bending mode near 14.85 μm) in a handful of sources (Cernicharo et al. 2001; Kraemer et al. 2006; Malek et al. 2011), absorption due to Earth's atmosphere limits its observation to bright IR-sources using space-based infrared telescopes (e.g., the Spitzer Space Telescope and the *Infrared Space Observatory*). Instead, it was suggested that benzonitrile (dipole moment = 4.5 D) might be used as a chemical proxy for benzene in the cold, starless ISM, as it is expected to form via the barrierless, exothermic neutral–neutral reaction between

CN and benzene (Woods et al. 2002; Trevitt et al. 2010). If linked to benzene, benzonitrile may be used to constrain the early stages of the aromatic chemistry in the ISM.

Following a tentative detection using data from the Nobeyama 45 m telescope, McGuire et al. (2018) conducted a deep integration search for benzonitrile in TMC-1 with the 100 m Robert C. Byrd Green Bank Telescope. They observed eight rotational transitions between 18 and 23 GHz, several of which displayed resolved hyperfine splitting, confirming the detection of benzonitrile and allowing derivation of its column density, $N_T = 4 \times 10^{11} \text{ cm}^{-2}$.

McGuire et al. (2018) modified the *kida.uva.2014* reaction network (Wakelam et al. 2015) to include the CN + C₆H₆ reaction, as well as a handful of destruction pathways in order to predict the abundance of benzonitrile in TMC-1. Currently, the *KIDA* database³ does not include benzonitrile but does include 13 ion–neutral pathways for benzene destruction and only five neutral–neutral pathways (mostly H-abstraction mechanisms). McGuire et al. (2018) used a reaction rate coefficient for CN + C₆H₆ of $3 \times 10^{-10} \text{ cm}^3 \text{ s}^{-1}$, based on the assumption that the reaction will occur upon every collision. Their model predicted a benzonitrile abundance a factor of four lower than what was observed in TMC-1. The authors suggested that the difference may be explained by other formation routes for benzene and/or benzonitrile that were not considered in their model.

Rate coefficients for the reaction between CN and benzene have been previously measured using Pulsed-Laser Photolysis-Laser Induced Fluorescence (PLP-LIF) at 295, 165, and 105 K by Trevitt et al. (2010), who found $k(T)$ to be relatively constant, ranging from 3.9 to $4.9 \times 10^{-10} \text{ cm}^3 \text{ s}^{-1}$. They attribute the lack of temperature dependence to a reaction mechanism that proceeds without an energy barrier in the

³ <http://kida.astrophy.u-bordeaux.fr/>, accessed 2020 January.

entrance channel and likely forms an addition complex, which is supported by theoretical calculations of the reaction potential energy surface (Balucani et al. 1999; Woon 2006; Lee et al. 2019). In addition to the overall rate coefficients, Trevitt et al. (2010) measured the products of the reaction at room temperature using synchrotron VUV photoionization mass spectrometry. They found that the photoionization efficiency curve at $m/z = 103$ could be well fit by benzonitrile photoionization spectrum with no detectable evidence for the H-abstraction product channel, $C_6H_5 + HCN$, nor the -NC isomer phenylisocyanide.

Here, we report rate coefficients for the reaction of benzene with the CN radical over a wide temperature range of 15–295 K using the Cinétique de Reaction en Ecoulement Supersonique Uniforme (or Reaction Kinetics in Uniform Supersonic Flow; CRESU) technique. These rate coefficients can be input into astrochemical models to assess the importance of the reaction as a production route for benzonitrile and therefore the robustness of benzonitrile as a chemical proxy for benzene at various temperatures in the ISM.

2. Experiment

The kinetics of the reaction between the CN radical and benzene were measured using PLP-LIF. The low gas temperatures were achieved using the CRESU technique, which has been described in detail previously (Sims et al. 1994; James et al. 1998; Cooke & Sims 2019) and will only be described here in brief. A dilute mixture (typically < 0.1%) of benzene (Sigma Aldrich, Anhydrous 99.8%) and the CN radical precursor in a buffer gas (He (99.995%), Ar (99.998%), or N_2 (99.995%); Air Liquide) expands isentropically from a high-pressure region (reservoir), into a low-pressure region (chamber) through a convergent-divergent Laval nozzle to generate a cold supersonic flow that is uniform in temperature and density for several tens of centimeters, corresponding typically to 100–500 μs . The high molecular density of the flow (10^{16} – 10^{17} cm^{-3}) results in collisions between the molecules, ensuring thermal equilibrium is maintained. A wide range of temperatures can be obtained by careful manipulation of the physical dimensions of the nozzle, the buffer gas used, and the flow conditions/pumping capacity. Characterizing the flow temperature is essential to study chemical kinetics and is determined using Pitot probe impact pressure measurements for each nozzle prior to undertaking kinetics experiments.

A Controlled Evaporation and Mixing (CEM) system was used to introduce benzene into the flow (Bronkhorst CEM; described in detail in Gupta et al. 2019). The system consists of a Coriolis liquid flow meter (Bronkhorst mini CORI-FLOW ML120V00) that introduces a metered flow of liquid benzene into an evaporator (Bronkhorst W-202A-222-K), followed by controlled dilution with a buffer gas via a thermal mass flow controller (Bronkhorst EL-FLOW Prestige). The CN radicals were generated by photodissociation of ICN (Acros Organics, 98%) at 248 nm using a KrF excimer laser (Coherent LPXPro 210) at a laser fluence in the reaction zone of ~ 25 $mJ cm^{-2}$. Photodissociation of ICN at 248 nm produces CN radicals primarily ($\geq 93\%$) in the $v = 0$ level of the $X^2\Sigma^+$ state (O’Halloran et al. 1987), and rapid rotational relaxation is ensured by frequent collisions due to the high density of the buffer gas.

The LIF/fluorescence signal was recorded with a photomultiplier tube (PMT; Thorn E6723) by excitation in the (0, 0)

band of the $B^2\Sigma^+ - X^2\Sigma^+$ electronic transition at ~ 388 nm using a dye laser (Laser Analytical Systems, LDL 20505, operating with 0.2 $g l^{-1}$ mixture of Exciton Exalite 389 dye in 1,4-dioxane) pumped by the frequency-tripled output at 355 nm of a Nd:YAG laser (Continuum, Powerlite Precision II). A narrowband interference filter centered at 420 nm (Ealing Optics, 10 nm FWHM) was used to select the off-resonant fluorescence into the first vibrational level of the ground state via the (0, 1) band. Delays ranging from -5 to hundreds of microseconds between the excimer and the LIF dye laser pulses, both operating at 10 Hz, were employed to record the time dependence of the CN radical fluorescence during the reaction.

The experiments were performed under pseudo-first-order conditions with benzene in excess. The UV absorption cross-section of ICN at 248 nm has been measured as 4.7×10^{-19} cm^2 (Felps et al. 1991). For the density of ICN used in the gas flow ($\sim 10^{12}$ cm^{-3}), there is an estimated CN ($X^2\Sigma^+$) concentration of $< 1 \times 10^{10}$ cm^{-3} , which is lower than the concentration of benzene by at least a factor of one hundred.

The LIF signals were recorded using a gated integrator (Stanford Research Systems) at 400 evenly spaced time delays and were averaged typically 5 times. These were fit to single exponential decays using Scipy’s curve fit optimization package (Virtanen et al. 2019), yielding pseudo-first-order rate coefficients, k_{1st} . Plots of k_{1st} versus the benzene concentration were the fit with a weighted linear regression (Seabold et al. 2017, as developed on GitHub) to calculate the second-order rate coefficient. The procedure was repeated for various temperatures using eight different Laval nozzles. The experimental parameters and the measured rate coefficients with their uncertainties are summarized in Table 1.

3. Results

Figure 1(a) shows an example CN LIF decay trace and second-order kinetics plot, obtained at 72 K. The signal decays were recorded for 140–200 μs following the firing of the photolysis laser to capture the fast CN decay in the presence of benzene. LIF measurements were also taken at negative time delays (5 μs before the excimer laser fires) to establish a pre-trigger baseline. An exponential decay function was fit to the LIF data after ≥ 10 μs to allow enough time for rotational relaxation of CN and for the photomultiplier tube to recover from scatter due to the excimer laser.

The LIF decay traces were recorded for the CN decay in the presence of at least eight different concentrations of benzene. The number of points and the range of benzene concentration used for each nozzle are shown in Table 1. The upper limit for the concentration of benzene is determined by an experimental constraint imposed due to the formation of benzene dimers, which could cause the rate coefficients to be underestimated. This effect is particularly significant at low temperatures, where dimerization occurs at much lower reactant concentrations than at room temperature. Hamon et al. (2000) measured the rate coefficients for dimerization of benzene in helium. They found that the onset of significant complex formation at 25 K occurred when $[C_6H_6] \geq 1 \times 10^{14}$ cm^{-3} . We obtain the bimolecular rate coefficients by fitting benzene concentrations $< 2.5 \times 10^{13}$ cm^{-3} , except for at room temperature, where the fit concentrations are $< 1 \times 10^{14}$ cm^{-3} .

The nonzero intercept observed in the second-order plots (e.g., in Figure 1(b)) is due to other losses of CN, a

Table 1
Rate Coefficients for the Reaction of the CN Radical with Benzene Measured at Different Temperatures, with the Associated Experimental Parameters

T (K)	Buffer Gas	Total Density (10^{16} cm^{-3})	Range of $[\text{C}_6\text{H}_6]$ (10^{12} cm^{-3})	No. of Points	Rate Coefficient, $k(T)$ ($10^{-10} \text{ cm}^3 \text{ s}^{-1}$)
15	He	5.02	2.19–19.7	13	5.45 ± 0.90
			2.19–17.5	14	5.36 ± 0.86
					5.4 ± 0.6
17	He	4.85	2.03–14.2	13	4.5 ± 0.7
24	He	4.85	2.08–22.8	11	5.1 ± 0.7
36	He	5.31	1.48–14.8	11	5.37 ± 0.70
		5.27	1.47–20.6	14	5.49 ± 0.94
		5.27	1.47–14.7	11	5.18 ± 0.77
					5.3 ± 0.6
72	He	6.01	1.54–24.6	14	5.47 ± 0.63
		6.01	3.00–16.5	12	5.12 ± 0.73
					5.4 ± 0.6
83	N_2	4.61	2.06–16.5	8	3.89 ± 0.70
			2.04–24.6	12	3.85 ± 0.62
					3.9 ± 0.4
110	Ar	2.71	1.66–19.9	11	4.2 ± 0.6
200	N_2	5.27	2.52–20.2	13	3.7 ± 0.8
294	N_2	7.04	1.52–76.1	9	3.47 ± 0.40
293	N_2	9.78	1.53–76.6	9	3.45 ± 0.39
		18.5	2.21–69.6	8	3.33 ± 0.54
293	He	5.27	6.25–37.5	9	3.98 ± 0.57
		6.92	2.03–81.3	10	3.35 ± 0.46
		9.39	2.16–63.4	6	4.08 ± 0.55
295	He	9.10	1.50–74.8	9	4.02 ± 0.46
					3.6 ± 0.4

Note. Quoted uncertainties are calculated using the standard error evaluated from the second-order plot, multiplied by the appropriate Student's t factor for 95% confidence, and then combined in quadrature with an estimated systematic error of 10%. Entries in bold are the variance weighted mean values of rate coefficients measured at the same temperature, where the standard error on the mean is combined in quadrature with an estimated systematic error of 10%.

combination of CN diffusion out of the probed beam area and reaction with ICN and/or other impurities in the buffer gas. The second-order rate coefficients are derived from the slopes of the weighted linear least-squares regressions to the second-order kinetics plots and are shown in Table 1 along with their uncertainties, which are calculated using 95% confidence limits of the standard error from the two-sided Student's t distribution combined with an estimated 10% systematic error. The measured rate coefficients over the temperature range $T = 15$ –295 K are shown in Figure 2 along with the rate coefficients measured by Trevitt et al. (2010) and the rate coefficient used by McGuire et al. (2018) to model the abundance of benzonitrile in TMC-1. Within the experimental uncertainty the measured rate coefficient for the $\text{CN} + \text{C}_6\text{H}_6$ reaction remains essentially constant between 15 and 295 K. The weighted average of all of the rate coefficients between 15 and 295 K is $4.4 \pm 0.2 \times 10^{-10} \text{ cm}^3 \text{ s}^{-1}$.

Care was taken to ensure photodissociation of C_6H_6 was negligible during the kinetics experiments as reaction between the phenyl radical and CN is expected to be rapid. The absorption cross-section for benzene at 248 nm is $1.4 \times 10^{-19} \text{ cm}^2$ (Nakashima & Yoshihara 1982) yielding a maximum phenyl radical concentration of less than 10^{10} cm^{-3} at the laser fluence used of $\sim 25 \text{ mJ cm}^{-2}$. Kovács et al. (2009) have suggested the possibility of two-photon absorption via the $^1\text{B}_{2u}$ state, leading to dissociation of benzene; they found a high

total absorption cross-section for the second photon of $2.8 \times 10^{-17} \text{ cm}^2$. For the highest benzene concentration used here ($\sim 1 \times 10^{14} \text{ cm}^{-3}$) and with the laser fluence used, all photolysis of benzene occurs by two-photon dissociation. The resulting phenyl radical concentration is too low ($<1\%$) to affect the kinetics of the reaction. The concentrations of the phenyl radical are even lower in reality due to quenching of the excited $^1\text{B}_{2u}$ state by the buffer gas. To experimentally verify this, we measured the first-order rate coefficient at $T = 22.9 \text{ K}$ and $[\text{C}_6\text{H}_6] = 2 \times 10^{13} \text{ cm}^{-3}$ while varying the excimer laser fluence over the range of 19–30 mJ cm^{-2} and found that k_{1st} remained constant.

4. Discussion

4.1. Chemical Kinetics

The rate coefficients for the reaction of CN with C_6H_6 , measured here between 15 and 295 K, are consistent with those previously measured by Trevitt et al. (2010) at 295, 165, and 105 K with a pulsed CRESU apparatus and PLP-LIF. Trevitt et al. (2010) predicted the reaction would remain rapid at even lower temperatures, as confirmed by our measurements. The lack of temperature dependence observed in both studies is consistent with a barrierless entrance channel and the formation of an addition complex. It has been shown both experimentally and theoretically that addition–elimination reactions between

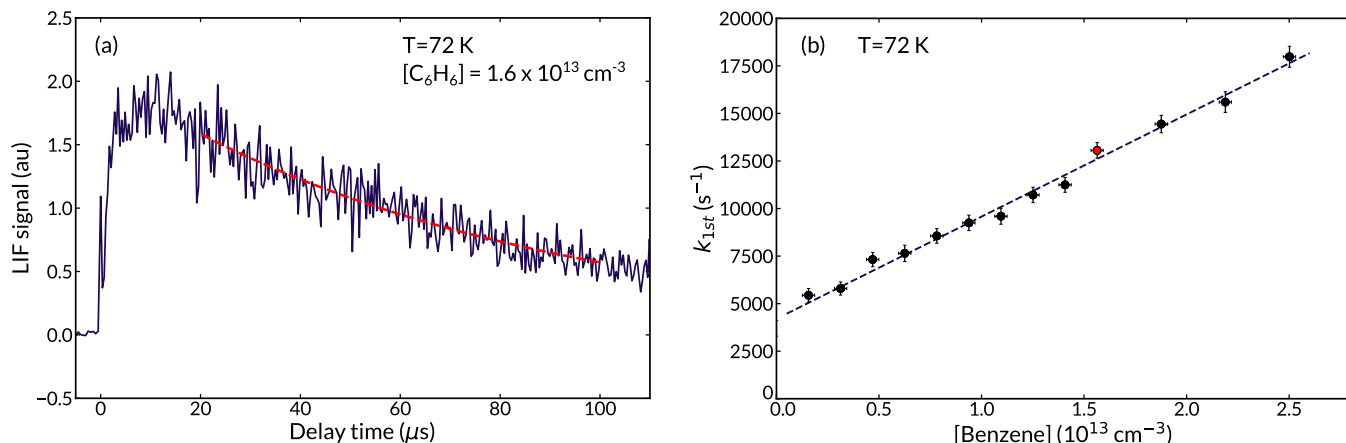


Figure 1. Typical kinetics data obtained using PLP-LIF in continuous CRESU flows, shown for a temperature of 72 K. (a) LIF signal decay of $\text{CN}(B^2\Sigma^+ \rightarrow X^2\Sigma^+)$ at a benzene density of $1.6 \times 10^{13} \text{ cm}^{-3}$ fit with an exponential decay function (red dashed line). (b) Second-order kinetics plot where the pseudo-first-order rate coefficients are plotted against the benzene concentration. The dashed line shows a linear least-squares regression to the data yielding the second-order bimolecular rate coefficient. The red point corresponds to the k_{1st} obtained from (a).

CN and unsaturated hydrocarbons typically have no barriers in their entrance channel due to the formation of intermediate radical adducts that are relatively stable (Carty et al. 2001). In general, for this class of reactions, there is usually at least one exothermic exit channel to products. Goulay & Leone (2006) found a similarly large rate coefficient for the reaction between the ethynyl radical (C_2H) and benzene with essentially no temperature dependence between 105 and 298 K.

The rate coefficients presented here and those of Trevitt et al. (2010) are similar to those of Woon (2006), who used trajectory calculations to predict the rate coefficients between 50 and 300 K. The calculated rate coefficients ranged from 3.15 and $3.5 \times 10^{-10} \text{ cm}^3 \text{ s}^{-1}$ when back reactions to reform $\text{CN} + \text{C}_6\text{H}_6$ are excluded. Woon (2006) also investigated the pressure dependence of the reaction by including back-dissociation of the $\text{C}_6\text{H}_6\text{-CN}$ intermediate complex using a multiwell treatment and found a slight temperature dependence at 10^{-3} mbar, which converges with the high-pressure limit rate coefficient by 50 K. We measured the room temperature rate coefficient at three different pressures for both nitrogen and helium buffer gases and did not observe a pressure dependence. It is important to note, however, that the laboratory experiments were likely conducted within the high-pressure limit.

4.2. Reaction Products

Previous theoretical and experimental studies have shown that benzonitrile is the major species produced in the reaction between CN and benzene, with negligible or no production of the -NC isomer phenylisocyanide nor the H-abstraction product, the phenyl radical. Woon (2006) calculated the reaction potential energy surface and relative product yields and found that while the $\text{C}_6\text{H}_5\text{CN} + \text{H}$ products form exothermically and barrierlessly, there is a 25 kJ mol^{-1} barrier to form the isocyano product pair $\text{C}_6\text{H}_5\text{NC} + \text{H}$ after initial barrierless formation of the $\text{C}_6\text{H}_5\text{NC}$ adduct, which was found to be extremely rare in multiwell calculations.

Crossed-beam experiments conducted under single-collision conditions at much higher energies have demonstrated that the benzonitrile is the main reaction product (Balucani et al. 1999, 2000a, 2000b). Balucani et al. (1999) conducted crossed-beam experiments at collision energies between 19.5 and

34.4 kJ mol^{-1} as well as electronic structure and RRKM calculations. Neither the $\text{C}_6\text{H}_6\text{CN}$ adduct nor the phenylisocyanide isomer $\text{C}_6\text{H}_5\text{NC}$ were found to contribute to the crossed-beam scattering signal. It was concluded that the dominant reaction entrance channel is barrierless leading to the formation of a CN-addition complex that subsequently dissociates to form benzonitrile + H, with the $\text{C}_6\text{H}_5\text{NC}$ product channel contributing less than 2%.

Lee et al. (2019) studied the reaction of benzene + CN indirectly using microwave discharge experiments and cavity Fourier-transform microwave spectroscopy, in combination with electronic structure calculations. They found that the reaction produces benzonitrile in high yield, with <0.1% relative abundance of phenylisocyanide. Isotopic measurements confirmed that the CN bond remains intact during the product formation. In contrast to previous computations, they found formation of the *iso*-adduct requires surmounting a barrier of $\sim 17 \text{ kJ mol}^{-1}$ as well as a second barrier for H atom loss; implying that phenylisocyanide formation should be highly disfavored under low-temperature conditions. While these very sensitive experiments provide important insights into possible reaction pathways, it is important to note that they were not conducted under conditions of kinetic isolation, nor at thermal equilibrium. Under these conditions it is difficult to probe any specific reaction mechanism as multiple reaction paths may contribute and it is unclear how well the product-branching ratios obtained reflect those that would be obtained for the elementary reaction $\text{CN} + \text{C}_6\text{H}_6$ at a well-defined temperature. Low-temperature kinetics experiments are still needed to identify and confirm the product channel-specific rate coefficients that are critical parameters for models of astrochemical environments and planetary atmospheres.

Chirped-pulse Fourier-transform microwave spectroscopy has recently been combined with CRESU flows to measure the channel-specific rate coefficients at low temperature (Abeysekera et al. 2015). This technique (named Chirped-Pulse in Uniform flows, or CPUF) can be used to establish product-branching ratios at low temperatures, which are critical for astrochemical models but are challenging to obtain experimentally. K_a -band ($\sim 28\text{--}40 \text{ GHz}$) and E -band ($\sim 60\text{--}90 \text{ GHz}$) spectrometers have been coupled to the continuous CRESU flows in Rennes that will allow the formation of benzonitrile in

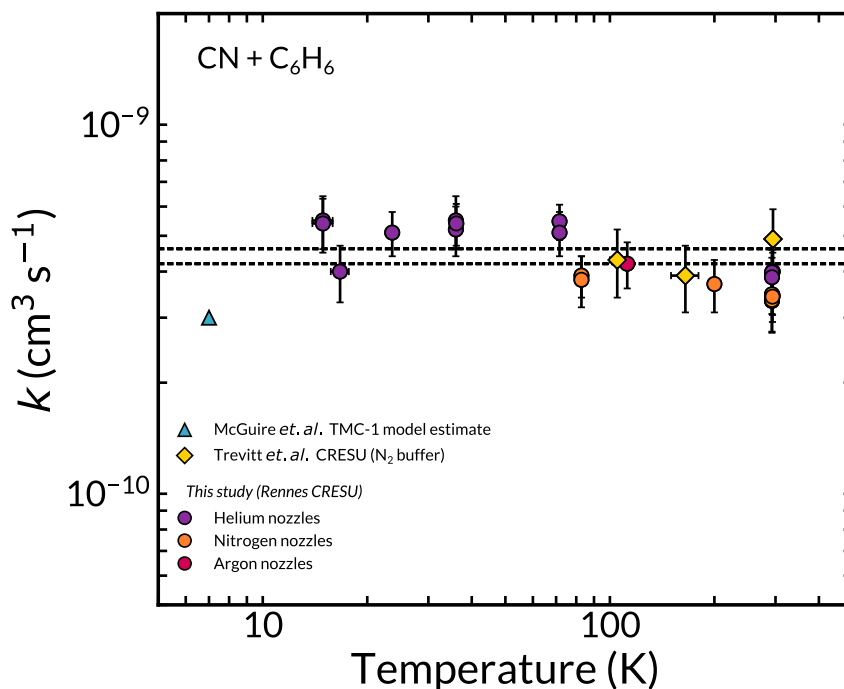


Figure 2. Rate coefficients for the reaction of the CN radical with benzene as a function of temperature displayed on a log–log scale. The circles are the data taken here using the continuous CRESU in Rennes, with helium buffer gas in purple, nitrogen in orange, and argon in pink. The yellow diamonds are the data taken by Trevitt et al. (2010) using a pulsed CRESU. The teal triangle shows the estimated rate coefficient used by McGuire et al. (2018) to model the abundance of benzonitrile in TMC-1 at 7 K. The dashed lines show the upper and lower limits set by the standard error ($\pm 1\sigma$) on the variance weighted mean of the readings at all temperatures.

the $\text{CN} + \text{C}_6\text{H}_6$ reaction to be measured down to low temperatures. Figure 3 shows how the CRESU flow acts as an efficient rotational refrigerator, shifting the Boltzmann distribution of the rotational lines into the range of the chirped-pulse spectrometers in Rennes. While benzonitrile is expected to be the sole product of $\text{CN} + \text{C}_6\text{H}_6$, the CUPF technique can be used to measure the product-branching ratios for other multichannel reactions involving CN and aromatics.

4.3. Astrophysical Implications

The rate coefficients measured here for the CN reaction with benzene are consistent with (albeit somewhat higher than) the value used in the astrochemical model of McGuire et al. (2018) to predict the abundance of benzonitrile in TMC-1, $k(T) = 3 \times 10^{-10} \text{ cm}^3 \text{ s}^{-1}$ (C. N. Shingledecker 2019, private communication). It is therefore unlikely that this reaction is the cause of the discrepancy between the abundance of benzonitrile in their model versus that observed in TMC-1. The large rate coefficients observed over the full temperature range suggest that the reaction should be rapid in astronomical sources that have sufficient density of benzene and CN. Instead, the discrepancy between the observed and modeled abundances is likely due to the underproduction of benzene, due to missing production routes and/or underestimation of the rates for those already in the reaction network.

A photochemical model has been recently developed by Loison et al. (2019) to investigate the production of aromatics in the atmosphere of Titan. While the model predicted significant formation of toluene and ethylbenzene, benzonitrile was not predicted to be abundant due to efficient consumption of CN by methane.

It is likely that other radicals can add to benzene with similarly rapid rate coefficients, indicating that other benzene

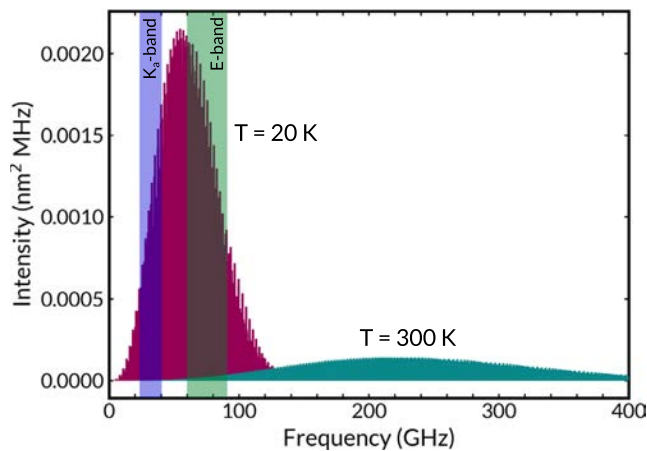


Figure 3. Simulated benzonitrile spectra at 20 K (magenta) and room temperature (teal). The vertical blocks show the bandwidth of the two CUPF spectrometers in Rennes, one covering the K_a band from 26.5 to 40 GHz and the other the E band from 60 to 90 GHz. The spectra were simulated using data from the Cologne Database for Molecular Spectroscopy and Pickett’s spfit/spcat program (Pickett 1991).

derivatives may be present in the cold ISM. The reaction of CH with benzene was measured by Hamon et al. (2000) at 25 K and found to be similarly rapid with a rate coefficient of $2.7 \times 10^{-10} \text{ cm}^3 \text{ s}^{-1}$. Rate coefficients for the reaction of OH with benzene down to 58 K were presented in a review by Hansmann & Abel (2007) and were found to be an order of magnitude lower; however, a complete kinetics study has yet to be published. The reaction of CN with other aromatics may also be rapid and produce products with high dipole moments that could lend themselves to astronomical detection. An alternative route to benzonitrile formation could involve the

radiative association reaction between the phenyl (C_6H_5) and CN radicals, which may be rapid under ISM conditions but has not yet been investigated. The reactions of CH and OH with anthracene have both been measured in CRESU flows (Goulay et al. 2005, 2006), though reactions of CN with aromatics larger than benzene have not yet been studied.

The formation of benzene under interstellar conditions is not as well understood and is a major source of uncertainty in astrochemical models of aromatic chemistry. Jones et al. (2011) investigated benzene formation via the reaction of C_2H with 1,3-butadiene. Benzene was observed at significant fractions ($30\% \pm 10\%$) with the dominant reaction product the thermodynamically less stable isomer, hexa-1,3-dien-5-yne. However, Lockyear et al. (2015) also studied the products of this reaction using synchrotron photoionization mass spectrometry. The photoionization spectra indicated that fulvene is the major reaction product, with a branching fraction of $\sim 60\%$. They did not detect benzene as a product and placed an upper limit on the production of benzene and hexa-1,3-dien-5-yne isomers of 45%. Lee et al. (2019) likewise observed evidence for fulvene formation in a microwave discharge containing HC_3N (a C_2H precursor) and 1,3-butadiene. The discrepancy may be due the high collisional energy of the crossed-beam experiment, emphasizing the importance of studying reactions under both single-collision and thermal conditions. The main formation route for benzene in the kida.uva.2014 network is the dissociative recombination of $C_6H_7^+$ with an electron. McGuire et al. (2018) also added the reaction between $C_2H+1,3$ -butadiene to the kida.uva.2014 network with a rate coefficient of $3 \times 10^{-10} \text{ cm}^3 \text{ s}^{-1}$. It is therefore possible that the benzene abundance in their model is overestimated since they do not account for the low (or zero) fraction of benzene likely produced by this reaction at low temperatures. In addition, 1,3-butadiene has not been detected in the ISM and thus it is unknown whether the reaction could produce significant quantities of benzene in TMC-1.

5. Conclusions

The CRESU technique, combined with PLP-LIF, has been used to measure the kinetics of the reaction between CN and benzene over the temperature range 15–295 K. We find that the rate coefficients for this reaction do not display an obvious temperature dependence over this temperature range, confirming that the $CN + C_6H_6$ reaction will remain rapid at temperatures relevant to the cold ISM. These results suggest that benzonitrile is indeed a robust chemical proxy that can be used to infer the abundance of benzene from observations made using radio astronomy. They also indicate that the discrepancy between the observed and modeled abundances of benzonitrile in TMC-1 is likely due to missing or inaccurate kinetic data for benzene production routes.

The authors thank Jonathan Courbe, Jonathan Thiévin, Didier Biet, Ewen Gallou, and Alexandre Dapp for technical support. The authors thank Brett McGuire, Christopher Shingledecker, and Mitchio Okumura for helpful discussions. J.P.M. was supported by the National Science Foundation Graduate Research Fellowship (NSF GRFP) and the National Science Foundation Graduate Research Opportunities Worldwide (NSF GROW) programs. J.P.M. would also like to thank the Office for Science and Technology of the Embassy of France in the United States for a Chateaubriand Fellowship.

The authors acknowledge funding from the European Research Council (ERC) under the European Union’s Horizon 2020 research and innovation programme under grant agreement 695724-CRESUCHIRP and under the Marie Skłodowska-Curie grant agreement 845165-MIRAGE. The authors are also grateful for support from the European Regional Development Fund, the Region of Brittany and Rennes Metropole. This work was supported by the French National Programme “Physique et Chimie du Milieu Interstellaire” (PCMI) of CNRS/INSU with INC/INP co-funded by CEA and CNES.

Software: SciPy (Virtanen et al. 2019), NumPy (van der Walt et al. 2011), Matplotlib (Hunter 2007), StatsModels (<http://www.statsmodels.org>).

ORCID iDs

Ilsa R. Cooke  <https://orcid.org/0000-0002-0850-7426>

Divita Gupta  <https://orcid.org/0000-0002-6639-4909>

Joseph P. Messinger  <https://orcid.org/0000-0001-7305-3945>

Ian R. Sims  <https://orcid.org/0000-0001-7870-1585>

References

- Abeysekera, C., Joalland, B., Ariyasingha, N., et al. 2015, *J. Phys. Chem. Lett.*, **6**, 1599
- Balucani, N., Asvany, O., Chang, A. H. H., et al. 1999, *JChPh*, **111**, 7457
- Balucani, N., Asvany, O., Huang, L. C. L., et al. 2000a, *ApJ*, **545**, 892
- Balucani, N., Asvany, O., Osamura, Y., et al. 2000b, *P&SS*, **48**, 447
- Carty, D., Le Page, V., Sims, I. R., & Smith, I. W. M. 2001, *CPL*, **344**, 310
- Cernicharo, J., Heras, A. M., Tielens, A. G. G. M., et al. 2001, *ApJL*, **546**, L123
- Cherchneff, I., Barker, J. R., & Tielens, A. G. G. M. 1992, *ApJ*, **401**, 269
- Chiar, J. E., Tielens, A. G. G. M., Adamson, A. J., & Ricca, A. 2013, *ApJ*, **770**, 78
- Cooke, I. R., & Sims, I. R. 2019, *ESC*, **3**, 1109
- Dwek, E., Arendt, R. G., Fixsen, D. J., et al. 1997, *ApJ*, **475**, 565
- Felps, W. S., Rupnik, K., & McGlynn, S. P. 1991, *JPhCh*, **95**, 639
- Goulay, F., & Leone, S. R. 2006, *JPCA*, **110**, 1875
- Goulay, F., Rebrion-Rowe, C., Biennier, L., et al. 2006, *JPCA*, **110**, 3132
- Goulay, F., Rebrion-Rowe, C., Le Garrec, J. L., et al. 2005, *JChPh*, **122**, 104308
- Gupta, D., Cheikh Sid Ely, S., Cooke, I. R., et al. 2019, *JPCA*, **123**, 9995
- Hamon, S., Le Picard, S. D., Canosa, A., Rowe, B. R., & Smith, I. W. M. 2000, *JChPh*, **112**, 4506
- Hansmann, B., & Abel, B. 2007, *Chem. Phys. Chem*, **8**, 343
- Hunter, J. D. 2007, *CSE*, **9**, 90
- James, P. L., Sims, I. R., Smith, I. W. M., Alexander, M. H., & Yang, M. 1998, *JChPh*, **109**, 3882
- Jones, B. M., Zhang, F., Kaiser, R. I., et al. 2011, *PNAS*, **108**, 452
- Kaiser, R. I., Parker, D. S. N., & Mebel, A. M. 2015, *ARPC*, **66**, 43
- Kovács, T., Blitz, M. A., Seakins, P. W., & Pilling, M. J. 2009, *JChPh*, **131**, 204304
- Kraemer, K. E., Sloan, G. C., Bernard-Salas, J., et al. 2006, *ApJL*, **652**, L25
- Lee, K. L. K., McGuire, B. A., & McCarthy, M. C. 2019, *PCPP*, **21**, 2946
- Lockyear, J. F., Fournier, M., Sims, I. R., et al. 2015, *IJMSp*, **378**, 232
- Loison, J. C., Dobrijevic, M., & Hickson, K. M. 2019, *Icar*, **329**, 55
- Lovas, F. J., McMahon, R. J., Grabow, J.-U., et al. 2005, *JACS*, **127**, 4345
- Malek, S. E., Cami, J., & Bernard-Salas, J. 2011, *ApJ*, **744**, 16
- McGuire, B. A., Burkhardt, A. M., Kalenskii, S., et al. 2018, *Sci*, **359**, 202
- Nakashima, N., & Yoshihara, K. 1982, *JChPh*, **77**, 6040
- O’Halloran, M. A., Joswig, H., & Zare, R. N. 1987, *JChPh*, **87**, 303
- Pickett, H. M. 1991, *JMoSp*, **148**, 371
- Seabold, S., Perktold, J., Fulton, C., et al. 2017, statsmodels/statsmodels, Version 0.8.0, Zenodo, doi:10.5281/zenodo.275519
- Sims, I. R., Queffelec, J., Defrance, A., et al. 1994, *JChPh*, **100**, 4229
- Tielens, A. G. G. M., & Charnley, S. B. 1997, in *Planetary and Interstellar Processes Relevant to the Origins of Life*, ed. D. C. B. Whittet (Berlin: Springer), **23**
- Trevitt, A. J., Goulay, F., Taatjes, C. A., Osborn, D. L., & Leone, S. R. 2010, *JPCA*, **114**, 1749
- van der Walt, S., Colbert, S. C., & Varoquaux, G. 2011, *CSE*, **13**, 22

Virtanen, P., Gommers, R., Oliphant, T. E., et al. 2019, CoRR, arXiv:1907.10121

Wakelam, V., Loison, J.-C., Herbst, E., et al. 2015, *ApJS*, 217, 20

Woods, P. M., Millar, T. J., Zijlstra, A. A., & Herbst, E. 2002, *ApJL*, 574, L167

Woon, D. E. 2006, *CP*, 331, 67

Rate Constants of the CN + Toluene Reaction from 15 to 294 K and Interstellar Implications

Joseph P. Messinger, Divita Gupta, Ilsa R. Cooke, Mitchio Okumura,* and Ian R. Sims*

Cite This: *J. Phys. Chem. A* 2020, 124, 7950–7958

Read Online

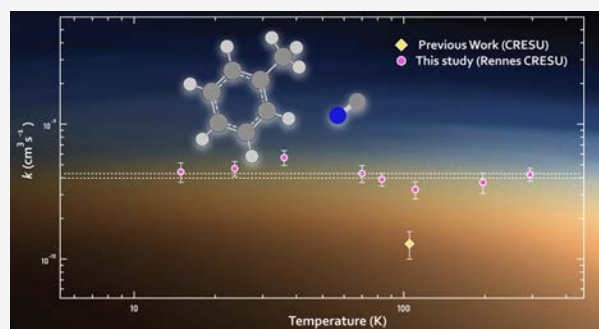
ACCESS |

Metrics & More

Article Recommendations

Supporting Information

ABSTRACT: CN is known for its fast reactions with hydrocarbons at low temperatures, but relatively few studies have focused on the reactions between CN and aromatic molecules. The recent detection of benzonitrile in the interstellar medium, believed to be produced by the reaction of CN and benzene, has ignited interest in studying these reactions. Here, we report rate constants of the CN + toluene (C_7H_8) reaction between 15 and 294 K using a CRESU (*Cinétique de Réaction en Ecoulement Supersonique Uniforme*; reaction kinetics in uniform supersonic flow) apparatus coupled with the pulsed laser photolysis–laser-induced fluorescence (PLP–LIF) technique. We also present the stationary points on the potential energy surface of this reaction to study the available reaction pathways. We find the rate constant does not change over this temperature range, with an average value of $(4.1 \pm 0.2) \times 10^{-10} \text{ cm}^3 \text{ s}^{-1}$, which is notably faster than the only previous measurement at 105 K. While the reason for this disagreement is unknown, we discuss the possibility that it is related to enhanced multiphoton effects in the previous work.



INTRODUCTION

The CN radical has long been known to be abundant in the interstellar medium (ISM), where it was first detected in the 1940s,^{1,2} and in the atmosphere of Titan, where it leads to the formation of nitrile compounds, including C_2H_3CN and HC_3N .^{3–5} At the low temperatures found in these environments, reactions between CN and other compounds are known to have fast rate constants, on the order of $10^{-10} \text{ cm}^3 \text{ s}^{-1}$, and thus must be included in gas-phase models. Reactions between CN and hydrocarbons are among the fastest of these rates and proceed through either an abstraction or an addition mechanism.⁶ A number of cyano-containing molecules linked to these reactions have been found in ISM, including molecules as large as HC_9N and $(CH_3)_2CHCN$.^{7,8} On Titan, the photolysis of these nitrile compounds formed from CN reactions may contribute to the formation of particulate matter.⁹

On Titan, toluene has been detected in the upper atmosphere by the Cassini Ion and Neutral Mass Spectrometer,¹⁰ and while it is currently undetected in the lower atmosphere, models suggest it has a high abundance there as a product of the fast association reaction between C_6H_5 and CH_3 .¹¹ In addition to benzene and toluene, a large number of specific polycyclic aromatic hydrocarbons (PAHs) have also been identified.¹² These PAHs are believed to form from smaller aromatic compounds and to be an important component of the thick haze in Titan's atmosphere.¹³

On the other hand, very few specific aromatic molecules have been directly detected in the ISM, in part due to their low dipole moments making them difficult to observe by radio astronomy. Benzene has been observed through infrared observations,¹⁴ and PAHs are widely believed to be abundant in the ISM owing to observations of the strong infrared bands characteristic of these molecules, but the broad, overlapping nature of these bands has precluded the identification of specific PAHs.¹⁵ Despite this lack of definitive identifications, PAHs are believed to hold a large fraction of carbon in the ISM,^{16,17} and so their formation has been the subject of extensive study.^{18–20} The formation of the first aromatic ring is believed to be the rate limiting step in PAH formation,²¹ and so understanding the chemistry of these monocyclic aromatic compounds is necessary.

The recent detection of benzonitrile in the ISM²² has suggested a new route for understanding aromatic formation. Benzonitrile is believed to be the product from the CN + benzene reaction, which we have recently shown to be fast at low temperatures,²³ with a rate constant of $(4.4 \pm 0.2) \times 10^{-10}$

Received: July 28, 2020

Revised: August 31, 2020

Published: September 2, 2020



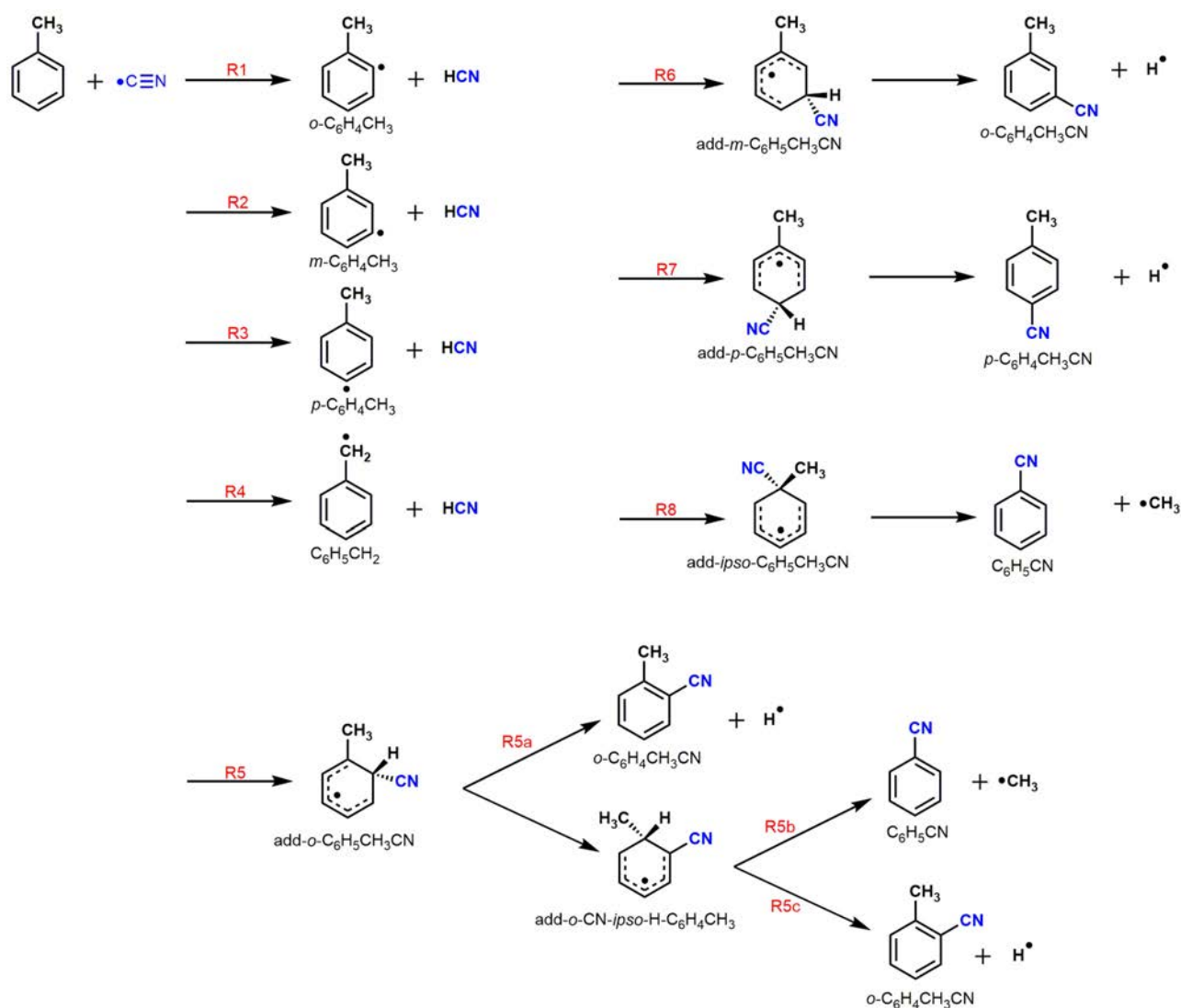


Figure 1. Reaction pathways of the CN + toluene reaction and possible products of the abstraction (R1–R4) and CN addition (R5–R8) channels that are considered in the theoretical calculations.

$\text{cm}^3 \text{s}^{-1}$ over the 15–294 K range, in good agreement with earlier work by Trevitt et al. down to 105 K.²⁴ Observations of benzonitrile therefore can be used as a proxy for the abundance of benzene. Other aromatic nitriles may also serve as proxies for undetected aromatic compounds in the ISM, as the addition of the cyano moiety gives these compounds large dipole moments and makes them visible to radio astronomy. The identification of additional specific aromatic compounds would significantly constrain models of PAH formation in the ISM.

However, little is known about the reaction of CN with other aromatic molecules and whether these reactions also result in the formation of nitrile compounds. Only one rate constant for the reaction between CN and toluene, one of the simplest aromatics, has been measured, by Trevitt et al.²⁴ They studied this reaction at 105 K and found a rate constant of $(1.3 \pm 0.3) \times 10^{-10} \text{ cm}^3 \text{ s}^{-1}$ using pulsed laser photolysis–laser-induced fluorescence (PLP–LIF) measurements in conjunction with a pulsed Laval nozzle. This rate constant is a factor of 3 lower than the rate constants measured for the CN +

benzene reaction measured in the same study as well as our own,^{23,24} suggesting that the structure of aromatic molecules can play a large role in the reaction rates. Furthermore, they observed nonexponential decays of CN at room temperature in the presence of toluene and were therefore unable to measure a rate constant, in contrast with their measurements of benzene under the same conditions. They suggested that this could be due to dissociation of the products back to the CN + toluene reactants, and that further studies would be necessary to better understand these results.

The difference between the rate constants of the CN + benzene and CN + toluene reactions would seem to suggest that the structure of an aromatic compound can play a large role in the reaction dynamics. This makes it questionable whether nitrile compounds may be formed from the reactions of CN with larger, more complex aromatic compounds, and it is essential to verify the reliability of using cyano-substituted compounds as a proxy for larger aromatic species. To that end, we have conducted measurements of the CN + toluene rate constant between 15 and 294 K to gain further insight into this

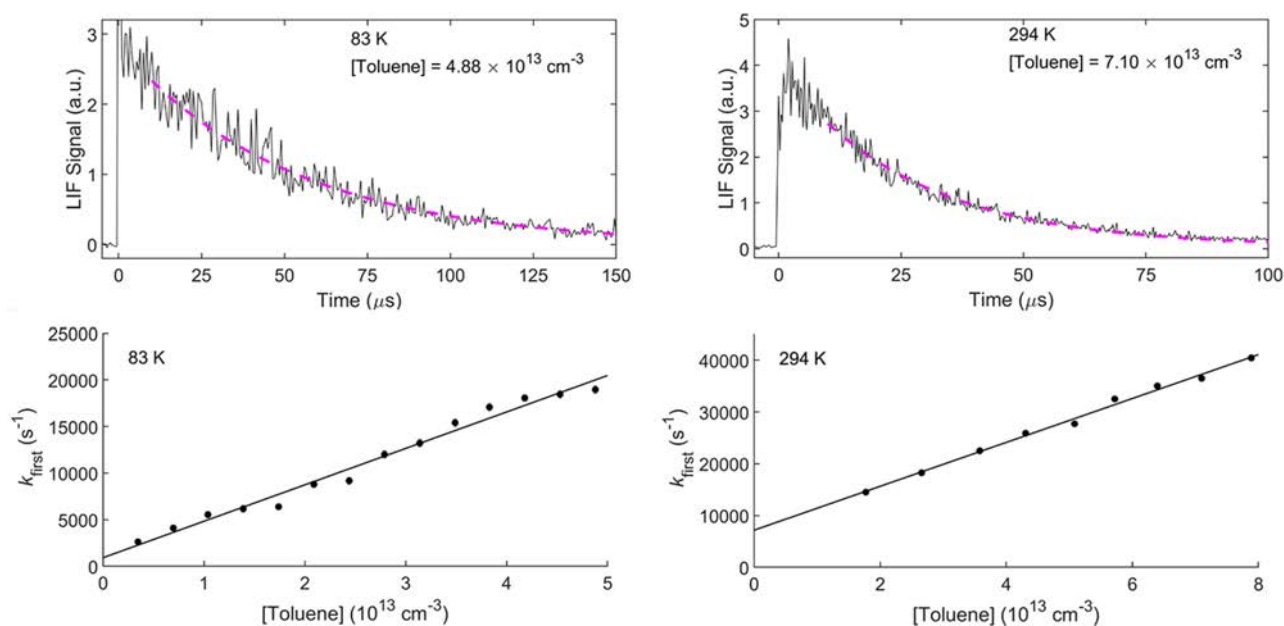


Figure 2. Typical experimental kinetics of the CN radical measured using PLP-LIF, showing decays of the CN signal and resulting second-order plots at 83 K (left) and 294 K (right).

reaction, especially at the low temperatures relevant to the ISM and Titan. Furthermore, we have computed stationary points on the potential energy surface (PES) of the CN + toluene reaction to better understand the possible products and mechanism of this reaction.

EXPERIMENTAL SECTION

Rate constants were determined using the PLP-LIF technique. Temperatures down to 15 K were achieved using the CRESU technique (*Cinétique de Réaction en Écoulement Supersonique Uniforme*; reaction kinetics in uniform supersonic flow), which has been described in detail previously.^{6,25,26} Briefly, toluene (Sigma-Aldrich, 99.9%) was introduced into the gas flow with a Controlled Evaporation and Mixing system (Bronkhorst CEM), as described in Gupta et al.²⁷ The toluene and ICN (Acros Organics, 98%), used as the CN precursor, were mixed in a buffer gas of He (99.995%, Air Liquide), Ar (99.998%, Air Liquide), or N₂ (99.995%, Air Liquide), depending on the desired CRESU conditions. Concentrations of toluene and ICN were kept $\lesssim 0.1\%$ of the total density in order not to affect the uniformity of the gas flow. The mixture was flowed isentropically from a high pressure reservoir through specifically designed convergent-divergent Laval nozzles, into a low pressure chamber to generate a uniform supersonic flow at the appropriate temperature with a density of 10^{16} – 10^{17} cm⁻³. Each nozzle was characterized with Pitot probe impact pressure measurements prior to experiments to determine the temperature, density, and uniformity of the gas flow. For measurements at 294 K, where a supersonic expansion is not required, the pumping speed was decreased such that the pressures in the reservoir and the chamber were equal, while maintaining complete gas turnover for each laser shot.

CN radicals were generated by the 248 nm photolysis of ICN using a KrF excimer laser (Coherent LPXPro 210) operating at 10 Hz, with a laser fluence of 25 mJ cm⁻². The third harmonic of a Nd:YAG laser (Continuum, Powerlite

Precision II), also operating at 10 Hz, was used to pump a dye laser (Laser Analytical Systems, LDL 20505) containing Exalite 389 (Exciton) in 1,4-dioxane (Sigma-Aldrich, 99.8%) to produce ~ 389 nm light to excite the CN B² Σ^+ –X² Σ^+ (0,0) transition. Fluorescence was detected from the CN (0,1) transition at ~ 420 nm by a photomultiplier tube (Thorn EMI 6723) preceded by a 420 nm bandpass filter (Ealing Optics). The delay time between the excimer and the Nd:YAG pump laser was varied from -5 to 200 μ s to record the time dependence of the CN signal. The LIF signal was recorded by a gated integrator for 400 evenly spaced points and averaged 5 times. The resulting kinetic trace was fit to an exponential decay starting ≥ 10 μ s after photolysis to allow for rotational thermalization of CN.

Kinetic measurements were taken under pseudo-first-order conditions with [toluene] \gg [CN]. Typical toluene concentrations were on the order of 10^{12} – 10^{13} cm⁻³, while we estimate the CN concentration to be roughly 10^{10} cm⁻³ on the basis of the ICN concentration ($\sim 10^{12}$ cm⁻³) and the 248 nm absorption cross section of 4.7×10^{-19} cm².²⁸ More than 90% of the CN radicals from the photolysis of ICN at 248 nm are in the ground vibrational state,²⁹ and we do not observe any influence of the relaxation of excited vibrational states on our kinetic measurements.

COMPUTATIONAL DETAILS

Investigation of possible channels for the reaction between CN and toluene, with identification of all the stationary points (minima, complexes, and transition states), was done using Gaussian 09 software;³⁰ all included channels can be seen in Figure 1. All the species, including the reaction complexes and transition states, were optimized at the (U)M06-2X/aug-cc-pVTZ level,^{31–33} and zero-point corrected energies were calculated for each. In addition, intrinsic reaction coordinate (IRC) calculations were performed at (U)M06-2X/6-311G to determine the minimum energy path that the transition states followed to confirm the connection between the appropriate

reactants and products. Gibbs energies ($\Delta_r G^\circ$ (298 K)) for all included channels were also calculated at the (U)M06-2X/aug-cc-pVTZ method. Both addition–elimination channels, leading to nitrile formation, and abstraction channels, leading to HCN formation, were considered. While reactions involving the CN radical may produce both cyano and isocyano compounds, only the former pathways are considered in these calculations. Previous work on the CN + benzene reaction³⁴ showed a significant barrier (28 kJ mol⁻¹) to isocyano products, which suggests that this pathway will not be relevant in the ISM.

RESULTS

Typical LIF decays of CN at 83 and 294 K and the second-order plots can be seen in Figure 2, respectively. The nonzero intercepts seen on the second-order plots arise from the loss of CN via side chemistry and diffusion out of the region probed by LIF. From experiments at room temperature, using N₂ as a buffer gas and varying the total density of the gas flow, we found that the rate constants had no pressure dependence, implying that the reaction is either a bimolecular reaction or a termolecular reaction in the high pressure limit in our experimental conditions. Unlike the room temperature measurements of Trevitt et al., we see no evidence for nonexponential decays at any toluene concentration or total gas density used in these experiments, and the measured rate constants are in good agreement with our values at all other temperatures. Additional experiments at room temperature demonstrate that changing the buffer gas from N₂ to He does not affect our measured rate constants.

Results of the experiments between 15 and 294 K are shown in Table 1 and Figure 3. At least nine points with varying toluene concentrations were taken for each measurement under pseudo-first-order conditions, with toluene in excess. At high reactant concentrations, the formation of toluene dimers causes nonlinear behavior in the second-order plots at the lowest temperatures. This therefore imposes an upper limit on the toluene concentration used in experiments in order to minimize any effect of the reaction between CN and toluene dimers on our measurements.

To test whether the photolysis of toluene at 248 nm affected our measurements, we also conducted experiments varying the power of the excimer laser at 110 K, with [toluene] = 9×10^{12} cm⁻³. We found no significant change in the measured pseudo-first-order rate constants k_{first} as a function of our laser power. With the excimer laser fluence of 25 mJ cm⁻² and the toluene absorption cross section at 248 nm of 2.9×10^{-19} cm²,³⁵ we expect roughly 1% of the toluene to photolyze if the photolysis quantum yield is 1, which should not measurably affect the observed rate constants. It has also been suggested that two-photon absorption at 248 nm can photolyze toluene to form H atoms among other potential processes,³⁶ with the total absorption cross section for the second photon experimentally determined to be 1.7×10^{-17} cm². For the highest toluene concentrations used ($\sim 1 \times 10^{14}$ cm⁻³), we estimate at most 4.8×10^{11} cm⁻³ of toluene undergoes two-photon absorption, though it is likely much less than that, as discussed in greater detail in the following section, and is unlikely to affect the rate constants measured.

As shown in Figure 4, both stationary points (reactants, products, intermediates, transition states) for both the abstraction (eqs R1–R4) and addition–elimination (eq R5–R8) channels were characterized for the reaction between

Table 1. Rate Coefficients Determined for the CN + Toluene Reaction between 15 and 294 K with Experimental Parameters for Each Measurement^a

temp (K)	buffer gas	total density (10 ¹⁶ cm ⁻³)	[toluene] (10 ¹² cm ⁻³)	no. of points	rate constant (10 ⁻¹⁰ cm ³ s ⁻¹)
15	He	5.04	1.87–10.4	10	4.4 ± 0.8
24	He	4.83	1.76–19.5	11	4.7 ± 0.6
36	He	5.27	1.25–17.7	14	5.9 ± 0.8
36	He	5.32	1.28–12.7	9	4.9 ± 1.0
					5.7 ± 0.7
70	He	6.00	2.54–15.2	11	4.4 ± 0.7
70	He	6.09	1.34–18.7	13	4.2 ± 0.7
					4.3 ± 0.6
83	N ₂	4.63	3.48–48.8	14	3.9 ± 0.5
83	N ₂	4.63	1.72–31.3	14	3.8 ± 0.4
					3.9 ± 0.4
110	Ar	2.71	1.28–14.1	11	3.3 ± 0.5
197	N ₂	5.32	2.13–21.4	11	3.7 ± 0.6
294	N ₂	10.5	15.4–92.9	11	3.7 ± 0.6
294	N ₂	3.75	9.50–47.6	9	4.3 ± 0.6
294	N ₂	8.20	17.7–78.9	9	4.3 ± 0.5
294	He	9.41	18.0–54.0	11	4.5 ± 0.5
					4.3 ± 0.5

^aUncertainties in the rate constant are the 95% confidence interval from the appropriate Student's *t* test combined in quadrature with a 10% systematic error. Bolded values represent the weighted average and uncertainty for temperatures with multiple measurements.

CN and toluene. An additional substitution channel, leading to the formation of benzyl cyanide, was found to be exothermic at (U)M06-2X/aug-cc-pVTZ, but it has a large barrier (~ 20 kcal mol⁻¹) and, hence, will not be relevant under interstellar conditions; thus, it is excluded. The relative reaction energy $\Delta_r U^\circ$ and Gibbs energy at 298 K $\Delta_r G^\circ$ for all calculated product channels can be seen in Table 2. Intermediates formed from the addition of CN to the aromatic ring were found to form barrierlessly, followed subsequently by passage over submerged barriers leading to the formation of stable nitrile products. This mechanism closely resembles the mechanism of benzonitrile formation from the reaction of benzene and CN,^{34,37} although it does differ from the reaction between toluene and OH, which features both prereactive complexes and barriers before formation of the addition product.³⁸ The energies determined for the addition–elimination channels are generally similar to those calculated for the CN + benzene reaction done at G3//B3LYP and BCCSD(T)//B3LYP.³⁴

Abstraction pathways, shown in blue in Figure 4, were found to have slightly submerged transition states and, therefore, are possible products at low temperatures. However, higher level calculations are needed to confirm these barrier values, as similar abstraction pathways from aromatic compounds have been shown to possess positive barriers.^{37,38} At the level of theory used, these barrier values are likely within the error of the calculations. An important point to note is that no transition state or complex could be characterized for the abstraction channels, though we do not rule out the existence of these stationary points.

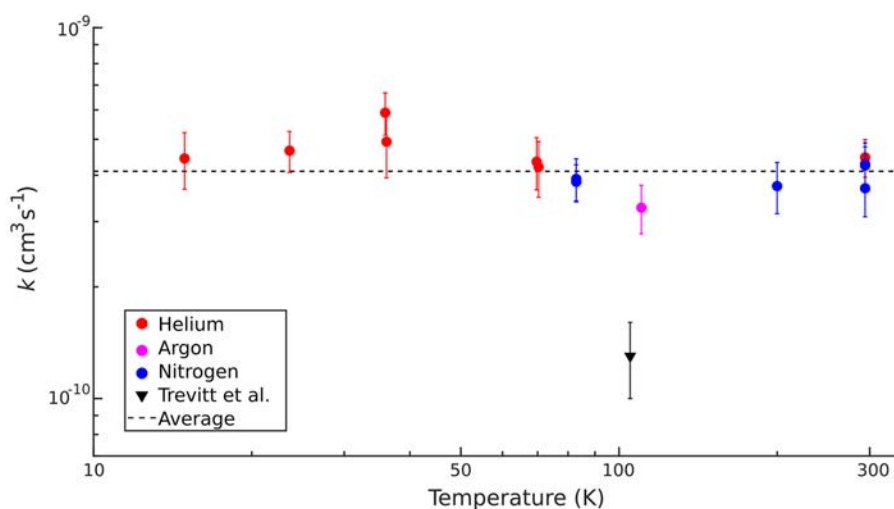


Figure 3. Experimental measurements for the CN + toluene rate constant from this work (●) and Trevitt et al. (▼); the weighted average value of the measurements presented in this work, $4.1 \times 10^{-10} \text{ cm}^3 \text{ s}^{-1}$, is also plotted.

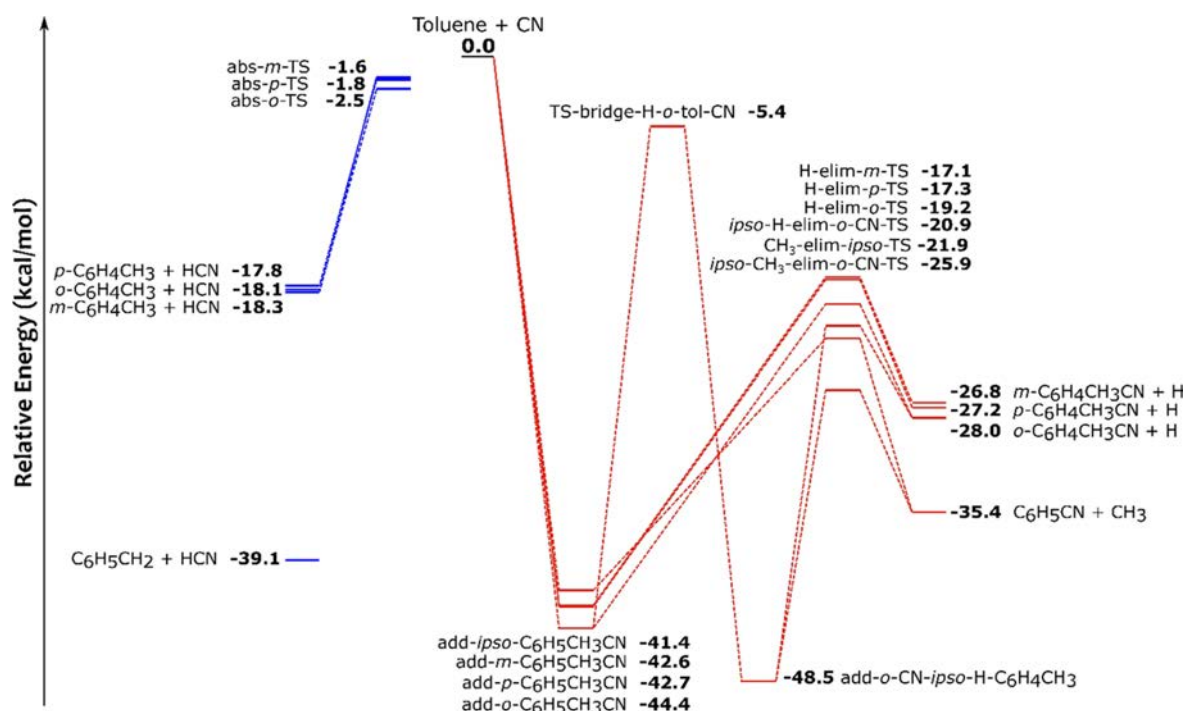


Figure 4. Stationary points for PES for the CN + toluene reaction, performed at (U)M06-2X/aug-cc-pVTZ including zero-point energy corrections, showing the abstraction (abs) pathways (blue) and addition–elimination (add and elim) pathways (red), the latter of which can undergo an internal hydrogen shift (bridge). Note that neither a barrier leading to the formation of $\text{C}_6\text{H}_5\text{CH}_2 + \text{HCN}$ nor any prereactive complexes for the abstraction pathways are included, though we do not preclude their existence.

DISCUSSION

As Figure 3 demonstrates, we find that the rate constant of the CN + toluene reaction is independent of temperature over the 15–294 K range, with a weighted average value of $(4.1 \pm 0.2) \times 10^{-10} \text{ cm}^3 \text{ s}^{-1}$. Our results are in contrast to the results of Trevitt et al., who measured a rate constant of $(1.3 \pm 0.3) \times 10^{-10} \text{ cm}^3 \text{ s}^{-1}$ at 105 K in their LIF experiments. They used a similar LIF method to detect CN, under similar experimental conditions of total density, and CN and toluene concentrations. Furthermore, this group measured CN + benzene rate

constants that agree well with recent results from our group,²³ which suggests that this discrepancy is related to the toluene system.

Trevitt et al. reported observing nonexponential decays of CN at room temperature, which they suggested might be due to back-dissociation of adduct complexes. However, no such behavior was observed in this work, suggesting that the discrepancy might have arisen from differences in the photolysis step. Trevitt et al. photolyzed their sample at a wavelength of 266 nm, with a laser fluence of 40 mJ cm^{-2} (5.0

Table 2. Zero-Point Corrected Reaction Energies and Gibbs Energies of the Reaction Products Calculated in This Work^a

reaction channel products	reaction energy $\Delta_r U^{\circ}$ (kcal mol ⁻¹)	Gibbs energy $\Delta_r G^{\circ}$ (298 K) (kcal mol ⁻¹)
(<i>o</i> -C ₆ H ₄ CH ₃ + HCN) (R1)	-18.1	-18.1
(<i>m</i> -C ₆ H ₄ CH ₃ + HCN) (R2)	-18.3	-18.6
(<i>p</i> -C ₆ H ₄ CH ₃ + HCN) (R3)	-17.8	-18.2
(C ₆ H ₅ CH ₂ + HCN) (R4)	-39.1	-38.1
(= R5c, <i>o</i> -C ₆ H ₄ CH ₃ CN + H) (R5a)	-28.0	-23.6
(= R8, C ₆ H ₅ CN + CH ₃) (R5b)	-35.4	-35.5
(= R5a, <i>o</i> -C ₆ H ₄ CH ₃ CN + H) (R5c)	-28.0	-23.6
(<i>m</i> -C ₆ H ₄ CH ₃ CN + H) (R6)	-26.8	-22.5
(<i>p</i> -C ₆ H ₄ CH ₃ CN + H) (R7)	-27.2	-23.8
(= R5b, C ₆ H ₅ CN + CH ₃) (R8)	-35.4	-35.5

^aNote that some reaction pathways result in the same products.

$\times 10^{16}$ photons cm⁻², in a probable 3–6 ns long pulse), in contrast to the 248 nm laser beam with a fluence of 25 mJ cm⁻² (3.1×10^{16} photons cm⁻², 22 ns long pulse) used in this work. The ICN photolysis cross sections are similar at these two wavelengths.^{28,39} At room temperature, the toluene absorption cross section to the S₁ state at 266 nm is 1.3×10^{-19} cm².⁴⁰ The S₁ state fluoresces with a lifetime of 86 ns when excited at 266 nm at low pressures.⁴¹ At 248 nm, the cross section is larger (2.9×10^{-19} cm²),⁴⁰ but the fluorescence lifetime is much shorter due to rapid internal conversion to S₀, displaying approximately equal intensity 3 and 26 ns components at low pressures.⁴² As discussed above, multiphoton absorption at 248 nm of toluene is known to lead to photolysis³⁶ and may additionally lead to photoionization, as the excited toluene is higher in energy than the ionization onset of toluene (8.3 eV).⁴³ Both of these processes are also likely to occur in the 266 nm experiments.

The above considerations suggest that single-photon excitation of toluene is occurring at both photolysis wavelengths, but only multiphoton effects are likely to give rise to interferences. Possible pathways for CN generation on the time scale of the experiment exist by either two-photon photodissociation or two-photon ionization, particularly at 266 nm by quadrupled Nd:YAG lasers. Such effects are likely to be significantly lower when toluene is excited at 248 nm light produced by an excimer, due to the longer pulse duration and rapid internal conversion of the S₁ state. This is in good agreement with the experimental measurements reported here, showing no relationship between excimer power and k_{first} and no evidence for nonexponential decays. In the experiments of Trevitt et al. at 266 nm, however, the long lifetime of the S₁ state, short photolysis pulse duration, and higher laser fluence may have caused larger amounts of multiphoton absorption to occur, such that photodissociation or photoionization products could have affected their measurements for toluene. Such effects would not be observed upon 266 nm excitation of benzene, however, as 266 nm lies below the absorption threshold for the benzene S₁ state; so, two-photon dissociation would have to occur by a nonresonant process.

Further work from Trevitt et al. measured branching ratios at room temperature, using slow flow reactors in conjunction

with product detection by multiplexed photoionization mass spectrometry (MPIMS) to identify species by mass and photoionization spectrum. They found that the reaction between CN and toluene exclusively forms tolunitrile (methylbenzonitrile), with no evidence for the hydrogen abstraction channels or for benzonitrile formation. Due to the similarities in the calculated photoionization spectra of the *ortho*, *meta*, and *para* isomers of the tolunitrile, they were unable to distinguish the precise isomers of tolunitrile formed from this reaction. They found a similar result for the reaction of CN with benzene, with benzonitrile being the only detected product. Lenis and Miller also measured the products of the CN + toluene reaction, using the 254 nm photolysis of ICN and analyzing the resulting products with GC-MS,⁴⁴ and observed both tolunitrile and a small yield (9%) of benzonitrile. While it is unclear if this benzonitrile is formed as a result of CN + toluene or side chemistry, particularly in light of its nondetection in the MPIMS experiments by Trevitt et al., our calculations do show potential pathways to benzonitrile formation from *ortho* or *ipso* addition of CN to the aromatic ring.

The rate constants measured here are in good agreement with the value of $(4.4 \pm 0.2) \times 10^{-10}$ cm³ s⁻¹, independent of temperature over the 15–295 K range, that we determined for the reaction between CN and benzene.²³ In conjunction with the similarities in products measured by MPIMS, this suggests that the major mechanism is the same for reactions between the CN radical and either benzene or toluene, and results in formation of cyano-substituted aromatic compounds. Investigation of other substituted compounds, such as xylenes or deuterium-substituted benzene, may yield further insight into whether this mechanism is general for these reactions. This will aid in future astronomical searches to improve our understanding of the formation of small aromatic rings in the ISM.

The submerged barriers found for the various channels using quantum chemical calculations highlight the diversity of the products that could be formed from this reaction at low temperatures. While the abstraction channels were found to have slightly submerged barriers, calculations at a higher level of theory are necessary to correctly estimate their energies. Furthermore, the transition state(s) and/or a possible complex in the case of the hydrogen abstraction from the methyl group pathway remain to be explored further. This will also provide the accuracy necessary for master equation calculations, which would further elucidate the mechanism and product branching ratios of this reaction.

On Titan, the CN radical is mainly generated from the photolysis of HCN, which is formed through reactions of N(⁴S) or through ion chemistry.^{4,5} Once formed, CN reacts primarily with the highly abundant CH₄ to re-form HCN. This cycle can be interrupted, however, by CN reactions with other compounds, most commonly C₂H₂ or HC₃N. While this reaction has not explicitly been included in models, recent work has suggested that the concentrations of benzene and toluene in the Titan atmosphere are similar, peaking at a mole fraction of 10⁻⁶ at an altitude of roughly 1000 km above the surface.¹¹ Benzonitrile has not been detected on Titan and is predicted to be formed in low quantities, largely due to CN being sequestered by reaction with CH₄. Even with the larger rate constants measured in this work, this is likely also the case for the products of the reaction between CN and toluene, though implementation of these results into Titan models may

still be beneficial to determine if they have any influence in the atmosphere.

Astronomical searches for toluene and the tolunitrile products of this reaction would test the robustness of using cyano-containing species as proxies for the unsubstituted hydrocarbons. While benzene has no permanent dipole moment, toluene has a small one (0.37 D)⁴⁵ and may be observable via radio astronomy, though it would have to be present in higher abundance than, say, benzonitrile, to be detectable. The use of velocity stacking, which averages the signal of multiple transitions together to increase the signal-to-noise ratio,^{46–48} may assist in searching for toluene in the ISM. While there have been no previous detections of toluene in the ISM, it has been argued that the protonated toluene ion, C₇H₉⁺,⁴⁹ and methyl-substituted PAHs^{50,51} are possible carriers of the 6.2 and the 3.4 μm unidentified infrared bands, respectively. Definitive detection of toluene and related compounds, such as these, would allow us to constrain aromatic pathways and, in particular, could test the bottom-up mechanism for PAH formation, wherein small molecules, such as toluene, react progressively to form large clusters.

The origin of the first aromatic ring in the interstellar medium in molecules such as benzene and toluene remains unknown. It has been argued that the reaction between C₂H and isoprene (C₅H₈; 2-methyl-1,3-butadiene), a barrierless reaction that produces toluene, may be a source of it at low temperatures,⁵² but it is unknown whether isoprene is present in the ISM: Isoprene is not included in astrochemical databases such as the Kinetic Database for Astrochemistry⁵³ (kida.obs.u-bordeaux1.fr, accessed July 2020). Other mechanisms, such as ion-neutral reactions, may also contribute, but further investigation is necessary.

In order to better understand the potential formation pathways of these products of this reaction in the ISM, more accurate measurements of the product ratios are required and, specifically, the branching ratio for the tolunitrile and potential benzonitrile products. While challenging for many techniques due to the similarities of the isomers, recent work has coupled low temperature supersonic uniform flows to microwave spectrometers^{54,55} in order to determine branching ratios relevant for astrochemistry. As each of these compounds will have a unique rotational spectrum, this technique is well-suited for quantitatively measuring the product branching ratio of this reaction.

CONCLUSIONS

We have measured rate constants for the CN + toluene reaction between 15 and 294 K and find that the rate constant is independent of temperature over this range. These results closely match our recent study on the reaction of CN with benzene but are higher than the only previous measurement of this rate constant at 105 K, for reasons that remain unresolved but may be related to multiphoton effects at the higher laser intensities and 266 nm photolysis wavelength used in that study. This similarly suggests that the reactions between CN and simple aromatics proceed through an analogous mechanism, which is supported by our theoretical calculations and previous product measurements. Further work, particularly on the products formed from this reaction, would be beneficial to determine their potential detectability in the ISM. The ability to detect and use cyano-substituted aromatics, which have large dipole moments, as proxies for unsubstituted

aromatic compounds in the ISM would help advance our knowledge of PAH formation.

ASSOCIATED CONTENT

Supporting Information

The Supporting Information is available free of charge at <https://pubs.acs.org/doi/10.1021/acs.jpca.0c06900>.

Geometries of calculated structures for all molecules and transition states (PDF)

AUTHOR INFORMATION

Corresponding Authors

Mitchio Okumura – Arthur Amos Noyes Laboratory of Chemical Physics, Division of Chemistry and Chemical Engineering, California Institute of Technology, Pasadena, California 91125, United States; orcid.org/0000-0001-6874-1137; Email: mo@caltech.edu

Ian R. Sims – Univ Rennes, CNRS, IPR (Institut de Physique de Rennes) - UMR 6251, F-35000 Rennes, France; orcid.org/0000-0001-7870-1585; Email: ian.sims@univ-rennes1.fr

Authors

Joseph P. Messinger – Arthur Amos Noyes Laboratory of Chemical Physics, Division of Chemistry and Chemical Engineering, California Institute of Technology, Pasadena, California 91125, United States; Univ Rennes, CNRS, IPR (Institut de Physique de Rennes) - UMR 6251, F-35000 Rennes, France; orcid.org/0000-0001-7305-3945

Divita Gupta – Univ Rennes, CNRS, IPR (Institut de Physique de Rennes) - UMR 6251, F-35000 Rennes, France; orcid.org/0000-0002-6639-4909

Ilsa R. Cooke – Univ Rennes, CNRS, IPR (Institut de Physique de Rennes) - UMR 6251, F-35000 Rennes, France; orcid.org/0000-0002-0850-7426

Complete contact information is available at: <https://pubs.acs.org/10.1021/acs.jpca.0c06900>

Notes

The authors declare no competing financial interest.

ACKNOWLEDGMENTS

The authors thank Jonathan Courbe, Jonathan Thiévin, Didier Biet, Ewen Gallou, and Alexandre Dapp for technical support. We would like to acknowledge Mayank Saraswat for helpful discussions regarding the PES calculations. J.P.M. was supported by the National Science Foundation Graduate Research Fellowship (NSF GRP) and the National Science Foundation Graduate Research Opportunities Worldwide (NSF GROW) programs. J.P.M. would also like to thank the Office of Science and Technology of the Embassy of France in the United States for a Chateaubriand Fellowship. The authors acknowledge funding from the European Union's Horizon 2020 research and innovation programme under the European Research Council (ERC) grant agreement 695724-CRESU-CHIRP and under the Marie Skłodowska-Curie grant agreement 845165-MIRAGE. Acknowledgment is made to the donors of The American Chemical Society Petroleum Research Fund for partial support of this research. The authors are also grateful for support from the European Regional Development Fund, the Region of Brittany, and Rennes Métropole. This work was supported by the French National Programme "Physique et Chimie du Milieu Interstellaire"

(PCMI) of CNRS/INSU with INC/INP cofunded by CEA and CNES.

REFERENCES

- (1) Adams, W. S. Some Results with the Coude Spectrograph of the Mount Wilson Observatory. *Astrophys. J.* **1941**, *93*, 11–23.
- (2) McKellar, A. Evidence for the Molecular Origin of Some Hitherto Unidentified Interstellar Lines. *Publ. Astron. Soc. Pac.* **1940**, *52*, 187–192.
- (3) Yung, Y. L.; Allen, M.; Pinto, J. P. Photochemistry of the Atmosphere of Titan - Comparison between Model and Observations. *Astrophys. J., Suppl. Ser.* **1984**, *55*, 465–506.
- (4) Loison, J. C.; Hebrard, E.; Dobrijevic, M.; Hickson, K. M.; Caralp, F.; Hue, V.; Gronoff, G.; Venot, O.; Benilan, Y. The Neutral Photochemistry of Nitriles, Amines and Imines in the Atmosphere of Titan. *Icarus* **2015**, *247*, 218–247.
- (5) Wilson, E. H.; Atreya, S. K. Current State of Modeling the Photochemistry of Titan's Mutually Dependent Atmosphere and Ionosphere. *J. Geophys. Res.* **2004**, *109*, E06002.
- (6) Cooke, I. R.; Sims, I. R. Experimental Studies of Gas-Phase Reactivity in Relation to Complex Organic Molecules in Star-Forming Regions. *ACS Earth Space Chem.* **2019**, *3*, 1109–1134.
- (7) Broten, N. W.; Oka, T.; Avery, L. W.; Macleod, J. M.; Kroto, H. W. The Detection of HC9N in Interstellar Space. *Astrophys. J.* **1978**, *223*, L105–L107.
- (8) Belloche, A.; Garrod, R. T.; Muller, H. S. P.; Menten, K. M. Detection of a Branched Alkyl Molecule in the Interstellar Medium: Iso-Propyl Cyanide. *Science* **2014**, *345*, 1584–1587.
- (9) Gudipati, M. S.; Jacovi, R.; Couturier-Tamburelli, I.; Lignell, A.; Allen, M. Photochemical Activity of Titan's Low-Altitude Condensed Haze. *Nat. Commun.* **2013**, *4*, 1648.
- (10) Magee, B. A.; Waite, J. H.; Mandt, K. E.; Westlake, J.; Bell, J.; Gell, D. A. INMS-Derived Composition of Titan's Upper Atmosphere: Analysis Methods and Model Comparison. *Planet. Space Sci.* **2009**, *57*, 1895–1916.
- (11) Loison, J. C.; Dobrijevic, M.; Hickson, K. M. The Photochemical Production of Aromatics in the Atmosphere of Titan. *Icarus* **2019**, *329*, 55–71.
- (12) Lopez-Puertas, M.; Dinelli, B. M.; Adriani, A.; Funke, B.; Garcia-Comas, M.; Moriconi, M. L.; D'Aversa, E.; Boersma, C.; Allamandola, L. J. Large Abundances of Polycyclic Aromatic Hydrocarbons in Titan's Upper Atmosphere. *Astrophys. J.* **2013**, *770*, 132.
- (13) Wilson, E. H.; Atreya, S. K. Chemical Sources of Haze Formation in Titan's Atmosphere. *Planet. Space Sci.* **2003**, *51*, 1017–1033.
- (14) Cernicharo, J.; Heras, A. M.; Tielens, A. G. G. M.; Pardo, J. R.; Herpin, F.; Guelin, M.; Waters, L. B. F. M. Infrared Space Observatory's Discovery of C4H2, C6H2, and Benzene in CRL 618. *Astrophys. J.* **2001**, *546*, L123–L126.
- (15) Lovas, F. J.; McMahon, R. J.; Grabow, J. U.; Schnell, M.; Mack, J.; Scott, L. T.; Kuczkowski, R. L. Interstellar Chemistry: A Strategy for Detecting Polycyclic Aromatic Hydrocarbons in Space. *J. Am. Chem. Soc.* **2005**, *127*, 4345–4349.
- (16) Chiar, J. E.; Tielens, A. G. G. M.; Adamson, A. J.; Ricca, A. The Structure, Origin, and Evolution of Interstellar Hydrocarbon Grains. *Astrophys. J.* **2013**, *770*, 78.
- (17) Dwek, E.; et al. Detection and Characterization of Cold Interstellar Dust and Polycyclic Aromatic Hydrocarbon Emission, from COBE Observations. *Astrophys. J.* **1997**, *475*, 565–579.
- (18) Wakelam, V.; Herbst, E. Polycyclic Aromatic Hydrocarbons in Dense Cloud Chemistry. *Astrophys. J.* **2008**, *680*, 371–383.
- (19) Kaiser, R. I.; Parker, D. S. N.; Mebel, A. M. Reaction Dynamics in Astrochemistry: Low-Temperature Pathways to Polycyclic Aromatic Hydrocarbons in the Interstellar Medium. *Annu. Rev. Phys. Chem.* **2015**, *66*, 43–67.
- (20) Tielens, A. G. G. M. Interstellar Polycyclic Aromatic Hydrocarbon Molecules. *Annu. Rev. Astron. Astrophys.* **2008**, *46*, 289–337.
- (21) Tielens, A. G. G. M.; Charnley, S. B. Circumstellar and Interstellar Synthesis of Organic Molecules. *Origins Life Evol. Biospheres* **1997**, *27*, 23–51.
- (22) McGuire, B. A.; Burkhardt, A. M.; Kalenskii, S.; Shingledecker, C. N.; Remijan, A. J.; Herbst, E.; McCarthy, M. C. Detection of the Aromatic Molecule Benzonitrile (C-C6H5CN) in the Interstellar Medium. *Science* **2018**, *359*, 202–205.
- (23) Cooke, I. R.; Gupta, D.; Messenger, J. P.; Sims, I. R. Benzonitrile as a Proxy for Benzene in the Cold Ism: Low-Temperature Rate Coefficients for CN + C6H6. *Astrophys. J., Lett.* **2020**, *891*, L41.
- (24) Trevitt, A. J.; Goulay, F.; Taatjes, C. A.; Osborn, D. L.; Leone, S. R. Reactions of the CN Radical with Benzene and Toluene: Product Detection and Low-Temperature Kinetics. *J. Phys. Chem. A* **2010**, *114*, 1749–1755.
- (25) James, P. L.; Sims, I. R.; Smith, I. W. M.; Alexander, M. H.; Yang, M. B. A Combined Experimental and Theoretical Study of Rotational Energy Transfer in Collisions between NO(X(2)Pi(1/2), V = 3J) and He, Ar and N2 at Temperatures Down to 7 K. *J. Chem. Phys.* **1998**, *109*, 3882–3897.
- (26) Sims, I. R.; Queffelec, J. L.; Defrance, A.; Rebrionrowe, C.; Travers, D.; Bocherel, P.; Rowe, B. R.; Smith, I. W. M. Ultralow Temperature Kinetics of Neutral-Neutral Reactions - the Technique and Results for the Reactions CN+O2 Down to 13 K and CN+NH3 Down to 25 K. *J. Chem. Phys.* **1994**, *100*, 4229–4241.
- (27) Gupta, D.; Cheikh Sid Ely, S.; Cooke, I. R.; Guillaume, T.; Abdelkader Khedaoui, O.; Hearne, T. S.; Hays, B. M.; Sims, I. R. Low Temperature Kinetics of the Reaction between Methanol and the CN Radical. *J. Phys. Chem. A* **2019**, *123*, 9995–10003.
- (28) Felps, W. S.; Rupnik, K.; Mcglynn, S. P. Electronic Spectroscopy of the Cyanogen Halides. *J. Phys. Chem.* **1991**, *95*, 639–656.
- (29) O'Halloran, M. A.; Joswig, H.; Zare, R. N. Alignment of CN from 248 nm Photolysis of ICN - a New Model of the a Continuum Dissociation Dynamics. *J. Chem. Phys.* **1987**, *87*, 303–313.
- (30) Frisch, M. J.; et al. *Gaussian 09*; Gaussian, Inc.: Wallingford, CT, 2009.
- (31) Kendall, R. A.; Dunning, T. H.; Harrison, R. J. Electron-Affinities of the 1st-Row Atoms Revisited - Systematic Basis-Sets and Wave-Functions. *J. Chem. Phys.* **1992**, *96*, 6796–6806.
- (32) Woon, D. E.; Dunning, T. H. Gaussian-Basis Sets for Use in Correlated Molecular Calculations 3. The Atoms Aluminum through Argon. *J. Chem. Phys.* **1993**, *98*, 1358–1371.
- (33) Zhao, Y.; Truhlar, D. G. The M06 Suite of Density Functionals for Main Group Thermochemistry, Thermochemical Kinetics, Noncovalent Interactions, Excited States, and Transition Elements: Two New Functionals and Systematic Testing of Four M06-Class Functionals and 12 Other Functionals. *Theor. Chem. Acc.* **2008**, *120*, 215–241.
- (34) Lee, K. L. K.; McGuire, B. A.; McCarthy, M. C. Gas-Phase Synthetic Pathways to Benzene and Benzonitrile: A Combined Microwave and Thermochemical Investigation. *Phys. Chem. Chem. Phys.* **2019**, *21*, 2946–2956.
- (35) Koban, W.; Koch, J. D.; Hanson, R. K.; Schulz, C. Absorption and Fluorescence of Toluene Vapor at Elevated Temperatures. *Phys. Chem. Chem. Phys.* **2004**, *6*, 2940–2945.
- (36) Kovacs, T.; Blitz, M. A.; Seakins, P. W.; Pilling, M. J. H Atom Formation from Benzene and Toluene Photoexcitation at 248 nm. *J. Chem. Phys.* **2009**, *131*, 204304.
- (37) Woon, D. E. Modeling Chemical Growth Processes in Titan's Atmosphere: 1. Theoretical Rates for Reactions between Benzene and the Ethynyl (C2H) and Cyano (CN) Radicals at Low Temperature and Pressure. *Chem. Phys.* **2006**, *331*, 67–76.
- (38) Zhang, R. M.; Truhlar, D. G.; Xu, X. F. Kinetics of the Toluene Reaction with OH Radical. *Research-China* **2019**, *2019*, 1.
- (39) Myer, J. A.; Samson, J. A. R. Vacuum-Ultraviolet Absorption Cross Sections of CO, HCl, and ICN between 1050 and 2100 Å. *J. Chem. Phys.* **1970**, *52*, 266.

- (40) Fally, S.; Carleer, M.; Vandaele, A. C. UV Fourier Transform Absorption Cross Sections of Benzene, Toluene, Meta-, Ortho-, and Para-Xylene. *J. Quant. Spectrosc. Radiat. Transfer* **2009**, *110*, 766–782.
- (41) Hickman, C. G.; Gascooke, J. R.; Lawrance, W. D. The S1-S0(1b2–1a1) Transition of Jet-Cooled Toluene: Excitation and Dispersed Fluorescence Spectra, Fluorescence Lifetimes, and Intramolecular Vibrational Energy Redistribution. *J. Chem. Phys.* **1996**, *104*, 4887–4901.
- (42) Jacon, M.; Lardeux, C.; Lopez-Delgado, R.; Tramer, A. On the “third decay channel” and vibrational redistribution problems in benzene derivatives. *Chem. Phys.* **1977**, *24*, 145–157.
- (43) Lu, K. T.; Eiden, G. C.; Weisshaar, J. C. Toluene Cation - Nearly Free Rotation of the Methyl-Group. *J. Phys. Chem.* **1992**, *96*, 9742–9748.
- (44) Henis, N. B. H.; Miller, L. L. Mechanism of Gas-Phase Cyanation of Alkenes and Aromatics. *J. Am. Chem. Soc.* **1983**, *105*, 2820–2823.
- (45) Rudolph, H. D.; Dreizler, H.; Jaeschke, A.; Wendung, P. Mikrowellenspektrum Hinderungspotential Der Internen Rotation Und Dipolmoment Des Toluols. *Z. Naturforsch., A: Phys. Sci.* **1967**, *22*, 940.
- (46) Loomis, R. A.; et al. Non-Detection of Hc11n Towards Tmc-1: Constraining the Chemistry of Large Carbon-Chain Molecules. *Mon. Not. R. Astron. Soc.* **2016**, *463*, 4175–4183.
- (47) Walsh, C.; Loomis, R. A.; Oberg, K. L.; Kama, M.; van 't Hoff, M. L. R.; Millar, T. J.; Aikawa, Y.; Herbst, E.; Widicus Weaver, S. L.; Nomura, H. First Detection of Gas-Phase Methanol in a Protoplanetary Disk. *Astrophys. J., Lett.* **2016**, *823*, L10.
- (48) Langston, G.; Turner, B. Detection of ¹³C Isotopomers of the Molecule HC7N. *Astrophys. J.* **2007**, *658*, 455–461.
- (49) Douberly, G. E.; Ricks, A. M.; Schleyer, P. V. R.; Duncan, M. A. Infrared Spectroscopy of Gas Phase Benzenium Ions: Protonated Benzene and Protonated Toluene, from 750 to 3400 cm⁻¹. *J. Phys. Chem. A* **2008**, *112*, 4869–4874.
- (50) Joblin, C.; Tielens, A. G. G. M.; Allamandola, L. J.; Geballe, T. R. Spatial Variation of the 3.29 and 3.40 Micron Emission Bands within Reflection Nebulae and the Photochemical Evolution of Methylated Polycyclic Aromatic Hydrocarbons. *Astrophys. J.* **1996**, *458*, 610–620.
- (51) Wagner, D. R.; Kim, H. S.; Saykally, R. J. Peripherally Hydrogenated Neutral Polycyclic Aromatic Hydrocarbons as Carriers of the 3 Micron Interstellar Infrared Emission Complex: Results from Single-Photon Infrared Emission Spectroscopy. *Astrophys. J.* **2000**, *545*, 854–860.
- (52) Dangi, B. B.; Parker, D. S.; Kaiser, R. I.; Jamal, A.; Mebel, A. M. A Combined Experimental and Theoretical Study on the Gas-Phase Synthesis of Toluene under Single Collision Conditions. *Angew. Chem., Int. Ed.* **2013**, *52*, 7186–9.
- (53) Wakelam, V. A Kinetic Database for Astrochemistry (KIDA). *Astrophys. J., Suppl. Ser.* **2012**, *199*, 21.
- (54) Abeysekera, C.; Joalland, B.; Ariyasingha, N.; Zack, L. N.; Sims, I. R.; Field, R. W.; Suits, A. G. Product Branching in the Low Temperature Reaction of CN with Propyne by Chirped-Pulse Microwave Spectroscopy in a Uniform Supersonic Flow. *J. Phys. Chem. Lett.* **2015**, *6*, 1599–1604.
- (55) Hays, B. M.; Guillaume, T.; Hearne, T. S.; Cooke, I. R.; Gupta, D.; Abdalkader Khedaoui, O.; Le Picard, S. D.; Sims, I. R. Design and Performance of an E-Band Chirped Pulse Spectrometer for Kinetics Applications: OCS - He Pressure Broadening. *J. Quant. Spectrosc. Radiat. Transfer* **2020**, *250*, 107001.